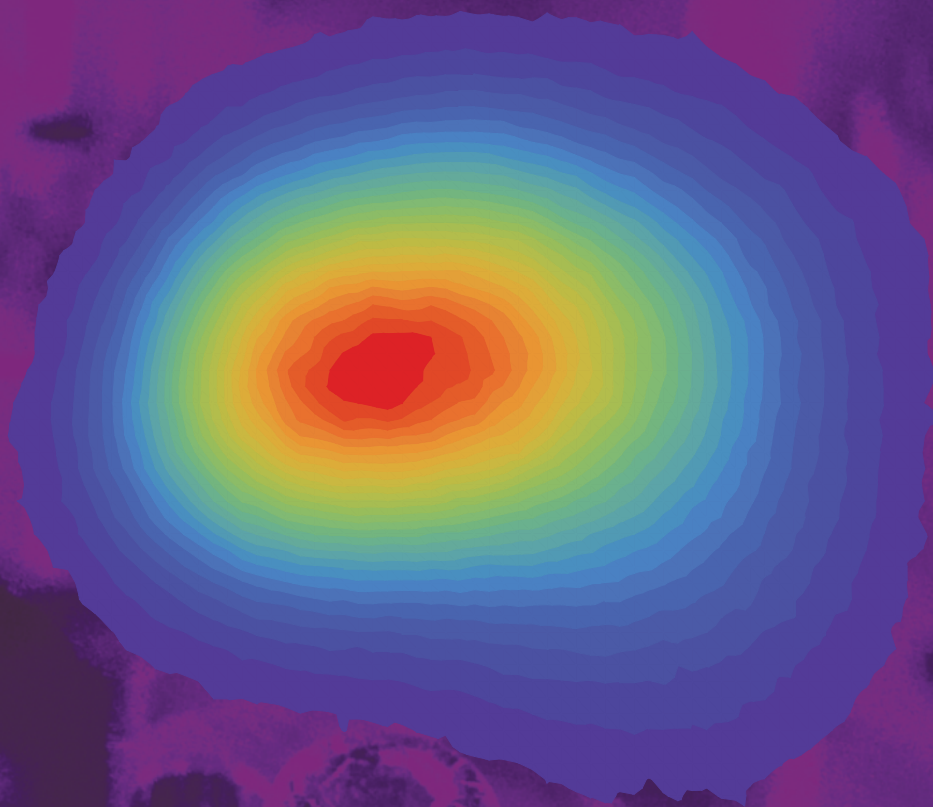


Simon Hofsäss

Laser Cooling of Atoms and Molecules in the Deep Ultraviolet



Laser Cooling of Atoms and Molecules in the Deep Ultraviolet
PhD Thesis, Radboud Universiteit, Nijmegen, The Netherlands

© 2023 Simon Lennart Tonio Hofsäas
ISBN: 978-94-6473-291-7
Printed by Ipskamp Printing, Enschede

The cover design features a colorized photograph of a cloud of about 10 million cadmium atoms, taken during laser cooling in a magneto-optical trap by imaging the fluorescence radiation.

The work described in this thesis has been performed in the Molecular Physics department at the Fritz Haber Institute of the Max Planck Society in Berlin, Germany.

FRITZ-HABER-INSTITUT
MAX-PLANCK-GESELLSCHAFT



Laser cooling of atoms and molecules in the deep ultraviolet

Proefschrift ter verkrijging van de graad van doctor
aan de Radboud Universiteit Nijmegen
op gezag van de rector magnificus prof. dr. J.M. Sanders,
volgens besluit van het college voor promoties
in het openbaar te verdedigen op
maandag 4 december 2023
om 16:30 uur precies

door

Simon Lennart Tonio Hofsäss

geboren op 8 februari 1991
te Freiburg im Breisgau, Duitsland

Promotor: Prof. dr. G.J.M. Meijer

Copromotor: Dr. S. Truppe (*Imperial College London, Verenigd Koninkrijk*)

Manuscriptcommissie:

Prof. dr. S.Y.T. van de Meerakker

Dr. K. Erath-Dulitz (*Universität Innsbruck, Oostenrijk*)

Dr. G. Valtolina (*Fritz-Haber-Institut der Max-Planck-Gesellschaft, Duitsland*)

Laser cooling of atoms and molecules in the deep ultraviolet

Dissertation to obtain the degree of doctor
from Radboud University Nijmegen
on the authority of the Rector Magnificus prof. dr. J.M. Sanders,
according to the decision of the Doctorate Board
to be defended in public on
Monday, December 4, 2023
at 4:30 pm

by

Simon Lennart Tonio Hofsäss

born on February 8, 1991
in Freiburg im Breisgau, Germany

Supervisor: Prof. dr. G.J.M. Meijer

Co-supervisor: Dr. S. Truppe (*Imperial College London, United Kingdom*)

Manuscript Committee:

Prof. dr. S.Y.T. van de Meerakker

Dr. K. Erath-Dulitz (*University of Innsbruck, Austria*)

Dr. G. Valtolina (*Fritz Haber Institute of the Max Planck Society, Germany*)

Contents

1	Introduction	1
1.1	Motivation	2
1.2	Cold atoms and molecules	4
1.3	Laser cooling of AlF molecules	6
1.4	Cadmium as an intermediate test candidate	9
1.5	Thesis outline	10
2	Molecular structure of AlF	13
2.1	Introduction	13
2.2	Early characterization of AlF	17
2.3	The molecular Hamiltonian	20
3	Experimental setup	31
3.1	Introduction	31
3.2	Pre-cooling molecules	32
3.3	Choosing a molecular beam source	33
3.4	Laser system	39
3.5	Laser induced fluorescence detector	40
3.6	Buffer gas machine characterization	46
3.7	Velocity distribution of the AlF beam	56
3.8	Summary	62
4	Optical cycling of AlF molecules	65
4.1	Introduction	65
4.2	Calibration of laser-induced fluorescence	67
4.3	Leaks from the optical cycle to $v'' = 1$	71
4.4	Other loss channels	78
4.5	Optical cycling rate	87
4.6	Summary	100

5	Isotope-shift spectroscopy on an atomic beam of cadmium	103
5.1	Introduction	103
5.2	Historical background	107
5.3	Theoretical background	108
5.4	Experimental setup	111
5.5	Atomic beam spectroscopy	114
5.6	Summary	134
6	Deep-UV magneto-optical trap for cadmium atoms	137
6.1	Introduction	137
6.2	Laser cooling theory	140
6.3	Experimental setup	148
6.4	MOT characterization	154
6.5	Summary	175
6.6	Outlook	177
	Summary	179
	Samenvatting	181
	Bibliography	183
	Curriculum Vitae	211
	List of Publications	213
	Acknowledgements	215

Chapter 1

Introduction

This thesis studies aspects of the interaction of light with matter—one of the most fundamental processes in nature. A detailed understanding of the properties of atoms and molecules can be achieved by spectroscopic studies in the gas phase, for example, in a collimated beam. These studies can reveal ever greater detail when ever better control over the motion of the species is achieved. A configuration of laser beams can control the movement of atoms and molecules in three dimensions, which is the process of laser cooling. Atoms and molecules can be slowed from hundreds of meters per second, their typical speed at room temperature, to almost a standstill. This increases the available interaction time and improves the accuracy of spectroscopic measurements accordingly. The temperature of a trapped gas can be lowered such that the thermal de Broglie wavelength exceeds the inter-particle distance and wave packets of particles begin to overlap. With further cooling, bosons condense into a single quantum state, which has been extensively studied in atomic physics but is still a long-standing goal for molecular physics [1]. The work in this thesis rep-

resents the first steps in demonstrating that the diatomic molecule aluminum monofluoride (AlF) can be laser cooled and trapped at high density. Tools and techniques to control this molecule are established using cadmium (Cd) atoms as a test system.

1.1 Motivation

Over the past few decades, many atomic species have been laser-cooled and are currently used for precision spectroscopy, quantum computing, and metrology applications [2–5]; precise instruments, such as atomic clocks, magnetometers, gravimeters, and accelerometers, have been developed [6–10]. In recent years, substantial progress has been made in the development of techniques for directly cooling molecules instead of associating ultracold, laser-cooled atoms to a molecule. In addition, complementary tools for classes of molecules that can not be laser-cooled have been developed, such as Stark and Zeeman deceleration and optoelectrical Sisyphus cooling [11–13]. Direct laser cooling of molecular ions is the subject of ongoing studies [14,15]. Precision measurements of atoms and ions are the foundation for measuring time* and can even be used to measure the stability of fundamental constants over time [17]. Ultracold molecules hold great promise for having a similarly profound impact on science and technology; for example, the rich internal energy level structure of molecules and their long-range dipolar interactions provide opportunities for quantum information science and quantum simulation [18–20]. Furthermore, the effective electric field experienced by the valence electron in polarized molecules such as

*“The second, symbol s, is the SI unit of time. It is defined by taking the fixed numerical value of the caesium frequency $\Delta\nu_{\text{Cs}}$, the unperturbed ground-state hyperfine transition frequency of the caesium-133 atom, to be 9192631770 when expressed in the unit Hz, which is equal to s^{-1} .” [16]

ThO, YbF, or HfF⁺ is significantly larger than in atoms [21–23]. This makes molecules more sensitive to symmetry-violating effects. Such molecules can be promising candidates for searches for new physics through permanent electric dipole moments of fundamental particles, such as the electron [24]. However, molecules also present new challenges: more sophisticated cooling mechanisms are needed, and beam sources are less efficient; as a result, the number of trapped molecules and the phase-space density in the trap are currently orders of magnitude lower than for atoms (see Chapter 4). In this thesis, I show how these obstacles can be overcome by choosing the AlF molecule as a candidate for laser cooling.

The AlF isotopologue ²⁷Al¹⁹F that we study in the laboratory has astronomical importance as it can be found in the photosphere of the sun and the circumstellar envelopes of carbon-rich stars such as IRC-10216 and CRL 2688 [25–28]. AlF is one of the main fluorine carriers in the gas phase in the outflow of evolved stars. Thus, the detection of AlF may lead to a better understanding of the nucleosynthesis production of fluorine in space [29]. Radioactive ²⁶Al has a lifetime of 7.2×10^5 years and can only be found in trace amounts on Earth, where it plays a role in dating the terrestrial age of small solar system bodies such as comets or meteorites. In connection to that, a recent study discovered the radioactive isotopologue ²⁶Al¹⁹F in the remnant of an ancient explosion in space [30]. This study identified stellar mergers as a galactic source of ²⁶Al. Since ²⁶Al¹⁹F has never been measured in the laboratory, the identification of this alien isotopologue is based on accurately known spectroscopic constants of ²⁷Al¹⁹F combined with the known isotopic scaling laws for these constants.

1.2 Cold atoms and molecules

The first experimental realization of controlling gas phase atoms with radiation is believed to have been in 1933, when Frisch[†] proved Einstein’s theory of radiation recoil [33]. He observed that light from a sodium lamp leads to the deflection of an atomic sodium beam by about 0.029 m/s per absorbed photon.[‡] This proved the particle-like behavior of light quanta and was followed by many more experiments using lasers in combination with various atomic and molecular beams [35–39].

Decades after Frisch’s experiments, in 1970, Ashkin proposed a scheme for translational control as well as quantum-state and isotope selection of atoms from an atomic beam by using the radiation pressure of high-intensity monochromatic light [40]. In 1975, Hänsch and Schawlow extended this scheme for cooling a low-density gas of neutral atoms using the radiation pressure of red-detuned pulsed lasers [41]. The temperature of such a laser-cooled gas depends on the detuning of the trapping laser frequency and its intensity. Both factors govern the rate at which photons are absorbed and emitted. At the same time, Wineland and Dehmelt proposed a scheme to cool ions in a Penning trap in all degrees of freedom to far below room temperature [42]. The first demonstration of three-dimensional laser cooling took another ten years. In 1985, Steven Chu and coworkers studied sodium atoms in an “optical mo-

[†]Otto Robert Frisch was an associate of Otto Stern in Hamburg at that time. In the same year, they also published their measurement of the magnetic moment of the proton [31]. Two days after the publication date, Frisch’s contract was terminated under Nazi racial laws. He emigrated to Great Britain soon after with the help of Stern [32].

[‡]Many years later, in 1995, sodium was one of the first atoms used to demonstrate Bose-Einstein condensation [34]. Wolfgang Ketterle shares the 2001 Nobel Prize in physics with Eric Cornell and Carl Wieman “for the achievement of Bose-Einstein condensation in dilute gases of alkali atoms, and for early fundamental studies of the properties of the condensates.”

lasses” [43].[§] By measuring the ballistic expansion of the atoms after switching off all confining fields, they determined a microkelvin translational temperature of the atoms. This corresponds to an increase in interaction time of a factor 10^4 .[¶] This research culminated in the experimental realization of a new state of matter, the Bose-Einstein condensate, in 1995 [1].

The history of direct laser cooling of molecules follows similar milestones as for atoms but at a significantly faster pace. The first directly laser-cooled molecule was SrF. From the first experimental measurement of a radiative force on this molecule in 2009 and transverse laser cooling in the next year, it took a total of five years until SrF was successfully loaded into a magneto-optical trap (MOT) at a temperature of 2.4 mK [37,44,45]. Albeit considered a “straightforward extension of atomic techniques”, the laser setup was significantly more sophisticated and included three additional vibrational repump lasers with radio-frequency sidebands for recovering population lost to optically dark states [45].^{||} In the following years, the list of laser-cooled molecules was extended with calcium monofluoride (CaF) molecules that were first laser slowed and then cooled to 50 μ K [46, 47]. Shortly after, other molecules such as yttrium oxide (YO) were trapped and laser-cooled [48]. Today the list of successfully laser-cooled diatomic molecules further contains YbF, BaH, CaH, and BaF [49] [39,49–51]. Several other candidates are being investigated, such as TlF, AlCl, CH, and MgF [52–57]. The list of polyatomic molecules considered by the community includes SrOH, YbOH, CaOCH₃, and CaOH, of which the latter has been successfully trapped [58–61]. In contrast to laser-coolable diatomic molecules,

[§]Chu shares the 1997 Nobel Prize in physics with William D. Phillips and Claude N. Cohen-Tannoudji “for development of methods to cool and trap atoms with laser light.”

[¶]Compared to a room temperature gas and a ≈ 1 cm diameter laser beam.

^{||}Atoms are usually not actual two-level systems as they also have an internal structure. However, one repump laser is sufficient for most cases.

polyatomics have parity doublet states that allow for internal comagnetometry and strong rejection of systematic errors [59]. However, the number and density of trapped molecular gases is three to four orders of magnitude lower than that of laser-cooled atoms, which severely limits their applications. This has not impeded the loading of optical [62,63] and magnetic traps [64,65], to study molecular collisions [66] and to observe long rotational coherence times [67]. The low density in molecular MOTs severely limits the subsequent use of laser-cooled molecules to study strongly interacting, many-body quantum systems. Despite these challenges, a recent demonstration achieved deterministic entanglement of individually controlled molecules within an optical tweezer array using the electric dipole interaction between pairs of molecules [68]. If the laser cooling community overcomes limitations in the number, density, and temperature of directly laser-cooled molecules, this opens the door for future applications in quantum science such as quantum information processing, quantum-enhanced sensing, simulation of quantum many-body systems, and tests of fundamental physics [17, 18, 58, 59].

1.3 Laser cooling of AIF molecules

Lasers can control the internal state of molecules through optical pumping and can also manipulate their center of mass motion if the process is repeated several thousand to ten thousand times. Quasi-closed optical cycles between specific vibrational levels of two electronic states in a molecule can only be established if the vibrational wave functions of both states largely overlap. Branching to rotational or hyperfine states that are not part of the cycle can be reduced by taking advantage of quantum-mechanical selection rules. Molecules with

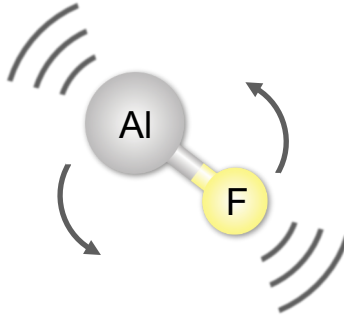


Figure 1.1: Unlike atoms, which are typically treated as spherical particles, molecules possess additional degrees of freedom. In addition to their translational motion, molecules, such as AlF, can rotate and vibrate around their symmetry axes.

a favorable energy structure can repeatedly absorb and emit photons from a laser beam. A molecule experiences two momentum kicks per cycle, one for the absorption of a photon from the laser beam and one in a random direction during the spontaneous emission following each absorption event. This leads to a net force from the direction of the laser beam. If the cycle is not fully closed, the molecule could end up in a final state that is vibrating or rotating, as depicted in Figure 1.1. Preventing losses to other vibrational or rotational states that are not part of the cooling cycle is a central challenge in molecules. Leaks can be closed by optical pumping back to the main cycling transition. However, for a large number of leaks, this can become impractical [69]. The optical scattering force, $F_{\text{opt.}}$, is proportional to $1/\lambda^4$, where λ is the wavelength of light. $F_{\text{opt.}}$ is derived from the product of the spontaneous decay rate of the electronically excited state ($\Gamma \propto 1/\lambda^3$) and the transferred momentum per photon absorption ($\Delta p \propto 1/\lambda$). A short-lived excited state leads to a high cycling rate and, thus, a significant force that can rapidly slow molecules down

to a velocity where they can be captured and stored in a trap. This provides the starting point for studying the behavior of matter at very low temperatures. As will be described in Chapter 2, our molecule of choice, aluminum monofluoride, has a strong transition deep in the ultraviolet region of the spectrum, the transferred photon momentum per optical cycle is thus large and occurs at a higher rate than for molecules with transitions in the visible range. This leads to an exceptionally large acceleration a_{\max} that can theoretically stop a molecular beam over a travel distance of a few centimeters (see Figure 1.2). Losses from the optical cycle are lower in AlF than for successfully laser-cooled diatomic molecules, which allows to efficiently deflect a molecular beam of AlF with a single laser (see Chapter 4).

To close the gap to atoms in the obtainable number and density of molecules that can be trapped, it is beneficial to start with a large number of molecules in a slow and cold molecular beam. This is usually achieved by creating molecules in a buffer gas beam source (for details see Chapter 3). AlF, in contrast to other laser-cooled molecules, has no unpaired electrons in the ground state and can be created in the gas phase with an order of magnitude higher efficiency [70]. The large optical forces and the increased production efficiency of AlF suggest that the number of trapped molecules in a MOT can potentially be increased by several orders of magnitude as compared to other successfully laser-cooled species. This thesis encompasses pivotal accomplishments towards this goal, including an examination of molecular source productivity, investigation of loss channels, successful demonstrations of optical pumping and repumping, as well as the deflection of a molecular beam.

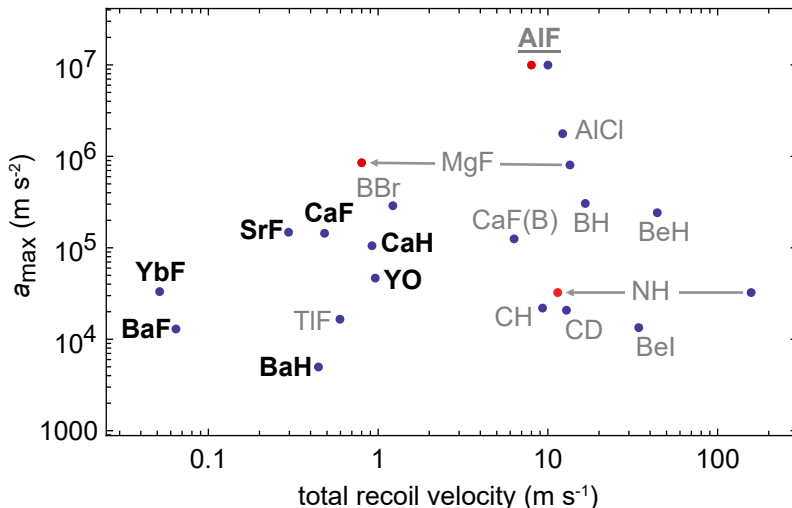


Figure 1.2: Predicted maximum acceleration a_{\max} and calculated recoil velocity before vibrational branching to a dark state. Blue data points are derived from the Franck-Condon factors from Reference [71]. Red data points represent measured Einstein A coefficient ratios, which can lead to considerably lower total recoil velocity due to the dependence of the transition dipole moment on the inter-nuclear distance [57, 72, 73]. Data points with bold labels represent successfully laser-cooled species. AIF surpasses these species by more than an order of magnitude, making it one of the most promising diatomic molecules currently considered or previously proposed for direct laser cooling (grey labels). This figure is adapted from a compilation of data from Sid Wright of the diatomic molecule database [71].

1.4 Cadmium as an intermediate test candidate

In recent years, the development of narrow-band DUV laser systems in the range near 230 nm made big leaps. In a recent study, we demonstrated the suitability of such laser systems for spectroscopic studies [72]. However, the required level of optical technology to reliably provide high output power, as required for laser cooling of AIF molecules, is still under development and is the limiting factor at the moment. Additionally, compared to other species, AIF demands significantly larger magnetic field gradients to resolve the broad

excited state distribution of the cooling transition in a magnetic field. We build a prototype trap from permanent magnets to approach the challenging goal of laser cooling AlF molecules in a magneto-optical trap. We test this setup by loading cadmium atoms from an atomic buffer gas beam (see Chapter 6). Cadmium has a strong laser cooling transition that can be reached with our existing laser systems and there are no loss channels from the optical cycle other than ionization. Spectroscopic studies of cadmium have their own merit extending beyond laser cooling applications. Cadmium has eight stable isotopes, each with a slightly different transition frequency due to variations in the number of neutrons, impacting the mass, shape, and charge distribution of the nucleus. Measuring the optical isotope shift can give insight into the nuclear structure without requiring high-energy accelerators or nuclear reactors. Deviations from trends in the isotope shifts can be a sensitive probe for new physics beyond the standard model of particle physics [74]. In addition, cadmium has narrow clock transitions that are suitable for high-precision measurements and it has one of the smallest fractional blackbody radiation shifts, which is currently the major cause for the inaccuracy in optical lattice clocks [75–78].

1.5 Thesis outline

The outline of this thesis is as follows. After this general introduction to the history of laser cooling and the motivation to explore cold molecules and aluminum monofluoride molecules in particular, Chapter 2 introduces the energy structure of AlF. The formalism and required spectroscopic constants to describe the energy structure down to the hyperfine structure are presented. Chapter 3 presents the experimental setup and components used in this thesis. The beam

source is characterized, and the number of produced molecules and atoms is measured. A new method to measure the longitudinal velocity distribution of molecular beams is described, and a scheme to determine the transverse velocity spread using a narrow spectroscopic line is explained.

In Chapter 4 the cycling rate and loss channels from the cycling transition are investigated. Ionization can cause severe loss from the optical cycle. Dark hyperfine states can severely limit the cycling rate in AIF. We benchmark a theoretical model of the cycling rate against experimental measurements and find that polarization modulation of the driving electromagnetic field can overcome this limitation.

As a first step to building a DUV trap for AIF, we perform spectroscopic studies on cadmium. While working with cadmium, it became apparent that the isotope shift and the lifetime of the laser cooling transition had never been studied with high accuracy, and existing literature values only offered partial agreement. In addition, a subtle quantum interference effect with the potential to significantly alter the lineshape had been overlooked in the past. To address these gaps, we undertook an extensive spectroscopic analysis specifically focused on measuring the optical isotope shift of cadmium. Chapter 5 presents the detailed results of this study.

With this knowledge, we build a magneto-optical trap for cadmium on the DUV laser cooling transition, which is described in Chapter 6. The experimental setup is characterized to establish measurement techniques in the lab that can later be applied to the more complex AIF molecule. We use a buffer gas beam source and compare it to more commonly used dispenser sources. A short Zeeman slower is used to greatly enhance the fraction of atoms trapped from the atomic beam in an efficient slowing region. We show that photoioniza-

tion losses can be reduced by a frequency ramping scheme. This scheme allows for the accumulation of atoms from successive shots and provides a means to construct a quasi-continuous magneto-optical trap (MOT).

Chapter 2

Molecular structure of AlF

2.1 Introduction

In the early 2000s, researchers in the field of atomic, molecular, and optical physics began exploring the possibility of transferring the technique of laser cooling from atoms to molecules [80]. In addition to fine and hyperfine structure, molecules exhibit an internal energy structure because of their vibrational and rotational degrees of freedom. This leads to a more complex theoretical description and experimentally limits applications that require high densities, since an ensemble of molecules is spread over various states of vibration and rotation, effectively reducing the density of molecules in one specific state such as the ground rotational state. However, this internal structure can also be a new handle on studying long-range dipolar interactions, which are more pronounced

This chapter is based on
[72] – S. Truppe, *et al.*, “Spectroscopic characterization of aluminum monofluoride with relevance to laser cooling and trapping.” In *Physical Review A* **100** 052513 (2019)
[79] – S. Hofsäss, *et al.*, “Optical cycling of AlF molecules.” In *New Journal of Physics* **23** 075001 (2021)

in molecules. One of the molecules on the shortlist for directly laser-coolable molecules at that time was AlF on the $^1\Pi \leftarrow ^1\Sigma^+$ transition. Even though deemed challenging due to the wavelength in the deep-UV at 227.5 nm, AlF was considered one of the most promising candidates because of the exceptional probability of an excited molecule to decay back into the same vibrational ground state [80]. It took almost 15 years of laser technology development before laser cooling of AlF came into reach. This was the starting point for thorough spectroscopic investigations to find out whether laser cooling of AlF will be feasible [72].

2.1.1 Why some molecules can be laser cooled

Atomic candidates for laser cooling must possess an electronic and hyperfine level structure that allows engineering an optically closed cycle between two electronic levels. Such cycles can also be engineered in the energy scheme of some diatomic molecules. However, the vibrational wavefunctions in the ground and excited state must largely overlap, in order to reduce losses to higher vibrational states in the electronic ground state. Whether or not a molecule is suitable for laser cooling can be quantified by the Einstein A coefficients $A_{v',v''}$, which describe the rate of spontaneous decay between two vibrational states v'' and v' , where the prime denotes the excited state and the double prime is the ground state. Molecules that can be laser cooled typically have $A_{0,0} \gg A_{0,i}$ with $i \geq 1$ [80]. The intensity I of an emission line between two electronic states ϵ' and ϵ'' , with transition frequency ν is proportional to the Einstein A coefficient $I \propto \nu^2 A_{v',v''}$. Since nuclei have a significantly larger mass than electrons, we can assume that electronic transitions take place in a stationary nuclear framework. The equilibrium distance and shape of the

potential energy surface vary between electronic states. Nuclear motion is governed by the potential energy surface, which changes during the electronic transition. The nuclei adjust to the change in charge distribution and may begin to vibrate. We follow the notation in Reference [81] and describe the wavefunction of a vibronic state in the Born-Oppenheimer approximation as $|\epsilon v\rangle = \Psi_\epsilon(\mathbf{r}, \mathbf{R})\Psi_v(\mathbf{R})$, where \mathbf{r} is the electronic coordinate and \mathbf{R} is the nuclear coordinate. The probability P for a molecule to end up in a certain quantum state is then given by

$$P = \langle \epsilon' v' | \mu | \epsilon'' v'' \rangle = \int \Psi_{\epsilon'}^*(\mathbf{r}, \mathbf{R}) \mu_e \Psi_{\epsilon''}(\mathbf{r}, \mathbf{R}) d\tau_e \int \Psi_{v'}^*(\mathbf{R}) \Psi_{v''}(\mathbf{R}) d\tau_N \quad (2.1)$$

$$= \mu_{\epsilon'', \epsilon'} S(v', v'').$$

Here μ is the coordinate-dependent transition dipole moment $\mu = \mu_e + \mu_N$ of the electrons and the nuclei, respectively, and τ_e and τ_N are their spatial coordinates. The term with μ_N vanishes, and the first factor on the right-hand side is the electronic transition moment $\mu_{\epsilon'', \epsilon'} = \int \Psi_{\epsilon'}^*(\mathbf{r}, \mathbf{R}) \mu_e \Psi_{\epsilon''}(\mathbf{r}, \mathbf{R}) d\tau_e$ and $S(v', v'') = \int \Psi_{v''}^* \Psi_{v'} d\tau_N$ is the vibrational overlap integral. $|S(v', v'')|^2$ with $\sum_{v''} |S(v', v'')|^2 = 1$ is referred to as the Franck-Condon factor (FCF). The branching ratio, r , is determined by the ratio of the Einstein A coefficient to the sum of all possible decay channels:

$$r_{v', v''} = A_{v', v''} / \sum_{v''} A_{v', v''} \quad (2.2)$$

where v'' are the ground state vibrational levels. For AlF, the spontaneous decay rate on the $A^1\Pi, v' = 0 \rightarrow X^1\Sigma^+, v'' = 0$ transition is $A_{00} \approx \sum_i A_{0,i}$. This means that decay to higher vibrational states is strongly suppressed.

The class of molecules that were directly laser-cooled so far, apart from YO, consist of alkaline earth and alkaline earth-like atoms bonded to fluorine, hydrogen, or a hydroxyl ligand to form a $^2\Sigma^+$ ground state. These radicals have an unpaired electron that is localized at the metal atom, and laser excitation promotes it without changing the bond length of the molecule. The Franck-Condon factors are close to one for this class of molecules. As a result, the number of vibrational repump lasers that are required is two or three. The situation is slightly different for AlF, which combines a group III element with fluorine to form an $X^1\Sigma^+$ ground state. The AlF bond is mostly ionic*, with the 3p electron of Al being primarily transferred to the fluorine atom [88]. Laser excitation promotes one electron from the $7\sigma^2$ molecular orbital, which has primarily Al 3s character [89], into a 3π orbital which has primarily Al 3p character (see Figure 2.1). This results in an $A^1\Pi$ or an $a^3\Pi$ state, depending on the orientation of the spin of the electron. Figure 2.2 shows the potential energy curves for the three electronic states relevant to laser cooling. Electronic structure calculations can aid in understanding why the Franck-Condon matrix is close to being diagonal, despite the lack of an unpaired electron. Figure 2.3 shows the calculated electron density and molecular orbitals of the electronic states relevant to this study.† The bottom part of each panel shows the highest occupied molecular orbital (HOMO) of the $X^1\Sigma^+$ electronic state and for the $A^1\Pi$ electronic state additionally, the lowest unoccupied molecular orbital

*The definition of the ionic character of a molecular bond is not unique [82–87]. Depending on the definition used, the bond in AlF is characterized as mostly ionic or at the border between polar covalent and ionic.

†The electron density (top of each panel) has been calculated within the multi-reference-configuration-interaction (MRCI) method available in MOLPRO 2019.2 [92]. The MRCI calculations are fed with the natural orbitals resulting from a Multi-Configuration Self-Consistent Field (MCSCF) calculation with a complete active space (CAS) consisting of nine orbitals with A_1 symmetry, three with B_1 symmetry, and three with B_2 symmetry associated with the point group C_{2v} .

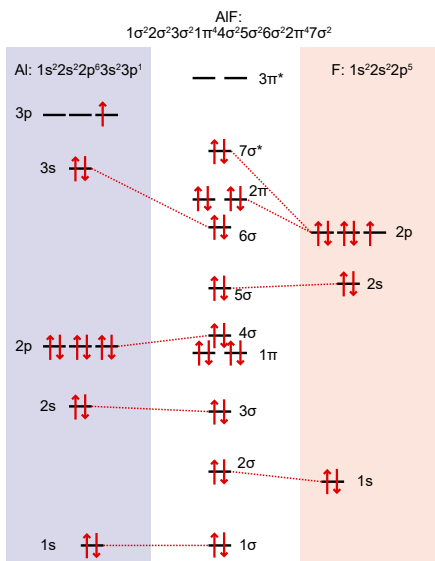


Figure 2.1: Molecular orbital toy model of the highest occupied molecular orbital of AlF in the ground state which is anti-bonding 7σ .

(LUMO) on the left side of the HOMO.[‡] The electron density in the $X^1\Sigma^+$ and $A^1\Pi$ state is very similar, and the electronic excitation resembles that of an atomic transition between s and p orbital [94]. It involves only a minimal change in the molecular bond, resulting in a highly diagonal Franck-Condon matrix and allowing optical cycling of more than 200 photons with a single laser before a loss to a higher vibrational state occurs.

2.2 Early characterization of AlF

The first band-spectrum of AlF at 220-235 nm was observed in 1939 by absorption spectroscopy after heating of aluminum fluoride (AlF_3) in a graphite furnace [95]. The spectra were attributed to a vibrational sequence of the

[‡]The calculations are carried out by employing the AVQZ [93] basis set for each atom.

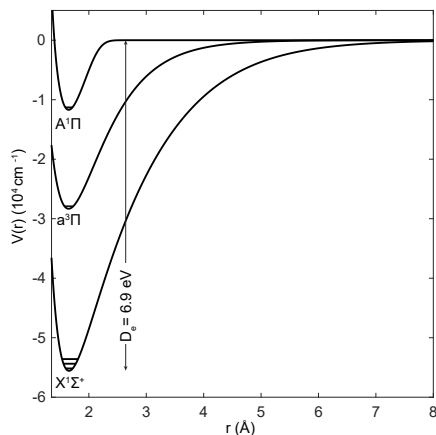


Figure 2.2: Potential energy curves of the three lowest electronic states of AlF. The RKR potentials are derived by fitting both Morse and expanded Morse oscillator (EMO) functions to precise spectroscopic data [90,91]. Calculations and figure provided by Jesús Pérez-Ríos.

$A^1\Pi \leftarrow X^1\Sigma^+$ band of AlF with no resolution of rotational structure. In 1953, the $A^1\Pi \rightarrow X^1\Sigma^+$ band was observed in emission, and the rotational constant in the $X^1\Sigma^+, v = 0$ state was estimated to be $B = 0.54 \text{ cm}^{-1}$ [96]. In the early 1950s, emission spectra of AlF were recorded that improved the vibrational constants of the $A^1\Pi \rightarrow X^1\Sigma^+$ band and the corresponding rotational constants in the ground state. However, the rotational structure on the $A^1\Pi \rightarrow X^1\Sigma^+$ band was still unresolved [97–99]. In 1974, an estimate of the relative energies of the lowest singlet and triplet states was made based on observed perturbations between levels in the $A^1\Pi$ and $b^3\Sigma^+$ states, which are separated by just 855 cm^{-1} for the lowest vibrational states [90]. This estimate was confirmed in 1976 when the intercombination emission of $a^3\Pi \rightarrow X^1\Sigma^+$ was observed in low-resolution spectra from flames produced by Al with SF_6 , NF_3 , and F_2 [100]. Shortly thereafter, the first rotationally resolved absorption spectrum of the spin-forbidden

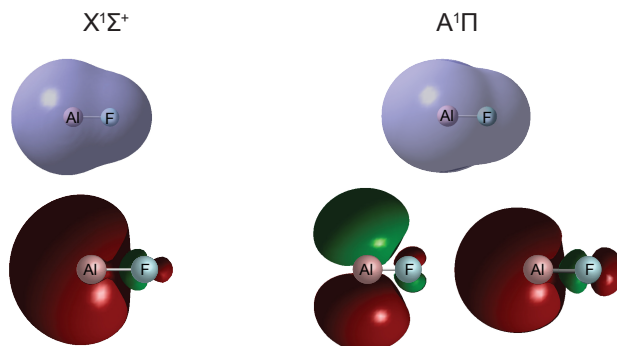


Figure 2.3: Calculated electron density (top) and molecular orbitals of AlF (bottom). For the ground state, the HOMO is shown; for the excited state, the LUMO and HOMO are shown side by side (from left to right). The electron density is very similar in the two electronic states, and the electronic excitation resembles an atomic transition between s and p orbitals. The molecular bond changes minimally, limiting vibrational branching and thus the number of repump lasers required for laser cooling. The calculations and figure are provided by Xiangyue Liu.

$a^3\Pi \leftarrow X^1\Sigma^+$ band in AlF was recorded [101]. The first microwave spectrum of AlF using Stark modulation spectroscopy on the $J = 0 \rightarrow 1$ transition in the $X^1\Sigma^+$ electronic ground-state was reported in 1963, which led to improved spectroscopic constants that were later confirmed and refined by millimeter and sub-millimeter measurements of higher rotational levels [102–104]. The microwave rotation spectrum of the $J = 0 \rightarrow 1$ transition in the $X^1\Sigma^+, v = 0$ state was also used to measure the Zeeman splitting to determine the magnetic moment [105].

2.3 The molecular Hamiltonian

The Hamiltonian to describe the energy level structure of a diatomic molecule can be written in a general form as

$$H = H_{\text{ev}} + H_{\text{rot}} + H_{\text{fs}} + H_{\text{hfs}}, \quad (2.3)$$

where H_{ev} contains the terms describing the electronic and vibrational part, H_{rot} the rotational, H_{fs} the fine-structure and H_{hfs} the hyperfine structure. In the following, each of these terms is evaluated with the goal of describing the energy structure in the $A^1\Pi$ state with reasonable accuracy.

The vibronic term H_{ev}

The electronic and vibrational term of the Hamiltonian determines the vibrational energy levels E_v for a given electronic state and can be approximated by

$$E_v = T_e + \omega_e(v + 1/2) - \omega_e x_e(v + 1/2)^2 + \dots, \quad (2.4)$$

where T_e is the electronic term energy, i.e., the minimum of the potential energy, ω_e is the vibrational energy, with its first order correction term $\omega_e x_e$. The constants are given in Table 2.1. The main cooling transition for AlF is on the $A^1\Pi \leftrightarrow X^1\Sigma^+$ band between the two lowest vibrational levels in the ground ($v'' = 0$) and excited state ($v' = 0$). The energy difference corresponds to a wavelength of 227.5 nm. Figure 2.4 shows the relevant vibronic energy levels for the optical cycle of AlF, together with the transition wavelengths and calculated branching ratios. Without any repump lasers to address the vibrational branching to $v'' > 0$, the average number of photons that can

Table 2.1: Spectroscopic constants of AlF in units of cm^{-1} from Reference [71]. T_e is the term energy, ω_e and $\omega_e x_e$ are the vibrational constants, B_e is the rotational constant, α_e is the rotation-vibration constant and D_e is the centrifugal distortion constant. The subscript e refers to the values at equilibrium distance.

Electronic state	T_e	ω_e	$\omega_e x_e$	B_e	α_e	$D_e (10^{-7})$
$X^1\Sigma^+$	0	802.26	4.77	0.55248	0.00498	10.464
$A^1\Pi$	43949.2	803.94	5.99	0.5564	0.00534	10.56

be scattered is $\langle n_{\text{ph}}^\infty \rangle = 1/(1 - r)$ (see Section 4.3 for more details), which is determined by equation 2.2 as $r = A_{00}/\sum_{v''=0}^\infty A_{0v''} = \tau_0 A_{00}$, where r is the probability for a molecule to decay back to $v'' = 0$ and $\tau_0 = 1.9$ ns is the lifetime of the $A^1\Pi, v' = 0$ level. Decay to higher vibrational states $v'' > 0$ has a probability of less than 0.005. This population must be brought back into the cooling cycle by “repumping” with a second laser at 231.7 nm. Spontaneous decay on the spin-forbidden $A^1\Pi \rightarrow a^3\Pi$ transition is weakly allowed due to spin-orbit mixing with the nearby $b^3\Sigma^+$ state. This causes a small leak from the optical cycle, which is quantified in Section 4.4. When the molecule is in the $A^1\Pi$ state, another photon of the same color can bring the molecule energetically above the ionization potential and create AlF^+ . The photo-ionization probability is investigated in Section 4.4.

The rotational term H_{rot}

The rotational term can be written as

$$H_{\text{rot}} = A_v (\mathbf{L} \cdot \mathbf{S}) + B_v (\mathbf{J} - \mathbf{L} - \mathbf{S})^2 - D_v (\mathbf{J} - \mathbf{L} - \mathbf{S})^4, \quad (2.5)$$

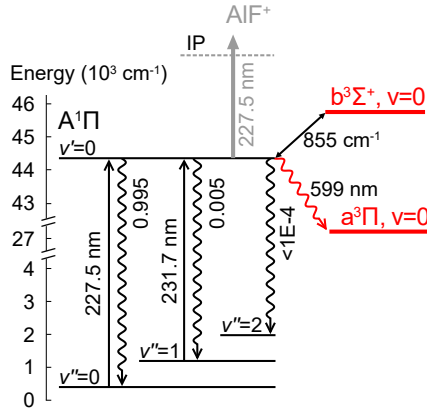


Figure 2.4: Electronic and vibrational states relevant for laser cooling of AlF . The main cooling ($v' = 0 \leftarrow v'' = 0$) and repump ($v' = 0 \leftarrow v'' = 1$) transitions are indicated with solid arrows. Wavy arrows indicate spontaneous emission. Allowed transitions show the calculated branching ratios. Ionization to AlF^+ above the ionization potential (IP) can take place via absorption in a 1+1 process. There is a small loss channel to the intermediate $a^3\Pi$ state due to the proximity of the $A^1\Pi$ and $b^3\Sigma^+$ state.

where A_v is the electron spin-orbit coupling constant, $B_v = B_e - \alpha_e(v + 1/2)$ the rotational constant with B_e the rotational constant at equilibrium, α_e the rotation-vibration coupling constant, and D_v the centrifugal distortion constant, \mathbf{J} the total angular momentum of the molecule in the absence of hyperfine interactions, \mathbf{L} the total orbital angular momentum, and \mathbf{S} the total spin of the electrons. The spin-orbit interaction splits electronic states with non-zero values of L and S into Ω manifolds, where $\Omega = \Lambda + \Sigma$, with Λ the projection of \mathbf{L} and Σ the projection of \mathbf{S} along the internuclear axis, as depicted in Figure 2.5. We can describe both the ground and excited state with the quantum number J , since there is no spin angular momentum in the ground and excited state, and therefore $\mathbf{J} \equiv \mathbf{N} = \mathbf{R} + \mathbf{L}$. The rotational angular momentum of the nuclei, \mathbf{R} , and the electronic orbital angular momentum, \mathbf{L} , form the total

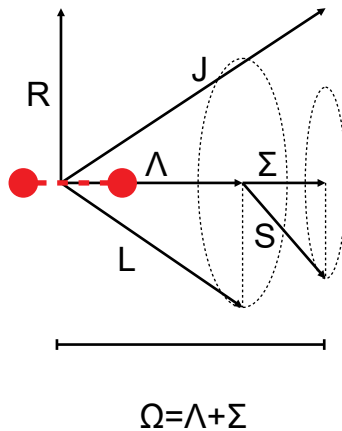


Figure 2.5: Vector representation of angular momentum coupling in Hund's case a. The electronic orbital angular momentum, L , is strongly coupled to the inter-nuclear axis. The electron-spin angular momentum, S , is coupled to L by spin-orbit coupling. The projections Λ and Σ onto the inter-molecular axis are well-defined but can have positive or negative magnitude, which can lead to Λ - and Ω -doubling. The total angular momentum, J , is the sum of Ω and the rotational angular momentum of the nuclei, R . The red circles indicate two atoms of a diatomic molecule.

angular momentum of the system, \mathbf{J} . Following Reference [106], the rotational energy for Hund's case (a) can be evaluated as

$$\langle \psi | (\mathbf{J} - \mathbf{L} - \mathbf{S})^2 | \psi \rangle = J(J+1) - \Omega^2 + S(S+1) - \Sigma^2. \quad (2.6)$$

Terms with S vanish and $\Omega = \Lambda$ because the total spin is zero, and we get

$$E_{\text{rot}} = B_v(J(J+1) - \Lambda^2) - D_v(J(J+1) - \Lambda^2)^2. \quad (2.7)$$

Since $J_{\text{min}} \geq \Lambda$, there are no rotational levels with $J = 0$ in the $A^1\Pi$ state [107].

Figure 2.6 shows the rotational structure of the lowest excited states. To prevent rotational branching, it is common to use the strict parity and angular

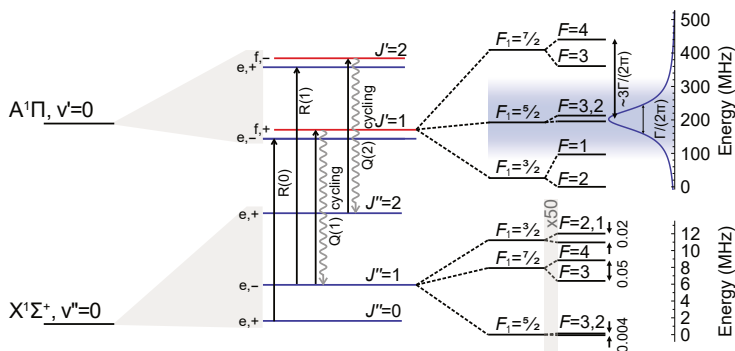


Figure 2.6: Energy level diagram of the states relevant for laser cooling of AlF. Λ -doubling in the excited state results in two opposite parity states per rotational level. R(J'') and P(J'') lines reach e levels while Q(J'') lines reach f levels and are rotationally closed according to the notation in Reference [109]. The aluminum nuclear spin splits $J = 1$ levels into three F_1 components, each of which is split again by the fluorine nuclear spin into two F levels. The hyperfine structure in the ground state is small compared to the natural linewidth of the $A^1\Pi$ state ($\Gamma/(2\pi) = 84$ MHz) and ultimately unresolved. The splitting of the F_1 components is shown magnified by a factor of 50.

momentum selection rules of electric dipole transitions [108]. In AlF, each Q line of the $A^1\Pi \leftrightarrow X^1\Sigma^+$ transition is rotationally closed due to parity selection rules. This is a key difference from $^2\Sigma^+$ ground state molecules laser cooled so far. The number of photons a molecule can scatter with a single laser is in the case of AlF dominated by losses to higher vibrational levels. The rotationally open P and R transitions can be used to pump molecules between states separated by $\Delta J = 2$ in a few photon scattering events, which is described in more detail in Section 4.2. Rotational branching may occur in electric fields, which is investigated in Section 4.4.

Hyperfine structure

Both the aluminum nucleus and the fluorine nucleus have an unpaired proton. Therefore, both carry a nuclear spin, given by $I_{\text{Al}} = 5/2$ and $I_{\text{F}} = 1/2$ that combines to the total angular momentum $\mathbf{F} = \mathbf{F}_1 + \mathbf{I}_{\text{F}}$, where $\mathbf{F}_1 = \mathbf{J} + \mathbf{I}_{\text{Al}}$. The hyperfine interaction splits the $J = 0, 1,$ and 2 levels into two, six, and ten hyperfine levels, respectively, and into 12 F levels for $J \geq 3$.

Figure 2.6 presents the relevant energy level structure for $A^1\Pi, v' = 0, J' = 1$ and $X^1\Sigma^+, v'' = 0, J'' = 1$. In the electronic ground state, the hyperfine structure is dominated by the interaction of the electric quadrupole moment of the Al nucleus with the local electric field gradient. As a result, the intermediate angular momentum $\mathbf{F}_1 = \mathbf{J} + \mathbf{I}_{\text{Al}}$ is a good quantum number. The total span of the hyperfine structure in the $X^1\Sigma^+$ state lies well within the natural linewidth $\Gamma/(2\pi) = 84\text{MHz}$ of the $A - X$ transition, where $\Gamma = \sum_{v''} A_{0v''} = 1/\tau_0$ is the spontaneous decay rate. This means that the hyperfine structure in the ground state can be addressed with a single laser and no radio frequency sidebands or additional lasers are needed.

In the $A^1\Pi$ excited state, each J' -level consists of a closely-spaced pair of opposite parity levels which appear split due to Λ -doubling, with Λ being the projection of \mathbf{L} onto the internuclear axis. The Hamiltonian for Π states (Reference [110] eq. (9.69)) in the case for $A^1\Pi$ in AlF can be written as

$$\langle \psi | \mathcal{H}_{\text{LD}} | \psi \rangle = (-1)^{J-S} \delta_{\Sigma, \Sigma'} (1/(2\sqrt{6})) q (-1)^{J+\Omega} \begin{pmatrix} J & 2 & J \\ \Omega & -2 & \Omega' \end{pmatrix} \times \quad (2.8)$$

$$[(2J-1)(2J)(2J+1)(2J+2)(2J+3)]^{1/2} \quad (2.9)$$

which for $\Omega = -\Omega' = 1$, corresponds to $E_{\text{LD}} = q \frac{J(J+1)}{2}$ with q the lambda

doubling parameter from Table 2.2. The round brackets indicate the Wigner $3j$ -symbol.

The hyperfine interaction splits each Λ -doublet component into an equal number of F -levels. The interactions arising from the Al and F nuclei are comparable, and F_1 is not a good quantum number. The diagonal elements of the Hamiltonian \mathcal{H}_{hfs} for the magnetic hyperfine interaction can be written as (Reference [110] eq. (9.50)):

$$\langle \psi | {}_J \mathcal{H}_{\text{hfs}} | \psi \rangle_J = (a\Lambda + (b_F + (2/3)c)\Sigma)\Omega \frac{F(F+1) - J(J+1) - I(I+1)}{2J(J+1)} \quad (2.10)$$

for the case of AlF in the ${}^1\Pi$ state ($\Omega = \Lambda = 1$, $\Sigma = 0$), the energy of the hyperfine state with the largest F ($F = I_{\text{Al}} + I_{\text{F}} + J = 3 + J$) can be expressed as $E_{\text{hfs}} = \frac{a(I_{\text{Al}} + I_{\text{F}})}{1+J}$. We can define a parameter for each atom (a_{Al} and a_{F}) which are given in Table 2.2. It becomes clear that the hyperfine structure collapses with increasing J . However, the opposite is true for the splitting between the Λ -doublet components.

The electric quadrupole coupling is described by the quadrupole coupling constant eq_0Q . The diagonal elements of the nuclear electric quadrupole coupling Hamiltonian \mathcal{H}_Q in the $A^1\Pi$ state (Reference [110] eq. (9.53)) with curly brackets indicating the Wigner $6j$ -symbol evaluate to

$$\langle \psi | \mathcal{H}_Q | \psi \rangle = \frac{eq_0Q}{4} (-1)^{J'+I+F+J-\Omega} ((2J+1)(2J'+1))^{1/2} \quad (2.11)$$

$$\times \left\{ \begin{matrix} J' & I & F \\ I & J & 2 \end{matrix} \right\} \left(\begin{matrix} J & 2 & J' \\ -\Omega & 0 & \Omega' \end{matrix} \right) \left(\begin{matrix} I & 2 & I \\ -I & 0 & I \end{matrix} \right)^{-1} \quad (2.12)$$

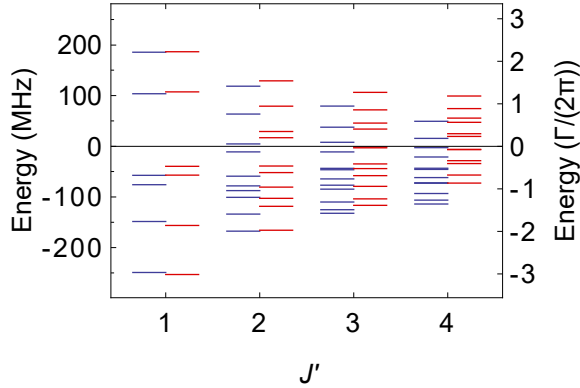


Figure 2.7: Hyperfine splittings of the $A^1\Pi, v' = 0, J'$ levels with respect to their gravity center. The e levels are blue, and the f levels are in red. The hyperfine structure collapses for increasing J' . The hyperfine levels in the lowest rotational levels in the $X^1\Sigma^+, v'' = 0$ state are unresolved and are spread by about 10 MHz (not shown).

which for AlF in the $^1\Pi$ state is negligible, typical values are $E_Q(J, F) \ll eq_0Q$. For example $E_Q(J = 1, F = 4) = \frac{eq_0Q}{40}$. Figure 2.7 summarizes the description of the Λ -doubling and hyperfine energy splitting of the $A^1\Pi, v' = 0$ level for $J' = 1$ to $J' = 4$ with respect to their gravity center by using the parameters presented in Table 2.2. In the ground state, the situation is different, here the electric quadrupole moment is the main contribution to the hyperfine splitting and $eq_0Q(X^1\Sigma) = 37.527(7)$ MHz [72]. The hyperfine intervals in the lowest J' level of the excited state ($\approx 5\Gamma/(2\pi)$) are approximately 50 times larger than in the ground state. However, the hyperfine splitting decreases as J' increases. For $J' = 4$, it reduces to around $\approx 2\Gamma/(2\pi)$, whereas it remains at approximately 10 MHz in the ground state. This small splitting in the ground state has nevertheless significant implications for optical cycling (see Chapter 4).

Table 2.2: Spectroscopic constants in units of MHz with standard deviation to calculate the hyperfine structure of AlF [72]. q is the lambda doubling parameter, $a(\text{Al})$ and $a(\text{F})$ are two hyperfine parameters and eq_0Q is the quadrupole coupling constant.

$X^1\Sigma^+$	$A^1\Pi$
$eq_0Q(\text{Al})$ -37.5260(3)	q -2.94(6)
	$a(\text{Al})$ 113(5)
	$a(\text{F})$ 181(5)

Analysis of a rotational spectrum

With the theoretical examination in the previous section, we can now describe the energy structure down to the hyperfine level with values for the spectroscopic parameters taken from Tables 2.1 and 2.2. This is typically enough in order to reproduce measured frequencies in the laboratory with an absolute error of $\approx 0.01\text{cm}^{-1}$ ($\approx 0.3\text{GHz}$). As a summary, we can now examine a typical Q branch ($J'' = J'$) spectrum and look at the collapse of the hyperfine structure in the excited state.

In a Q-branch spectrum of the $A^1\Pi, v' = 0 \leftarrow X^1\Sigma^+, v'' = 0$ band as shown in Figure 2.8 a) we can only see one of the Λ components due to the parity selection rules. The hyperfine structure collapses quickly with increasing J' . In comparison to a Q-branch spectrum of $A^1\Pi, v' = 0 \leftarrow X^1\Sigma^+, v'' = 1$, the spacing of the peaks is more narrow, from which the difference of the rotational constants of $v'' = 0, 1$ in the electronic ground state can be extracted. The spectra in Figure 2.8 are recorded at low laser intensity to avoid power broadening or radiation pressure deflection effects. The individual hyperfine transitions of all Q-lines overlap due to the large linewidth. It is sufficient to assign three Gaussians to three F_1 components of the excited state for the Q(1) line and one to each of the higher Q lines. Due to the overlap in the Q(1)

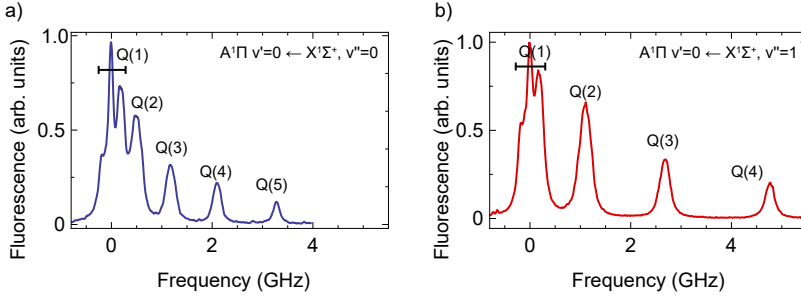


Figure 2.8: Laser-induced fluorescence spectrum of the Q-branch of the $A^1\Pi, v' = 0 \leftrightarrow X^1\Sigma^+$ transition from the two lowest vibrational states in the ground state a) $v'' = 0$ and b) $v'' = 1$. The increased spacing of the $v'' = 1$ spectrum indicates a smaller rotational constant for $X^1\Sigma^+, v'' = 1$ than for $v'' = 0$, according to $B_v = B_e - \alpha_e(v + 1/2)$.

line, it is not considered in the analysis, which also neglects the centrifugal distortion term since $B_v \gg D_v$. The differences of rotational constants follow from equation 2.7:

$$\Delta E_{\text{rot}}^{v,v''}(J) = E_v(J) - E_{v''}(J) \approx (B_v - B_{v''})J(J+1) = \Delta B_{v,v''}J(J+1).$$

With $\Delta B_{0,0} = 115.3(2)$ MHz and $\Delta B_{0,1} = 262.6(2)$ MHz follows that $B_1 - B_0 = 147.4(4)$ MHz where the brackets indicate the statistical uncertainty. The predicted difference via $B_v = B_e - \alpha_e(v + 1/2)$ is $B_1 - B_0 = -\alpha_e = -149.3$ MHz, with α_e from Table 2.1. This difference was also measured by microwave spectroscopy to be 148.40(7) MHz, see Table 2.3 [102]. The deviation from the more accurate microwave spectroscopy data is 1.0(4) MHz, within the wavemeter uncertainty (see Section 5.5.3).

Table 2.3: Experimentally determined rotational constants of the states of AlF that are most relevant for laser cooling.

Electronic state		B_v (MHz)
$A^1\Pi$	$v = 0$	16601.9(3) [72]
$a^3\Pi$	$v' = 0$	16634.7458(10) [72]
$X^1\Sigma^+$	$v'' = 0$	16488.3548(3) [72]
	$v'' = 0$	16488.36(5) [102]
	$v'' = 1$	16339.96(5) [102]

Chapter 3

Experimental setup for producing and probing cold molecular beams

3.1 Introduction

Our experiment aims to produce a dense and cold quantum gas of polar molecules, using direct laser cooling. The starting point for such an experiment is a large number of molecules in an already cold and intense molecular beam. These molecules are then laser-cooled to lower temperatures. This is only possible for molecules for which a closed optical cycle can be engineered.

Diatomic monofluorides are unstable at high pressure and must be pro-

This chapter is based on [79] – S. Hofsäss, *et al.*, “Optical cycling of AlF molecules.” In *New Journal of Physics* **23** 075001 (2021)

duced in situ. The efficient creation of gas-phase molecules for laser cooling is currently being investigated through theoretical and experimental studies [70,111]. This process involves vaporizing metal atoms from a solid precursor material with an intense laser beam. This chapter demonstrates the production of a bright pulsed beam of AlF in a cryogenic buffer gas cell. We experimentally determine a molecular beam brightness of $> 10^{12}$ molecules per steradian per pulse in a single rotational state. A new method to determine the forward velocity distribution of a pulsed molecular beam is presented, and the transverse velocity distribution is measured. An atomic beam of cadmium is characterized in the same experimental setup as a first step towards a magneto-optical trap of cadmium atoms in Chapter 6. This chapter outlines the experimental setup for all studies in this thesis, including the molecular beam source, the laser system, and the fluorescence detector.

3.2 Pre-cooling molecules

In the absence of buffer gas, the ablated Al atoms have an initial temperature of approximately $T = 3400 \pm 1000$ K measured via the Doppler width in absorption inside the cell [70]. This corresponds to a thermal velocity of Al atoms of $v = 1770 \pm 260$ m/s. The activation energies for the reactions to form AlF are corresponding to a temperature of $T = 2990$ K ($\text{Al} + \text{NF}_3 \rightarrow \text{AlF} + \text{NF}_2$) or $T = 4800$ K ($\text{Al} + \text{SF}_6 \rightarrow \text{AlF} + \text{SF}_5$) [112]. Consequently, the AlF molecules are initially equally hot and are distributed across various vibrational

and rotational states, determined by the Maxwell-Boltzmann equation.:

$$P(J) = \frac{(2J+1)}{Z} \exp\left\{-\frac{E_{\text{rot}}(J)}{k_{\text{B}}T}\right\} \quad (3.1)$$

$$Z = \sum_J (2J+1) \exp\left\{-\frac{E_{\text{rot}}(J)}{k_{\text{B}}T}\right\} \quad (3.2)$$

where Z is the partition function, k_{B} is the Boltzmann constant, T is the gas temperature, and $E_{\text{rot}}(J)$ is the rotational energy (equation 2.7 for AlF). Cooling the internal and external degrees of freedom through collisions with a cold gas is essential for achieving a dense beam of molecules in the same quantum state. In the case of AlF, the population in $J = 0$ is not immediately suitable for laser cooling because there is no rotationally closed transition to the excited state. Figure 3.1 illustrates the temperature at which each J'' state has the highest population (as $D \ll B$) given by $J_{\text{max}} = \sqrt{\frac{kT}{2B}} - \frac{1}{2}$. The highest fraction of $J = 1$ molecules occurs at approximately $T \approx 3$ K, which is the desired final temperature. This can be achieved by commercial closed-cycle cryocoolers. Population transfer from $J'' = 0$ to $J'' = 1$ can further increase the population (see Section 4.4).

3.3 Choosing a molecular beam source

This section discusses the differences between the two main categories of beam sources used in atomic and molecular beam experiments which are supersonic and effusive beams. These sources operate in different regimes determined by their collisional dynamics. A beam source can be described as an ideal atomic gas inside a container, where the atoms form a beam by exiting through an orifice. The distance an atom can travel before colliding with another atom is

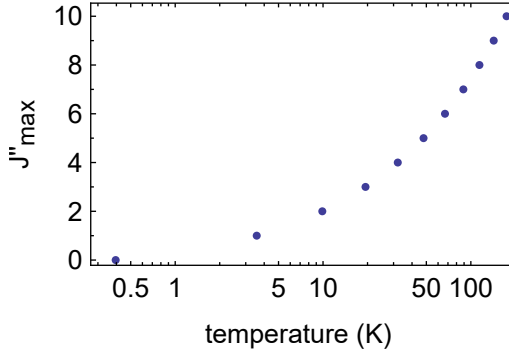


Figure 3.1: Rotational levels in $\Sigma^+, v'' = 0$ are populated according to the Maxwell-Boltzmann distribution. Hot molecules formed in the reaction between Al and a fluorine donor gas ($T \approx 3400$ K) are spread over many rotational states. After buffer gas cooling ($T \approx 3$ K), most of the population is found in $J = 1$.

known as the mean free path, given by $\lambda = \langle v \rangle \langle \tau \rangle = \frac{1}{\sqrt{2}\pi d^2 n}$, where $\langle v \rangle$ and $\langle \tau \rangle$ represent the mean velocity and period between collisions, d is the atom's diameter, and n is the number density. For a typical gas at room temperature and ambient pressure, $\lambda \sim 10^{-7}$ m [113]. The flow regime is determined by the number of collisions that occur as atoms exit the container, characterized by the Knudsen number $K = \lambda/L$. This dimensionless quantity relates the mean free path to a characteristic length L , such as the radius of the orifice, over which macroscopic flow properties change significantly.

For $K \ll 1$, indicating a supersonic flow regime, the number of collisions with the container walls is significantly smaller compared to the number of collisions between atoms. To generate a beam with a narrow velocity distribution (typically around 10 K), a carrier gas such as helium seeded with SF_6 , is adiabatically expanded through a periodically opened and closed small nozzle controlled by a solenoid (see Figure 3.2). The stagnation pressure is typically up to 50 bar. During expansion, collisions cool the external and internal de-

degrees of freedom, and the mean forward velocity can be adjusted by selecting carrier gases with different atomic masses and by choice of the valve temperature. The maximum gas flow velocity is limited by the molar enthalpy and heat capacity, C_p , giving $u_{\max} = \sqrt{\frac{2C_p T_0}{m}}$. For an ideal gas with $C_p = \frac{5}{2}k_B$, this becomes $u_{\max, \text{ideal}} = \sqrt{\frac{5k_B T_0}{m}}$ [114, 115]. Inside the expansion region, the beam can be seeded with hot metal atoms from an ablation source, which then react with the seeded SF_6 gas to form the desired molecules. The heavy molecules are accelerated by the more abundant light carrier gas to reach the thermal velocity of the carrier gas (approximately 600 m/s for neon or 1400 m/s for helium). Supersonic sources offer kHz repetition rates, a narrow forward velocity distribution, and they are suitable for experiments involving Stark and Zeeman deceleration [116]. Additionally, the pulsed nature of the source reduces gas load and the strain on vacuum pumps.

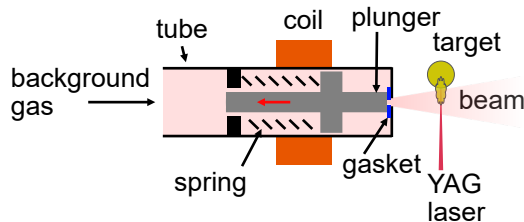


Figure 3.2: Schematic representation of a molecular beam created in the supersonic expansion region of a pulsed valve by laser ablation of a metal target. The plunger is actuated by an electromagnetic coil for a short period. This allows the high-pressure background gas to expand through a small orifice or nozzle. The typical background pressure for Even-Lavie type valves is around 30-50 bar, and the typical pulse width is around 20 μs .

In the regime where $K \gg 1$, atoms primarily collide with the walls of the container rather than with each other. In an effusive beam, atoms with high transverse velocity components relative to the beam direction diverge more significantly due to the lack of collision partners after expansion. This type of

beam is produced by heating a sample material to create a vapor that expands into a vacuum chamber through an orifice. The velocity of the particles is determined by the thermal kinetic energy of the vapor at the orifice, following the Maxwell-Boltzmann distribution described by:

$$P(v)dv = \frac{m^2}{2(k_{\text{B}}T_0)^2} v^3 \exp\left(-\frac{mv^2}{2k_{\text{B}}T_0}\right) dv \quad (3.3)$$

where m is the molar mass of the atom or molecule, k_{B} is the Boltzmann constant, and T_0 is the temperature of the reservoir. The most probable velocity is given by $\langle v \rangle = \sqrt{\frac{3k_{\text{B}}T}{m}}$ [117]. Due to the low vapor density, collisions between particles are rare, resulting in a broad distribution of forward velocities.

For spectroscopy experiments, a room-temperature supersonic beam source with a high repetition rate and narrow forward velocity is often a good choice. However, trapping molecules from such a beam would require scattering a significant number of photons. Each scattered photon used for slowing the molecule down increases the risk of ending up in a dark state. For AIF at a velocity of just 40 m/s, this already corresponds to approximately 1000 photon cycles. Laser cooling applications require considering the forward velocity and also the total flux of species in the beam, which is why we choose a different type of source, described in the following.

Introducing the buffer gas beam source

We choose a source type that operates in a regime between thermal and supersonic beams. So-called buffer gas beam sources (BGS) precool hot molecules by collisions with a cryogenic buffer gas, which continuously replenishes and re-thermalizes with the walls of a copper cell, in which the ablation and the

cooling take place. The pre-cooled molecules, together with the buffer gas, are extracted into a hydrodynamic molecular beam. The majority of extracted buffer gas is immediately pumped by cryogenic charcoal shields which are held at $T \approx 3\text{K}$. The mean forward velocity of the molecular beam is mainly determined by the thermalized buffer gas atoms (for helium $v \approx 140\text{m/s}$ for $T = 3\text{K}$). Typical BGS for the production of diatomic molecules are pulsed and can achieve a repetition rate of up to 100 Hz [118].* This method yields a significantly higher flux compared to typical molecular supersonic beam sources, as illustrated in Figure 3.4, but also produces a broader range of forward velocities and thus results in a wider time of flight pulse when measured in a detector downstream.

The buffer gas cell, shown in Figure 3.3, is attached to the second stage of a cryocooler and contains a metal target from which atoms are ablated using a pulsed Nd:YAG laser (operating at 1064 nm, pulse energy 15-30 mJ, spot size of about 0.4 mm). The target can be rotated and translated inside a copper cell with external dimensions of (w, h, l) = (35, 35, 45) mm and an internal bore with a diameter of 10 mm. The length of the total cell is 30 mm, while the ablation takes place at 20 mm from the cell aperture. For the production of AlF, the gas phase Al atoms collide with a reactant gas, which flows continuously into the cell via a copper tube insulated from the cell walls. We use either NF_3 or SF_6 gas at flow rates of 0.001 and 0.03 sccm, respectively. Precooled molecules are extracted through a 4 mm aperture at the front of the cell. An optional double-stage cell configuration can be used to reduce the forward velocity (not

*The technique was first applied to cool ions inside an ion trap and was described as a “viscous drag which lowers the mean kinetic energy of the ions” [119]. In contrast to this method, we use the buffer gas inside the molecular beam source to cool the species within the source.

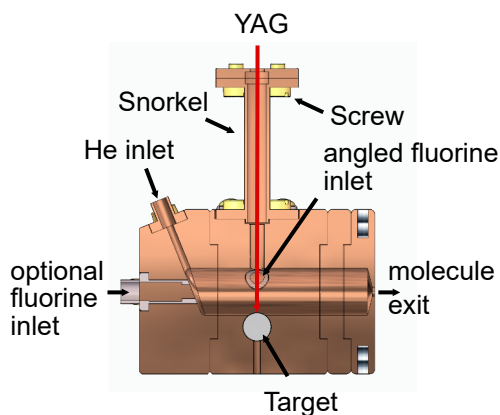


Figure 3.3: Pre-cooled molecules can be produced in a cryogenic buffer gas beam source (sectional view). AlF molecules are produced using a pulsed YAG laser that ablates part of the aluminum target. In the presence of SF_6 or NF_3 the hot Al molecules react to form AlF and subsequently cool by collisions with the cold buffer gas.

shown) [120,121]. The design is based on the pioneering work presented in [122,123] and the design by *Truppe et al.* [47]. The operation principle of such a cryogenic buffer gas molecular beam has been extensively reviewed [124]. Figure 3.4 compares the fluorescence signal of AlF molecules generated in a supersonic beam source to that of a buffer gas beam source at different ablation energies. The buffer gas beam source offers intense molecular beams with a low average forward velocity, beneficial for trapping applications. However, it exhibits a wider velocity distribution compared to supersonic sources. This broader distribution provides the advantage of measuring the same spectrum at different interaction times, enabling insights into the optical cycling rate of a transition (see Section 4.5).

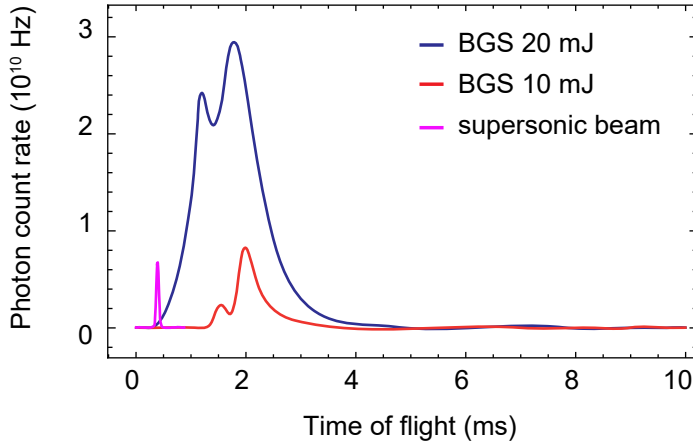


Figure 3.4: Laser-induced fluorescence of the non-cycling $R(0)$ line of the laser cooling transition in AlF ($A^1\Pi, v' = 0, J' = 1 \leftarrow X^1\Sigma^+, v'' = 0, J'' = 0$) for two different source types, measured in the same detector at a distance of about 40 cm from the source. The BGS is the preferred choice for applications such as laser cooling, where large quantities of molecules are required. The buffer gas beam source (BGS) produces orders of magnitude higher flux compared to a supersonic expansion in neon.

3.4 Laser system

To produce the necessary UV light for our experiments, we use a Ti:sapphire laser that produces narrowband CW light. We employ two successive nonlinear doubling stages to frequency-quadruple the laser frequency, resulting in more than 100 mW of DUV radiation near specific wavelengths such as 227.5 nm for the $0 - 0$ band of the AlF laser cooling transition ($A^1\Pi \leftarrow X^1\Sigma^+$), 231.7 nm for the $0 - 1$ band, or 228.8 nm for the cadmium resonance line $^1P_1 \leftarrow ^1S_0$. For spectroscopy and laser cooling of AlF and cadmium, stability and long-term accuracy of the laser frequency can be achieved by stabilizing the lasers with a commercial wavemeter which is referenced to a calibrated and temperature-stabilized HeNe laser. We use a HighFinesse WS8-10 wavemeter with an abso-

lute accuracy of 10-30 MHz and resolution of 0.4 MHz (1.6 MHz quadrupled). The feedback to the laser is updated at about 100 Hz.

3.5 Laser induced fluorescence detector

To conduct spectroscopy experiments, laser beams intersect with a molecular beam at various positions along its propagation direction, at right angles. The resulting laser-induced fluorescence is imaged onto either a photomultiplier tube (PMT) or a UV-sensitive sCMOS camera. The detection probability of an emitted photon is mainly limited by the optics' collection efficiency, which covers a solid angle of 1 steradian. Figure 3.5 illustrates the detector's geometry. Figure 3.6 shows a ray-tracing simulation of the optics and 3.7 shows which area of the detector solid angle is vignetted.[†] Accounting for transmission losses through the vacuum window, lenses, and mirror reflectivity, the total detection efficiency is 0.025 and 0.016 for the two detectors (PMT/Camera), respectively.

To apply a homogeneous electric field within the interaction region and study optical cycling in the presence of dc electric fields (see Section 4.4), a fine stainless steel mesh with 80% transparency can be inserted above and below the molecular beam. To measure the two-photon ionization rate of AlF, the LIF detector can be replaced by a Wiley-McLaren type time-of-flight mass spectrometer, combined with a microchannel plate detector.

3.5.1 Photomultiplier tubes

This section describes some of the characteristics of PMT detectors which can be used to detect the weak fluorescence signal of atomic and molecular beams.

[†]Software used for ray tracing is OSLO from Lambda research.

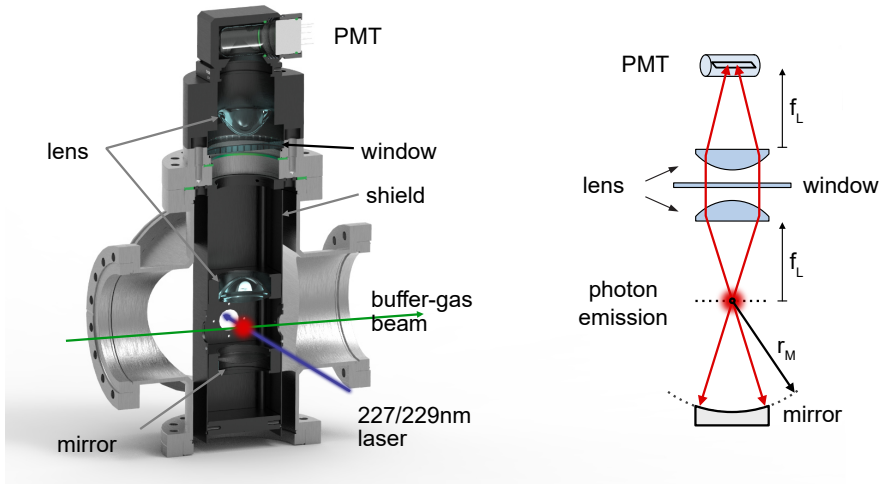


Figure 3.5: Laser-induced fluorescence is collected using an imaging system. A spherical mirror at $2f = r_M$ retro-reflects the emitted light. Two lenses create a 1:1 image on a UV-sensitive photomultiplier tube (PMT) or sCMOS camera outside the vacuum chamber. The mirror is removed for better clarity in imaging applications to eliminate the mirror image caused by reflection.

The PMT operates on the principle of the photoelectric effect, which causes the release of electrons from the photosensitive cathode when it is exposed to incoming photons (as illustrated in Figure 3.8). These electrons are then focused onto a charged dynode, where each electron is multiplied into secondary electrons. This process continues through successive stages of dynodes, with each stage having an increasing electric potential relative to the cathode, ensuring that the secondary electrons are always accelerated onto the next dynode. The amplification factor, or gain, takes into account the collection efficiency of the secondary electrons and can range from 10^5 to 10^7 depending on the model and the voltage supplied between the cathode and anode. The anode then collects the secondary electrons and converts them into an electronic signal. The maximum number of incident photons on the cathode $N_{\max}^{\text{cathode}}$ is limited by

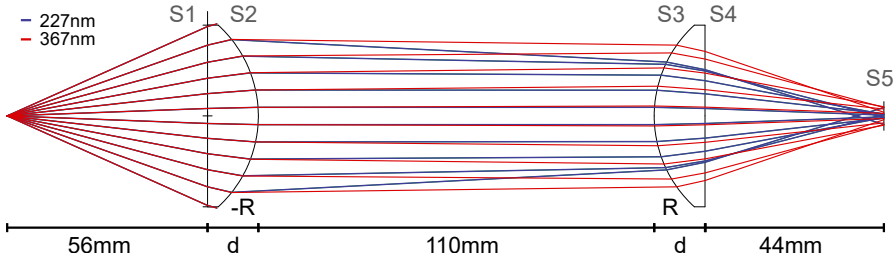


Figure 3.6: Optimized lens geometry for 227 nm light (blue rays) for a typical LIF detector setup made of plano-spherical lenses with radius $R = 34.39\text{mm}$ and a back focal length of 56 mm. Spherical aberration leads to a washed-out image. Chromatic aberration leads to different beam paths for a fan of rays of another wavelength (blue, red).

the maximum current that the cathode and anode can sustain.

$$N_{\max}^{\text{cathode}} = \frac{I_{\text{cathode,max.}}}{e\epsilon_{\text{QE}}}$$

$$N_{\max}^{\text{anode}} = \frac{I_{\text{anode,max.}}}{e\epsilon_{\text{QE}}g}$$

The maximum current that the cathode material can sustain in the linear response regime is typically around $I^{\text{cathode}} = 0.1\ \mu\text{A}$. With a photo-cathode quantum efficiency of $\epsilon_{\text{QE}} = 0.35$, this limits the maximum number of incident photons to $N_{\max}^{\text{cathode}} = 1.8 \times 10^{12}\ \text{s}^{-1}$. On the other hand, the maximum current that the anode can sustain is typically on the order of $I^{\text{anode}} = 0.1\ \text{mA}$. With a typical gain of 10^6 , the anode has to handle significantly higher currents than the cathode. Thus, the maximum current on the anode limits the number of photons to $N_{\max}^{\text{anode}} = 1.8 \times 10^9\ \text{s}^{-1}$, three orders of magnitude lower than the cathode limit. In our experimental setup, this photo-current is usually

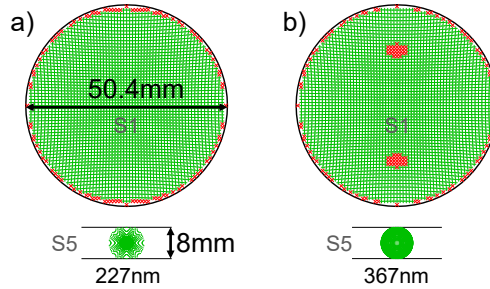


Figure 3.7: To scale drawing of a ray tracing analysis of the imaging setup in Figure 3.6 for two wavelengths. The analysis shows that approximately 96% of all the rays projected onto surface S1 are successfully projected onto the imaging surface S5. The height of S5, corresponds to the short side of the PMT cathode (8 mm \times 24 mm). The majority of the rays that are cut off or not projected onto S5 (indicated by the red marks) are blocked by the edge of surface S1. Due to spherical aberration, the symmetric vignetting pattern for 367 nm results in a slightly reduced solid angle, given the specific distance between surfaces S4 and S5. The spot pattern on S5 is more confined and for the optimized wavelength.

converted to a voltage using a transimpedance amplifier with a gain of 10^4 V/A. The hard limit for avoiding damage to the anode at $I^{\text{anode}} = 0.1$ mA is thus a voltage of 1 V in continuous operation, which can be higher in pulsed operation. In practice, signal shape distortion due to the non-linearity of the PMT signal was observed above 0.5 V in quasi-continuous operation, and it is thus strongly recommended not to exceed this value.

The advantage of PMTs becomes apparent when comparing the minimum number of photons that can be measured with the same signal-to-noise ratio on photodiode detectors. In this example $S/N=1$. PMTs have a high gain with significantly lower noise than, e.g., photodiode (PD) detectors, which do not have an electron multiplication gain.[‡] A PMT has a typical dark current of 1-10 nA, which corresponds to $10^{-4} - 10^{-5}$ of the maximum rated output,

[‡]Avalanche PDs, which are the solid-state analogon to PMTs are an exception.

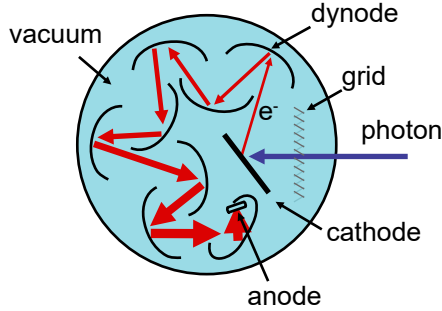


Figure 3.8: When photons hit the photo-cathode, they are converted into electrons through the photoelectric effect. These electrons are then multiplied at each stage by a series of dynodes. Finally, the anode collects the charges and converts the electrons into an electrical signal. This signal is proportional to the number of incoming photons.

and the anode sensitivity is on the order of $5 \times 10^5 \text{ A/W}$. A typical gain of 10^6 corresponds to an equivalent incoming power of $2 \times 10^{-15} \text{ W}$. The equivalent noise input P_{\min} is defined by

$$P_{\min} = \frac{\sqrt{2qI_{\text{dark}}^{\text{anode}} \mu \Delta f}}{S} \quad (3.4)$$

where q is the elementary charge, $I_{\text{dark}}^{\text{anode}}$ is the anode dark current, μ is the gain, Δf is the system's bandwidth and S is the anode radiant sensitivity. For the Hamamatsu R7154 PMT this comes out as $P_{\min} = 3.5 \times 10^{-17} \sqrt{\Delta f} \text{ W}/\sqrt{\text{Hz}}$ or $2 \times 10^{-15} \text{ W}$ for $\Delta f = 3 \text{ kHz}$. This is the detection limit for bandwidths below a few kHz. Above that, the shot noise, which is caused by random fluctuations of the electronic signal becomes the limiting factor.

The PDs that we use in the laboratory (Thorlabs PDA10A2) are GaP-based, switchable gain amplified detectors with a responsivity of 0.02 A/W with variable gain between 0-70 dB ($1.5 \times 10^3 - 4.8 \times 10^6 \text{ V/A}$). This results in a sensitivity of $30 - 10^5 \text{ A/W}$. The electronic gain of the PD comes at the cost

of 570 μV RMS noise (at 70 dB) on the output, which can be translated into a noise equivalent power (NEP) $2 \times 10^{-11} \text{W}/\sqrt{\text{Hz}}$ at a measurement bandwidth of $\Delta f = 2.6 \text{ kHz}$ at peak sensitivity. This corresponds to a minimum detectable power of $P_{\text{min}} = \text{NEP}(\lambda) \times \sqrt{\Delta f} = 0.2 \times 10^{-9} \text{ W}$ (or 0.4 μW for 0 dB amplification) at around $\lambda = 230 \text{ nm}$. In summary, PMTs have about 5-8 orders of magnitude better signal-to-noise ratio and are the best choice for amplifying weak fluorescence signals.

On the quantum efficiency of PMTs

We use a Hamamatsu R7154 PMT with a quantum efficiency of $\epsilon_{\text{QE}} = 0.35(5)$ for all light measurements near 230 nm (see Table 3.1. The manufacturer's data sheet provides the mean value, while the error is the standard deviation of the same signal measured using three PMTs of the same model in our laboratory on different detectors. Relying only on the datasheet for the value of the quantum efficiency can be problematic due to aging or usage outside the specified range. On the other hand, the uncertainties of other parameters such as collection efficiency, laser intensity, scattering rate, and beam profile have a greater influence than the quantum efficiency uncertainty of the PMT. It is thus sufficient to estimate this value by comparing the PMT signal to that of a photodiode with a known responsivity and amplification factor (Thorlabs PDA10A2). We do this in a measurement with $S/N \gg 1$, which corresponds to $> 10^{12}$ photons per second in the peak. We found that the PMT/PD signal agreement was 1.24(13). However, the GaN-based photodiode's detection surface also undergoes aging, making this calibration method only suitable for a rough comparison. As a second method, we used a calibrated Thorlabs S120VC photodiode that accurately measures 10^{-6} W of a weak laser beam. This power

Table 3.1: Specification of two Hamamatsu PMTs used in the studies presented here. The window material is transparent to UV radiation for both models. The cathode material mainly governs the spectral range of applications.

model	cathode material	spectral range	cathode QE@ λ
R7154	Cs-Te	160-320 nm	0.35@230 nm
R928	Sb-Na-K-Cs	160-900 nm	0.25@230-400 nm

is still three orders of magnitude higher than the maximum the anode of the PMT can handle. This power was reduced by a factor of 10^6 using a calibrated attenuator to fall within the PMT's linear range. This measurement showed agreement within the established uncertainty of 20%.

3.6 Buffer gas machine characterization

In all of the experiments described in this thesis, we use a cryogenic buffer-gas beam source (refer to Section 3.3), unless noted otherwise, to produce a pulsed beam of AlF molecules or cadmium atoms, which are then detected by laser absorption, laser-induced fluorescence, or two-photon ionization. The typical experimental apparatus is shown schematically in Figure 3.9. Two radiation shields surround the buffer gas cell. An inner layer cooled to 2.7 K, and an outer layer cooled to 30 K. The 2.7 K shield is covered with coconut-derived charcoal, which acts as a sorption pump for helium and keeps the pressure in the source chamber below 10^{-7} mbar during operation. The apparatus cools to below 3 K in about four hours and can be heated to room temperature in about three hours using resistive cartridge heaters with a total power of 150 W. The molecular beam is collimated by a 10 mm and 15 mm aperture in the inner and outer radiation shields. About 2 cm from the cell aperture, a laser beam intersects the molecular beam at right angles to measure the extraction time,

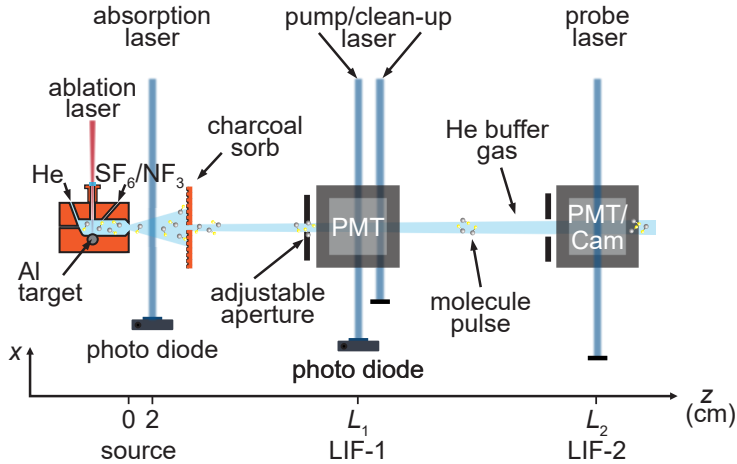


Figure 3.9: A schematic of the experimental setup. The AlF molecules are produced in a cryogenic helium buffer gas cell by laser ablation of aluminum in the presence of SF_6 or NF_3 . The cell is surrounded by two layers of radiation shields held at ≈ 30 K and ≈ 3 K, respectively. The inside of the 3 K shield is coated with coconut-derived charcoal, which acts as a sorption pump for the helium buffer gas. The molecules pass through an aperture in the shields and can be probed at various locations along the beam. For the cycling and deflection experiments presented in Chapter 4, the width of the transverse velocity distribution is reduced by increasing the distance of the detectors to the source and using an adjustable aperture.

absolute molecule number, gas density, and transverse velocity distribution. An additional, adjustable aperture, located 4 cm before the center of the first detector (LIF-1), with diameters between 1 and 15 mm, can be used to restrict the transverse velocities that enter the optical pump and probe regions.

We have two similar molecular beam machines that are identical in principle but come with slightly different distances from the source to the fluorescence detectors. Beam machine one is used for the SF_6 source characterization and the optical cycling experiments presented in this thesis. For the source characterization in this chapter, the distances to the first and second detectors are $L_1 = 35$ cm and $L_2 = 63$ cm, respectively. Beam machine two is used to

characterize the NF_3 source for AlF with $L_1 = 20$ cm and $L_2 = 44$ cm in this chapter. Later, machine one was upgraded with a corrosion-resistant flow controller (Alicat MCS-0.5 SCCM) to use NF_3 on that machine as well. Because of the hazardous properties of cadmium dust, we exclusively use machine one for experiments with cadmium.

Molecular beam measurements

The properties of the molecular beam are characterized using the non-cycling R(0) rotational line of the $A^1\Pi, v' = 0 \leftarrow X^1\Sigma^+, v'' = 0$ band (see Figure 2.6). The R(0) line is a rotationally open transition from $J'' = 0$ to $J' = 1$ in the excited state. After three optical cycles, the molecule ends up in $J'' = 2$ where it is not resonant to the R(0) light (see Section 4.2). If this transition is saturated, the fluorescence signal can be used as a calibration for a corresponding signal of three photons per molecule. We probe the density of the molecules in the SF_6 beam via absorption spectroscopy at a distance of 2 cm from the cell aperture and at a distance of 35 cm from the cell via laser-induced fluorescence as well as absorption. Figure 3.10 shows a typical arrival time profile of AlF, measured in the two different beam machines with different fluorine donor gases. The one shown in red results from a single-stage cell using SF_6 as fluorine donor gas (1.8×10^{12} srad $^{-1}$ pulse $^{-1}$ in $J'' = 0$) with a distance of $L_1 = 35$ cm after the source. In blue, we show a molecular beam emerging from a double-stage cell using NF_3 (0.2×10^{12} srad $^{-1}$ pulse $^{-1}$ in $J'' = 0$), which produces molecules with a lower forward velocity. However, this beam also has a larger divergence and the number of molecules that reach the detector is reduced accordingly. The distance to LIF-1 is set to $L_1 = 42$ cm from the cell aperture. The detection laser is locked to the center of the spectral line,

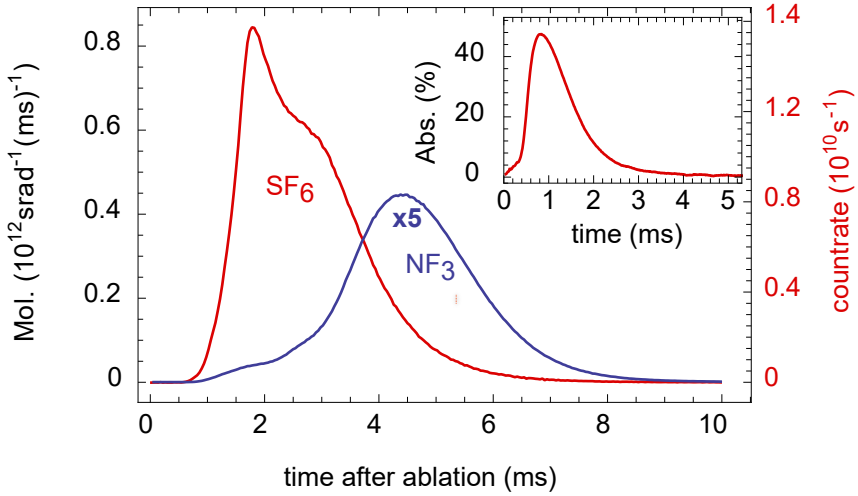


Figure 3.10: Time of flight fluorescence signal of the cryogenic buffer gas molecular beam of AlF using a single (red, SF₆) and double-stage (blue, NF₃) cell. The inset shows laser absorption, measured at a distance of 2 cm downstream from the cell aperture as a function of time. These measurements are performed on the R(0) line of the $A^1\Pi, v' = 0 \leftarrow X^1\Sigma^+, v'' = 0$ band.

and the laser power is chosen to saturate the transition. The inset depicts the temporal absorption profile for the SF₆ beam, recorded 2 cm from the cell aperture, with the frequency of the detection laser locked to the center of the Doppler broadened absorption feature (1 GHz FWHM) and power of 0.1 mW ($I \approx 10^{-3} I_{\text{sat}}$, I_{sat} is the saturation intensity). The low laser intensity prevents pumping the molecules to dark rotational states during their interaction with the laser beam and ensures uniform absorption. The number of molecules leaving the cell in the rotational ground state can be quickly estimated by time-integrating the resonant-absorption signal for a geometry as in Figure 3.11. This method requires a good guess of the geometry of the molecular beam and the intersection with the laser beam, which are often not well known. The

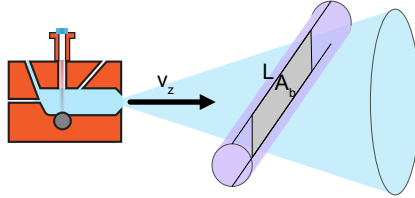


Figure 3.11: Illustration of laser absorption measurements behind the cell exit. Atoms and molecules exit the buffer gas cell source with a broad transverse velocity distribution that allows measuring the opening angle.

number of molecules can be estimated as

$$N = \frac{A_b v_z}{L \sigma_D} \int \ln(P_i/P_t) dt,$$

where A_b is the cross-sectional area of the molecular beam with the absorption laser, v_z is the forward velocity, and L is the absorption length, which is defined by an aperture in the molecular beam. P_i and P_t are the incident and transmitted laser power, respectively. To find the peak absorption cross-section, we model the absorption spectrum using the spectroscopic constants from [72] together with Voigt profiles, whose Lorentzian contribution is 84 MHz and whose Gaussian contribution is used to fit the experimental spectrum. The result is a peak absorption cross-section of $\sigma_D = 1.6 \times 10^{-11} \text{ cm}^2$ for the R(0) rotational line. For the SF_6 beam, this amounts to $N = 2.5 \times 10^{12}$ molecules per steradian per molecular pulse in the rotational ground state, which compares well to *atomic* cryogenic buffer gas beams of Yb, which typically contain about $10^{12} - 10^{13}$ atoms per pulse [120, 124]. A comparable number of Al atoms is produced in our cell. The reaction efficiency of hot Al with NF_3 or SF_6 to form AlF is close to unity [70]. Absorption measurements close to the cell aperture to determine the density of the molecules can sometimes be misleading due to

collisions with the high density of helium buffer gas in this region that alter the beam propagation dynamics. It is thus advised to measure the number of molecules in the detection region where the trap will be located in the final experimental setup. Due to the transverse and longitudinal velocity spread, the density is significantly lower at that point. Molecular sources typically do not produce the required optical density to perform such measurements far away from the cell aperture. We thus estimate the molecule number via the emitted fluorescence in LIF-1. The total collection efficiency of the optics is estimated to be $\epsilon = 0.07(1)$. The detected solid angle of the molecular beam is determined by a 15 mm diameter aperture that restricts the molecular beam and the measured laser beam diameter (e^{-2}) of 2 mm to $\Omega = 2.4(5) \times 10^{-4}$. To measure the molecular beam brightness, we carefully characterize the fluorescence detector shown in Figure 3.5b). The transverse velocities of the molecular beam can be restricted using a variable aperture, and a camera is used to measure the spatial distribution of the molecular fluorescence for the different apertures. This allows us to calibrate the imaging system and compare it to the results of ray-tracing software[§]. The total collection efficiency of the optics, ϵ , includes the transmission through the lenses and window. The quantum efficiency of the PMT is ϵ_{QE} . The detected solid angle of the molecular beam, Ω , includes the laser's beam profile. The beam brightness is

$$\Phi = \frac{N_c}{\epsilon \epsilon_{\text{QE}} \Omega \langle n_{\text{ph},R}^{\infty} \rangle} \quad (3.5)$$

molecules per steradian per pulse, where N_c is the total number of photon counts per pulse. The number of emitted photons is independent of the for-

[§]OSLO EDU, Lambda Research

ward velocity of the molecules if the fluorescence yield on the R(0) line is saturated ($\langle n_{\text{ph},R}^{\infty}(J'' = 0) \rangle = 3$, refer to Section 4.2). The molecular beam brightness in this measurement is $\Phi = 1.7(4) \times 10^{12}$ molecules per steradian per pulse in the rotational ground state. This agrees well with the absorption measurement close to the source. Additionally, we verify this measurement by restricting the molecular beam using an aperture with a diameter smaller than the spot size of the excitation laser. This defines the solid angle more precisely and ensures that all molecules experience the same laser intensity. A study comparing the production yield of other diatomic monofluoride molecules, including MgF, CaF, and YbF, showed that the production yield of AlF is about a factor of 10 higher. This increase in molecule number allows us to measure a weak absorption signal of the probe laser in LIF-1 of $P_i/P_{t,\text{min}} \simeq 4(1) \times 10^{-3}$ (peak absorption) using a differential photodiode. The calculated peak absorption cross-section, including the hyperfine structure and the residual Doppler broadening of 40 MHz is $\sigma = 5 \times 10^{-11} \text{ cm}^2$. The peak absorption corresponds to a peak density of $5 \times 10^7 \text{ cm}^{-3}$ and about 5×10^8 molecules within the anticipated capture volume of the MOT. The time integral of the absorption profile allows converting the absorption signal into a beam brightness of 1.5×10^{12} molecules per steradian per pulse in the rotational ground state, consistent with the fluorescence measurement (see Table 3.2).

The extraction time of the molecular pulse of AlF created using SF₆ (Figure 3.10) peaks at ≈ 1 ms. The signal decays on a similar timescale. These measurements are typically taken at 1-2 cm from the cell orifice, corresponding to an extraction time of about 0.8-0.9 ms with a forward velocity of 200 m/s. Later arriving molecules are slower and extracted at a later time, compressing the true pulse shape compared to the measured one. The extraction time

Table 3.2: Fluorescence (f) and absorption (a) measurements at a distance z after the source to determine the number of Cd atoms and AlF molecules in the ground state ($X^1\Sigma^+, v = 0, J = 0$) that are produced in the buffer gas beam source. Absorption

	number ($\text{srad}^{-1}\text{pulse}^{-1}$)	density (cm^{-3})
AlF ^a (SF ₆) $z=2$ cm	2.5×10^{12}	-
Cd ^a $z=2$ cm	1.5×10^{12}	4×10^{11}
AlF ^a (SF ₆) $z=35$ cm	1.5×10^{12}	5×10^7
AlF ^f (SF ₆) $z=35$ cm	1.8×10^{12}	-
AlF ^f (NF ₃) $z=35$ cm	0.2×10^{12}	-

^f fluorescence measurement
^a absorption measurement

is crucial, requiring the diffusion time τ_{diff} of pre-cooled molecules inside the source to the cell walls to be significantly smaller than the pump-out time τ_{pump} through the orifice. The diffusion time depends on the density of buffer gas in steady-state, $\bar{n}_{0,b}$, and the thermally averaged elastic collision cross section σ_{b-s} of the species with buffer gas atoms. $\bar{n}_{0,b}$ is calculated from the molecular flow, approximately $f_{0,b} \approx 4.5 \times 10^{17} \text{ s}^{-1} \text{ sccm}^{-1}$, resulting in a stagnation density of buffer gas at a flow of 1, sccm in our cell design of $\bar{n}_{0,b} \approx 1 \times 10^{15} \text{ cm}^{-3}$. Typical values for σ_{b-s} are 10^{-14} cm^2 . According to a theoretical study, the thermally averaged diffusion cross-section for AlF at 20 K is around $7 \times 10^{-15} \text{ cm}^2$, similar to that of YbF in helium [125]. With a thermal velocity of helium at 4 K, $v_{0,b} = 145 \text{ m s}^{-1}$, we can calculate:

$$\tau_{\text{diff}} = \frac{16}{9\pi} \frac{A_{\text{cell}} \bar{n}_{0,b} \sigma_{b-s}}{\bar{v}_{0,b}} \quad (3.6)$$

$$\tau_{\text{pump}} = \frac{4V_{\text{cell}}}{A_{\text{ap}} \bar{v}_{0,b}}. \quad (3.7)$$

The calculated diffusion time for AlF in our cell is $\tau_{\text{diff}} = 0.14 \text{ ms}$, while the calculated extraction time is $\tau_{\text{pump}} = 3.4 \text{ ms}$. The discrepancy between the

calculated and observed extraction time suggests that the cooling process dynamics are not adequately captured by this model. Firstly, the molecular beam velocity is faster than expected from the cell temperature, measuring 8 K instead of 4 K from a velocity of ≈ 200 m/s. Additionally, the extraction efficiency is highly sensitive to the ablation laser alignment, which has the tendency to promote metal ablation in the direction of gas flow. To achieve a 1 ms extraction time, we assume the effective cell length is halved, and only atoms with a velocity vector aligned with the buffer gas flow direction are extracted.

Cadmium absorption measurement

The number of molecules can be compared to the efficiency of producing a cadmium atomic beam. Measuring absorption on the $^1P_1 \leftarrow ^1S_0$ transition of cadmium is straightforward due to the absence of internal structure in the ground and excited state. The absorption is dependent on the spatial distribution of the density, $n(z)$, along the z -axis, which represents the direction of the laser light. The measured absorption is represented by I_f/I_i . When considering absorption on a closed transition, the absorption cross section on resonance for an individual atom is given by σ_0 , as described by Reference [126]:

$$\sigma_0 = \frac{2J' + 1}{2J'' + 1} \frac{\lambda^2}{2\pi}. \quad (3.8)$$

For Cd on the $^1P_1 \leftarrow ^1S_0$ transition $\sigma_0 = 3 \frac{\lambda^2}{2\pi} = 2.5 \times 10^{-10} \text{cm}^2$. When the Doppler width $\sigma_D \gg \sigma_0$, $\sigma_D = \frac{\sqrt{\pi}}{2} \frac{\Gamma}{\Gamma_D} \sigma_0$, with Γ_D , the transverse Doppler width (FWHM) and $\Gamma/(2\pi)$ is the natural linewidth measured in Hz.

In order to estimate the number of atoms that are produced in the buffer gas cell, the absorption of a low-intensity laser beam is measured about 1 cm

behind the cell with the goal to optimize the number of produced atoms. Under typical conditions at YAG energies exceeding 10 mJ, the probe light is totally absorbed near the source in a ≈ 2 GHz wide region around the line center, as shown in Figure 3.12. Reducing the source output by lowering the ablation

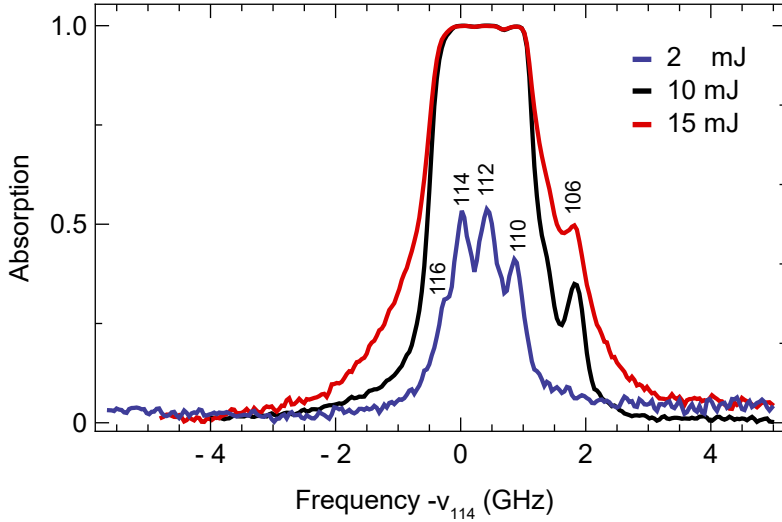


Figure 3.12: Absorption spectrum of cadmium isotopes in the atomic beam behind the buffer gas cell aperture for different ablation laser intensities (red, black, blue curves). Isotopes 110,112,114,116 have the highest abundance and saturate completely. ^{106}Cd appears as an isolated peak at a detuning of 2 GHz. ^{108}Cd is hidden in the shoulder of the saturated peaks.

energy brings partial resolution to the isotopes with the lowest abundance and makes the absorption measurement usable for this purpose. For one measurement, the YAG laser power is deliberately reduced (blue curve) to show the absorption spectrum of an optically thin sample. The optical thickness of isotopes 110, 112, 114, and 116 leads to 100% absorption of the probe light in normal operation. We thus use isotope ^{106}Cd to estimate the density, which has an abundance of just 1.25% and appears as a relatively isolated peak on

the high-frequency side. The ^{108}Cd peak can not be resolved well in the shoulder. If we estimate the background absorption of the abundant isotopes in the region around ^{106}Cd and remove it, we find $\frac{I_i}{I_f}(^{106}\text{Cd})=0.82(1)$. In the case of this measurement, we can approximate $\sigma_D \approx \sigma_0/5$ and calculate

$$n_{\text{peak}} = -\ln(I_f/I_i) \frac{1}{\sigma_0/5z}$$

as $n_{\text{peak}} = 5(1) \times 10^9 \text{cm}^{-3}$ for ^{106}Cd with an uncertainty of the transverse velocity opening angle estimated from Figure 3.16 that corresponds to an absorption length of $z = 0.8(2)\text{cm}$. Correspondingly, the peak density of all cadmium isotopes is then at least $4(1) \times 10^{11} \text{cm}^{-3}$. Assuming a typical mean forward velocity of $\bar{v} = 150 \text{m/s}$ and a mean density \bar{n} over a time interval of $\Delta t = 1 \text{ms}$ with half the peak density, we can estimate the total number of atoms measured by the probe laser beam to be

$$N = \bar{v} A_{\text{ap}} \bar{n} \Delta t,$$

where $A_{\text{ap}} = \pi(z/2)^2$ is the cross section of the atomic beam at the position of intersection with the absorption laser beam (see Figure 3.11). The result is a flux of $N = 1.5(8) \times 10^{12}$ cadmium atoms over one millisecond from a natural sample, which reasonably agrees with observations of other atomic beams [70] and the estimate for AIF in the previous section.

3.7 Velocity distribution of the AIF beam

Buffer gas beam sources produce molecular beams with a wide range of forward velocities, unlike, for example, supersonic beam sources. These buffer

gas beams have a significantly higher total flux and a lower average forward velocity, making them ideal for laser cooling applications. However, the velocity distribution of a beam of molecules with a large natural linewidth and hyperfine structure cannot be measured using traditional techniques involving Doppler spectroscopy with an angled probe laser. This section presents a novel method to measure the velocity distribution of such molecules by using an optical pumping laser to create a time-dependent rotational state distribution (subpulses) within the molecular pulse. This distribution is then probed at another location, allowing the velocity distribution to be measured by assigning velocities to each subpulse based on their time of flight. This method is quite general and only requires a transition that can be used for optical pumping.

Longitudinal velocity distribution $f(v_{\parallel})$

The large natural linewidth and the hyperfine structure in the excited state of AIF preclude using Doppler-sensitive LIF detection to determine the forward velocity distribution of the molecular beam. Instead, a new optical pump-probe scheme in combination with time-of-flight[¶] measurements was developed. An intense laser beam ($I \approx 5 \text{ W/cm}^2 \approx 5I_{\text{sat}}$), tuned to the R(0) line ($J' = 1 \leftarrow J'' = 0$), intersects the molecular beam in LIF-1 and pumps $> 90\%$ of the interacting molecules to $J'' = 2$. Further downstream, in LIF-2, the same laser probes the population left behind in $J'' = 0$ with a ten times lower intensity. By rapidly shuttering the pump laser using an acousto-optical modulator, we divide a single time-of-flight profile into ten temporal segments. The velocity of the molecules within each segment is measured via their time-of-flight to

[¶]For fluorescence measurements, time-of-flight refers to the time of arrival at the detector and should not be confused with ion time-of-flight measurements.

the second LIF detector 22 cm further downstream (figure 3.13 a). The spikes in the top panel of Figure 3.13 a) are caused by molecules that are already present in the detection volume when the laser light is rapidly turned on. This simple technique allows to record the forward velocity as a function of the arrival time in a single shot as shown in Figure 3.13b). This method provides

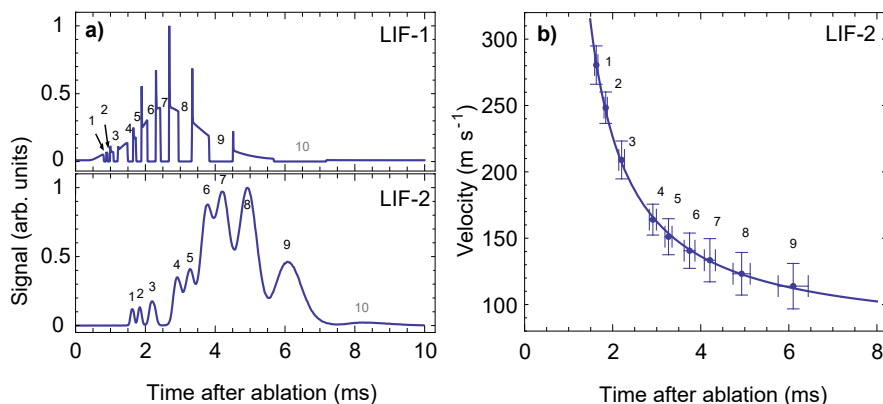


Figure 3.13: Demonstration of a new method to determine the longitudinal velocity distribution with a single laser frequency using a pump-probe scheme on the R(0) line. This example is for the AIF beam created using NF_3 from Figure 3.10. a) A rapidly shuttered high-power laser beam chops the TOF profile in LIF-1 into narrow temporal segments by pumping molecules to the dark $J'' = 2$ level (top). A low-power laser beam in LIF-2 probes the population in $J'' = 0$ (bottom). Each trough in the top panel (molecules are not pumped) has a corresponding peak in the bottom panel. The time difference between the center of the trough and the center of the peak determines the mean velocity of the molecules within this segment. c) Mean velocity of each segment (data points) and FWHM of the velocity distribution (vertical error bars) as a function of arrival time with the fit (solid curve, $v(t) = a + b/(t - t_0)$).

a fast and accurate alternative to Doppler-sensitive LIF detection. A fit to the data is used to convert the time-of-flight profile from panel a) into a velocity distribution, shown in panel d). With the fit from Figure 3.13b) we can now transform the time axis into a velocity axis and find the number of molecules

produced by the source as a function of the forward velocity as in Figure 3.14. If both beam machines are operated under identical conditions, the forward

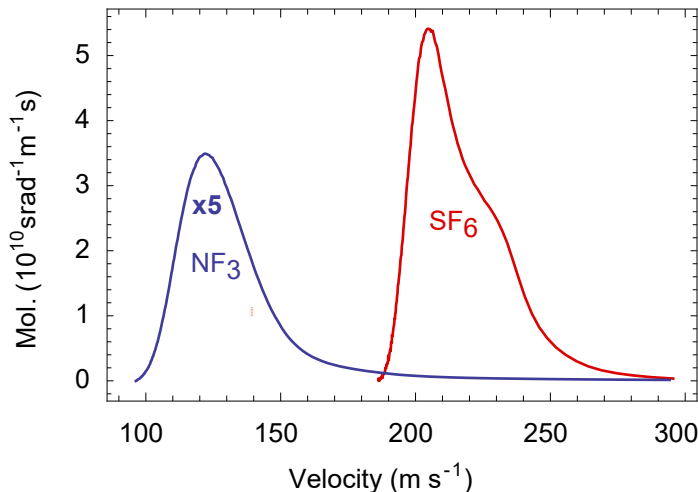


Figure 3.14: Longitudinal velocity distribution of the cryogenic buffer gas molecular beam of AIF using a single (red, SF_6) and double-stage (blue, NF_3) cell. The TOF profiles from Figure 3.10 are converted to a velocity distribution using the fit function obtained by the method in Figure 3.13.

velocity for the NF_3 beam is typically 10-15% lower, and the brightness is similar within a factor of 2. However, when using SF_6 as a fluorine donor, we observe a steady increase in the molecular beam velocity with the number of ablation pulses. This is most likely caused by a build-up of fluoride and sulfur compounds (“ablation dust”) inside the buffer gas cell, see also Figure 3.15. The dust prevents the helium buffer gas from thermalizing with the cell walls after being heated by the ablation plasma, which results in a faster and hotter molecular beam. Cleaning the cell with, e.g., a citric agent restores a slow beam. Flowing He and SF_6 for a day through a clean cell without the ablation laser running results in a slow beam, indicating that this effect is not caused by SF_6 ice or poor helium pumping. These issues can be mitigated by

using a cell with a larger volume, which is less sensitive to dust build-up and heating effects but produces molecular pulses that are longer in time and less dense. In summary, when NF_3 is used instead of SF_6 , the molecular beam has

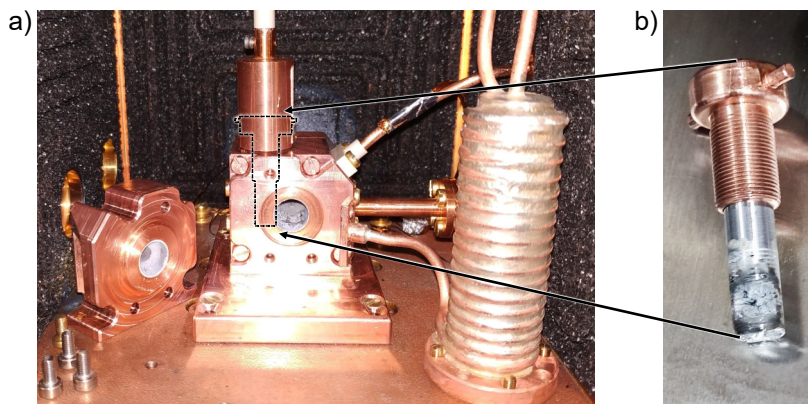


Figure 3.15: a) Rear view of the opened buffer gas beam source. After weeks of operation, there is a thick layer of dust inside the chamber. The charcoal on the exit is coated with particles. b) During that time, the ablation laser vaporized approximately 2 mg of metal from the cadmium target, which is mounted in a slot in the aluminum rod.

a lower forward velocity (170 m/s, single-stage cell, and 130 m/s double-stage) and does not speed up over time. The number of AlF molecules produced this way is equivalent and saturates at a significantly lower flow rate of the fluorine donor gas. The SF_6 beam delivers more molecules to the detector due to the lower divergence and slightly higher forward velocity. This beam is adequate for spectroscopy and optical cycling experiments. However, for loading a MOT, a more stable beam with a lower forward velocity might be more advantageous.

Transverse velocity distribution $f(v_{\perp})$

The distribution of velocity perpendicular to the direction of observation causes a broadening of the spectral lines. If we know the original shape of the lines,

we can analyze the measured spectrum to determine the velocity distribution that caused the broadening. To accomplish this, we measure the R(2) line ($A^1\Pi, v' = 0, J' = 3 \leftarrow X^1\Sigma^+, v'' = 0, J'' = 2$) under two conditions. First, we take a measurement in absorption near the aperture of the buffer gas cell where the density is high, and the transverse velocity contributions broaden the spectrum significantly more than the hyperfine structure. Second, we take a measurement further downstream behind a narrow slit to reduce the Doppler contribution. Here the spectral width is dominated by the hyperfine structure in the excited state, which is significantly larger than the Doppler broadening. The mathematical description to deconvolute two Gaussians of the form $G_i(\nu, \sigma) = \frac{1}{\sqrt{2\pi}\sigma_i} \exp\left\{-\frac{\nu^2}{2\sigma_i^2}\right\}$ as a function of the frequency ν and standard deviation σ to arrive at the velocity distribution $\rho(\nu, \sigma_{\text{fl}}, \sigma_{\text{abs}})$ from the convolution $G_2 = G_1 * \rho$ by performing Fourier transformation \mathcal{F} is adapted following Reference [127].

$$\mathcal{F}(G_2(\nu)) = \mathcal{F}(G_1(\nu))\mathcal{F}(\rho)$$

$$\rho(\nu, \sigma_1, \sigma_2) = \mathcal{F}^{-1}\left(\frac{\mathcal{F}(G_2(\nu))}{\mathcal{F}(G_1(\nu))}\right) = \frac{\exp\frac{-\nu^2}{2\sigma_1^2 - 2\sigma_2^2}}{\sqrt{-\sigma_1^2 + \sigma_2^2}}$$

The standard deviations of the two Gaussians measured in absorption $G_{\text{abs}}(\nu, \sigma_{\text{abs}})$ and in fluorescence $G_{\text{fl}}(\nu, \sigma_{\text{fl}})$, shown in Figure 3.16 are $\sigma_{\text{abs}} = 249.9$ MHz and $\sigma_{\text{fl}} = 142.2$ MHz respectively. The mean longitudinal velocity in this measurement was estimated to be 150 m/s. Figure 3.16 shows the velocity distribution ρ where $\nu \rightarrow \frac{v_{\perp}}{c}\nu_0 = \frac{v_{\parallel} \tan(\Theta)}{c}\nu_0$ as a distribution of the spherical coordinate Θ .

In this measurement, the transverse velocity distribution of molecules leav-

ing the cell has a full-width at half maximum (FWHM) of 110 m/s, corresponding to a divergence of $\Delta\Theta = 40^\circ$. In comparison, an effusive beam has a divergence of $\Theta = 120^\circ$. The molecular beams we are working with experience an increase in forward velocity due to collisions with the buffer gas, while the transverse velocity remains constant. The measured divergence is close to the expected value given by $\Delta\Theta = 2 \arctan\left(\frac{\Delta v_\perp/2}{\Delta v_\parallel}\right) \approx 2\sqrt{\frac{m_b}{m_s}}$, which is approximately $\Delta\Theta = 33.8^\circ$ for AlF in a He buffer gas [124]. The FWHM solid angle is $\pi \tan(20^\circ)^2 \approx 0.4$.

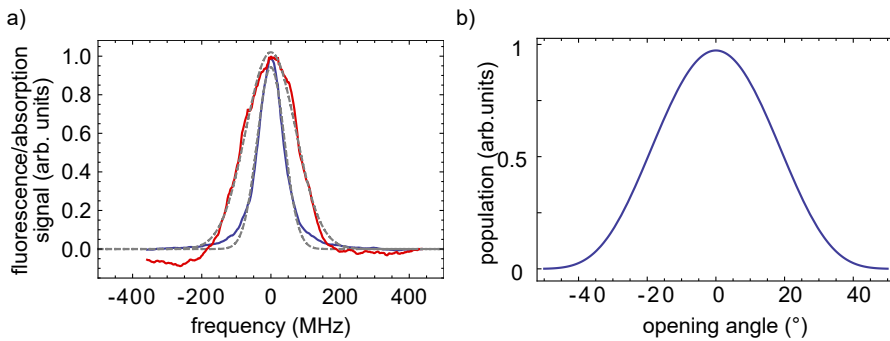


Figure 3.16: Transverse velocity distribution obtained by deconvoluting spectra shown in a), which are measured after exiting the cell in absorption (red curve) and further downstream in fluorescence (blue curve). The dashed curves represent the corresponding Gaussian fits. The mean forward velocity is 150 m/s. b) the population of transverse velocities is obtained by deconvoluting the two spectra and has a FWHM of approximately 40° .

3.8 Summary

This chapter explored the use of buffer gas cooling as a method to create a bright and slow molecular beam of AlF molecules for laser cooling experiments. To determine the density of molecules in the beam, absorption spectroscopy was

used at a distance of 2 cm from the cell aperture, and laser-induced fluorescence and absorption at a distance of 35 cm from the cell. The production efficiency of AIF was found to be significantly larger than that of comparable molecular beam sources, with a similar number of particles per pulse as atomic buffer gas beam sources. It was discovered that using NF_3 as a fluorine donor gas greatly improved the long-term stability of the molecular beam without affecting its brightness. This allows the delivery of approximately 5×10^8 molecules per pulse into the MOT capture volume, in a single rotational state. A novel method for measuring the forward velocity distribution of a molecular beam involving optical pumping was presented. This technique provides a fast and accurate alternative to Doppler-sensitive LIF detection.

Chapter 4

Optical cycling of AlF molecules

4.1 Introduction

The density of diatomic molecules in a typical MOT is significantly lower than that of their atomic counterparts. This becomes clear when comparing the typical numbers and densities of trapped atoms in atomic MOTs (e.g. Rb $N \approx 1 \times 10^8$, $\rho = 10^{10} \text{cm}^{-3}$) to that of CaF or YbF ($N \approx 1 \times 10^5$, $\rho \approx 10^6 - 10^7 \text{cm}^{-3}$) [48,129,130]. This is partly due to the challenges of producing bright molecular beams, but also because the radiation pressure of light is typically lower for molecules than for atoms. Zeeman slowing is not straightforward for molecules,

This chapter is based on

[79] – S. Hofsäss, *et al.*, “Optical cycling of AlF molecules.” In *New Journal of Physics* **23** 075001 (2021)

[128] – M. Doppelbauer, *et al.*, “Characterization of the $b^3\Sigma^+$, $v = 0$ state and its interaction with the $A^1\Pi$ state in aluminium monofluoride.” In *Molecular Physics* **119**(1-2) e1810351 (2021)

which leads to a reduced slowing efficiency [131, 132]. Alternatives such as chirped slowing or white light slowing are less efficient techniques since these tools are not selective to a narrow velocity range. This can be explained by looking at the diatomic radicals SrF, CaF, and YO which have all been laser-cooled in a three-dimensional MOT. To prevent optical pumping into dark rotational states, the P(1) rotational line of the $A^2\Pi_{1/2} \leftrightarrow X^2\Sigma^+$ electronic transition is used for laser cooling. The number of hyperfine states in the ground state n_g involved in the optical cycle is larger than the number of coupled hyperfine states in the excited state n_e . The scattering rate is further reduced by leaks to higher vibrational states in the ground state, since the population will remain in these states for some time, before being repumped to the main cooling cycle [44]. As a result, the effective spontaneous decay rate $\Gamma_{\text{eff}} = \frac{2n_e}{n_g+n_e}\Gamma$ is typically $\Gamma/10$, while for alkali atoms such as potassium on the D2 line $\Gamma_{\text{eff}} = \Gamma$ [133]. This leads to a long slowing distance and the characteristically low capture velocity of molecular MOTs of around 20 m/s [134, 135]. In this chapter, we show how the implementation of a fast optical cycling scheme provides a large spontaneous scattering force that can bring a beam of AlF molecules to near-zero velocity in a distance of a few centimeters. This scheme significantly increases the capture velocity of a magneto-optical trap and allows a large fraction of molecules from a typical molecular beam to be loaded into the trap. Laser-cooling of AlF molecules on the $A^1\Pi \leftrightarrow X^1\Sigma^+$ transition has the advantage that all Q-lines are rotationally closed, unlike $^2\Sigma^+$ molecules, where only the P(1) line is rotationally closed. This means that a high photon scattering rate can be sustained on all Q-rotational lines ($J'' = J'$), despite the complex hyperfine structure. The short lifetime of the $A^1\Pi$ state ($\tau = 1.9$ ns), the highly diagonal Franck-Condon matrix, and the specific

hyperfine structure allow for a simple, highly closed, and fast optical cycling scheme. We measure the dispersed fluorescence spectrum in order to measure the ratio of Einstein- A coefficients A_{01}/A_{00} and compare this to measurements of the ratio of the relative absorption strengths on the $0 - 1$ to $1 - 1$ band and to theoretical calculations. Further, we quantify the number of optical cycles on the Q(1) line in saturation by calibrating the fluorescence yield using a rotationally open transition. We also investigate other loss channels such as losses to the intermediate triplet state on the $A^1\Pi \rightarrow a^3\Pi$ band, electric field-induced parity mixing in the excited state, and losses due to two-photon ionization. We probe the population in $v'' = 1$ before and after optical pumping and find an increase in $v'' = 1$ population that corresponds to the determined vibrational loss rate. We measure the radiation pressure force by deflecting the molecular beam transversely and demonstrate efficient repumping from $v'' = 1$. Numerical simulations of the optical cycling process are in good agreement with the experimental results. A rate-equation model describes the optical cycle well for low laser intensities but fails to predict the scattering rate accurately at high intensities.

4.2 Calibration of laser-induced fluorescence

Direct laser cooling can only be applied to molecules that have a specific energy structure that allows engineering a quasi-closed optical cycle. It is important to understand how long this cycling process can be maintained before the molecule is lost from the cycle and requires to be repumped by a second laser. To determine this, we measure the maximum number of photons that can be scattered before the molecule enters a dark state. A straightforward way to determine the

number of optical cycles a molecule has undergone is by comparing the fluorescence yield from a cycling transition to that of a rotationally open transition. For the cycling Q lines, the average number of photons that can be scattered is mainly determined by the leak to higher vibrational states (see next section). However, the rotationally open P and R transitions can be used to calibrate the detected laser-induced fluorescence. The rotational branching ratios, derived through the theory of angular momentum, determine the average number of photons a molecule scatters before ending up in a dark rotational state. The branching ratio is determined by the Hönl-London factors $S_J^{\Delta J}(J'')$, which for a ${}^1\Pi - {}^1\Sigma^+$ transition are given by

$$S^P(J'') = \frac{1}{2}J'' - \frac{1}{2} \quad \text{for } J'' \geq 2 \quad (4.1)$$

$$S^Q(J'') = J'' + \frac{1}{2} \quad \text{for } J'' \geq 1 \quad (4.2)$$

$$S^R(J'') = \frac{1}{2}J'' + 1 \quad \text{for } J'' \geq 0, \quad (4.3)$$

where $\sum_{\Delta J} S^{\Delta J}(J'') = 2J'' + 1$ is the total degeneracy [136,137]. The branching ratios can be written as

$$r_P(J'') = \frac{S^P(J'')}{S^P(J'') + S^R(J'' - 2)} \quad (4.4)$$

$$r_Q(J'') = 1 \quad (4.5)$$

$$r_R(J'') = \frac{S^R(J'')}{S^R(J'') + S^P(J'' + 2)}. \quad (4.6)$$

with a limiting value for the number of photons scattered by a molecule $\langle n_{\text{ph},P}^\infty \rangle = 2 - 1/J''$ and $\langle n_{\text{ph},R}^\infty \rangle = 2 + 1/(J'' + 1)$ for P and R lines, respectively. For $J'' \rightarrow \infty$ the maximum number that can be scattered $\langle n_{\text{ph},P,R}^\infty \rangle \rightarrow 2$. There

is an additional vibrational loss of 1/213 per cycle, which lowers the expected number of photons for each line by about 1%. When including the hyperfine structure, the limiting values must be corrected to account for additional hyperfine dark states, which can lower the expected number of scattered photons by up to 10%. In principle, we can now use this calibration method to quantify how many photons each molecule has scattered in order to determine the vibrational loss channel. However, the emission pattern is dependent on the relative weight of σ^+ , σ^- , and π polarized radiation. We define an angle θ between the polarization of the excitation light and the detector, where $\theta = 0$ is the quantization axis. The fluorescence intensity of π and σ polarized light has an angular dependence according to $I_\pi \propto \sin^2 \theta$ and $I_\sigma \propto (1 + \cos^2 \theta)/2$, where θ is the angle between the \mathbf{k} -vector of the fluorescence light and the polarization vector of the excitation light.

We perform a consistency check to ensure that our method of using rotationally open transitions as “standard candles” is suitable for calibrating the fluorescence of the cycling transitions. To restrict off-axis excitation, the molecular beam is collimated with a round, 2 mm diameter aperture placed 4 cm before the first LIF detector. For the data presented here, the laser beam is collimated to a e^{-2} diameter of $w_z = 3.7$ mm and $w_y = 2.9$ mm. This ensures sufficient intensity is available to saturate the transition, that the transverse extent of the laser exceeds that of the molecular beam, and that the interaction volume can be reliably imaged onto the PMT. Figure 4.1 shows the laser-induced fluorescence for the R(1) and P(3) lines, time-integrated over the duration of the molecular pulse, as a function of the laser intensity. A low-intensity Q-branch spectrum allows us to normalize the LIF signals to the respective rotational state population in $J'' = 1$ and $J'' = 3$. We display the

saturation of the R(1) and P(3) lines because they both reach the same excited state. In saturation, the two LIF signals reflect the predicted ratio by the Hönl-London factors. A deviation from this ratio would lead to a systematic error in the calibration. The solid curves result from a theoretical simulation of the light-molecule interaction using rate equations, the measured velocity distribution, and the spatial profile of the molecular and laser beam. The P(3) line saturates at 1.5 photons and not at $\langle n_{\text{ph},P}^\infty \rangle = 5/3$ as predicted by Equation 4.4. This is due to optical pumping of molecules into the dark $M_{F''} = \pm 6$ Zeeman sublevels, which slightly lowers the average number of photons scattered per molecule. By averaging over all possible decay channels, we expect

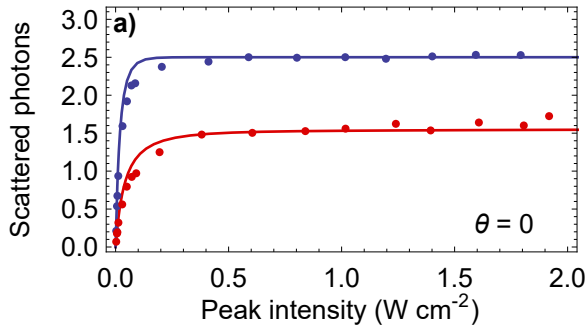


Figure 4.1: The fluorescence yield of the R(1) (blue data points) and the P(3) (red data points) lines saturates at 2.5 and 1.5 photons per molecule, respectively. Simulations based on a rate equation model are shown as solid curves. In this measurement, the polarization angle is set parallel to the axis to the detector ($\theta = 0$).

a periodic modulation of the detected fluorescence with an amplitude of 0.18 for the R(1) and -0.03 for the P(3) line. Figure 4.2 summarizes this effect. The points with error bars are the measured fluorescence normalized to their value for $\Theta = 0$. The solid curves are the predicted modulation by calculating the weighted sum over all possible decay channels. Therefore, it is crucial to

choose $\Theta = 0$, where the ratio of the two fluorescence signals in Figure 4.1 corresponds to the ratio of the Hönl-London factors. The same is true for the Q(1) line, whose periodic modulation has an amplitude of 0.11 (not shown), slightly less than the R(1) line. In conclusion, we can compare the fluorescence yield of rotationally closed transitions to that of rotationally open transitions in order to convert from fluorescence signal into the number of optical cycles per molecule. In order to do so, the fluorescence emission pattern needs to be considered.

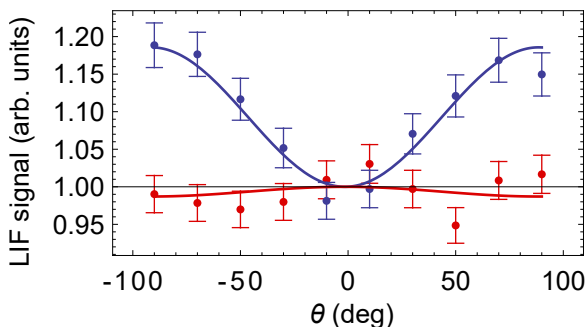


Figure 4.2: Rotating the polarization of the excitation laser changes the detected fluorescence intensity for the R(1) line (blue) significantly but not for the P(3) line (red). Only if the polarization is set along y , i.e., along the axis of the detector ($\Theta = 0$), the ratio of the signals from the P and R lines is equal to the ratio predicted by the Hönl-London factors.

4.3 Leaks from the optical cycle to $v'' = 1$

Optical cycling on a rotationally closed transition leads to a manifold increase in the signal-to-noise ratio of the observed LIF signal. However, the optical cycle is not fully closed, as losses to higher vibrational states can still occur. The leak to $X^1\Sigma^+$, $v'' = 1$ is the most significant loss channel for laser cooling of

AIF. There are no selection rules that restrict branching to higher vibrational states in the ground electronic state. We can however measure the number of optical cycles, N , when the transition is saturated. The probability distribution for a molecule to scatter exactly n photons, when this number is limited to N , is $p(n) = (1 - r)r^{n-1}$ for $n < N$, $p(n) = r^{n-1}$ for $n = N$, and $p(n) = 0$ for $n > N$. For a molecule that interacts with a laser for a time t_i , the maximum number of photons scattered is $N = Rt_i$, where R is the photon scattering rate. When an ensemble of molecules interacts with a laser beam, the fraction of molecules remaining in the initial state is given by $P(N) = r^N$ [80]. The average number of photons scattered is

$$\langle n_{\text{ph}} \rangle = \sum_{n=0}^N np(n) = \frac{1 - r^N}{1 - r} = \frac{1 - P(N)}{1 - r}. \quad (4.7)$$

The limiting value for $N \rightarrow \infty$ is given by $\langle n_{\text{ph}}^\infty \rangle = 1/(1 - r)$, and the standard deviation of the probability distribution is equal to the mean value. This means that there is a wide variation of the number of photons scattered by individual molecules [39, 80]. We can approximate r by the previously calculated ratio of Einstein coefficients $r = 1/(1 + A_{01}/A_{00}) = 0.9953$ [72] and arrive at a maximum mean number of scattered photons of $\langle n_{\text{ph}}^\infty \rangle = 213$.* The population in $v'' = 0$ decreases with N , according to $P_{v''=0}(N) = r^N$, which for $r \approx 1$ is well approximated by an exponential decay $P_{v''=0}(N) \simeq e^{-N(1-r)}$. In the limit of $\Gamma t_i \gg 1$ and $R \ll \Gamma$, with $\Gamma = 1/\tau_0$ being the spontaneous decay rate,

$$n_{\text{ph}}(t_i) = \frac{1 - e^{-R(1-r)t_i}}{1 - r}. \quad (4.8)$$

*Depending on the basis set and potential that is used to calculate the branching ratio, the uncertainty is estimated to be about 15%.

The limit of $\langle n_{\text{ph}}^{\infty} \rangle$ can only be reached if $R(1-r)t_i \gg 1$, where the fluorescence saturates [138].

Method 1: dispersed fluorescence

To determine the number of vibrational repump lasers that are necessary for laser slowing and cooling, we measure the Einstein coefficient A_{01} of the $A^1\Pi, v = 0 \rightarrow X^1\Sigma^+, v'' = 1$ (0-1) band relative to the Einstein A_{00} coefficient of the 0-0 band. We do this by dispersing the laser-induced fluorescence of the molecules using a compact spectrometer. For the dispersed fluorescence detection, we tune a cw laser to the Q(1) line of the 0-0 band near 227.5 nm (1 mm diameter beam, 90 mW) and cross it with the molecular beam about 320 mm from the source. The laser-induced fluorescence is collected, coupled into an optical fiber, and dispersed using a compact Czerny-Turner spectrometer (Avantes AvaSpec-ULS2048-EVO, 600 μm fiber, 25 μm entrance slit) with a resolution of 1.5 nm. A typical dispersed fluorescence spectrum is shown in Fig. 4.3 a). We average 4000 shots and subtract the background, measured without the molecular beam but with 90 mW of cw laser light present (Fig 4.3 b)). To fit the data, we first determine the line shape of the spectrometer at 227.5 nm and 231.7 nm by coupling narrow-band laser light directly into the spectrometer. We then use the two spectral response functions to fit the molecular emission spectrum. The only fit parameters are the two emission amplitudes. The fit to the data is shown as the red curve in Fig. 4.3. Figure 4.3 c) shows the emission of the molecules on the 0-1 band around 231.7 nm more clearly. The fit gives a ratio of emission amplitudes of $\nu_{01}A_{01}/(\nu_{00}A_{00}) = (7 \pm 3) \times 10^{-3}$. We account for the slightly different detection efficiency of the spectrometer at 231.7 nm and 227.5 nm. Light at 231.7 nm is detected with a $10 \pm 3\%$ higher efficiency than

light at 227.5 nm. To reduce the uncertainty, we repeat this measurement 14 times which gives a final result for the R(2) line of $A_{01}/A_{00} = (7.3 \pm 1) \times 10^{-3}$.

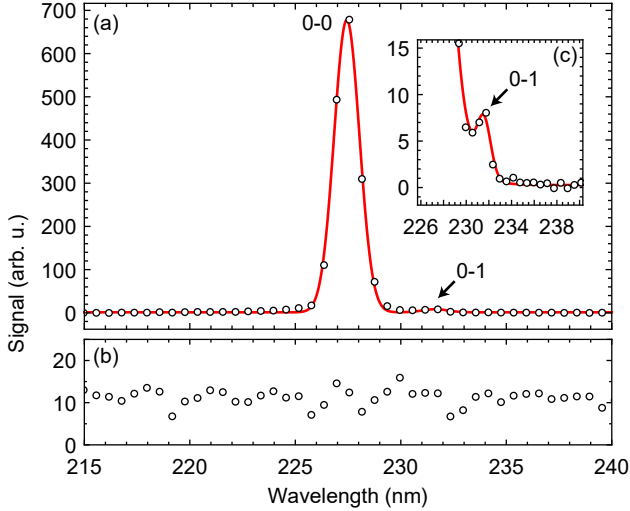


Figure 4.3: Dispersed fluorescence spectrum after excitation on the Q(1) line of the 0-0 band. The LIF is coupled into an optical fiber and dispersed using a grating spectrometer a). The red curve shows a fit to the data (circles) using the measured spectral response of the spectrometer. The background spectrum b) is recorded without the molecular beam but with the excitation laser present. The inset c) shows the 0-1 emission band on an enlarged scale.

Method 2: ratio of absorption strengths

As an alternative method, we can determine the ratio of Einstein B_{01}^{ab}/B_{11}^{ab} coefficients by comparing the absorption strengths of rotational lines, i.e. originating from the same $v'' = 1, J''$ -level in the $X^1\Sigma^+$ state, of the 0-1 band to the absorption strength of the same rotational lines of the 1-1 band. In this case, we measure the ratio $A_{01}/A_{11} = \nu_{01}^3 B_{01}^{ab}/(\nu_{11}^3 B_{11}^{ab})$, with ν_{01} and ν_{11} the transition frequencies of the rotational lines of the 0-1 and 1-1 band, respectively. In a molecular beam, the population distribution across vibrational levels in

the electronic ground state might change on the timescale of an experiment. Therefore, it is more precise to measure the ratio A_{01}/A_{11} instead of A_{01}/A_{00} . The experimental results of the two methods are compared to numerical calculations. By increasing the intensity of the ablation laser, we can increase the population in the $X^1\Sigma^+, v'' = 1$ state from about 4% to up to 15% of the overall population. This, however, also increases the mean velocity of the AlF molecules to over 300 m/s. For this measurement, we overlap two lasers and cross them with the molecular beam orthogonally. The frequency of one laser is locked to the center of the R(2) line of the 0-1 band near 231.7 nm, and the frequency of the second laser is locked to the R(2) line of the 1-1 band near 227.5 nm. We choose these lines specifically because they appear as isolated single lines. The spatial mode of each laser is cleaned up using pinholes resulting in a Gaussian intensity distribution in the interaction region with a $1/e^2$ diameter of 0.46 mm. The molecule fluorescence induced by each laser is imaged on a PMT, recorded on alternate shots to minimize the effect of source fluctuations, and averaged over 50 shots. The two ToF profiles are shown in Fig. 4.4. The circles show the ToF profile of the molecules excited on the 0-1 band with a laser power of 7.3 mW. The solid black curve results from excitation on the 1-1 band with a laser power of 0.045 mW. The power in each laser beam is adjusted such that the amplitudes of the two ToF profiles are nearly identical. Weak excitation is necessary to prevent optical pumping into dark rotational states. The difference between the two ToF profiles is shown in Fig. 4.4b). The ratio of laser powers directly reflects the ratio of Einstein coefficients $B_{01}^{abs}/B_{11}^{abs} = 6.2 \times 10^{-3}$, because $\nu_{00}A_{00}/(\nu_{11}A_{11}) \approx 1$. We repeat this measurement for 16 different pairs of laser powers. The mean and standard error of these measurements gives the final result of $A_{01}/A_{11} = (5.72 \pm 0.08) \times 10^{-3}$. We repeat the measurement

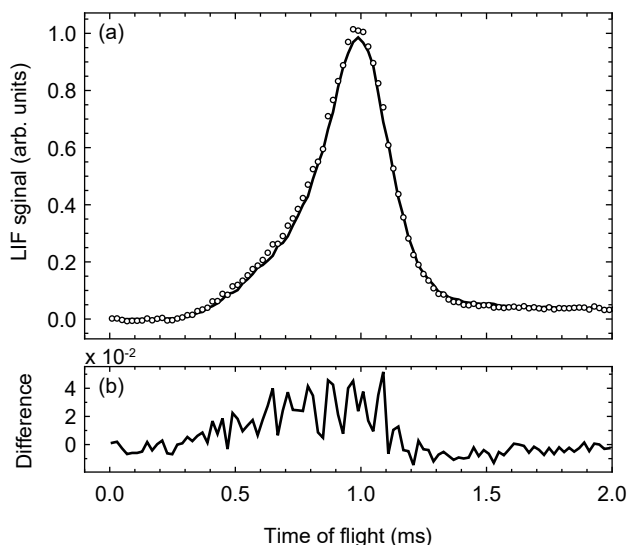


Figure 4.4: a) Two ToF profiles. One laser is locked to the R(2) line of the 1-1 band (white circles), and a second laser is locked to the R(2) line of the 0-1 band (solid black curve) of the $A^1\Pi \leftarrow X^1\Sigma^+$ transition. The two laser beams are overlapped and have the same Gaussian intensity profile. The powers are set to 0.045 mW for the 1-1 band and 7.3 mW for the 0-1 band. The difference between the two ToFs is shown in b).

using the R(1) rotational lines, giving $A_{01}/A_{11} = (5.59 \pm 0.02) \times 10^{-3}$. The results are summarized in Table 4.1 and compared to theoretical calculations by Jesús Pérez-Ríos that also yield the Franck Condon factors in Table 4.2.[†]

[†]The RKR potentials are derived by using Le Roy's program [139] to fit both Morse and expanded Morse oscillator (EMO) functions to precise spectroscopic data [90, 91]. These potentials are then used to calculate the Franck-Condon factors (f_{AX}), which are listed in Table 4.2 and compared to the Franck-Condon factors derived from *ab initio* calculations [140]. To predict the transition probability of the weak off-diagonal bands more precisely, we include the variation of the transition dipole moment with internuclear distance [141]. We use the multi-reference-configuration-interaction (MRCI) method available in MOLPRO 2019 [92] to perform *ab initio* calculations of the relevant transition dipole moment. The MRCI calculations are fed with the natural orbitals from a Multi-Configuration Self-Consistent Field (MCSCF) calculation with a complete active space (CAS) consisting of nine orbitals with A_1 symmetry, three with B_1 symmetry and three with B_2 symmetry associated with the point group C_{2v} . The calculations employ the AV5Z [93] basis set for each atom.

Table 4.1: Calculated and measured ratios of transition probabilities.

	Measured	Calculated
$(A_{01}/A_{00}) \times 10^3$	7.3 ± 1^a	4.7
$(A_{01}/A_{11}) \times 10^3$	5.59 ± 0.02^b	4.8
$(A_{02}/A_{00}) \times 10^3$	-	0.1

^a dispersed fluorescence^b ratio of absorption strengths

Table 4.2: Calculated Franck-Condon factors.

f_{AX}	Ab initio [140]	EMO	Morse
f_{00}	0.99992	0.996	0.9948
f_{01}	9×10^{-6}	0.0040	0.0005
f_{02}	7×10^{-5}	2.6×10^{-5}	2.7×10^{-5}

Method 3: saturation of laser-induced fluorescence

A more direct method to determine r is to measure $\langle n_{\text{ph}}^\infty \rangle$ by saturating the Q(1) fluorescence signal. Figure 4.5 shows two time of flight profiles of the molecular pulse with the laser tuned to the Q(1) (blue) and R(1) (black) lines. While the R(1) line can only scatter a maximum of 2.5 photons, the Q line is rotationally closed and does not suffer any rotational losses. Both traces are taken with the same laser intensity to qualitatively demonstrate the signal enhancement due to optical cycling. The time-integrated fluorescence spectrum of the Q-branch for low and high laser intensity is shown in Figure 4.6. The low-intensity spectrum is scaled by a factor of 20. Each Q-line shows a similar signal enhancement at high laser power, demonstrating that all Q-lines can cycle. The saturation of the Q(1) fluorescence for two forward velocities $v_z = 150$ m/s (blue) and $v_z = 300$ m/s (red), is shown in Figure 4.7. Here, the same signal is recorded with different laser intensities and then calibrated using the standard candle method from Section 4.2. The solid curves are simulations based on the optical

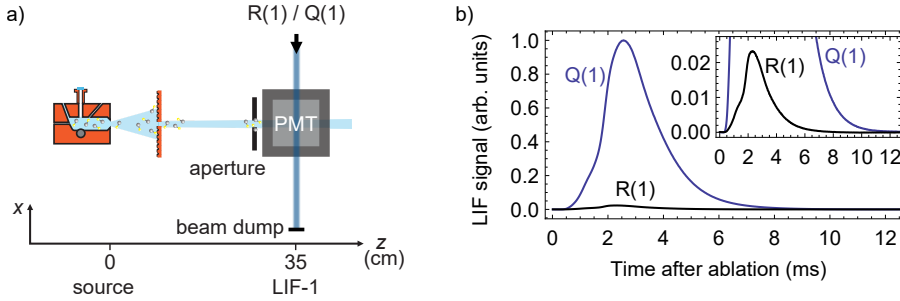


Figure 4.5: a) Demonstration of optical cycling on the rotationally closed Q-lines. The experimental setup is modified from the one presented in Section 3.6. b) Compared to a non-cycling transition (R(1), black), the LIF signal is strongly enhanced by using a cycling transition (Q(1), blue) to probe the molecular beam.

Bloch equations, and the dashed lines are the predictions from the rate equation model. The calculations of both models are described in detail in a recent PhD thesis [142]. We use the measured laser beam profile and forward velocity to predict $N = \int R(t)dt$ for each theoretical model and equation 4.7 to predict $\langle n_{\text{ph}} \rangle$. It is clear that a high optical cycling rate can be obtained despite the large number of hyperfine components involved in the cycling scheme. The rate equations do not account for the effects of coherent dark states and thus predict fluorescence saturation at a lower intensity. This method is suitable to demonstrate that the fluorescence of the Q(1) line indeed saturates at around 213 photons as predicted by theoretical calculations.

4.4 Other loss channels

When using a single laser frequency, the vibrational loss channel is expected to be the limiting factor. However, if a repump laser closes this channel, other loss channels become significant. These include losses to intermediate electronic

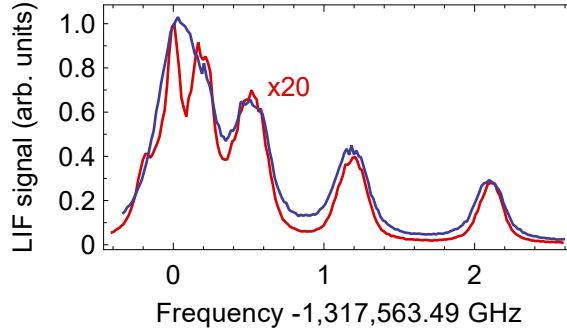


Figure 4.6: A Q-branch spectrum ($J = 1$ to $J = 4$), recorded using a low (red) and high (blue) laser intensity demonstrates that optical cycling is not hindered by the increasing complexity with increasing J . The low power spectrum is scaled up by a factor of 20.

states, rotational losses due to parity mixing, or $1+1$ ionization from the excited state. It is thus important to quantify these loss channels beforehand.

The $A^1\Pi \rightarrow a^3\Pi$ band

There are two triplet states that are relevant for laser cooling of AlF, which are also shown in Figure 2.4, the $a^3\Pi$ state which is the lowest electronic triplet state, and the $b^3\Sigma^+$ state, which is slightly higher in energy than the $A^1\Pi$ state [143]. The close proximity of the $b^3\Sigma^+$ state to the $A^1\Pi$ state leads to a mixture of singlet/triplet characters of the wavefunction of the $A^1\Pi$ state, which opens a loss channel to the $a^3\Pi$ state [128]. To directly probe the amount of triplet wave function mixed into the $A^1\Pi$ state, we measure the ratio R_A of the number of fluorescence photons emitted on the $A^1\Pi \rightarrow a^3\Pi$ and on the $A^1\Pi \rightarrow X^1\Sigma^+$ transition. The value for R_A is identical to the ratio of the Einstein A -coefficients for $A \rightarrow a$ and $A \rightarrow X$ emission, i.e., $R_A = A_{A,a}/A_{A,X}$. The value for R_A gives the loss from the main laser cooling cycle due to electronic branching to the $a^3\Pi$ state. Previously, we measured this electronic branching

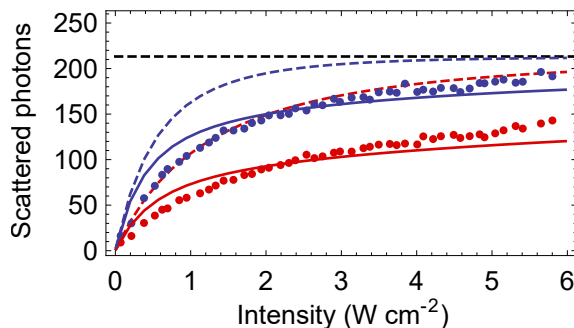


Figure 4.7: The number of optical cycles on the Q(1) line was determined by calibrating the laser-induced fluorescence with a standard candle. We measure the saturation of the Q(1) fluorescence for molecules traveling with $v_z = 150$ (blue points) and $v_z = 300$ m/s (red points). Simulations for each velocity based on optical Bloch equations and rate equations are shown as solid curves and dashed curves, respectively. The curves approach the limit of 213 photons for either increased interaction time or laser intensity.

ratio on the $A \rightarrow a$ bands indirectly to be at the 10^{-7} level by comparing the absorption strength of the $A^1\Pi, v = 0 \leftarrow a^3\Pi_0, v' = 0$ transition relative to the absorption-strength of the $A^1\Pi, v = 0 \leftarrow X^1\Sigma^+, v'' = 0$ transition [72]. In that analysis, we only considered the amount of singlet character in the wave function of the a state to determine the strength of the $A \leftarrow a$ transition. We did not account for the (then unknown) amount of triplet character in the wave function of the A state due to the interaction of the A and b states, which, as we will see here, turns out to be the dominant effect. In the experiment, we isolate the small amount of visible fluorescence from the strong UV fluorescence by a high-reflectivity UV mirror, which is transparent in the visible, in combination with a long-pass and two bandpass filters in front of the PMT (see inset in Figure 4.8). The transmission band of the filters is chosen such that only wavelengths that cover the $A^1\Pi, v' = 0 \rightarrow a^3\Pi, v'' = 0$ transition are detected by the PMT. The mirror reduces the UV fluorescence that is incident

on the spectral filters to the 10^{-6} level, suppressing their broadband phosphorescence when irradiated with UV light. The transmission of each optical element is measured individually at 227.5 nm and 599 nm, using laser light and a calibrated photodiode. The total detection efficiency, accounting for the transmittances and PMT responses, becomes $\eta_{uv} = 0.2 \pm 0.05$ for UV photons and $\eta_{vis} = 0.044 \pm 0.01$ for visible photons in the range of 596 – 604 nm. The ratio of Einstein coefficients becomes

$$R_A = \frac{n_{vis} \eta_{uv}}{n_{uv} \eta_{vis}}, \quad (4.9)$$

where n_{vis} and n_{uv} are the number of photons detected in the visible and UV, respectively. A typical measurement is presented in Figure 4.8. The molecules are optically pumped on the Q(1) line of the 0–0 band of the $A-X$ transition, and the LIF is imaged and detected by two different PMTs. The majority of the fluorescence is emitted in the UV and imaged onto the UV-sensitive PMT. The PMT is operated in current mode, which is converted into a voltage, amplified, and read into the computer. We calibrate this PMT output voltage against the output of the PMT in photon-counting mode for low incident light intensities. The small fraction of the LIF that is emitted in the visible is shown as red dots. The two time of flight profiles are very similar, with the detected signal in the visible as a fraction of the emission in the UV being $\frac{n_{vis}}{n_{uv}} = (1.3 \pm 0.05) \times 10^{-7}$. By accounting for the different detection efficiencies for the two wavelengths, the measured ratio is as given as $R_A = (6 \pm 2) \times 10^{-7}$. The total uncertainty in this measurement is dominated by the systematic uncertainty in the quantum efficiency of the two PMTs and by the uncertainty in the imaging efficiency for the two wavelengths. We also measure the ratio of the visible to the UV

fluorescence subsequent to excitation on the Q(1) line of the 1 – 1 band of the $A - X$ transition. Since the $A^1\Pi, v = 1$ level is energetically closer to the $b^3\Sigma^+, v = 0$ level, one might expect a significantly larger fraction of visible fluorescence. However, we find that the two ratios R_A are equal to within the 15% uncertainty of the measurement.

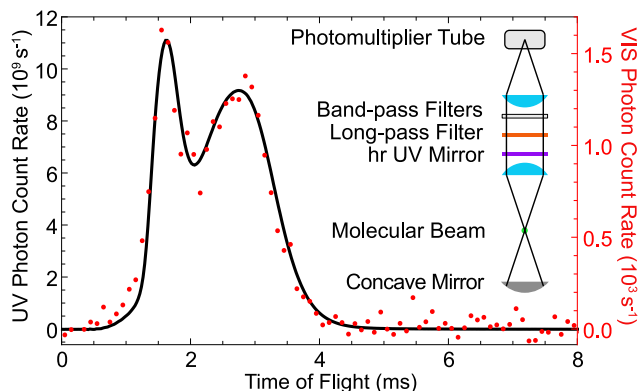


Figure 4.8: The LIF emitted in the UV (227.5 nm, black) and VIS (599 nm, red) as a function of time when the UV laser frequency is locked to the Q(1) line of the $A^1\Pi, v' = 0 \leftarrow X^1\Sigma^+, v'' = 0$ transition. The inset shows the configuration of the fluorescence detector used for the VIS experiment.

Rotational losses due to parity mixing

A small electric field can mix the closely spaced, opposite parity Λ -doublet levels in the $A^1\Pi$ state and therefore break the parity selection rule of an electric dipole transition. As a consequence, the molecules are pumped into dark rotational states in the ground state after scattering only a few photons, which means they are lost from the optical cycle.

The most substantial mixing in the $A^1\Pi, J' = 1$ level occurs between the opposite parity $M_{F'} = 1$ sublevels of $F' = 1$, whose energy-level spacing is less than a MHz. For very low electric fields, i.e., a small Stark shift compared to

the energy-level spacing, the fraction of the opposite parity that is mixed into a given parity level increases quadratically with the electric field, transitions to a linear increase for higher fields and converges to an equal mixture at high electric fields. Given the electric dipole moment of 1.45 Debye, an electric field of a few V/cm is sufficient to open a significant loss channel from the optical cycle. In the $X^1\Sigma^+$ state, the opposite parity levels are separated by at least twice the rotational constant, and parity mixing can be neglected.

When exciting on the Q(1) line, the parity mixing in the $A^1\Pi, J' = 1$ level leads to rotational branching to the dark $J'' = 0$ and $J'' = 2$ rotational levels in the electronic ground state. This effect reduces the average number of photons that can be scattered from $\langle n_{\text{ph},Q}^\infty \rangle = 1/(1 - \tau_0 A_{00})$ to a limiting value in high electric fields of only two.

To quantify this potential loss channel, we install electrodes in the optical pumping region (LIF-1), apply a uniform electric field, and measure the fraction of molecules that are pumped into $X^1\Sigma^+, v'' = 1$. The frequency of the pump laser is locked to the center of the Q(1) line and the population in $v'' = 1$ is probed in LIF-2, similar to the experiment described in Section 4.5. Figure 4.9 shows that the fraction of molecules pumped into the $v'' = 1$ level decreases rapidly with increasing electric field. Following the model described in Section 4.3, the population in the $v'' = 1$ level after N optical cycles is given by

$$P_{v''=1}(N, E) = \tau_0 A_{01} \sum_{n=0}^{N-1} \left(r - \gamma(1 - \tau_0 A_{00})E^2 \right)^n \quad (4.10)$$

$$\simeq \frac{1}{1 + \gamma E^2} \left(1 - e^{-N(1 - \tau_0 A_{00})(1 + \gamma E^2)} \right), \quad (4.11)$$

where $\tau_0 A_{01} \approx (1 - \tau_0 A_{00})$. We express the losses from the optical cycle induced

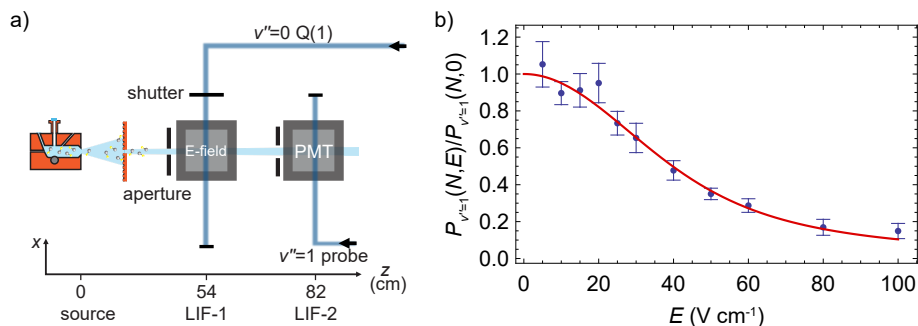


Figure 4.9: Rotational loss channels induced by stray electric fields can limit the photon scattering rate. Parity mixing in an external electric field opens a loss channel comparable to vibrational branching. a) Optical cycling in an electric field in LIF-1 is reduced by the influence of an electric field. The $v'' = 1$ population is measured in LIF-2 with an independent probe laser. The experimental setup was modified from the one presented in Section 3.6. b) The $v'' = 1$ population, $P_{v''=1}(N, E)$, is measured as a function of the applied electric field E and normalized to the value at zero electric field $P_{v''=1}(N, 0)$.

by parity mixing as $\gamma(1 - \tau_0 A_{00})E^2$ and assume a quadratic dependence with the electric field E . Assuming $N = 55 \pm 15$ we fit the model using γ as a fit parameter. The model fits the data well for $\gamma = 0.0034(6) \text{ cm}^2 \text{ V}^{-2}$. The losses due to vibrational branching and due to parity mixing become equal when $\gamma E^2 = 1$, which occurs at $17(2) \text{ V cm}^{-1}$. Only if the parity and vibrational losses are equal and $N \rightarrow \infty$ will $P_{v''=1} = 0.5$. The loss channel induced by parity mixing becomes negligible for stray electric fields below 1 V cm^{-1} .

Two-photon ionization

The $A^1\Pi, v' = 0$ state of AlF is located 5.45 eV above the $X^1\Sigma^+, v'' = 0$ state, more than halfway up to the ionization potential at 9.73 eV. Therefore, after excitation on the $A^1\Pi, v' = 0 \leftarrow X^1\Sigma^+, v'' = 0$ band near 227.5 nm, a second photon from the same laser can ionize the molecule, creating an AlF cation in

the $^2\Sigma^+$ electronic ground state and a free electron.

It is quite uncommon to observe such a single color (1+1) resonance-enhanced multiphoton ionization ((1+1)-REMPI) process for molecules using a cw laser. The cross-section for the excitation into the ionization continuum is many orders of magnitude smaller than the cross-section of the first resonant excitation step. The total ionization yield scales linearly with the time that the molecules spend in the electronically excited state. This makes ionization with a cw laser challenging, particularly if the intermediate state lives less than two nanoseconds. However, AlF can be excited on a quasi-cycling transition to increase the time the molecules spend in the excited state to $n_{\text{ph}}\tau$, which can be significantly larger than τ .

Ionization leads to a loss from the optical cycle, which can be expressed as

$$\gamma_i(I) = \frac{\Gamma_{\text{ion}}}{R} = \frac{\sigma_i I \tau}{\hbar\omega}, \quad (4.12)$$

where $\Gamma_{\text{ion}} = \sigma_i \rho_{ee}(I, \delta) I / \hbar\omega$, $\rho_{ee}(I, \delta)$ is the fraction of AlF molecules in the excited state, which depends on the intensity I and the detuning from resonance δ , σ_i is the photoionization cross-section from the $A^1\Pi$ state and $R = \rho_{ee}(I, \delta)\Gamma$ is the photon scattering rate. The ionization cross section for the $A^1\Pi$ state is independent of the rotational quantum number J'' , as is the lifetime τ . Figure 4.10 shows the total number of AlF cations produced as a function of the laser frequency while scanning a high power cw laser over the Q-branch of the $A^1\Pi, v' = 0 \leftarrow X^1\Sigma^+, v'' = 0$ band. The weak electric field mixes the opposite parity states in $A^1\Pi$, increasing the number of accessible levels and the ionization probability from the $F' = 3$ and $F' = 4$ states. This causes the Q(1) line to appear shifted by about 100 MHz. Moreover, the electric field used

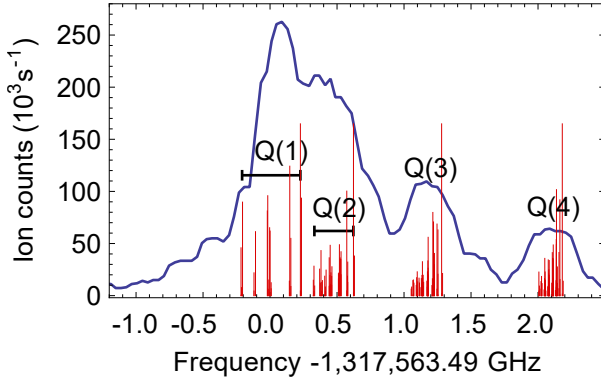


Figure 4.10: Two-photon ionization can limit the photon scattering rate. Q-branch spectrum up to $J = 4$ by detecting the molecular ions in a Wiley–McLaren time-of-flight detector. For efficient two-photon ionization, a large excited state population is required. Therefore, a very low ion-extraction field must be used to prevent optical pumping into a rotational dark state via parity mixing.

to extract the molecular ions from the ionization region must be low to prevent opening a rotational loss channel. The ion yield from (1+1) REMPI decreases with an increasing electric field.

The number of AIF molecules passing through the ionization volume per pulse is determined by absorption spectroscopy to $N_{\text{mol}} = 1.2 \times 10^8$, with a peak density of $5.5 \times 10^7 \text{ cm}^{-3}$. The number of ions detected from the same interaction region is measured using a compact, linear, Wiley-McLaren time-of-flight setup to $N_{\text{ion}} = 259/\epsilon = 650$ per pulse. The ion detection efficiency, $\epsilon \simeq 0.4$, is mainly determined by the open area ratio of the microchannel plates [144]. The number of detected ions is likely to be underestimated due to the low electric field (5 V/cm) used to extract the ions. With the laser frequency locked to the center of the Q(1) line, the fraction of the molecules that are ionized by the 17 W/cm^2 laser beam (peak intensity) $N_{\text{ion}}/N_{\text{mol}} = 5.4 \times 10^{-6}$ with $\Gamma_{\text{ion}} = N_{\text{ion}}/(t_i N_{\text{mol}}) = 1.6 \text{ s}^{-1}$, where $t_i = 3.3 \times 10^{-6} \text{ s}$ is the interaction

time of the molecules with the laser beam. During this time, the molecules scatter on average $\langle n_{\text{ph}} \rangle = 60$ photons. With $R = 18 \times 10^6 \text{ s}^{-1}$, the fractional loss from the optical cycle, due to ionization, becomes $\gamma_i = 4.7 \times 10^{-9} \text{ s}$, with $s = I/I_{\text{sat}}$ being the saturation parameter, and $\sigma_i = 2 \times 10^{-18} \text{ cm}^2$. The results presented here should be used as an order-of-magnitude estimate for the loss rate and the ionization cross-section. The low extraction voltage prevents determining the ionization volume precisely.

4.5 Optical cycling rate

Optical cycling on a deep-UV laser-cooling transition is a powerful method because each photon carries a significant momentum when it is absorbed. For AlF, this momentum corresponds to a velocity change of about $\Delta v = 3.8 \text{ cm/s}$. However, in order to completely stop an AlF molecule, this process needs to be repeated almost 4000 times because of the high initial velocity of $v = 150 \text{ m/s}$.

The previous section showed that multiple laser frequencies are required because there are some dark vibrational states that a molecule can end up in. In this section, we determine the optical cycling rate R by comparing the LIF (laser-induced fluorescence) signal from the cycling Q lines to the emission of a non-cycling rotational line. We measure the cycling rate as a function of the interaction time by probing different parts of the longitudinal velocity distribution. Secondly, we determine the rate at which the ground-state molecules are optically pumped into the dark $X^1\Sigma^+, v'' = 1$ state. Finally, we measure the acceleration, which is a product of the cycling rate and Δv , by deflecting the molecular beam from the propagation axis. However, it is important to note that these experiments are conducted with a single laser

frequency and linearly polarized light. Therefore, there may be dark hyperfine states in the optical cycle, which can limit the achievable scattering rate.

Method 1: saturation as a function of interaction time

We probe different parts of the velocity distribution to measure the fluorescence yield on the Q(1) line and compare it to a reference signal on a closed rotational line. Figure 4.11 shows the number of photons scattered as a function of the interaction time, defined by $t_i = w_z/v_z$, where w_z is the e^{-2} diameter of the laser beam. The solid curve is a fit to the data using equation 4.7 with R as fit parameter and $r = 0.9953$ as the predicted branching ratio. The fit gives $R = 17.2(2) \times 10^6 \text{ s}^{-1}$ for the effective scattering rate for a saturation parameter $s = I/I_{\text{sat}} = 6$. We estimate the systematic uncertainty in determining the number of photons scattered to be 10%. This is mainly due to uncertainties in the calibration procedure that arise from a non-linearity in the PMT gain, combined with variations in the source flux and velocity distribution.

Method 2: optical pumping into $X^1\Sigma^+, v = 1$

The second method to determine the photon-scattering rate is to measure the rate at which the molecules are pumped out of $X^1\Sigma^+, v'' = 0$ and into the dark $X^1\Sigma^+, v'' = 1$ level. For this we use a high-intensity laser beam ($\approx 20 \text{ W/cm}^2$ ($I/I_{\text{sat}} \approx 22$), $w_z = 1.3 \text{ mm}$, $w_y = 1.1 \text{ mm}$) tuned to the $A^1\Pi, v' = 0 \leftarrow X^1\Sigma^+, v'' = 0$ transition. To probe the molecules remaining in $X^1\Sigma^+, v'' = 0$, we split off a small fraction of the pump laser beam and intersect it with the molecular beam a second time in LIF-2 (see Figure 4.12a). Figure 4.12b) shows a Q-branch spectrum recorded in LIF-2 with the pump laser present (blocked) in LIF-1 in blue (red). The fraction of the $v'' = 0$ pop-

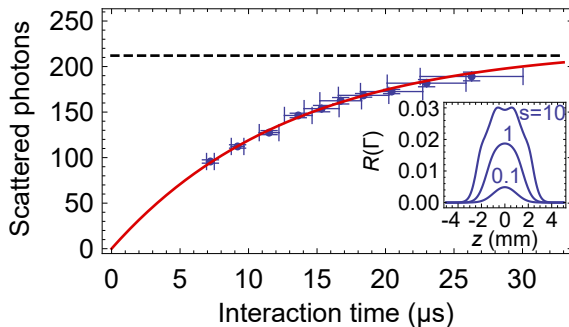


Figure 4.11: The number of photons scattered on the Q(1) line as a function of the interaction time $t_i = w_z/v_z$ with the laser, where $w_z = 3.7$ mm is the e^{-2} diameter of the laser beam along z . The number of optical cycles on the Q(1) line was determined by calibrating the laser-induced fluorescence with a standard candle. The solid curve is a fit to the data using equation 4.7. Inset: the simulated photon scattering rate expressed as a fraction of Γ as a function of z for $w_z = 3.7$ mm and three values of the saturation parameter s in the absence of losses to $v'' = 1$.

ulation that is pumped out by the high-intensity laser is 29%, 37%, 55%, and 67% for the Q(1) to Q(4) lines, respectively. The data indicates that higher Q lines scatter faster at the same laser intensity and therefore pump out more molecules for the same interaction time. The number of photons scattered by the molecules for the Q(1) through Q(4) lines is related to the population remaining in $v'' = 0$ by $\langle n_{\text{ph}} \rangle = -\ln(P_{v''=0})/(1-r) = 73(11)$, $98(15)$, $170(25)$ and $236(35)$, respectively. The pumped-out fraction for higher rotational lines is slightly overestimated because the molecules experience a radiation pressure force, leading to a Doppler shift in LIF-2 of about 17 MHz per 100 photons scattered (see next section). Additionally, the molecules are displaced from the center of the detection region, which decreases the detection efficiency slightly. The number of photons scattered on the Q(1) line corresponds to an effective scattering rate of $R = 16(2) \times 10^6 \text{ s}^{-1}$ which increases to $R = 42(7) \times 10^6 \text{ s}^{-1}$

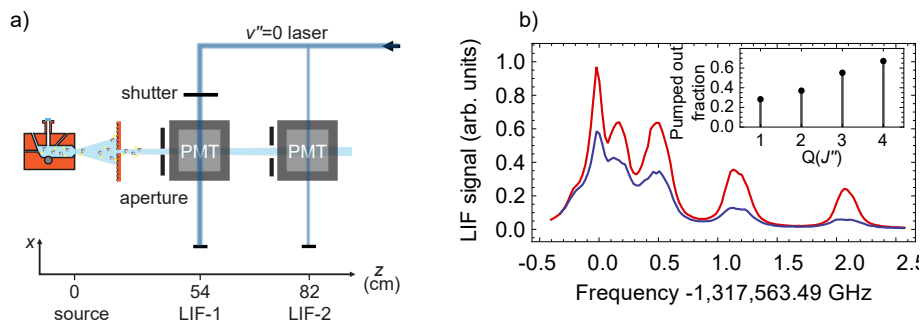


Figure 4.12: a) The depletion of the $v'' = 0$ population by a strong pump laser in LIF-1 is probed in LIF-2 with a low-intensity laser beam that has the same frequency as the pump laser. The experimental setup was modified from the one presented in Section 3.6. b) The spectrum in blue (red) is with the pump laser in LIF-1 on (off). Inset: fraction of molecules pumped from $v'' = 0$ to $v'' = 1$.

for the Q(4) line. This is in good agreement with the scattering rate determined in the previous section. We have not performed optical Bloch equation simulations for the high Q-lines, but we expect the peak scattering rate to increase for higher Q-lines. In addition, the higher Q lines reach the peak scattering rate at a lower intensity or shorter interaction time, which leads to an effectively higher scattering rate for the same laser-beam diameter. To verify that the molecules are indeed pumped to $X^1\Sigma^+, v'' = 1$, we probe the $v'' = 1$ population in LIF-2 (see Figure 4.13a)). Figure 4.13b) shows Q-branch spectra of the $A^1\Pi, v' = 0 \leftarrow X^1\Sigma^+, v'' = 1$ band using a second UV laser tuned to 231.7 nm with an output power of up to 150 mW. The top panel shows the 0 – 1 spectrum with (without) the 0 – 0 pump laser present in LIF-1 in blue (red). The top panel shows the 0 – 1 spectrum with the pump laser tuned to the Q(1) line. The bottom panel is the same spectrum but with the pump laser tuned to the Q(2) line. The total number of $v'' = 1$ molecules that are

produced in the source relative to the number of molecules in $v'' = 0$ is typically 9(2)%. The increase in $v'' = 1$ population (blue curves) corresponds to a fraction of molecules that are pumped out of $v'' = 0$ of 36(8)% and 31(7)% for the Q(1) and Q(2) lines, respectively. This is consistent with the pumped-out fraction shown in the inset of Figure 4.12a). The uncertainty is dominated by fluctuations in the $v'' = 1$ population relative to $v'' = 0$.

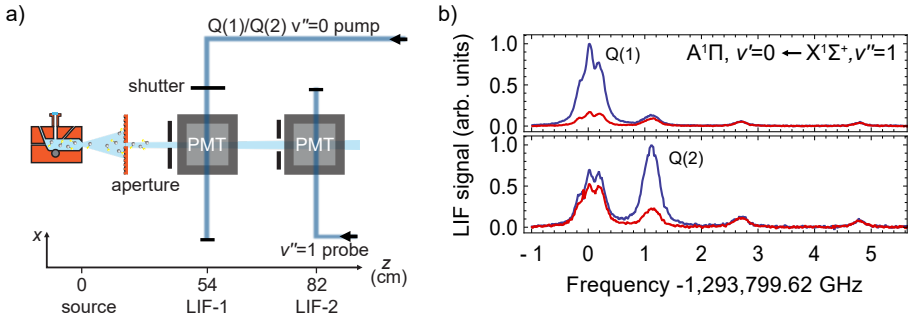


Figure 4.13: a) Optical pumping to $X^1\Sigma^+, v'' = 1$ by cycling on the Q(1) or Q(2) transition from $v'' = 0$ in LIF-1 is measured with an independent probe beam in LIF-2. The experimental setup is modified from the one presented in Section 3.6. b) The pump laser is tuned to the Q(1) (top) or Q(2) (bottom) line of the 0 – 0 band. The $v'' = 1$ population is probed in LIF-2 by recording a Q-branch spectrum of the $A^1\Pi, v' = 0 \leftarrow X^1\Sigma^+, v'' = 1$ band with (blue) and without (red) the pump laser present in LIF-1.

Method 3: deflection of the molecular beam by radiation pressure

The next step towards laser slowing and magneto-optical trapping is to demonstrate a measurable radiation pressure on the molecular beam. This method is also a straightforward way to determine the number of photons scattered by the molecules. Figure 4.14 shows a schematic of the experimental setup which is modified from the one presented in Section 3.6 by increasing the distance of the LIF zones from the source in order to reduce the transverse

velocity distribution ($L_1 = 54$ cm and $L_2 = 82$ cm). We use a high-intensity ($10 \text{ W/cm}^2 (I/I_{\text{sat}} \approx 11)$, $w_z = 0.9$ mm, and $w_y = 2$ mm) laser tuned to the Q(2) rotational line to exert radiation pressure onto the molecular beam and measure the transverse deflection by imaging the molecular fluorescence onto a sCMOS camera. A round 2 mm aperture located in front of the pump region in LIF-1 collimates the molecular beam transversely to 1 m/s (FWHM). This guarantees that the entire molecular beam can be imaged onto the camera. The imaging system is calibrated by translating the collimating aperture in LIF-1 along x and measuring the average displacement of the molecular fluorescence on the camera. A clean-up beam (100 mW in $w_z = w_y = 2$ mm) intersects the molecular beam a few cm downstream from the pumping region and recovers $> 95\%$ of the molecules lost to $v'' = 1$. The $v'' = 0$ molecules are detected in LIF-2 by splitting off a fraction of the $0-0$ pump light and directing it through LIF-2.

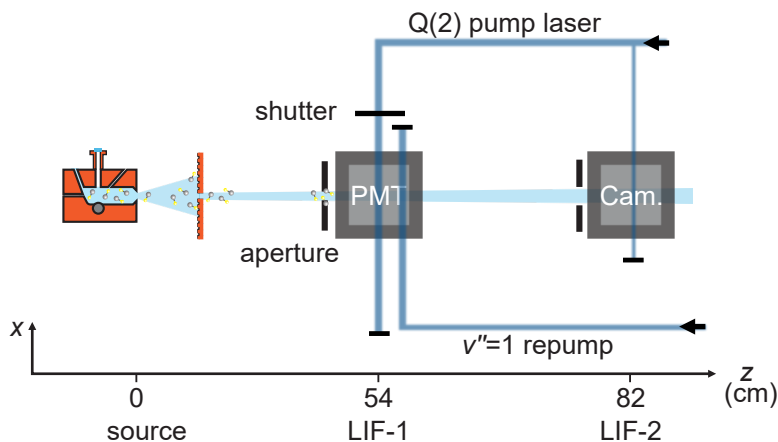


Figure 4.14: The experimental setup is similar to the one described in Section 3.6 but with increased distance from the source in order to reduce the transverse velocity distribution. An additional repump laser restores molecules from $v'' = 1$ before imaging the molecular beam in LIF-2.

The short excited state lifetime and small Franck-Condon factor of the 0–1 transition require a high laser intensity to saturate the transition. For future laser-slowing and cooling experiments, it is essential to reach a repumping rate that exceeds the rate at which molecules are pumped into $v'' = 1$. We measure a repumping rate of $\approx 10^6 \text{ s}^{-1}$, fast enough to guarantee efficient repumping. The clean-up beam pumps also the small population of $v'' = 1$ molecules produced in the source to $v'' = 0$ which is then detected in LIF-2 by the probe beam. We measure this fractional increase in $v'' = 0$ population by turning off the pump laser and determining the difference in LIF signal with and without the clean-up beam. The difference is subtracted from the image of the deflected beam because it originates from molecules that are not deflected by the radiation pressure force in LIF-1.

By absorbing a photon, the molecule acquires a linear momentum $\mathbf{p} = \hbar\mathbf{k}$ in the direction of this photon. The resulting deflection of the molecular beam, measured in LIF-2, is $d = \langle n_{\text{ph}} \rangle v_r L / v_z$, where $v_r = \hbar k / m = 3.8 \text{ cm/s}$ is the recoil velocity per photon, $L = 28 \text{ cm}$ is the distance between the pump and probe regions and $v_z = 270(20) \text{ m/s}$ is the forward velocity of the molecules.

Figure 4.15 summarizes the results of this experiment. Panel a) shows a binned camera image with the pump laser turned off (top) and turned on (bottom). The image is integrated and fitted with a Gaussian to determine the average displacement of $d = 2.15 \text{ mm}$ (panel b), indicating that the molecules scatter $\langle n_{\text{ph}} \rangle = 55(4)$ photons. This is consistent with the value derived from optical pumping, given the shorter interaction time due to the smaller waist diameter w_z . The recoil velocity is comparable to the width of the transverse velocity distribution of the molecular beam, which leads to a broadening of the molecular beam along x . This is a result of the random direction of the

spontaneously emitted photons which leads to velocity diffusion and therefore a symmetric broadening of the molecular beam. The diffusion coefficient can be approximated by $D \approx (\hbar k/m)^2 R$, with R being the photon scattering rate. This momentum diffusion gives rise to a characteristic velocity change of the molecules of $R/k = 0.54$ m/s [145], and therefore broadens the transverse velocity distribution by about 54%. A more accurate approximation is given in [36]. The upper bound for the transverse velocity after scattering $\langle n_{\text{ph}} \rangle = 55$ photons is $v_t = 2(v_z \Delta\theta + \sqrt{\langle n_{\text{ph}} \rangle} \hbar / (m\lambda)) = 1.33$ m/s, adding 0.33 m/s to the 1 m/s of the original beam. Here $\Delta\theta = 1.9$ mrad is the half-angular divergence of the molecular beam before the interaction with the laser. We measure a 33% increase in the width of the molecular beam, consistent with the approximation presented above. The symmetric broadening in Figure 4.15 b) indicates that the scattering rate along y is homogeneous. This is surprising since the laser beam $w_y = 2$ mm has the same diameter as the aperture that is used to collimate the molecular beam. However, the inset of Figure 4.11 shows that for high laser intensities ($s \geq 10$), the Gaussian wings contribute significantly to the overall scattering rate. The area under both curves in Figure 4.15 b) is identical, showing that the total number of molecules is conserved and verifying the effect of the repump laser. The Doppler shifts induced by the deflection are negligible because of the large transition linewidth. Figure 4.16 shows the deflection and the inferred average number of scattered photons for a slightly faster molecular beam ($v_z = 330$ m/s) as a function of the laser intensity. The solid red curve results from a Monte Carlo trajectory simulation using the rate equation model to predict the scattering rate, the measured laser beam profile, velocity distribution, and spatial distribution of the molecular beam as input parameters. The simulation results fit the data well, which shows that the

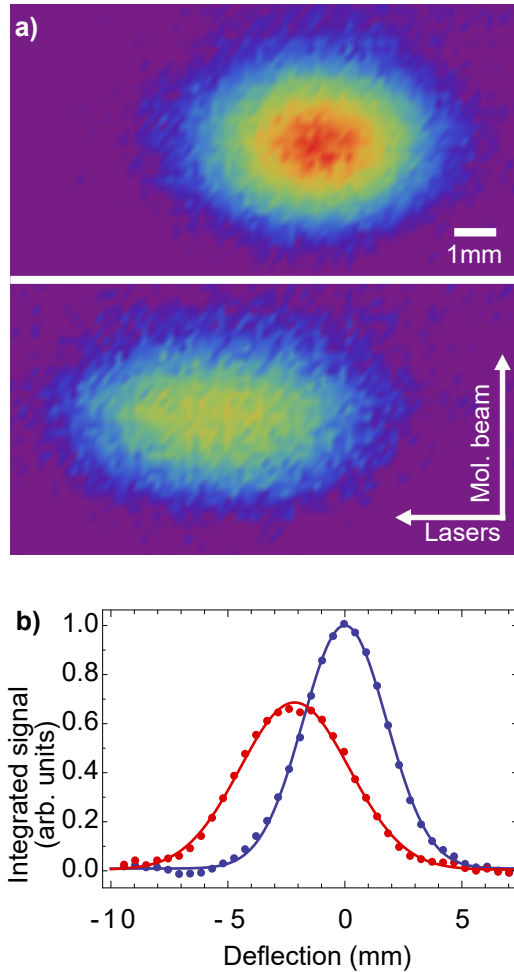


Figure 4.15: Deflection of the molecular beam by radiation pressure from a high-intensity pump laser tuned to the Q(2) rotational line of AlF (in LIF-1). A clean-up beam recovers the population from $v'' = 1$. A fraction of the pump laser beam is split off and used to probe the molecules in LIF-2. a) Image of the molecular beam passing through the probe laser beam with the pump laser beam off (top) and on (bottom). b) A Gaussian fit to the integrated image of the molecular beam yields a deflection of $d = 2.15$ mm.

rate equations predict the scattering rate well for short interaction times. The mean scattering rate of the molecules averaged over the interaction volume

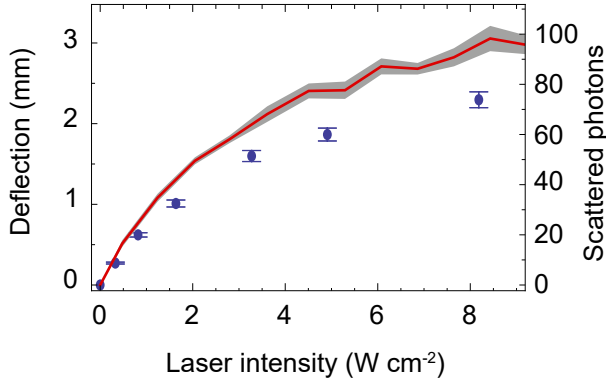


Figure 4.16: Deflection of the molecular beam by radiation pressure from a high-intensity pump laser tuned to the Q(2) rotational line of AlF (in LIF-1). A clean-up beam recovers the population from $v'' = 1$. A fraction of the pump laser beam is split off and used to probe the molecules in LIF-2. The plot shows deflection and the corresponding number of scattered photons as a function of the laser intensity. The red curve is a trajectory simulation using the rate-equation model to calculate the radiation pressure force exerted on the molecules. As expected, the rate-equation model slightly overestimates the number of scattered photons (see Section 2.3).

is $R = 23(4) \times 10^6 \text{ s}^{-1}$, which corresponds to an acceleration of $a = v_r R = 8.7(1.5) \times 10^5 \text{ m/s}^2$. This is more than an order of magnitude larger than the typical acceleration for an atomic MOT (e.g. rubidium), which is about 3000g.

To slow the molecular beam to rest using radiation pressure, the leak to $v'' = 1$ must be closed with a repump laser, which then allows to scatter about 10^4 photons. This typically lowers the scattering rate by at least a factor of two due to the additional ground-state levels that couple to the same excited state. However, the molecules also reach a higher peak scattering rate as they are not pumped to $v'' = 1$ by the low-intensity Gaussian wings of the laser beam. We estimate the stopping distance for the beams of AlF molecules produced from SF₆ and NF₃ conservatively to 6 and 2 cm, respectively.

4.5.1 Increase of cycling rate by polarization modulation

The peak cycling rate on Q(1) is $R = 16 \times 10^6 \text{ s}^{-1}$, which corresponds to about 3% excited state population. By modulating the polarization of the 0–0 light in a slowing configuration, the peak scattering rate could potentially be quadrupled, reducing the stopping distance to below 1 cm. Conveniently, the large hyperfine structure of the Q lines covers the Doppler width of the molecular beam. According to [146], a $J' = J'' \leftrightarrow J''$ transition, such as the cycling Q lines discussed here, has one dark state for any choice of polarization in zero magnetic field. Assuming linearly polarized light and the quantization axis along the polarization axis, the molecules are pumped into the dark $|J'', M_{J''} = 0\rangle$ state after scattering only a few photons. When a molecule is pumped into such a dark state it ceases to fluoresce because it does not couple to the excitation light anymore. This is detrimental to Doppler cooling.[‡]

In general, a dark state can either be an angular momentum eigenstate or a coherent superposition of these eigenstates. The former type is stationary, i.e., it does not evolve in time, and molecules accumulate and remain there indefinitely. The latter type of dark state can be non-stationary, i.e., it precesses between a dark and a bright state. We determine the dark state composition by following Reference [148] and find that for linear polarization, they are superpositions of states with different values of F_1 . The smallest F_1 splitting is $\sim \Gamma/30$ (see Figure 2.6). For a fixed linear polarization, this separation limits the scattering rate (see Section 2.3).

A common method to increase the scattering rate is to lift the degeneracy of the ground states by inducing a Zeeman splitting of the order of Γ [146]. To

[‡]Dark states are not always detrimental. Robust, velocity-selective dark states can be beneficial to cool molecules to very low temperatures below the recoil limit [147].

achieve this for AlF, a magnetic field of a few T is needed due to the small magnetic g -factor in the $^1\Sigma^+$ ground state. A second method is to switch the polarization of the light rapidly. Each polarization is associated with a set of dark states. Switching the polarization recovers a high scattering rate, provided the number of ground states is less than three times the number of excited states. For the Q-lines of AlF, the number of ground states equals the number of excited states, and all are accessible with a single laser frequency. As a result, polarization modulation can be applied to increase the scattering rate above the limit set by the ground state hyperfine structure (see below).

To simulate the optical cycling rate of the Q(1) line of AlF, we solve the optical Bloch equations for the 72-level system, following the notation presented in [149, 150]. The solid red lines in Figure 4.17 a) represent the excited-state population, ρ_{ee} for the Q(1) line as a function of the laser intensity, normalized to the two-level saturation intensity $I_{\text{sat}} = \pi\hbar c\Gamma/(3\lambda^3) = 0.93 \text{ W/cm}^2$. The laser frequency is set to the center of the Q(1) line. This is an idealized case, assuming no losses to $v'' > 0$, to demonstrate that a high scattering rate can be achieved despite the large number of hyperfine levels involved and despite the unresolved hyperfine structure in the ground state. As expected, with a linearly polarized laser and no polarization modulation ($\delta_{\text{PM}} = 0$), the scattering rate peaks at about $\Gamma/30$, limited by the precession of dark superposition states in the ground state. At high intensity, the laser interaction dominates over the hyperfine interaction, and this begins to stabilize the dark states. The excited state fraction falls off, and the system increasingly resembles the fine structure picture described above. The simulations also show that if the polarization axis rotates about the k -vector of the light at a rate $\delta_{\text{PM}} = \Gamma/2$, the dark states are effectively destabilized, and a high scattering rate is restored. The time-

evolution of the population in the ground and excited states is plotted for $I = 8I_{\text{sat}}$ and $\delta_{\text{PM}} = 0$ in Figure 4.17 b), showing that the steady state is reached at $\Gamma t = 1000$. The results from the optical Bloch equations can be compared to the

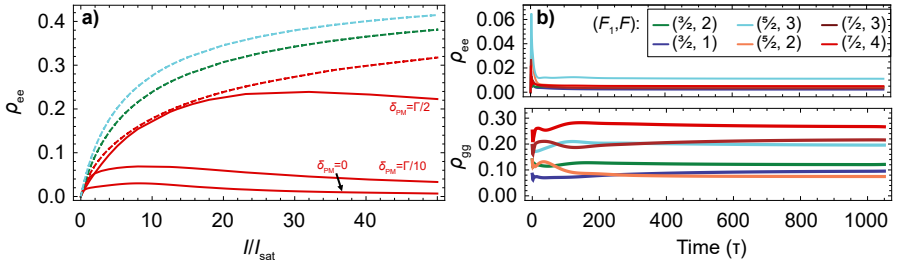


Figure 4.17: Comparison of the optical cycling rate derived from solving a rate-equation model (dashed) and the optical Bloch equations (solid) in the absence of any losses. a) Excited state population ρ_{ee} as a function of the saturation parameter $s = I/I_{\text{sat}}$, where $I_{\text{sat}} = \pi \hbar c \Gamma / (3\lambda^3) = 0.93 \text{ W/cm}^2$. The solution to the rate-equation model for the Q(1), Q(2), and Q(3) are shown in red, green, and light blue, respectively. The simulations using optical Bloch equations (solid red) for the Q(1) line are shown for three different polarization modulation rates δ_{PM} . The laser frequency is set to the center of each rotational line for all the simulations. The optical cycling rates on the Q(1) line obtained from the two theoretical models agree well at low intensities, but there is a significant difference at high intensities. b) Time-evolution of the populations in the various hyperfine levels in the $X^1\Sigma^+$, $v'' = 0$, $J'' = 1$ state for $\delta_{\text{PM}} = 0$ and $s = 8$.

solutions of a rate equation model, which neglects all coherences (dashed, red line in Figure 4.17 a)). The higher Q lines involve many more levels for which solving the Bloch equations becomes impractical. However, we solve the rate equations for the Q(2) and Q(3) lines shown as dashed green and dashed blue curves, respectively. The Figure demonstrates that the rate-equation model describes the complex multi-level system well for low laser intensities ($s \ll 1$). However, for high intensities, there are significant differences. The rate equations predict that the scattering rate increases for higher Q lines because

the span of the hyperfine structure reduces with increasing J' . The number of coherent dark states decreases from $1/3$ to $1/9$ of the total number of hyperfine transitions for the Q(1) to Q(4) lines. Therefore, the peak scattering rate is expected to increase for higher Q lines.

It is interesting to contrast AIF to the case of TIF, where recently, it was shown that unresolved hyperfine structure in the ground state significantly limits the optical cycling rate [151]. Here, the hyperfine structure in the excited state is about 30 times larger than in AIF, and the natural linewidth of the optical cycling transition is about 50 times narrower. The number of excited states which are accessible with a single laser is less than a third of the number of ground states, and polarization modulation alone is insufficient to recover the molecules pumped into dark states. Instead, laser polarization modulation must be combined with resonant microwave radiation to recover the molecules from the dark states.

4.6 Summary

The AIF molecule holds great promise for trapping and cooling molecules in a MOT at a density comparable to atomic MOTs. This is an essential step towards using laser-cooled molecules for new studies of strongly interacting many body systems and precision measurements. In this chapter, we demonstrated a method to calibrate the laser-induced fluorescence of a cycling transition to that of a non-cycling transition. This allows us to quantify the number of optical cycles performed in saturation and hence to measure the loss rate from the optical cycle. We confirm theoretical calculations of the Einstein A coefficients within our experimental uncertainties and find that losses to $v'' = 1$ limit the

optical cycle to on average 213 scattered photons. Interaction with the nearby triplet system opens a loss channel to an intermediate electronic state on the 10^{-7} level. Further, we investigate losses from the optical cycle due to parity mixing in the excited electronic state. If stray electric fields are well-controlled, approximately 10^4 photons can be scattered with only one repump laser. Further, 1+1 REMPI can lead to ionization with a probability in the 10^{-6} range. We compare three independent measurements of the optical cycling rate on a molecular beam: calibrated laser-induced fluorescence, optical pumping into the dark $A^1\Pi, v'' = 1$ state, and deflecting the molecular beam using radiation pressure. The measured scattering rate reaches $R = 17(2) \times 10^6 \text{ s}^{-1}$ for the Q(1) line, consistent with the simulations from the optical Bloch equations. Optical pumping and deflection measurements showed that the effective scattering rate increases for higher Q lines. A second UV laser was used to efficiently recover the molecules that were pumped to $v'' = 1$. The acceleration measured via molecular beam deflection will result in a very short slowing distance ($\approx 2 \text{ cm}$) and an exceptionally high capture velocity of the MOT ($\approx 50 \text{ m/s}$), both essential for a high-density MOT of molecules. The electronic structure of AlF allows a straightforward implementation of a Zeeman slower, which opens the possibility of accumulating molecules from a continuous molecular beam [118].

By solving the optical Bloch equations numerically for the 72-level system of the Q(1) line of the $A^1\Pi \leftrightarrow X^1\Sigma^+$ transition, we showed that for linear polarization, the obtainable peak scattering rate is limited to $R \approx \Gamma/30$ by the precession rate of coherent dark states. The scattering can be increased further by modulating the polarization. The numerical results were compared to a rate-equation model, that captures the dynamics well for low laser intensities or short interaction times but fails at high intensities. For low intensities, the

rate equations predict a higher scattering rate for higher Q lines because the hyperfine intervals in the $A^1\Pi$ state reduce with increasing J' .

Chapter 5

Optical isotope-shift spectroscopy on an atomic beam of cadmium

5.1 Introduction

The energy differences between isotopes of an atom or molecule are called isotope shifts (ISs). In atoms, the change in energy has two main contributions, the mass shift, an electronic factor, and the field shift, a nuclear factor proportional to (δr^2) , the change in the mean-square radius of the nucleus. The mass shift is caused by changes in the electronic wavefunction upon altering the nuclear mass, whereas the field shift arises from changes in the nuclear

This chapter is based on [152] – S. Hofsäss, *et al.*, “High-resolution isotope-shift spectroscopy of Cd I.” In *Physical Review Research* **5** 013043 (2023)

charge distribution [153]. The shifts in the energy levels can be probed spectroscopically, and if the ISs are caused by the mass shift and field shift only, there is a linear relationship between the ISs of two transitions, known as the King plot linearity. Slight deviations from this linearity can be a sensitive probe for higher-order terms in the mass shift, the quadratic field shift, or isotope-dependent nuclear deformation. If these factors can be ruled out, it may indicate a new physics, e.g. an unknown force between electrons and neutrons. Precise values for the mass shift and field shift factors or ratios thereof, and deviations from the expected linear behavior of the King plot, provide a valuable benchmark for atomic structure calculations.

Suitable candidates for optical high-precision isotope shift spectroscopy are required to exist in at least four stable, even-numbered (bosonic) isotopes, contain two narrow optical transitions, and ideally possess a laser-cooling cycle for preparation in, e.g., a magneto-optical trap. Candidates on this list are calcium (Ca), barium (Ba), zinc (Zn), cadmium (Cd), mercury (Hg), and ytterbium (Yb). So far, two candidate atoms from that list, Ca and Yb, have been investigated more thoroughly. A high-resolution King plot analysis of Ca ($Z = 20$), the lightest element with more than three stable even-numbered isotopes, recently found no evidence of non-linearity that a new bosonic force carrier could cause [154]. Since such a force that mediates between neutrons and electrons is likely to be more pronounced the more neutrons an atom has, Yb ($Z = 70$) is also an exciting candidate. High-precision measurements recently suggested a deviation from linearity at the 3σ -level [155–158]. Unfortunately, the Yb nucleus is among the most deformed nuclei in the stable region of the nuclear chart, which complicates the interpretation of the observed non-linearities because of isotope-dependent nuclear deformation. The

observed non-linearities in Yb place a limit on beyond Standard Model theories. However, without a thorough understanding of the nuclear deformation effects, it is very challenging to search for beyond Standard Model physics. Cadmium ($Z = 48$) exhibits an energy structure similar to alkaline earth elements despite being a transition metal. Cd possesses a strong cooling transition and weak intercombination lines that can be used for narrow-line cooling, precision spectroscopy, and metrology [159, 160], ideal for a sensitive measurement. In addition, cadmium has one of the smallest black-body radiation clock shifts, which mitigates the largest inaccuracy in optical lattice clocks [75]. Cadmium in its natural form has eight stable isotopes that each have an abundance of $\gtrsim 1\%$, six of which are bosons and suitable for non-linearity searches. The Cd nucleus ($Z = 48$) is only one proton pair below the $Z = 50$ proton shell closure. This significantly reduces potential non-linearities that arise from a deformed nucleus. Narrow transitions in neutral Cd and the Cd^+ ion are currently under investigation for research on atomic clocks and are suitable for precision measurements [161]. All this makes cadmium a promising candidate for the search of beyond standard model physics.

As a first step into this direction we recently showed that combining precise isotope-shift spectroscopy with new, state-of-the-art atomic structure calculations allows determining the differences in the radii of the nuclear charge distribution with high accuracy [74]. This provides an alternative, independent method to muonic X-ray spectroscopy or electron scattering. The charge radius is a fundamental property of the atomic nucleus, and precise measurements of small differences between isotopes through optical spectroscopy provide stringent tests for nuclear theory [162, 163]. In addition, highly accurate charge radii differences are critical to understanding the nuclear contributions to non-

linearities in a King plot.

5.1.1 Outline

This chapter presents the spectroscopic methods used to determine ISs of the bosonic $^1P_1 \leftarrow ^1S_0$ and $^3P_1 \leftarrow ^1S_0$ transitions in Cd I of all eight stable isotopes. For the $^1P_1 \leftarrow ^1S_0$ transition, we use enriched Cd ablation targets and a polarization-sensitive detection scheme to assign spectral lines of different isotopes that otherwise overlap. We measure the hyperfine intervals in the 1P_1 state of the two stable fermionic isotopes $^{111,113}\text{Cd}$ with MHz accuracy by analyzing subtle quantum interference effects in the laser-induced fluorescence. Knowing the exact lineshape allows us to significantly improve the ISs and resolve significant discrepancies among previous measurements. The radiative lifetime of the 1P_1 state is extracted by fitting the spectral lineshape. The absolute transition frequencies are determined with high accuracy. A King-plot analysis of the two transitions allows us to extract the intercept and slope and to determine precise values for the differences in the nuclear charge radii of the fermions. This measurement is also used to benchmark a recent high-level atomic structure calculation of the mass shift and field shift, with which we find excellent agreement [164]. In addition, we show that the off-diagonal, second-order hyperfine interaction in the fermions is $\lesssim 3$ MHz, in good agreement with calculations [164].

The methods presented here are relevant to the field of collinear laser spectroscopy of rare isotopes produced at accelerator facilities [165]. In these experiments, laser spectroscopy is used to determine the fundamental properties of nuclei, including the nuclear spin, the magnetic dipole moment, the electric quadrupole moment, and the charge radius. Due to the low number of atoms

produced in these experiments, these properties are obtained from strong transitions in the visible or UV part of the spectrum to increase the signal-to-noise ratio. We show that if quantum interference in the laser-induced fluorescence of strong transitions is not taken into account, it can cause significant systematic errors in determining the fundamental properties of nuclei.

5.2 Historical background

At the end of the 19th century, Michelson*, unaware of isotope shifts in general, tried to define a new absolute standard to measure length. For that, he found an atomic transition without structure that can be used as a homogeneous light source in a grating spectrometer. In his study of several elements, including hydrogen, oxygen, zinc, cadmium, thallium, and mercury, he found the cadmium red line near 643.9 nm to be well suited for this purpose, with the blue (480 nm) and green (508.6 nm) lines for calibration [166]. The first observation of different isotopes of the same element had unknowingly taken place in 1912 when Russell and Rossi compared the spectra of two isotopes of thorium ($^{230,232}\text{Th}$) that were at this time considered to be different elements [167]. It was not until further interferometry developments allowed to build of higher-resolution spectrographs that the shifts between two isotopes of lead were seen in 1918. This shift between radioactive and stable lead could not be attributed to the mass difference but more likely to a change in the charge distribution in the nucleus [168, 169]. Around 1932, the first formulations for an isotopic field shift were established [170, 171]. This effect was expected to have significance,

*Albert A. Michelson is famous for the Michelson interferometer, named after him. He received the 1907 Nobel prize in physics “for his optical precision instruments and the spectroscopic and metrological investigations carried out with their aid”.

especially for electrons that transition from or to an s orbital, since there is a higher probability of being at the position of the nucleus. Due to differing extents of electron shielding, this effect must also be considered for transitions where the probability of being at the position of the nucleus does not change from one state to the other. The largest effect is observed for transitions where the number of s electrons changes. Later, deformations in the nucleus of samarium (^{152}Sm) were found to cause a large field shift, especially for the lighter isotopes.

5.3 Theoretical background

In one-electron atoms and ions, the mass shift is also called the normal mass shift or the reduced mass effect. It is suitable to describe one-electron systems with the reduced mass μ of an electron with mass m_e and the mass of a point nucleus M , given as $\mu = \frac{m_e M}{M+m_e}$. In a semi-classical approximation, the energy difference of the binding energies of two orbitals n and m , and thereby the frequency of an optical transition, is $\nu_A = \frac{\mu_A}{m_e} c R_\infty Z^2 \left(\frac{1}{n^2} - \frac{1}{m^2} \right) \propto \frac{M_A}{M_A+m_e}$. The ratio of the shift of the transitions of two isotopes with different atomic mass A and A' relative to the transition frequency is given by $\delta\nu/\nu_A = \frac{\nu_A - \nu_{A'}}{\nu_A} = \frac{m_e(M_A - M_{A'})}{(M_A + m_e)(M_{A'} + m_e)}$. For the energy shift from hydrogen (^1H) to deuterium (^2H), this corresponds to a ratio of $2.72 \cdot 10^{-4}$. For atoms with more than one electron, the correlation between each electron with all other electrons needs to be taken into account as it perturbs the kinetic energy of the system.[†] This is the specific

[†]When correlation in systems with more than one electron is neglected, the normal mass shift drops quickly with increasing atom number, by about two orders of magnitude for zinc between mass numbers 64 and 66.

mass shift. The kinetic energy of a multi-electron system can be written as

$$E = \frac{\langle p^2 \rangle}{2(M_A + m_e)} = \frac{\langle p_1^2 + p_2^2 \rangle}{2(M_A + m_e)} + \frac{\langle p_1 \cdot p_2 \rangle}{M_A + m_e} \quad (5.1)$$

where the square of the sum of the momenta of two electrons, p_1 and p_2 is $p^2 = p_1^2 + p_2^2 + 2p_1 \cdot p_2$ where the last term is the correlation term. We can then write the term energy with the specific mass shift for many electrons as

$$T_A = \frac{\sum_i p_i^2}{2\mu_A} + \frac{1}{M_A} \sum_{i \geq j} p_i \cdot p_j \quad (5.2)$$

where the difference between two such energies is the specific mass shift $\delta\nu_{A,A'}$ with a mass term defined as $\mu^{A,A'} = \frac{1}{M_A} - \frac{1}{M_{A'}}$ and the second bracket as K_i :

$$\delta\nu_{\text{MS}}^{A,A'} = \left(\frac{1}{M_A} - \frac{1}{M_{A'}} \right) \left(- \sum_i \frac{1}{2\hbar} p_i^2 - \sum_{i \geq j} \frac{1}{\hbar} p_i \cdot p_j \right) \equiv \mu^{A,A'} K_i \quad (5.3)$$

The electromagnetic interaction between electrons and the nucleus leads to an energy shift due to the extent of the nuclear charge distribution in the nucleus. In a first approximation, the charge distribution of the nucleus can be approximated by the potential of a point charge, a Coulomb potential $V_c(r) = \frac{Ze^2}{4\pi\epsilon_0 r}$. Since the nucleus has a uniform charge distribution and constant particle density, the shape of the Coulomb potential is perturbed, and the shape changes as a function of the angular momentum of the electron. The change in energy is then proportional to the change in the probability of finding the electron at the position of the nucleus. Non-s-electrons contribute marginally to the field shift. Following reference [172], the energy for s-orbitals can be approximated

as $\delta E_{n,0}^A = \frac{2}{5} \frac{e^2}{4\pi\epsilon_0} \frac{Z^4}{n^3 a_\mu^3} R_A^2 \equiv F_i R_A^2$ and the field shift accordingly becomes

$$\delta\nu_{\text{FS}}^{A,A'} = \delta E_{n,0}^A - \delta E_{n,0}^{A'} \equiv F_i (\delta r^2)^{A,A'}. \quad (5.4)$$

In conclusion, the isotope shift $\delta\nu_i^{A,A'}$ for a specific transition i can be written as a sum of the mass shift and the field shift, which both depend on nuclear quantities ($\mu^{A,A'}$ and $(\delta r^2)^{A,A'}$) and on transition specific quantities that have no isotope dependence (K_i and F_i)

$$\delta\nu_i^{A,A'} = K_i \mu^{A,A'} + F_i (\delta r^2)^{A,A'} \quad (5.5)$$

$$\delta\bar{\nu}_i^{A,A'} = F_{ij} \delta\bar{\nu}_j^{A,A'} + K_{ij} \quad (5.6)$$

The isotope shifts of two transitions, $\delta\nu_i^{A,A'}$ and $\delta\nu_j^{A,A'}$ can be related to each other by dividing by one of the nuclear dependent parameters, usually the mass term, to get $\delta\bar{\nu}_i^{A,A'} = \delta\nu_i^{A,A'} / \mu^{A,A'}$. By expressing $\delta\bar{\nu}_i^{A,A'}$ as a function of $\delta\bar{\nu}_j^{A,A'}$, we arrive at equation 5.6 which is known as King linearity with the parameters $F_{ij} = F_i / F_j$ and $K_{ij} = K_i - F_{ij} K_j$. A new force between the electrons and neutrons could cause a violation of this linearity and result in an additional energy shift. Such a shift can be accounted for by adding a term of the form $\delta\nu_i^{A,A'} = \alpha_{\text{NP}} X_i \gamma^{A,A'}$ to equation 5.5, where α_{NP} is the coupling constant of the new force, X_i is a transition dependent term that describes the form of the new potential and $\gamma^{A,A'}$ is a nuclear dependent term [173]. However, this effect is significantly smaller than the measurement uncertainty in our measurements and new physics is thus beyond the scope of what can be achieved with this measurement.

5.4 Experimental setup

Figure 5.1a) shows a schematic representation of the experimental setup. We use a cryogenic buffer gas beam source to produce a slow, pulsed beam of Cd atoms as described in Chapter 3. We use a multi-sample target holder, enabling fast switching between targets with different isotopic compositions. The vaporized atoms are cooled to 3 K by a continuous flow of 1 sccm (standard cubic centimeter per minute) cryogenic helium buffer gas and are extracted into a beam through a 4 mm aperture in the buffer gas cell. The atomic beam is probed in a laser-induced fluorescence (LIF) detector located 0.73 m from the source aperture. A slit with a width of 2 mm along x restricts the transverse velocities of the atomic beam entering the LIF detector. This reduces the Doppler broadening of the $^1P_1 \leftarrow ^1S_0$ transition to below 2.7 MHz for a forward velocity of 150 m/s. To excite the atoms on the $^1P_1 \leftarrow ^1S_0$ transition, we use a frequency-quadrupled continuous-wave titanium-sapphire (Ti:Sa) laser that is described in Section 3.4. For the $^3P_1 \leftarrow ^1S_0$ transition at 326 nm, we use a frequency-doubled continuous wave ring-dye laser (Sirah Matisse 2DX) with a frequency doubling module (Spectra Physics; Wavetrain) and a Pound-Drever-Hall locking scheme. Using a temperature-stabilized reference cavity, this laser is stabilized to a linewidth of 100 kHz. The maximum output power is 80 mW in the UV. The laser polarization is purified with an α -BBO-Glan-Taylor polarizer (1 : 10^5 extinction ratio). For the measurements presented here, we couple the frequency-doubled light of the Ti:Sa into the wavemeter to avoid the effect of intermittent multimode frequency content at the fundamental wavelength. For the 326 nm light, we record the fundamental wavelength of the dye laser since fiber transmission at 326 nm is limited and influenced over

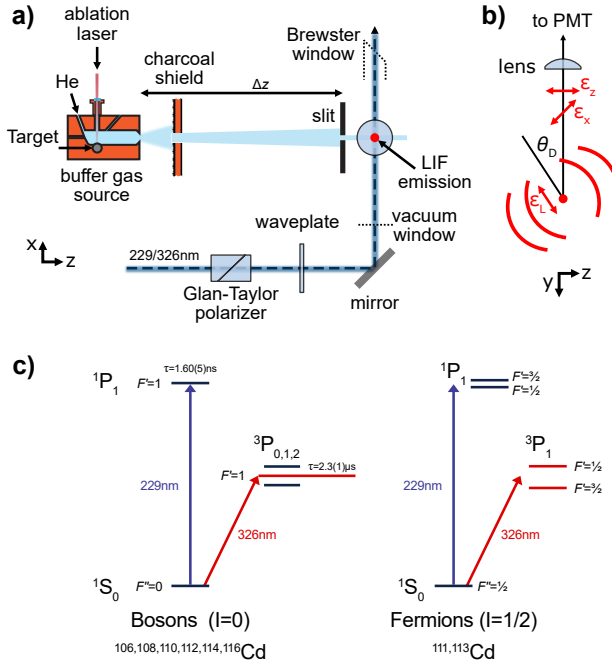


Figure 5.1: a) A collimated atomic beam from a pulsed cryogenic buffer gas source crosses the beam of a continuous wave UV laser at $\Delta z = 0.73$ m. The laser polarization is cleaned-up with a Glan-Taylor polarizer and is varied using a waveplate. b) Laser-induced fluorescence (LIF) is detected with a photomultiplier tube (PMT). The linear laser polarization (ϵ_L) forms an angle θ_D with the detector axis. Emitted photons are polarized along $\epsilon_{x,z}$. c) Energy level diagram for naturally abundant cadmium isotopes.

time by photo-degradation. The angle of the linear laser polarization with respect to the detector axis, θ_D , can be adjusted with a $\lambda/2$ waveplate. LIF of atoms that pass through the detection zone is detected with a photomultiplier tube (PMT). The laser beam intersects the atomic beam at right angles and exits the chamber through a Brewster window to avoid back reflection into the interaction zone.

For the $^1P_1 \leftarrow ^1S_0$ transition, we use a laser beam with a diameter of 5 mm, nearly flat-top intensity distribution, and a laser power of 0.5 mW. This corresponds to a saturation parameter of $s_0 = I_{\text{peak}}/I_{\text{sat}} \approx 1/400$, where $I_{\text{sat}} = \pi h c \Gamma / (3 \lambda^3) = 1.1 \text{ W cm}^{-2}$ is the two-level saturation intensity and $\Gamma = 1/\tau$, with $\tau = 1.60(5) \text{ ns}$ being the excited-state lifetime (see below). The scattering rate for small s_0 on resonance is approximately $s_0 \Gamma / 2 \approx 0.79 (\mu\text{s})^{-1}$. The mean interaction time of the atoms with the laser beam is about $30 \mu\text{s}$ so that each atom scatters on average 24 photons. This results in a radiation-pressure-induced Doppler shift of 1.7 MHz. In relative measurements, such a shift is comparable to the statistical uncertainty of several measurements; for absolute measurements, it is negligible compared to the absolute uncertainty of the wavemeter. For the $^3P_1 \leftarrow ^1S_0$ transition, 1 mW of laser power in a Gaussian beam with a spot size of 10 mm ($s_0 \approx 10$) is sufficient to saturate the transition. The Doppler broadening due to the transverse velocity distribution in the detector is 1.5 MHz and the radiation pressure detuning due to the scattering of 10 photons is 0.33 MHz.

The laser wavelengths are measured with a wavemeter (HighFinesse WS8-10) referenced to a calibrated, frequency-stabilized HeNe laser at 633 nm and has a resolution of 0.4 MHz. For the 229 nm transition, we measure the frequency-doubled wavelength near 458 nm, whereas for the 326 nm, we measure the fun-

damental wavelength near 652 nm.

5.5 Atomic beam spectroscopy

This section is split into three parts. Section 5.5.1 shows measured spectra of the $^1P_1 \leftarrow ^1S_0$ and $^3P_1 \leftarrow ^1S_0$ transitions and explains the experimental methods and the data analysis models. We benchmark a sophisticated model for the lineshape of the fermions and measure the linewidth of the $^1P_1 \leftarrow ^1S_0$ transition to infer the lifetime of the 1P_1 state. Section 5.5.2 discusses the results, analyzes the isotope shifts in a King plot, and calculates the nuclear charge radius differences for the fermions. Section 5.5.3 focuses on systematic uncertainty, which is the limiting factor in the accuracy of our measurements. To investigate systematic errors we compare our measurements in Cd with known properties of the hyperfine intervals of the 3P_1 state and measure well-known transitions in atomic copper at nearby wavelengths. We find that the accuracy of relative measurements is most reliably determined by probing the linearity of our wavemeter with an ultra-stable cavity, which is described in Section 5.5.3.

5.5.1 Measurements

Figure 5.2 shows two fluorescence spectra of the $^1P_1 \leftarrow ^1S_0$ transition around 229 nm for two different laser polarization angles θ_D . The natural linewidth of this transition and the hyperfine splitting of the fermionic isotopes (Δ_{HF}) of the 1P_1 state are of the same order of magnitude as the ISs. The result is a spectrum with a significant overlap of the spectral lines. This overlap complicates the determination of the resonance frequencies, making them dependent on the

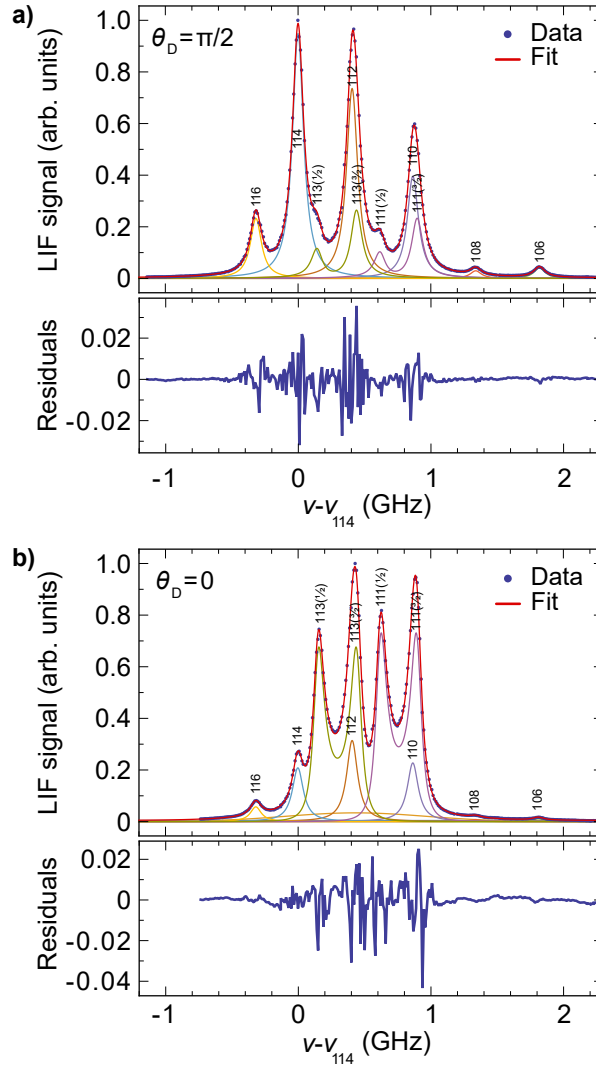


Figure 5.2: Isotope-shift spectrum of the $^1P_1 \leftarrow ^1S_0$ transition at 229 nm relative to ^{114}Cd , measured under two different laser polarization angles, fitted with the quantum interference model for fermions. The fit residuals are shown below the respective plot. a) $\theta_D = \pi/2$ maximizes the laser-induced fluorescence emission of the bosons towards the detector. b) $\theta_D = 0$ suppresses the fluorescence emission of the bosons and thus improves the accuracy in determining the transition frequencies of the fermions.

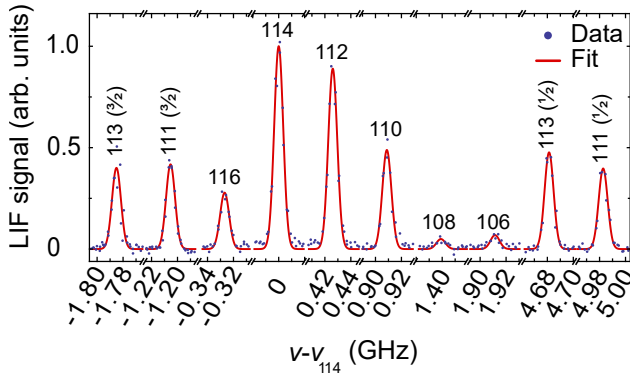


Figure 5.3: Representative spectrum for 326 nm relative to ^{114}Cd . The excited state hyperfine level of fermionic isotopes is indicated in brackets.

precise determination of the lineshape of fermionic and bosonic peaks. The spectroscopic lineshape of bosons and fermions is inherently different. Bosons have no nuclear spin and thus do not exhibit a hyperfine structure (see Figure 5.1c)). In this particular system of ($F = 1/2$, $F' = 1/2, 3/2$), we see a strong influence of quantum interference for fermions. We use isotope-enriched targets to separate between fermionic and bosonic peaks and take advantage of the differences between the fluorescence emission patterns of bosons and fermions.

A typical spectrum of the $^3\text{P}_1 \leftarrow ^1\text{S}_0$ transition around 326 nm is shown in Figure 5.3. Here, the lineshape is dominated by Doppler broadening with a full width at half maximum of 4.1 MHz. There is no spectral overlap between the lines, and the excited state hyperfine levels of the fermionic isotopes are split by approximately $10^5\Gamma$ with negligible influence of quantum interference. When the laser beam is not orthogonal to the atomic beam, the spectrum of atoms with a high forward velocity is shifted with respect to atoms with a low forward velocity. By optimizing the alignment of the laser beam to overlap the spectra of the fast and slow part, we can reduce the Doppler shift due to

misalignment to ≤ 1 MHz. We fit a Gaussian function to the spectral lines and determine the line centers with a statistical uncertainty of better than 1 MHz. The results are summarized in Table 5.2.

Spectral lineshape

The fluorescence emission pattern of the bosons corresponds to that of a classical Hertzian dipole. When the atoms are excited with linearly polarized light, and the detection direction forms an angle θ_D to the polarization axis, the detected intensity is proportional to $\sin^2 \theta_D$. Thus, when detecting in a small solid angle θ_C around $\theta_D = n\pi, n \in \mathbb{Z}$, the signal from the bosons is maximally suppressed. Following Reference [174], the emission pattern for the bosonic species, $\mathcal{S}^{(b)}$, is given by

$$\mathcal{S}^{(b)} = \frac{2}{3} (1 - P_2(\cos \theta_D) g(\theta_C)) \frac{1}{(\Gamma/2)^2 + (\omega - \omega_0)^2} , \quad (5.7)$$

where Γ is the spontaneous decay rate of the excited state, ω is the angular frequency of the laser, ω_0 is the transition angular frequency, $P_2(\cos \theta_D) = \frac{1}{2}(3 \cos^2 \theta_D - 1)$ is the second Legendre polynomial, and the factor $g(\theta_C) = \cos(\theta_C) \cos^2(\theta_C/2)$ accounts for the finite solid angle (half-angle θ_C) of the collection optics. In our measurements $\theta_C \approx 0.11$.

The emission pattern of the fermionic isotopes is more complex due to the presence of hyperfine structure in the excited states. Upon excitation with linearly polarized light, the $F' = 1/2$ excited magnetic sub-levels emit circular and linear light, which in sum is emitted isotropically, whereas the $F' = 3/2$ sub-levels show anisotropic emission. Further, the hyperfine interval in the excited state is about 3Γ , leading to significant interference between scattering

paths. This alters the observed lineshape in fluorescence and can be seen as the time-averaged analog of quantum beats. We again follow Reference [174] to model the lineshape. The fluorescence spectrum for the fermions, $\mathcal{S}^{(f)}$ is given by,

$$\begin{aligned} \mathcal{S}^{(f)} &= A + (B + C)P_2(\cos \theta_D)g(\theta_C), \\ A &= \frac{1}{(\Gamma/2)^2 + \Delta_{1/2}^2} + \frac{2}{(\Gamma/2)^2 + \Delta_{3/2}^2}, \\ B &= -\frac{1}{(\Gamma/2)^2 + \Delta_{3/2}^2}, \\ C &= -\left(\frac{1}{(\Gamma/2)^2 + \Delta_{1/2}\Delta_{3/2} + i\frac{\Gamma}{2}(\Delta_{1/2} - \Delta_{3/2})} + c.c. \right), \end{aligned} \tag{5.8}$$

where $\Delta_{F'} = \omega - \omega_{F'}$. $\omega_{F'}$ denotes the transition angular frequency to the excited-state hyperfine component F' , and *c.c.* is the complex conjugate. The first term of equation (5.8), A , is the emission averaged over the total solid angle, represented by a sum of Lorentzians. The second term, B , represents the anisotropy of emission from the $F' = 3/2$ excited state. The last term, C , accounts for the interference between decay paths. These last two terms reduce to zero by setting $\theta_D = \theta_{\text{magic}} = \arccos\left(\frac{1}{\sqrt{3}}\right)$, the so-called “magic angle”. To illustrate the angular dependence, we take spectra at seven different polarization angles, θ_D , and compare the two models $\mathcal{S}^{(f)}$ and $\mathcal{S}^{(b)}$ to fit the observed line shapes. Figure 5.4a shows a spectrum for $\theta_D = 0$ using an enriched target (^{113}Cd). Including the interference term, i.e., using $\mathcal{S}^{(f)}$, reduces the fit residual RMS by a factor of two. This is further substantiated by the data presented in Figure 5.4b, which shows the parameters Γ and Δ_{HF} as a function of θ_D , fitted using either a pure Lorentzian model ($\mathcal{S}^{(b)}$, red data points), or equation 5.8 ($\mathcal{S}^{(f)}$, blue data points). When a sum of two

Lorentzians is used to model the lineshape, the linewidth, and the measured hyperfine interval vary with the polarization angle. However, the polarization dependence disappears when equation 5.8 is used or when the measurement is done at the magic angle. The absolute position of the individual hyperfine components shifts by up to 20 MHz, while the center of gravity shifts only by about 8 MHz. We fit $A + BP_2(\cos \theta_D)$ to each of the data sets in Figure 5.4b). For the case of determining the hyperfine interval, we get $B = 25.4(3.2)$ MHz, which corresponds to a total error on the hyperfine splitting of 29(5) MHz. The fit for the linewidth yields $B = 13.4(3.3)$ MHz. For the 326 nm line, the maximum expected deviation $s_{\text{Lor}}(\Delta_{\text{HF}}) \approx 0.7$ Hz, far below the accuracy of this measurement. The absolute frequencies are in this case independent of θ_D , and we choose $\theta_D = \pi/2$ to maximize the detected boson fluorescence.

Isotope-shift measurement

For the measurements of the $^1P_1 \leftarrow ^1S_0$ transition, we record a spectrum of a ^{110}Cd enriched sample and determine the absolute transition frequency before and after each spectrum with the mixed target (see Figure 5.2). The fitted ^{110}Cd line-centers of all five measurements agree within the standard errors of the fits and are thus averaged with a standard error of 0.4 MHz. We then alternate between recording spectra of ^{110}Cd and ^{112}Cd enriched samples. Doing so allows us to precisely measure the IS($^{110,112}\text{Cd}$) as 457.5(7) MHz (statistical uncertainty) and to reduce the number of free parameters in the fit to the spectrum of Cd with natural abundance. The number of parameters is further reduced by fixing the relative amplitudes of each of the fermionic species in $\mathcal{S}^{(f)}$. We then fit a model that comprises a sum of eight terms, i.e., six Lorentzians ($\mathcal{S}^{(b)}$) for the bosons and two quantum interference line shapes

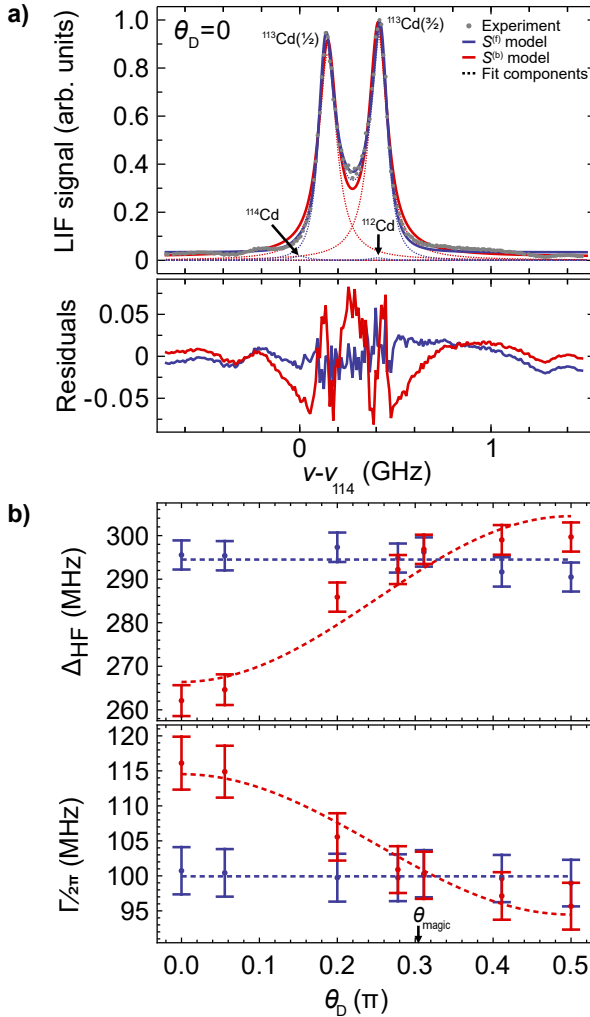


Figure 5.4: Isolated hyperfine structure of the ^{113}Cd isotope, measured using an enriched target at 229 nm, plotted including the systematic error of 3.3 MHz. The quantum interference model ($\mathcal{S}^{(f)}$, blue) is compared to a sum of two Lorentzian line shapes ($\mathcal{S}^{(b)}$, red). (a) The fit residuals reduce significantly by including quantum interference. (b) Measured hyperfine intervals Δ_{HF} and homogeneous linewidth $\Gamma/(2\pi)$ as a function of the polarization angle for the two lineshape models. Blue curves are our final result. The red dashed curve is a fit to the data.

Table 5.1: Comparison of the experimentally determined lifetime τ of the 1P_1 state in Cd with literature values.

τ (ns)	Year	[Ref]	Method
2.00(8)	1926	[175]	magneto-rotation ¹
1.99(10)	1931	[176]	line absorption ¹
0.38	1943	[177]	magnetic depolarization ¹
2.10	1944	[178]	alternating voltage ²
1.70(9)	1950	[179]	selective reflection
1.66(5)	1964	[180]	Hanle-effect
1.11	1965	[181]	magnetic depolarization ¹
1.66(5)	1969	[182]	Hanle-effect
2.1(3)	1970	[183]	phase-shift
1.65(8)	1970	[184]	Hanle-effect
1.90(15)	1973	[185]	beam-foil
1.75(20)	2004	[186]	time-resolved fluorescence
1.60(5)	<i>this work</i>		lineshape ³

¹ This method is today known as zero-field level crossing, also known as Hanle-effect

² Later referenced as phase-shift

³ from $\tau = \Gamma^{-1}$ with $\Gamma/(2\pi) = 99.7(3.3)$ MHz

($S^{(f)}$) for the fermions. This model fits the data well, as demonstrated by the small fit-residuals shown in Fig. 5.2. The relative heights of the peaks are not fixed to the corresponding relative abundance in a natural sample since we expect source fluctuations of up to 10% throughout a measurement. The deviation of the fitted relative abundance is consistent with this assumption.

Radiative lifetime

The radiative lifetime of the 1P_1 state has been studied for almost a century. It has since been experimentally determined many times using various methods

such as the Hanle-effect or time-resolved fluorescence (see Table 5.1)[‡]. Indirect methods used in the past to measure the lifetime of the 1P_1 state are more susceptible to systematic errors than a direct measurement of the time-resolved fluorescence or of the lineshape. Reported lifetimes range from 1.11-2.3 ns with an outlier at 0.38 ns. However, the authors themselves question this measurement [177]. Nowadays, the values given by Lurio (Reference [180][§], $\Gamma/(2\pi) = 95.9 \pm 2.9$ MHz) and Xu (Reference [186], $\Gamma/(2\pi) = 91 \pm 10$ MHz) are most commonly used in the literature.

To our knowledge, the lifetime has never been measured by fitting to a resonance line shape. Figure 5.4a) shows the spectrum of an enriched ^{113}Cd ablation target. Using an enriched sample allows us to benchmark the model presented in equation 5.8, and extract the linewidth and the hyperfine interval from the fitted lineshape. In addition, we determine the lineshape and linewidth of the bosons by using an enriched target of ^{112}Cd (not shown), where we use equation 5.7 to fit the data. To improve the fit, we include the residual isotopes ($< 2\%$), present in the enriched targets, in the fit. Doppler broadening is minimized by selecting atoms with a low forward velocity between $100 - 150 \text{ ms}^{-1}$ from the time-of-flight profile of the atomic beam. When atoms with a high forward velocity of $> 300 \text{ ms}^{-1}$ are selected, the fitted linewidth remains unaffected. Fitting a Voigt profile for ^{112}Cd does improve the fit residuals and results in a value for the Lorentzian contribution consistent with a regular Lorentzian model. In total, we record eight spectra of ^{112}Cd and 11 spectra of ^{113}Cd , including the 7 measurements presented in Figure 5.4. The spectral

[‡]One of the first values was measured by Mark W. Zemansky [176] at the Kaiser-Wilhelm-Institut für Physikalische Chemie und Elektrochemie, the original name of what currently is the Fritz Haber Institute of the Max Planck Society.

[§]*Thaddeus and Novick* (Reference [187]) cite *Lurio and Novick* (Reference [180]) as private communication with a slightly different value. We use the published value in Table 5.1.

linewidths, as extracted from the fits, agree within the standard errors and are averaged to $\Gamma/(2\pi) = 99.7 \pm 0.6_{\text{stat}} \pm 3.3_{\text{sys}}$ MHz, which corresponds to $\tau(^1\text{P}_1) = 1.60(5)$ ns. The Lorentzian linewidth of the spectrum of an enriched ^{110}Cd target is consistent within the 1 MHz statistical error when applying a large magnetic field ($B = 40$ G or 4 mT) parallel to the laser polarization. Zeeman broadening induced by the uncancelled magnetic field in the detection region can thus be neglected.

Experimentally obtained values for the lifetime of the $^3\text{P}_1$ state have been reported at least eight times with a weighted mean and standard error on the mean of $2.30(10)$ μs , corresponding to a linewidth of $69.1(27)$ kHz [178,188–194]. More recent literature refers to the value of Byron (Reference [188]), which is $2.39(4)$ μs , corresponding to $66.6(11)$ kHz. Doppler broadening in our setup is on the order of 5 MHz, which is about two orders of magnitude larger than the natural linewidth. In this setup we can thus not determine the lifetime of the $^3\text{P}_1$ state by measuring the linewidth of the transition.

5.5.2 Discussion

Table 5.2 summarizes our measured ISs relative to the ^{114}Cd line and compares them to literature values. The given uncertainty is the standard error of the mean of several measurements. The values for the ISs are consistent with a recent measurement using a magneto-optical trap of Cd [74]. For the $^1\text{P}_1 \leftarrow ^1\text{S}_0$ transition, our results are more precise than a recent measurement [195], and we observe a significant discrepancy that increases linearly with the frequency. Our results for the $^3\text{P}_1 \leftarrow ^1\text{S}_0$ transition agree well with other literature (see overview in [199]) and are significantly more precise and accurate, especially for the fermions.

Table 5.2: Isotope shifts relative to ^{114}Cd , given in MHz. The systematic uncertainty to determine relative frequencies in this work is determined to be 3.3 MHz and should be added to the given statistical uncertainty. For fermionic isotopes, the quantum number of the excited state is given in brackets. For completeness, we include our results from Reference [74] and add the isotope shifts of the fermionic spectral components in bold.

isotope	229 nm		326 nm	
	<i>this work</i>	literature ¹	<i>this work</i>	literature
116	-316.1(5)	-299(4)	-326.9(2)	-321.5(1.0) ²
114	0.0(5)	0(4)	0.0(5)	0.0
113(1/2)	147.8(4)	148(4)	4681.1(4)	4653(19) ⁵ 4533(23) ³
112	407.5(7)	392(5)	426.3(3)	429.9(1.0) ²
113(3/2)	443.4(7)	427(5)	-1785.2(3)	-1811(17) ³
111(1/2)	616.5(5)	592(6)	4982.2(9)	4947(24) ³
110	865.0(3)	826(6)	909.3(6)	914.7(1.0) ²
111(3/2)	899.2(4)	875(6)	-1205.3(4)	-1217(19) ³
108	1336.5(9)	1259(9)	1399.4(7)	1402.4(1.0) ²
106	1818.1(1.4)	1748(11)	1911.2(2)	1913.0(1.0) ²
111 c.g.	805.0(3)	781(4)	857.2(4)	862(12) ⁴
113 c.g.	344.9(5)	334(4)	370.2(2)	374(11) ⁴

¹ Beam measurement, Reference [195]

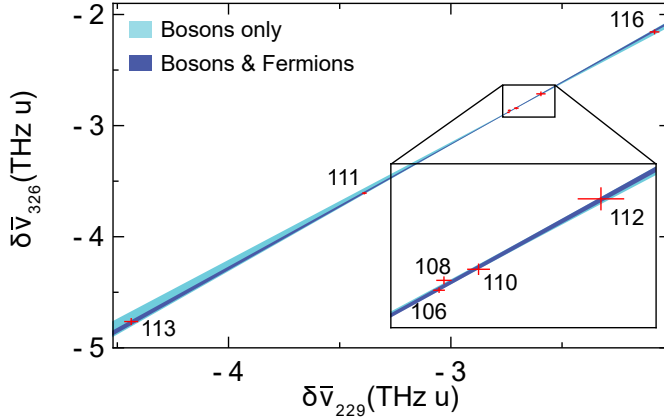
² MOT edge measurement, Reference [74]

³ Beam measurement, Reference [196]

⁴ Hollow cathode discharge, relative to $^{106,108}\text{Cd}$, Reference [197]

⁵ Reference [198]

Figure 5.5: King-plot analysis of the ISs of the transitions at 229 nm and 326 nm relative to ^{114}Cd . The error bars include the systematic uncertainty in determining relative frequencies of 3.3 MHz. The shaded areas show the 68% confidence intervals for a linear fit to the bosons only (light blue). The fit that includes the fermions is shown in dark blue. The ISs of the fermions (center of gravity) are consistent with the extrapolated linear fit to the bosons. The inset shows a zoom-in.



King plot

An accurate set of ISs on two transitions can be analyzed in a King plot. Figure 5.5 shows such a plot using the modified IS $\delta\bar{\nu}_i^{A,A'} = \delta\nu_i^{A,A'} / \mu^{A,A'}$, where $\mu^{A,A'} = 1/M_A - 1/M_{A'}$ is the nuclear mass-shift term. The linear fit has the form:

$$\delta\bar{\nu}_i^{A,A'} = F_{ij}\delta\bar{\nu}_j^{A,A'} + K_{ij},$$

where F and K are the field shift and mass shift coefficients, respectively, $F_{ij} = F_i/F_j$ is the slope and $K_{ij} = K_i - F_{ij}K_j$ is the y-axis intercept. The fit results in $F_{ij} = 1.10(3)$ and $K_{ij} = 0.13(10)$ THz u, if only the bosons are considered. Including the fermions reduces the fitting uncertainty by a factor

of ≈ 3 to

$$F_{ij} = 1.117(12) \text{ and } K_{ij} = 0.18(3) \text{ THz u.}$$

The fact that including the fermions reduces the uncertainty of the fit shows that potential shifts due to the second-order hyperfine interaction are negligible on the MHz level. These results can be compared to CI-MBPT calculations, which yield $F_{ij} = 1.133(80)$ and $K_{ij} = 0.25(49)$ THz u [200]. These results are consistent with ours, but our uncertainty is significantly lower, setting stringent benchmarks to improve the calculation. Due to correlations, the uncertainty of the calculated field shift ratio F_{ij} is likely significantly smaller than our estimate from the literature.

Nuclear charge radii

Our ISs for the fermions, measured using a narrow line where nearby peaks do not overlap and quantum interference is negligible, combined with the calculated negligible off-diagonal hyperfine shifts for this line [164], enable a reliable extraction for the RMS charge radius difference $(\delta r^2)^{A,114}$ from the center of gravity ISs given in Table 5.2, provided that the atomic parameters for this line are known. Here we use equation 5.5 with $F_{326} = -4354(62)$ MHz fm⁻² and $K_{326} = 1673(43)$ GHz u obtained by projecting accurate calculations in Cd⁺ using a King plot containing only bosons [74]. $(\delta r^2)^{A,114}$ are given in Table 5.3. They compare reasonably well to within two combined standard deviations with those obtained through muonic X-ray measurement [201], a calibrated King plot combining muonic x-rays and ISs in Cd⁺ [162, 202], and a determination based on the direct calculation of F_{326} and K_{326} [164]. The

Table 5.3: Nuclear charge radius difference $(\delta r^2)^{A,114}$ in fm² extracted from Table 5.2 with F_i and K_i from Reference [74].

isotope	<i>this work</i>	Ref. [164]	Ref. [201]	Ref. [202]
111	-0.296(5)	-0.269(15)	-0.289(4)*	-0.285(4)
113	-0.118(2)	-0.101(10)	-0.116(4)*	-0.113(2)

slight deviation from [164] is ascribed to the calculation only reporting numerical uncertainties. The slight deviation from determinations using muonic atoms is most likely due to their dependency on extrapolations of unknown higher-moment corrections from electron scattering, which has yet to be performed for most Cd isotopes.

Hyperfine intervals

Table 5.4 compares our measured hyperfine intervals for the 1P_1 and 3P_1 state with literature. For the 1P_1 state, we show that the spectral overlap caused a significant systematic error in previous experiments. For the 3P_1 state, we find that our values agree well with precise double-resonance measurements [187, 203, 204]. Recent atomic structure calculations [164, 205] agree to some extent and can be benchmarked with our results. This also allows us to benchmark the systematic uncertainty in the linearity of our wavemeter, as shown in Section 5.5.3.

Absolute frequencies

The fitted line centers of spectra taken over a period of a few weeks agree with the uncertainties of the fits. Using a calibrated wavemeter allows us to determine the absolute transition frequencies of the ^{114}Cd isotope for the two

Table 5.4: Comparison of experimentally determined values for the hyperfine splitting $\Delta_{\text{HF}}(^{111}\text{Cd}, ^{113}\text{Cd})$ in MHz with literature values.

	229 nm		326 nm	
	^{111}Cd	^{113}Cd	^{111}Cd	^{113}Cd
<i>this work</i>	282.7(3.3)	295.6(3.4)	6187.5(3.3)	6466.3(3.4)
[195], [187]	285(7)	251(5)	6185.72(2)	6470.79(2)
[199]	-	-	-	6444(18)
[196]	-	-	6164(31)	6344(28)
[198]	-	-	6183(30)	6465(21)

transitions:

$$^{114}\text{Cd } ({}^1\text{P}_1 \leftarrow {}^1\text{S}_0): \quad 1,309,864,341(20) \quad \text{MHz}$$

$$^{114}\text{Cd } ({}^3\text{P}_1 \leftarrow {}^1\text{S}_0): \quad 919,046,234(21) \quad \text{MHz}$$

The absolute frequency of the ${}^1\text{P}_1 \leftarrow {}^1\text{S}_0$ transition is consistent with a recent measurement (1,309,864,506(262) THz [195]) and 13 times more precise. The value given in reference [206] (1,309,864,580(86) THz) disagrees by about three standard deviations. The same reference [206] also lists the absolute frequency for the ${}^3\text{P}_1 \leftarrow {}^1\text{S}_0$ transition to 919,046,357(42) THz, which is also higher by about three times the stated standard deviation.

5.5.3 Systematic uncertainty

Our measurements have a typical statistical uncertainty of ≤ 1 MHz, which means we can reliably determine the line center of features in the ${}^1\text{P}_1 \leftarrow {}^1\text{S}_0$ transition to $\Gamma/100$. However, the wavemeter we use as a frequency reference is not necessarily linear over a range of several GHz. This will likely be the limiting factor in the accuracy when determining relative frequencies. The hyperfine intervals of the ${}^3\text{P}_1$ state are known with high accuracy and already

provide a good indication (see Table 5.4). Furthermore, the ratio of the nuclear magnetic moments of Cd determines the ratio of the hyperfine intervals for different isotopes and is known with high accuracy. We perform two additional tests to estimate this uncertainty. First, we measure the hyperfine structure of $^{63,65}\text{Cu}$ near 327.5 nm and 324.8 nm, which span a frequency range of up to 12.6 GHz and are known with a precision of 10 kHz. Second, we compare the linearity of our wavemeter to an ultra-stable cavity. The systematic uncertainty in determining relative frequencies is estimated conservatively to be 3.3 MHz. This uncertainty is independent of the frequency span and assumed to be identical for all measurements. For absolute frequency measurements, we are limited by the absolute accuracy of the wavemeter, which is 10 MHz in the fundamental frequency of the laser.

$^3\text{P}_1 \leftarrow ^1\text{S}_0$ nuclear magnetic moment ratios

The measured hyperfine splittings at 326 nm are given in Table 5.4. We find good agreement with precise literature values. Furthermore, the ratio of the nuclear magnetic moments $g(^{113}\text{Cd})/g(^{111}\text{Cd})$ has been determined with high accuracy to 1.0460842(2) [207]. In the approximation that hyperfine anomaly is negligible, we can assume that $g(^{113}\text{Cd})/g(^{111}\text{Cd}) = \Delta_{\text{HF}}(^{113}\text{Cd})/\Delta_{\text{HF}}(^{111}\text{Cd})$. For the $^1\text{P}_1 \leftarrow ^1\text{S}_0$ transition, we use this ratio as a fixed parameter. In our measurements of the $^3\text{P}_1 \leftarrow ^1\text{S}_0$ transition, we find a ratio of 1.04506(18) (statistical), which indicates an upper bound for the hyperfine anomaly of 4.3 MHz.

Hyperfine structure of copper

The D_1 (327.5 nm) and D_2 (324.8 nm) lines of Cu I lie about 1.3 nm on either side of the Cd 326 nm transition. The hyperfine splitting of the ground state is known with an accuracy of 10 kHz and has been determined to be 12568.81(1) MHz for ^{65}Cu and 11733.83(1) MHz for ^{63}Cu [208]. For this, we only replace the Cd ablation target in our buffer gas source with a Cu one and leave the remaining setup identical. We measure the ground state hyperfine splitting by the method of combination differences, using transition pairs involving a common excited state with total angular momentum F' . Spectra of the D_1 and D_2 lines are shown in Figure 5.6a). The difference between the extracted ground state splitting with the precisely known values are shown organized by isotope and F' in Figure 5.6b). The mean deviation of these frequency differences is 3.1 ± 2.0 MHz for ^{63}Cu and 1.8 ± 3.7 MHz for ^{65}Cu . The weighted mean and standard error of the mean of all measurements indicate a systematic error of 3.1(1.9) MHz.

Stable Fabry-Pérot Cavity

To measure the linearity of our wavemeter with better statistics than in the previous sub-sections, we use a stable cavity in combination with an electro-optic modulator (EOM) that phase-modulates the laser to generate radio-frequency sidebands spaced by precisely 22.051 MHz. The cavity is a near-confocal, pressure and temperature-stabilized Fabry-Pérot cavity with a Zerodur spacer, a free spectral range (FSR) of 150 MHz and a drift rate of 7.5 Hz per FSR per Kelvin [209]. The high-reflectivity coating of the cavity mirrors drops sharply above 740 nm, and we, therefore, tune the Ti:Sa to 740 nm. Scanning the laser

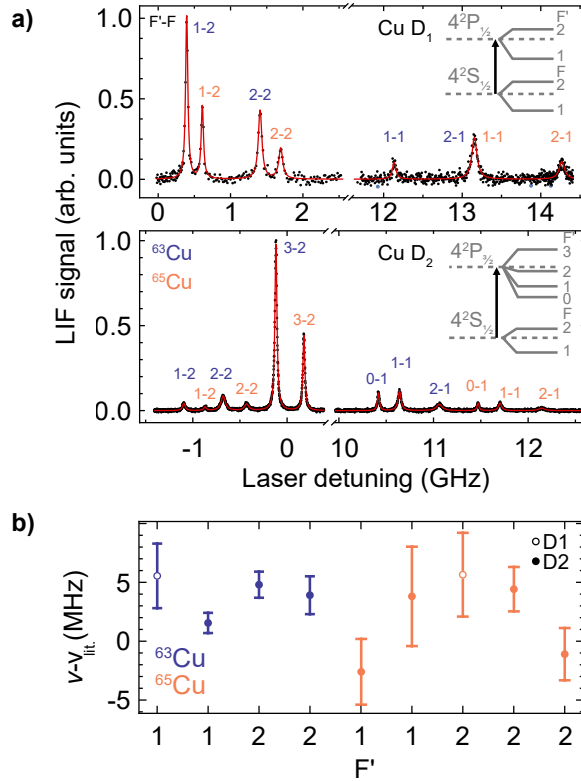


Figure 5.6: Copper spectra of the D_1 and D_2 lines near 326 nm to benchmark the linearity of our wavemeter. a) Laser-induced fluorescence spectra of hyperfine transitions. Experimental data points in black and a Lorentzian fit (red curve). b) Comparison of the measured hyperfine intervals measured via a common excited state F' to kHz-accuracy microwave data from Reference [208].

while monitoring the cavity transmission on a photodiode, as shown in Figure 5.7a), produces a comb of resonance peaks with a known frequency spacing. By fitting the transmission peaks on the frequency axis obtained with the wavemeter, the short-term (minutes) and long-term (hours) linearity of the wavemeter can be determined. Figure 5.7b) shows that the wavemeter is close to linear for short-term scans over a single FSR and also long-term when scanning slowly over a frequency range of about 14 GHz. Fitting to the cavity peaks gives a standard deviation of 1.0 MHz from the FSR for long-term scans (see inset in Figure 5.7a) and 0.34 MHz from the RF sidebands for short-term scans, which is close to the wavemeter resolution of 0.4 MHz. We repeat this measurement with the ring dye laser at 652 nm. From several measurements on different days using both spectroscopy lasers, we determine a conservative upper limit for the systematic uncertainty in determining the relative frequencies at 229 nm and 326 nm of 3.3 MHz.

Absolute accuracy

We use a temperature-stabilized HeNe laser at 633 nm whose absolute frequency is calibrated to 5 MHz as a reference for the wavemeter. Recently, we also measured the ISs of Yb to benchmark the absolute calibration and linearity of our wavemeter near 399 nm [210]. The known absolute frequencies in Yb were reproduced with an accuracy of 6 MHz and the relative ISs were measured with a standard deviation of 1.3 MHz. We determine the absolute frequency of ^{114}Cd from a weighted average of all measurements performed. The absolute frequency for 229 nm was repeatedly found with less than 1 MHz standard deviation. For 326 nm, it was reproducible over nine weeks with a maximum spread of 12 MHz and a standard deviation of 5 MHz. The manufacturer specifies the

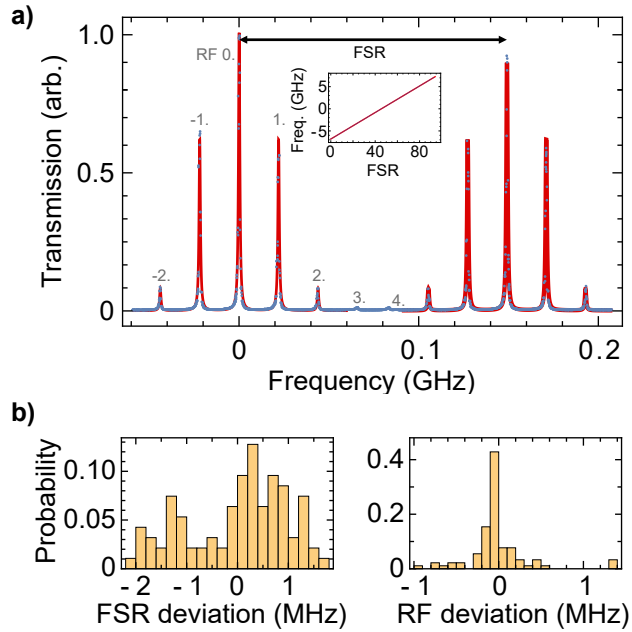


Figure 5.7: Comparison of wavemeter linearity to a stable Fabry-Pérot cavity. a) Transmission through the cavity (free spectral range of about 150 MHz) at 740 nm as a function of the laser frequency. An electro-optic modulator phase modulates the laser with a fixed RF frequency. The inset compares the frequency the wavemeter reads to the number of FSR peaks. b) The probability distribution of the residuals of a linear fit to the data has a standard deviation of 1.0 MHz. The observed spacing of the RF sidebands as measured by the wavemeter has a standard deviation of 0.34 MHz.

absolute accuracy in the fundamental light to be 10 MHz, which we take as an upper bound for the uncertainty in determining absolute frequencies.

5.6 Summary

We measured the optical isotope shift in Cd-I for the $^1P_1 \leftarrow ^1S_0$ and $^3P_1 \leftarrow ^1S_0$ transitions with a statistical uncertainty of typically < 1 MHz by fitting to the laser-induced fluorescence spectra from a pulsed cryogenic buffer-gas cooled atomic beam. The significant overlap of the spectral lines complicates measurements of the $^1P_1 \leftarrow ^1S_0$ transition. We resolve this issue by using enriched Cd ablation targets and by suppressing the emission from the bosonic isotopes towards the direction of the detector. We determined the hyperfine intervals in the 1P_1 state of the fermionic isotopes and showed that quantum interference effects affect the spectral lineshape. The accuracy of our wavemeter is calibrated against well-known hyperfine intervals in Cd and Cu and by using a stable reference cavity in combination with an EOM. We find an upper bound of 3.3 MHz for the systematic uncertainty in measuring relative shifts. The lifetime of the 1P_1 state is determined spectroscopically to be 1.60(5) ns, and the absolute transition frequencies were determined with unprecedented accuracy. Our results differ significantly from recent measurements, demonstrating the importance of understanding the spectral lineshape and measuring the linearity of the spectrometer. A King plot comprising both transitions was presented. All naturally occurring Cd isotopes follow a linear relation, and the fitted slope and intercept are consistent with recent atomic structure calculations. The second-order hyperfine interaction in the fermions is negligible at the MHz level. Combining our new measurements with recent

calculations of the isotope-shift parameters allowed us to extract the fermionic isotopes' precise nuclear charge radius differences. The measurements presented here resolve significant discrepancies in the recent literature and benchmark new atomic structure calculations, a first important step towards using King plots of Cd to search for new physics beyond the Standard Model. A large number of naturally occurring isotopes, the presence of narrow optical transitions, and the expected small Standard Model background make Cd an ideal candidate for such searches.

Chapter 6

Deep-UV magneto-optical trap for cadmium atoms

6.1 Introduction

This chapter demonstrates trapping cadmium (Cd) atoms in a magneto-optical trap (MOT) on the $^1P_1 \leftarrow ^1S_0$ transition in the DUV near 229 nm. To the best of our knowledge, Cd sets the current record for successful magneto-optical trapping furthest into the DUV.* Operating DUV MOTs is challenging due to the limited level of optical technology that is available below 265 nm. Commercially available light sources and optical components still severely limit laser applications in this spectral range and UV-resistant single-mode fibers are not yet commercially available [213,214]. Vacuum window coatings show substantial degradation over time, requiring compensation by slightly converging the

*Laser cooling of atomic silicon on the $^3D_3^o \leftarrow ^3P_2$ transition near 222 nm is currently under investigation [211,212].

laser beams or replacement of the optics in regular intervals. However, DUV light allows for generating significantly larger optical forces compared to visible light. This increase in optical force leads to shorter stopping distances and increased capture velocities of traps in the DUV.

Laser-cooling molecules is challenging because the internal energy structure is significantly more complex than a two-level system and often multiple additional lasers are required. To test our laser system and optical setup for trapping AIF molecules, we create a simple prototype trap using permanent ring magnets. We choose atomic cadmium as a test candidate because the electronic energy structure, shown in Figure 6.1, is similar to AIF (see Figure 2.4). Our existing laser systems can cover the transition, as it is between the cooling and repump wavelengths of AIF (see Table 6.1). Unlike AIF, the laser cooling transition for Cd bosons involves only 2 hyperfine levels instead of the 12 hyperfine levels for AIF on the Q(1) transition. The ground state of Cd is a singlet ($F = 0$) hyperfine state, eliminating the need for repump lasers. Similar to AIF, 1+1 photoionization can be a significant loss channel for laser cooling Cd. Cd is an ideal test candidate for the challenging goal of laser cooling AIF molecules due to the straightforward laser cooling scheme and the similarities in energy structure. In this experiment, Cd atoms are loaded from a buffer gas beam generated in the same source used for producing AIF molecules in Chapter 3.

The first demonstration of a DUV MOT of cadmium atoms was in 2007 [215]. *Brickman et al.* captured a few thousand cadmium atoms from a background vapor, using a laser power of 1.5 mW in a beam diameter of 1.0–3.0 mm, corresponding to laser intensities of $0.03 - 0.5 \text{ W/cm}^2$. Commercially available CW laser systems have since increased in available output power by at least

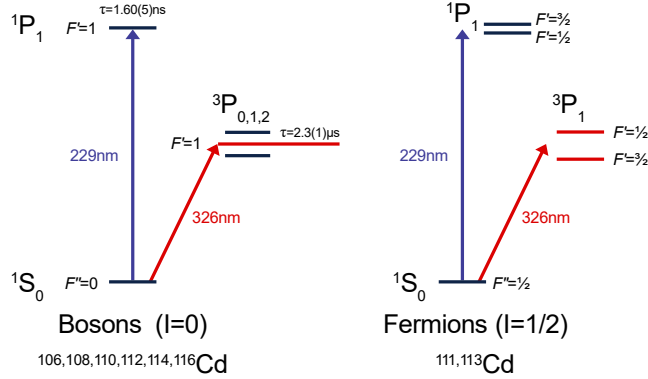


Figure 6.1: The energy level diagram of cadmium isotopes is similar to that of AlF molecules and alkaline earth elements in general with a 1S_0 ground state and a 1P_1 excited state and an intermediate $^3P_{0,1,2}$ triplet state. The lifetimes τ and the transition wavelengths are indicated. For simplicity we only show levels with $J = 1$ for fermions.

Table 6.1: Comparison of the properties relevant for laser cooling of AlF molecules and Cd atoms in the DUV. The excited state lifetime τ of the excited states are similar. However, Cd is more than twice as heavy as AlF.

	Transition	Mass (amu)	λ (nm)	τ (ns)	$\Gamma/2\pi$ (MHz)
AlF	$A^1\Pi \leftarrow X^1\Sigma^+$	46	227.5	1.90(3) [72]	84
Cd	$^1P_1 \leftarrow ^1S_0$	112	228.8	1.60(5) [152]	100

a factor of 100. This advancement enabled *Yamaguchi et al.* to trap 1×10^6 Cd atoms [160]. Recently, *Lavigne et al.* presented a DUV MOT holding 5×10^7 mercury (Hg) atoms, which are loaded from a background gas using the $^3P_1 \leftarrow ^1S_0$ transition near 254 nm [216].[†] In this section we will demonstrate that it is possible to capture a record number of cadmium atoms on the singlet transition of Cd ($^1P_1 \leftarrow ^1S_0$) from a cryogenic buffer gas beam. We present techniques to overcome limitations due to ionization, which can increase the number of atoms in the trap even further. In addition, we make use of enriched targets and accumulate multiple pulses in the trap in order to increase the atom number.

6.2 Laser cooling theory

This section examines light-matter interactions and provides the reader with the tools to describe the process of laser cooling. While focusing on cadmium atoms, we compare relevant parameters such as acceleration and stopping distance with AlF and other diatomic molecules to highlight similarities and differences.

To describe the interaction of light with a two-level atom we follow Reference [217] and define a Hamiltonian that has two parts $H = H_0 + H_I(t)$. The eigenvalues and eigenstates of H_0 are the energy levels E_n of the atom in a field-free environment. In addition, we consider laser radiation in the form of an oscillating electric field $\mathbf{E} = \mathbf{E}_0 \cos(\omega t)$, where $|\mathbf{E}_0|$ is the amplitude, and ω is the angular frequency. This field leads to a perturbation of the two-level system. The Hamiltonian for the interaction with the electric field can be written

[†]Although the singlet transition of Hg near 185 nm has a 3.5 times higher peak acceleration, there is currently insufficient laser power available at that wavelength.

as $H_I(t) = e\mathbf{r} \cdot \mathbf{E}_0 \cos(\omega t)$. This corresponds to the energy of an electric dipole $\mu = e\mathbf{r}$ in an electric field.

The atom is in a superposition of the two energy states and we can write the wavefunction as $\Psi(\mathbf{r}, t) = c_1(t)\psi_1(\mathbf{r})e^{-i\omega_1 t} + c_2(t)\psi_2(\mathbf{r})e^{-i\omega_2 t} = c_1|1\rangle e^{-i\omega_1 t} + c_2|2\rangle e^{-i\omega_2 t}$. The time dependent coefficients c_n satisfy $|c_1|^2 + |c_2|^2 = 1$ and we use $\omega_n = E_n/\hbar$, as the angular frequency of n -th energy level. Substituting Ψ in the time-dependent Schrödinger equation $H\Psi = i\hbar\frac{\delta\Psi}{\delta t}$ yields a set of two differential equations for the probability amplitudes. For systems close to resonance we can use the rotating-wave approximation to find

$$i\dot{c}_1 = c_2 e^{-i(\omega-\omega_0)t} \frac{\Omega}{2} \quad (6.1)$$

$$i\dot{c}_2 = c_1 e^{-i(\omega-\omega_0)t} \frac{\Omega^*}{2}. \quad (6.2)$$

Here we used the Rabi frequency $\Omega = \frac{\langle 1|e\mathbf{r}\cdot\mathbf{E}_0|2\rangle}{\hbar} = \frac{\mu_{12}\mathbf{E}_0}{\hbar}$, which is proportional to the transition dipole moment μ_{12} and describes the frequency at which the probability amplitudes of two atomic energy levels fluctuate in an oscillating electromagnetic field. For the initial condition $c_1(0) = 1, c_2(0) = 0$ we find the probability of finding an atom at time t in the excited state is $|c_2(t)|^2 = \frac{\Omega^2}{\Omega^2 + \Delta^2} \sin^2\left(\frac{\sqrt{\Omega^2 + \Delta^2}t}{2}\right)$ where $\Delta = \omega - \omega_0$. However, the finite radiative lifetime of the excited state damps the system to a steady state. In the optical Bloch model, this is the density matrix element ρ_{ee} , also known as the excited state fraction. In the limit of a strong driving field ($\Omega \rightarrow \infty$), the populations in the two levels become equal, and $\rho_{ee} = \frac{\Omega^2}{4\Delta^2 + 2\Omega^2 + \Gamma^2}$. With the saturation parameter $s_0 = \frac{2|\Omega|^2}{\Gamma^2} = I/I_{\text{sat}}$ where $I_{\text{sat}} = \frac{\pi\hbar c}{3\lambda^3\tau}$ is the saturation intensity, we can write ρ_{ee} as $\rho_{ee} = \frac{1}{2} \frac{s_0}{1+s_0+(2\Delta/\Gamma)^2}$. The scattering rate is given by $R_{\text{scat}} = \Gamma\rho_{ee}$, which has a maximum of $R_{\text{scat}}^{\text{max}} = \Gamma/2$ when on resonance ($\Delta = 0$)

and $s_0 \gg 1$ [218].

Without losses in the optical cycle, an atom can continuously absorb photons with momentum $p = \hbar k$ and eventually return to the ground state by emitting a photon in a random direction. The average emission over many cycles is isotropic, resulting in a net optical force given by $F_{\text{opt}} = \dot{p} = \hbar k R_{\text{scat}}$. The maximum optical force occurs at $R_{\text{scat}}^{\text{max}}$, where $F_{\text{opt}}^{\text{max}} = \hbar k \frac{\Gamma}{2}$. More important is, however, the peak acceleration. For this, we need to consider the atomic mass as well as the number of ground (n_g) and excited state levels (n_e) that are coupled. The effective scattering rate is $\Gamma_{\text{eff}} = \frac{2n_e}{n_e + n_g} \Gamma$. The peak acceleration for Cd bosons, when using linearly polarized light on the $^1P_1 \leftarrow ^1S_0$ transition yields $a^{\text{max}} \approx 5 \times 10^6 \text{ m s}^{-2}$. This is within a factor two of the AlF molecule ($a^{\text{max}} \approx 1 \times 10^7$). Table 6.2 shows that DUV transitions can lead to exceptionally short stopping distances for atomic beams of Cd or molecular beams of AlF of a few millimeters. In comparison, other diatomic molecules such as MgF, CaF, YbF, and BaF have a significantly lower peak acceleration, as shown in Table 6.2. This is in part due to the internal structure ($n_g > n_e$) which reduces the effective scattering rate. Additionally, the optical scattering force is proportional to the product of the spontaneous decay rate $\Gamma \propto 1/\lambda^3$ of the electronically excited state and the transferred momentum per photon absorption $\Delta p \propto 1/\lambda$. The optical force is then $F_{\text{opt.}} \propto 1/\lambda^4$, resulting in a significantly higher force for DUV transitions compared to the visible spectral range. The stopping distances in Table 6.2 assume that the peak acceleration can be maintained during the entire slowing process, which is not possible for molecules because of losses to higher vibrational states.

In practice, moving atoms or molecules experience a Doppler shift of $\Delta_D = kv$, where k is the wavevector, and v is the velocity relative to the lab frame.

For Cd on the DUV transition, this shift is about 4.4 MHz per 1 m/s. During the slowing process, the laser frequency needs to follow this shift. This can be achieved by broadening the frequency of the laser light or by chirping the laser frequency by several hundred MHz over a few milliseconds. The force profile for a laser with a detuning $\Delta \rightarrow \Delta' = \Delta \pm \Delta_D = \omega - \omega_0 \mp kv$ for a blue ($\omega > \omega_0$) and red ($\omega < \omega_0$) detuned laser as a function of velocity is shown in Figure 6.2a).

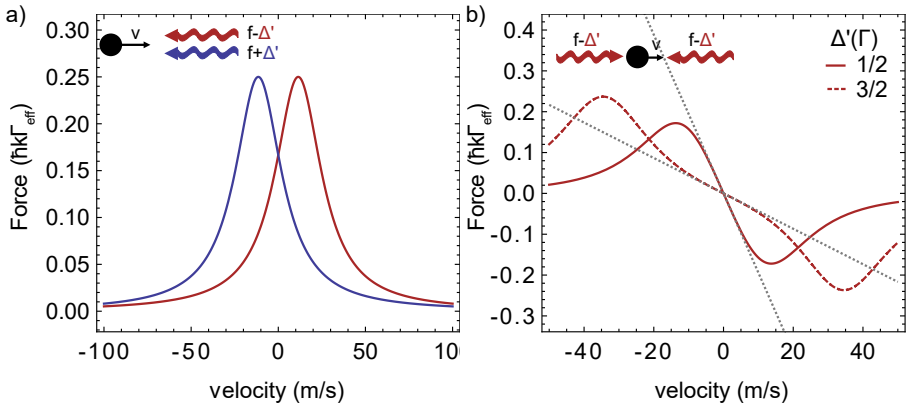


Figure 6.2: Force on a moving atom absorbing photons from a laser beam in units of $\hbar k \Gamma_{\text{eff}}$ with $s_0 = 1$. The detuning is set to $\Delta' = \Gamma/2$ relative to the atom at rest. a) When an atom moves towards a laser, the laser frequency is blue-shifted in the rest frame of the atom, making it resonant for a red-detuned laser. The atom becomes more transparent to blue-detuned light from the same direction. b) two red-detuned lasers from opposite directions can restrict the forward velocity in one dimension. Dashed lines represent Taylor approximations at $v=0$.

We can extend the scheme by adding a second, red-detuned laser that aligns collinearly with the existing laser. We analyze the optical force in this system, given by $F_{\text{OM}} = F_{\text{opt}}(\omega - \omega_0 - kv) - F_{\text{opt}}(\omega - \omega_0 + kv)$. By approximating this expression using a Taylor expansion in kv to lowest order in v (assuming that $kv \ll \omega - \omega_0$), we obtain $F_{\text{OM}} \approx \frac{8\hbar k^2 s \frac{\Delta}{\Gamma}}{(1+s+(\frac{2\Delta}{\Gamma})^2)^2} v \equiv -\beta v$. The resulting force

Table 6.2: Comparison of laser cooling transitions, wavelengths and calculated Γ_{eff} for cadmium and diatomic molecules such as AlF. The DUV transitions of Cd and AlF allow for significantly shorter stopping distances, assuming the peak acceleration is maintained using a single laser.

Species	Transition	$\lambda(\text{nm})$	$\Gamma_{\text{eff}}(\Gamma)$	$a^{\text{max}}(\text{m s}^{-2})$	$d_{\text{stop}}^{200 \text{ m s}^{-1}}(\text{m})$
Cd ferm.	$^1P_1 \leftarrow ^1S_0$	229	4/3	6×10^6	0.003
Cd bos.	—"—	229	1	5×10^6	0.004
AlF	$A^1\Pi \leftarrow X^1\Sigma^+$	228	1	1×10^7	0.002
MgF	$A^2\Pi_{1/2} \leftarrow X^2\Sigma^+$	359	1/2	8×10^5	0.025
CaF	—"—	606	1/2	1×10^5	0.14
YbF	—"—	552	1/2	3×10^4	0.6
BaF	—"—	859	1/2	1×10^4	1.5

is opposed to the velocity with a damping coefficient $\beta = -\frac{8\hbar k^2 s \frac{\Delta}{\Gamma}}{(1+s+(\frac{2\Delta}{\Gamma})^2)^2}$ and leads to a viscous damping of the motion of the atoms. Such a force profile is shown in Figure 6.2b) for two laser detunings (red curves, $\Delta = \{-\frac{1}{2}\Gamma, -\frac{3}{2}\Gamma\}$). The approximation (gray dashed lines) is in good agreement for velocities $|v| \leq 5 \text{ m/s}$.

Extending this scheme to three dimensions creates a linear force against motion in each spatial direction. This configuration, known as optical molasses, involves three intersecting and retro-reflected lasers that are red-detuned from resonance [117]. Atoms in such a laser field experience a force resembling viscous drag. The crucial point is that atoms at zero velocity scatter an equal amount of photons from all lasers, resulting in a net optical force of zero. This enables the use of an optical molasses to slow down atoms.

However, scattering events cause diffusive motion of the atoms in the trap, which leads to loss from the optical molasses. In order to also achieve spatial control, this scheme needs to be extended to include a restoring force towards the center of the trap. This is achieved by adding a magnetic quadrupole field. As atoms move out of the trap, the energies of the projections $m_F = \pm 1$

experience a linearly increasing (decreasing) energy shift as shown in Figure 6.3b). The key is that the linearly increasing magnetic field causes the transition probability to vary spatially for a given laser frequency and polarization. The energy shift has the same sign as m_F and makes the optical cycle sensitive

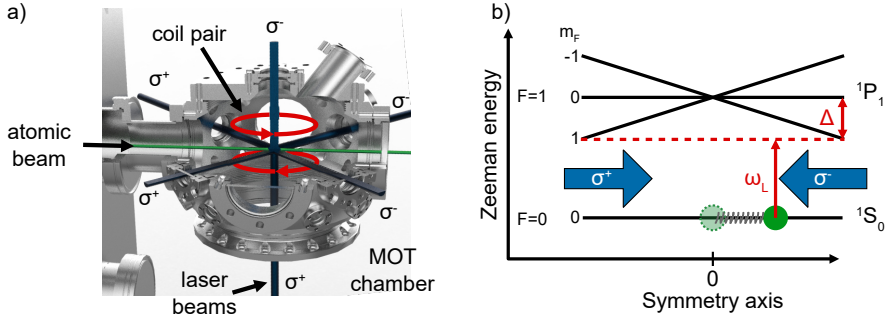


Figure 6.3: a) 3D rendered cut of a magneto-optical trap showing a buffer-gas cooled atomic beam (green) passing through the trapping region. Collinear laser beams (blue), with opposite circular handedness (σ^+ , σ^-), interact with the atoms. Electric current in two coils (red) generates a zero magnetic field at the center of the trap. b) 2D representation of the Zeeman shift along one laser beam axis. The magnetic-field gradient causes a linear shift of the magnetic sub-states of the excited state. The cooling lasers are detuned such that they become resonant with atoms leaving the trap, leading to a restoring force analog to a harmonic oscillator.

to the polarization of the light and thus determines the direction of the force in a MOT configuration. The resulting restoring force causes atoms to move towards the center of the trap in a damped oscillating motion, similar to a harmonic oscillator [219]. The combination of an optical molasses with such a magnetic field is called a magneto-optical trap. We can express the spatially dependent shift in energy, the Zeeman shift, by

$$\Delta E_Z(x, y, z) = g_F \mu_B m_F B(x, y, z) \quad (6.3)$$

with the Zeeman energy ΔE_Z , $B(0, 0, z) = A_z z$ is the magnetic field with radial gradient A_z and $g_F \approx g_J \frac{F(F+1) - I(I+1) + J(J+1)}{2F(F+1)}$ (where $g_J = 1$ for a $S = 0$ system) is the Landé factor in the approximation that the nuclear magneton is negligible due to the ratio of the electron to proton mass. μ_B is the Bohr magneton ($\mu_B \approx 1.4 \text{ MHz/Gauss}$). The radiation force can now be expressed with an additional term in $\Delta \rightarrow \Delta'' = \Delta \mp \Delta_D \pm \Delta E_Z$. In a typical MOT setup, the horizontal laser beams are under $\theta = 45 \text{ deg}$ with respect to the atomic beam, as shown in Figure 6.3a). This is accounted for by projecting all vectors with $\cos \pi/4 = \frac{1}{\sqrt{2}}$. The force of one laser beam in a 3D MOT can then be expressed as

$$F_{\pm}(x, v) = \mp \frac{\hbar k}{\sqrt{2}} \frac{\Gamma_{\text{eff}}}{2} \frac{s_0}{1 + s_{\text{tot}} + (2(\Delta \mp \Delta_D \pm \Delta E_Z)/\Gamma)^2} \quad (6.4)$$

where the saturation parameter in the denominator includes the saturation of other laser beams in $s_{\text{tot}} = \sum_i I_i/I_{\text{sat}}$. The total force of two pairs of horizontal laser beams is then $F = 2(F_- + F_+) = mx''$. The equation of motion of atoms in the MOT then follows $x'' = -\omega^2 x - \beta x'$, which is a damped harmonic oscillator. The trap frequency ω and the damping constant β follow as

$$\omega^2 = -\frac{4\sqrt{2}}{3m} \frac{\Gamma_{\text{eff}}}{\Gamma} \frac{k(\Delta/\Gamma)s_{\text{eff}}g_F\mu_B m_F A}{(1 + s_{\text{eff}} + (2\Delta/\Gamma)^2)^2} \quad (6.5)$$

$$\beta = -\frac{4}{3m} \frac{\Gamma_{\text{eff}}}{\Gamma} \frac{\hbar k^2 (\Delta/\Gamma)s_{\text{eff}}}{(1 + s_{\text{eff}} + (2\Delta/\Gamma)^2)^2}. \quad (6.6)$$

Here $\Gamma_{\text{eff}}(\text{Cd}) = \frac{3}{2}\Gamma$ is the effective scattering rate and the effective saturation parameter, $s_{\text{eff}}(\text{Cd}) = \frac{2}{3}s$, accounts for the multi-level nature of Cd atoms in the three-dimensional laser field of the MOT [220].

For a magneto-optical trap of cadmium, typically expected values are in a

range of $\omega = 11(2) \times 10^3 \text{s}^{-1}$ and $\beta = 13(3) \times 10^3 \text{s}^{-1}$ for a typical detuning of $\Delta = -1.5(2)\Gamma$, $A = 200(50) \text{G cm}^{-1}$ and $s = 2.0(5)$. The uncertainties given in brackets indicate the absolute frequency uncertainty or refer to the range of values for A and s . We expect to achieve similar values for a MOT of AlF. The expected result is more than an order of magnitude larger than for MOTs in the visible such as Rb and CaF [220–222].

Temperature limit in a MOT

The mean square momentum over many photon absorption and emission cycles is non-zero and leads to heating and eventually a diffusive motion of atoms out of the optical molasses. To determine the lowest achievable equilibrium temperature in a MOT, we compare the cooling and heating rates. The cooling rate is the derivative of the change in kinetic energy $\frac{dE_{\text{kin}}}{dt}|_{\text{cool}} = \frac{d}{dt} \frac{p^2}{2m} = F_{\text{OM}} \cdot v = -\beta v^2$. In contrast, heating due to the momentum kicks in the emission of the optical cycle is proportional to the number of random walk steps, N_p , with $N_p = 2R_{\text{scat}}2t$. Here the first factor two is for the two laser beams, the second factor two is for the complete processes of absorption and emission and t is the time. We can now express the mean square momentum as $\langle p^2 \rangle = (\hbar k)^2 N_p$. Similarly to before, the heating rate is the change in kinetic energy $\frac{dE_{\text{kin}}}{dt}|_{\text{heat}} = \frac{d}{dt} \frac{p^2}{2m} = \frac{2(\hbar k)^2}{m} R_{\text{scat}}$.

The heating and cooling rate of such a system of two counter-propagating laser beams will lead to an equilibrium temperature and we can solve $\frac{dE_{\text{kin}}}{dt}|_{\text{heat}} = \frac{dE_{\text{kin}}}{dt}|_{\text{cool}} \Leftrightarrow -\beta v^2 = 4(\hbar k)^2 R_{\text{scat}}$ to find $v^2 = -\frac{\hbar \Gamma^2}{8m\Delta}(1 + s_0 + (2\Delta/\Gamma)^2)$. From the equipartition theorem of statistical mechanics follows that the kinetic and thermal energy are equal, $E = \frac{1}{2}k_{\text{B}}T = \frac{1}{2}mv^2$, and thus that $T = \frac{mv^2}{k_{\text{B}}} = -\frac{\hbar \Gamma^2}{8k_{\text{B}}\Delta}(1 + s_0 + (2\Delta/\Gamma)^2)$. This temperature has a minimum

in the low-intensity limit ($s \rightarrow 0$) at $\Delta \rightarrow -\Gamma/2$, which is called the Doppler temperature

$$T_D = \frac{\hbar\Gamma}{2k_B}. \quad (6.7)$$

Typically for atoms $T_D \leq 1$ mK. For cadmium, due to the short excited state lifetime of 1.6 ns it is 2.4 mK.

There are several methods to cool species below the Doppler limit by using additional cooling steps to the limit of one photon recoil [223]. The recoil limit follows similarly from the kinetic energy in equilibrium with thermal energy with the velocity expressed by $v = p/M$:

$$T_r = \frac{\hbar^2 k^2}{mk_B} \quad (6.8)$$

where m is the atomic mass. T_r only depends on the wavelength and the mass of the atom. The recoil temperature for Cd is $T_r(\text{Cd}) \approx 3 \mu\text{K}$, which is similar to the one for AlF ($8 \mu\text{K}$).

6.3 Experimental setup

Figure 6.4 shows a schematic representation of the experimental setup. We use a cryogenic buffer gas beam source to produce a slow, pulsed beam of Cd atoms with a brightness of approximately 10^{13} atoms per steradian per pulse and a forward velocity of 100 – 150 m/s, which has been described in detail in Chapter 3. The capture volume of the MOT for a buffer gas beam in this setup is spherical with a diameter of approximately 3 mm, corresponding to a solid angle of about 4×10^{-5} sr. This means that approximately 4×10^8 atoms

pass through the capture volume per pulse. Alternatively, we load the MOT from a dispenser source, mounted approximately 5 cm from the trap center. The heated dispenser source fills the vacuum chamber with atomic vapor that can also be loaded into the trap.

From the geometry of the setup in the approximation of a spherical capture volume with 3 mm in diameter, this corresponds to a solid angle of $\approx 4 \times 10^{-5}$ rad, which means about 4×10^8 atoms are passing through the capture volume per pulse. To excite the laser cooling transition, we use the laser setup

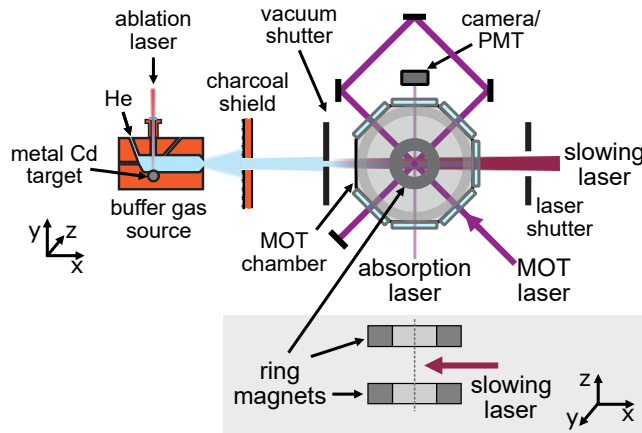


Figure 6.4: Magneto-optical trap (MOT) setup designed to capture and cool atoms originating from a pulsed cryogenic buffer gas beam source. The MOT arrangement is a hybrid configuration involving a free-space folded beam in the x - y -plane and a retro-reflected laser beam parallel to the z -axis. The atoms are laser-slowed to velocities below the capture velocity of the MOT by using a slowing laser parallel to the z axis. Fluorescence from both the atomic beam and the trapped atoms is imaged onto either a photomultiplier tube or a camera for detection. Absorption imaging is done with a camera and optics (not shown) outside of the vacuum.

described in Section 3.4. The MOT laser beam is divided into two beams: one for the horizontal plane ($x - y$ -plane), passing through the MOT center four times in a folded-beam configuration, and one for the vertical axis (parallel to

the z -axis), retro-reflected after the first pass. The laser power in the MOT center increases by a factor of 2.6 in the horizontal and 1.5 in the vertical due to transmission losses on the optical elements, resulting in discrepancies from the expected factors of 4 and 2, respectively. For a typical incoming laser power of 42 mW in a 3.5 mm diameter beam, this results in a typical average beam intensity of 0.5 W/cm^2 in the horizontal plane and 0.17 W/cm^2 along the vertical axis. An in-vacuum shutter blocks the constant flow of helium buffer gas when there are no atoms present in the beam (see section 6.4.5). Optical shutters in front of the vacuum window on the atmosphere side block the lasers when not needed, to avoid window degradation due to extended exposure to DUV light. The fundamental laser frequencies are measured with a wavemeter (HighFinesse WS8-10) which is referenced to a calibrated, temperature- and frequency-stabilized HeNe laser at 633 nm.

The magnetic quadrupole field

The magnetic field of magneto-optical traps is usually created by two current-carrying coils that are mounted in an anti-Helmholtz configuration to create a tunable and switchable gradient of a few Gauss per centimeter in the center of the trap. The required magnetic field gradient for resolving the excited states of AlF and Cd is, however, orders of magnitude larger and such a coil is not trivial to manufacture. For a proof of concept we produce a quadrupole magnetic field by using permanent ring magnets as shown in Figure 6.5a). The magnetic field is of the form $\vec{B}(x, y, z) = A_z(z\vec{e}_z - 1/2(x\vec{e}_x + y\vec{e}_y))$ where $A_z = \frac{\partial B}{\partial z}$ denotes the magnetic field gradient in axial direction and \vec{e}_i are the unit vectors. The magnetic field is zero in the center and the radial gradient is half of the axial gradient. The magnets both have a uniform magnetization $|M| = 290 \text{ kA/m}$,

which points along $\pm x$, and are separated by distance $d = 25$ mm. We use two sets of magnets that only differ by the inner bore diameter, which was cut using a water jet. We refer to them as the high-gradient ($d_{\text{in}} = 22$ mm) and low-gradient set ($d_{\text{in}} = 30$ mm). The outer radius of the rings is $R_{\text{out}} = 40$ mm and they share the same thickness $h = 9$ mm.

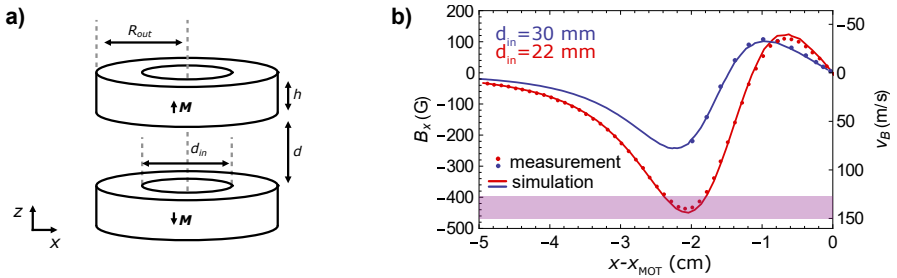


Figure 6.5: a) Drawing of ring magnets used in the MOT setup. The diagram shows the geometric arrangement in the experiment. b) The magnetic field B_x of the trapping magnets along the x axis near the MOT center. The left axis shows measured data points and simulated B_x profiles (solid lines). The right axis plots the atomic velocity $v_B = \mu_B B_x / (h\lambda)$ along x that would be required to cancel the Zeeman shift of the $m_F = +1$ state. The purple shaded bar indicates the span of the transition linewidth in these units.

Of interest for our trap is the radial field component B_x in the propagation direction of the atomic beam at the center of the trap. Figure 6.5b) shows the field profiles for the trapping magnet system. Near the origin, the field components show the expected behavior of a quadrupole field, forming the trap for our experiment. Further away from the trap center, the radial component passes through zero and displays an additional field maximum. The field profile in the region of 2 cm to 1 cm from the trap center is almost ideal for Zeeman slowing of atoms approaching the trap along x . The magnetic field sharply increases to a magnitude well above that experienced by atoms in the MOT. This arrangement enables the implementation of a short and simple Zeeman

slower for the atomic beam. The steep slope of more than $150 \text{ Gauss cm}^{-1}$ before entering the trapping region corresponds to a Zeeman energy shift of 210 MHz (corresponding to 67 m s^{-1} at $1.4 \text{ MHz Gauss}^{-1}$) and is ideal for rapid Zeeman slowing of atoms to below the capture velocity. This all happens on the timescale of $< 1 \text{ ms}$. However, since the pulse extends over several milliseconds and the shutter delay is on the ms timescale, we keep the optical shutter of the slowing laser open for 10 ms from the time of ablation. The lifetime and absolute number of atoms in the trap are unaffected by small variations in this timing.

Imaging system

In the MOT chamber, we can image the atomic beam only via fluorescence, as the gas is too dilute to cause detectable absorption. Once the trap is loaded, we can image this dense gas either via fluorescence or absorption. For spatial information, we use a UV-sensitive camera, and for temporal information, we use photo-multiplier tubes. Absorption measurements in the MOT require an additional laser beam on resonance. We use a $4f$ lens setup as shown in Figure 6.6. The focal lengths and geometry parameters of the lenses are given in Table 6.3. For absorption imaging, it is beneficial to use aspheric lenses, as these produce an image with fewer aberrations. For fluorescence detection on a PMT, on the other hand, it is sufficient to work with spherical lenses as they are more readily available. We capture images using a camera (Kepler KL400 from FLI) with a fluorescing coating on its sensor, converting UV light to visible light for detection. The chip of this camera consists of $(2048 \times 2048 \text{ pixels})$ with a

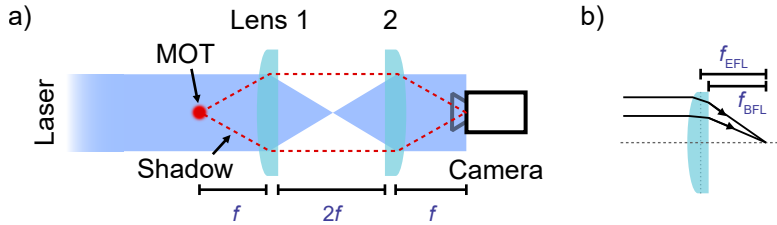


Figure 6.6: a) An imaging setup for absorption measurements requires two lenses to image the magneto-optical trap in a $4f$ configuration. b) the focal length of plano-convex or plano-aspheric lenses is usually given as the back focal length which is measured from the plane surface. The effective focal length is measured from the principal plane of the lens.

size of $11\ \mu\text{m}$ each.[‡] The read-out electronics reads one line of pixels in $10.26\ \mu\text{s}$ before shifting the entire image one row for the next line of pixels to be read out. This leads to a rolling shutter effect, which means that over $1\ \text{mm}$ cloud size, there is a time gradient of $933\ \mu\text{s}$ and any dynamics on that timescale will be present in the image. The rolling shutter effect can be an interesting feature when capturing dynamics that take place on this timescale. It can also in part be mitigated by recording images with different trigger delays and stitching an image together line by line. The camera continuously reads out pairs of lines one after the other, i.e., up to 2 whole lines are read out before the trigger pulse takes effect and clears the chip for the subsequent acquisition. We observe this as a delay between 0 and $20.52\ \mu\text{s}$, which corresponds to the uncertainty in time for all measurements with this camera. This uncertainty can potentially be lowered to $1.5\ \mu\text{s}$ by connecting a GPS module to the camera, which allows

[‡]This sCMOS camera was used for the trap frequency measurements in this chapter. This particular camera model is designed for astronomy applications with extended exposure times and turned out to be not well-suited for capturing triggered exposures in the millisecond range because of software issues. For the absorption measurements in this chapter, we upgraded to an EMCCD camera (Teledyne Princeton ProEM-HS: 1024B eXcelon). Note that the EMCCD camera has a pixel size of $13\ \mu\text{m}$ and different readout timings than described in the text.

recording the exact timestamp of each measurement.

Table 6.3: Lens parameters at $\lambda = 227.5$ nm and refractive index $n=1.52252$ of the lenses predominantly used in this thesis. The radius R , central thickness CT, conical constant k , and aspheric coefficients of n -th order A_n . The back focal length (BFL) and effective focal length (EFL) are given in mm.

Type	parameters	BFL	EFL
spherical 2"	$R = 34.39$ mm, CT=14.2 mm	56.7	65.9
aspherical 2"	$R = 39.396$ mm, CT=14.2 mm, $k = -0.67$ $A_4 = -2.11 \times 10^{-7}$, $A_6 = -2.47 \times 10^{-11}$	66.2	75.4

6.4 MOT characterization

This section highlights characteristics of loading a MOT from a pulsed cryogenic atomic beam. Compared to steady-state cw-loaded cadmium traps, loading a short pulse boosts the peak atom number in the trap beyond the point where the loading rate equals the loss rate. We find that the measured trap frequency is significantly lower than expected and attribute this to an error in determining the total laser intensity, which is not trivial to determine because of the non-Gaussian beam shape. This also affects the accuracy of determining the scattering rate and consequently the conversion of fluorescence signal to the number of atoms in the trap. In order to measure the absolute number more reliably by absorption, we increase the density by making use of the integrated Zeeman slowing region. This enables us to measure laser absorption by the trapped gas and to determine density and atom count accurately. We find that the ionization rate limits the lifetime of the trap, which hinders accumulating multiple shots to further increase the number of atoms in the trap. We implement a scheme to significantly reduce the ionization loss rate and show

that multiple shots can be accumulated until an equilibrium atom number is reached. We then measure the temperature of the trapped gas imaging the ballistic expansion and calculate the phase space density.

6.4.1 Loading rate

Figure 6.7a) compares the fluorescence signal of MOTs loaded from a dispenser source (red curve) with that of a buffer gas beam source with the use of the slowing laser (blue curve). A typical time trace of a pulse from a buffer gas beam is shown in black, where the MOT is off and a perpendicular probe beam is used. The MOT fluorescence signals are adjusted by the calculated scattering rate, as both setups have different optimum detuning. The peak atom flux in the MOT region from a buffer gas beam is similar to the continuous atom flux from an oven source. However, the atoms are delivered to the capture volume in a few milliseconds, have a lower forward velocity, and a significantly narrower velocity distribution. Rapid loading of a larger number of atoms can be highly advantageous when the trap lifetime and thus the equilibrium number of atoms in the trap is limited by loss channels such as ionization. The peak fluorescence signal from the buffer gas source in Figure 6.7a) is at least a factor of 5 higher than for a background loaded trap. In order to estimate the peak loading rate, we model the loading process with a Gaussian pulse of atoms $R(t)$ by following

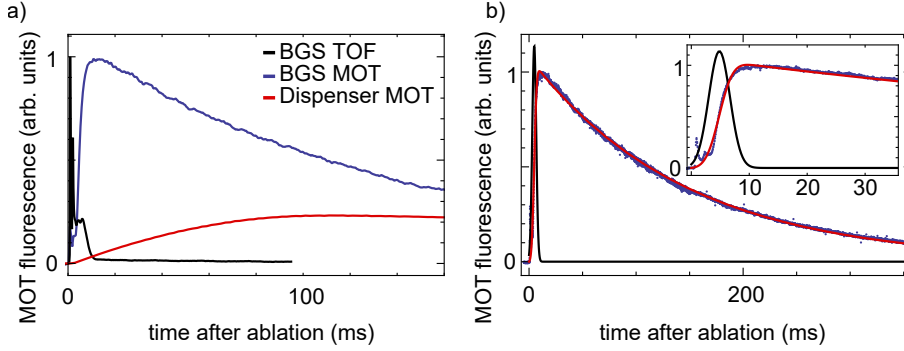


Figure 6.7: a) the MOT loading curve (blue curve) from a typical buffer gas pulse (black curve, arbitrary scale). The loading curve from a background-gas-loaded MOT, shown in red, has a lower loading rate and reaches an equilibrium number significantly lower than the peak number of the buffer-gas loaded MOT. b) The loading rate can be modeled with a Gaussian pulse and an exponential loss rate γ .

Reference [224] as:

$$\frac{dN}{dt} = R(t) - \gamma N(t) \quad (6.9)$$

$$R(t) = \frac{n_{\text{tot}}}{w\sqrt{2\pi}} \exp\left(-\frac{(t-t_0)^2}{2w^2}\right) \quad (6.10)$$

$$N(t) = \frac{n_{\text{tot}}}{2} \exp\left(\frac{\gamma}{2}(-2(t-t_0) + \gamma w^2)\right) \left(\text{erf}\left(\frac{t_0 + \gamma w^2}{\sqrt{2}w}\right) - \text{erf}\left(\frac{-t + t_0 + \gamma w^2}{\sqrt{2}w}\right)\right) \quad (6.11)$$

where w is the width of the Gaussian pulse at a given time t_0 and the loss rate γ is multiplied by the number of atoms in the trap $N(t)$. The peak loading rate is then $R_{\text{max}} = R(t_0)$. Background-loaded MOTs of Cd on the DUV transition typically have a loading rate of $\approx 1 \times 10^7$, atoms s^{-1} [160]. Our fluorescence estimate in Figure 6.7 suggest the total number of Cd atoms transported into the trapping volume is 2.1×10^6 atoms, with a peak loading rate of 4.5×10^8 atoms s^{-1} in a Gaussian pulse lasting 4.0 ms (FWHM) with a

loss rate of 6.9 s^{-1} . The peak loading rate is significantly increased compared to previous studies for Cd, but it falls short in comparison to other buffer-gas beam loaded atomic MOTs that can achieve loading rates exceeding 1×10^{10} , atoms s^{-1} [133, 224]. The discrepancy arises from the significantly larger $1/e^2$ MOT beam diameters that were used in these studies, leading to an increase in MOT solid angle by a factor of approximately 10-30 compared to our MOT.

6.4.2 Trap frequency

The center of mass motion of the cloud follows that of a damped single particle in a harmonic potential. When disturbed from the equilibrium position, it exhibits damped oscillations, returning back to the equilibrium position over time. We perturb the atoms by the radiation pressure of a resonant laser beam. By studying this motion, we can determine the trap frequency and damping coefficient, described in equation 6.6. The position relative to the equilibrium position x_0 is represented by $x - x_0 = \exp\{-\beta t/2\} \cos\left(\sqrt{\frac{\omega^2 - \beta^2}{4}} t - \phi\right)$ with the trap frequency ω , damping coefficient β , and where ϕ is a phase parameter [220]. The rolling shutter effect can be seen in the images in Figure 6.8a), which capture large parts of the dynamics of the oscillation. The experiment was also conducted using repeated push pulses (Figure 6.9). However, observing parametric resonance was not possible due to the large damping constant preventing overdriving of the system. In the analysis, we average three lines in the center of the image where the peak of the MOT is detected and observe the displacement of the cloud along the line dimension of the camera, which means the exposure time of these rows averages over $30.78 \mu\text{s}$. The time resolution is on the order of the length of the push pulse (typically $50 \mu\text{s}$) and is suitable to measure the oscillation, which is on the time scale of milliseconds.

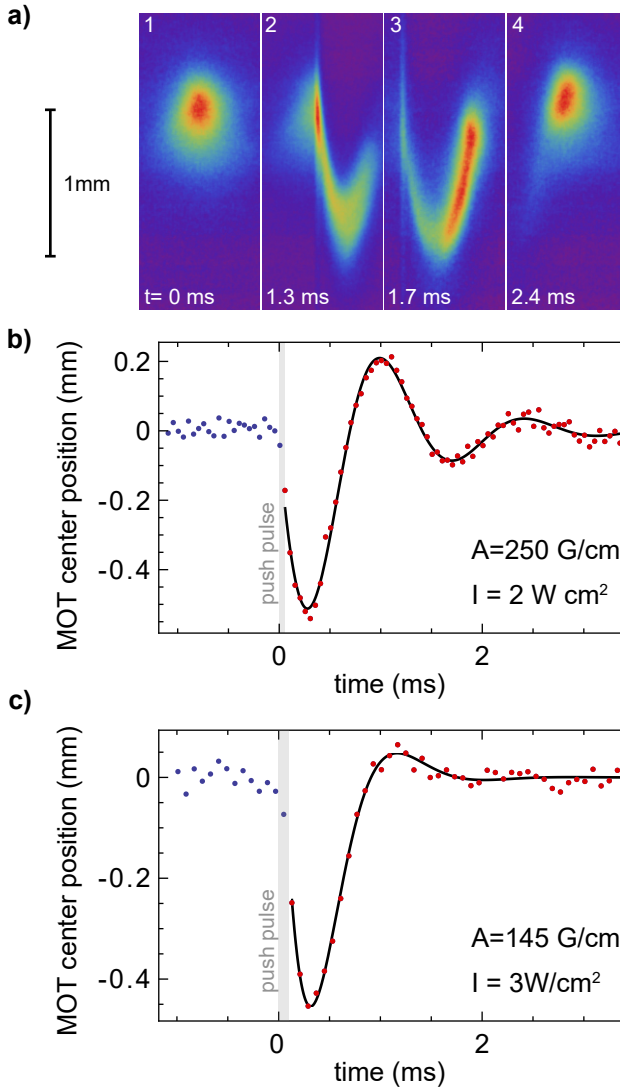


Figure 6.8: Center of mass oscillations in the magneto-optical trap are driven by flashing the slowing laser, now tuned close to resonance (typically -75 MHz), which pushes trapped atoms out of equilibrium. a) camera images include temporal information as the rolling shutter effect reads the sensor line by line (here in the horizontal direction). b) low field gradient oscillation c) high field gradient with the same settings except double laser intensity leads to the same trap frequency, but the damping factor is half.

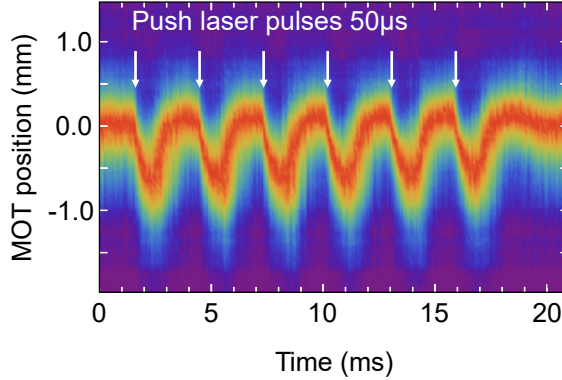


Figure 6.9: Center of mass oscillation of a repeatedly driven oscillation out of equilibrium. The false-color image consists of the central three lines of 1000 individual images taken in steps of $20 \mu\text{s}$ that are each normalized.

For the fit of the oscillation shown in Figure 6.8, data points before the end of the push beam are omitted. We measure this oscillation with both magnet sets. For the measurement with a high magnetic field gradient, the MOT lasers are detuned by $\Delta = -1.5\Gamma$ from the ^{112}Cd resonance. The push beam is detuned by -74MHz relative to ^{112}Cd as a means to adjust the peak amplitude of the oscillation, rather than changing the laser power or the length of the push pulse. The MOT laser power corresponds to a total intensity of $I_{\text{tot}} = 2\text{W cm}^{-2}$. For the low gradient measurement, we use the same detuning but set the intensity to $I = 3\text{W cm}^{-2}$, where the same trap frequency is measured for this magnet pair. This allows us to measure the ratio of the radial damping constants for the two gradients which should reflect the ratio of the radial magnetic field gradients since $\omega^2 \propto \beta \frac{\partial B}{\partial r}$. From the values in Table 6.4 we find a ratio of 2.1(2), while the ratio measured with a Hall-probe in the radial direction is 1.8. Surprisingly, the measured values are in disagreement with the predicted values in section 6.2. This inconsistency suggests that the

Table 6.4: Typical parameters for measuring the trap frequency.

	$I_{\text{tot}}/I_{\text{sat}}$	$\Delta(\Gamma)$	A (G/cm)	ω (10^3s^{-1})	β (10^3s^{-1})
low gradient	3.0(5)	-1.45(20)	140(10)	4.5	5.3
high gradient	2.2(5)	-1.45(20)	250(10)	4.5	2.5

actual saturation parameter in the experiment is significantly lower than assumed. From the measured value for β , the saturation parameter is $s = 0.6$ for the low gradient measurement and $s = 0.27$ for the high gradient measurement. Misalignment between the small beams can lead to an effective lower intensity, and we conclude that the scattering rate of atoms in this experiment should not be estimated by measuring the laser beam intensities outside the vacuum chamber. This is usually done to attribute a fluorescence signal to a number of atoms in the trap via the scattering rate. Absorption measurements can provide the atom number more accurately since they are independent of the scattering rate. In order to measure absorption we need to maximize the atom number and for this we have to characterize the slowing laser as is done in the following section.

6.4.3 Integrated Zeeman slower

The slowing laser is aligned collinearly with the atomic beam and gently focused onto the source output. The laser detuning is typically set to about -7Γ with an intensity of about 0.5 W cm^{-2} , which corresponds to a velocity of 160 m s^{-1} ($\approx 23\text{ m s}^{-1}$ per Γ). This configuration slows a large fraction of the atomic beam below the capture velocity of the trap, enhancing the number of trapped atoms of ^{112}Cd by typically at least a factor of 10, as compared to a buffer-gas loaded MOT without Zeeman slower (see Figure 6.7). We can trap all Cd

isotopes in the MOT, as shown in Figure 6.10, where the frequency axes are set to zero for the field-free frequency of the ^{112}Cd transition. We record the LIF signal with a photo-multiplier tube, averaged from 50-150 ms after ablation. This allows enough time for atoms that are not interacting with the slowing light to pass through the MOT region. The measurement is performed line-by-line, starting at the bottom of Figure 6.10 and alternating the MOT frequency detuning direction between two lines. The intensity in the vertical columns for a given isotope shows the decrease of atom signal from the source throughout one measurement, which lasts for about 60 min. The inset in Figure 6.10 is a separately color-coded snippet of the region with low abundance (^{106}Cd , ^{108}Cd). The MOT brightness per isotope closely resembles the natural abundance in the sample. Since the isotope shifts are larger than Γ , the laser detuning can be set such that one or at most 2 isotopes are trapped at the same time. Measuring the fluorescence is a rough measure of the number of trapped atoms. Since the fluorescence and trapping efficiency both depend on the detuning, the maximum fluorescence does not necessarily correspond to the maximum number of atoms in the trap. The optimum MOT detuning is typically found at $\approx -1.5\Gamma$ from resonance.

Two cuts through this plot are shown in Figure 6.11. Figure 6.11a) shows the MOT signal as a function of slowing laser detuning, while the MOT frequency is fixed to ^{112}Cd (black dotted vertical line). For the slowing laser we use circularly polarized light with opposing handedness (σ^1 , σ^2) and linear polarization. We note that the quantitative behavior changes depending on the alignment and the laser power used. Qualitatively, the linear and only one specific handedness of circular light results in a double peak structure with a local minimum. In contrast, the opposite circular polarization shows a more narrow,

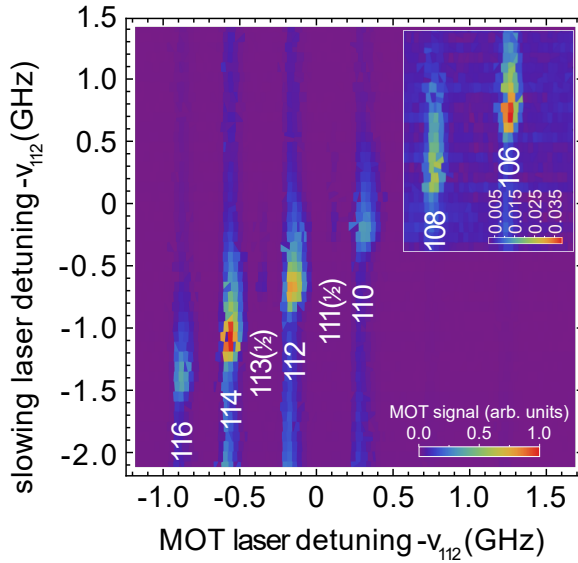


Figure 6.10: False color image showing the relative fluorescence from the MOT 50 ms after firing the ablation laser, as the slowing and MOT lasers are scanned. The inset has a separate intensity scale.

single peak. The double peak structure could stem from nearby fermions, which should follow a different optimum for slowing. However, this effect also occurs for ^{110}Cd and ^{114}Cd (not shown). Since ^{114}Cd is not overlapped with a fermion, we attribute the double peak structure to two slowing regimes, fixed frequency slowing in a region with a constant magnetic field and the actual Zeeman slowing in the region with the magnetic field gradient. Figure 6.11b) shows the MOT signal as a function of MOT laser detuning, while the slowing frequency is fixed to ^{112}Cd (black dotted vertical line) with the polarization set to σ^1 . We record two shots for each pair of laser frequencies: one with the slowing light on and one with the slowing light off. The slower is efficiently working over a

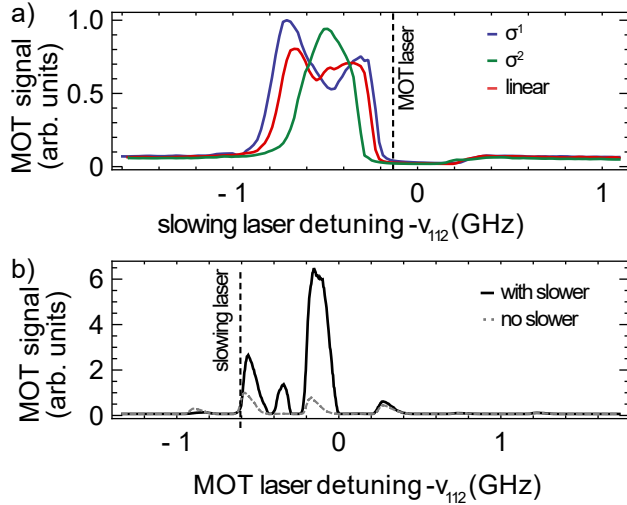


Figure 6.11: a) slowing laser frequency scan for circular and linearly polarized light. The MOT laser detuning is fixed and is indicated by the black dashed line. b) MOT laser frequency scan with the slowing laser toggled on and off. The MOT fluorescence signal is increased for the targeted isotope (^{112}Cd) and nearby isotopes. The use of the slowing laser enables a MOT very close to resonance, even though this means that the capture velocity is reduced.

broad spectral region of several hundred MHz. With the slower set for slowing ^{112}Cd (factor of 2.7 higher peak signal), the ^{114}Cd signal increases as well, and the $^{113}\text{Cd}(1/2)$ peak becomes visible. This indicates that the capture velocity for the fermions is lower than for the bosons, because the $F \leftarrow F' = F = 1/2$ transition has a loss channel, while the $F = 3/2 \leftarrow F' = 1/2$ transition is closed, as shown by Figure 6.12. Presumably, the nearby fermions ^{111}Cd and ^{113}Cd are co-trapped with the isotopes ^{110}Cd and ^{112}Cd respectively. The optimum MOT detuning with the slower present is shifted approximately 20 MHz closer to resonance, where the scattering rate is also higher. In conclusion, the slowing laser increases the fluorescence signal in the MOT by more than an order of magnitude. This leads to an increase in density and allows us to

measure the MOT in absorption.

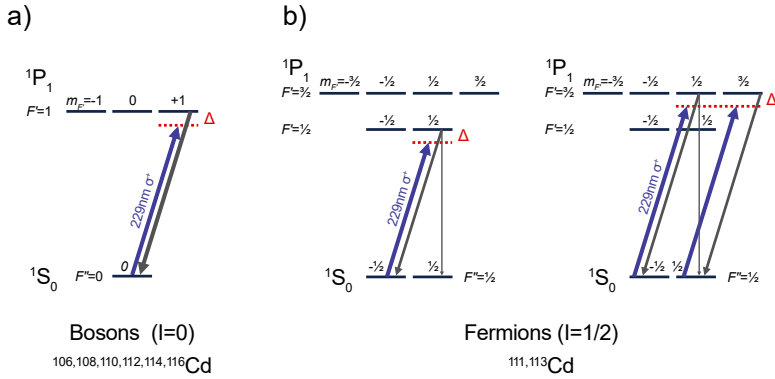


Figure 6.12: a) Laser cooling transition for bosonic and fermionic isotopes. The laser is detuned by Δ from resonance. When the atom becomes resonant by moving out of the trap, it can absorb a photon. This cycle is indefinite for bosons, but fermions on the $F'' = F' = 1/2$ transition can only do this a couple of times before the atom is trapped in a dark state where it cannot be pumped with this circularity of light. This is not an issue on the $F'' \neq F'$ transition.

6.4.4 Imaging the MOT

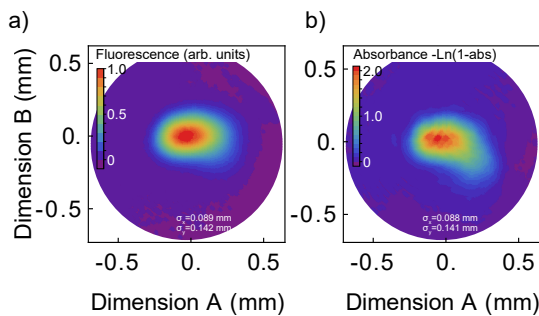


Figure 6.13: Camera images were obtained using a) fluorescence imaging of a dense ^{112}Cd MOT from a sample with natural abundance and b) absorption imaging in the same configuration. Note that axes A and B do not correspond to the axial and radial axes as the image was rotated for analysis.

Under typical conditions, the DUV fluorescence can be imaged onto a piece of white paper where it becomes visible to the eye. Figure 6.13a) shows a fluorescence and an absorption image of the MOT taken with a camera. The resonant absorption cross-section σ_{abs} of an atomic transition in the absence of broadening effects is

$$\sigma_{\text{abs}} = \frac{2J' + 1}{2J'' + 1} \frac{\lambda^2}{2\pi} \quad (6.12)$$

$$\sigma_{\text{abs}}(\text{Cd } ^1P_1 \leftarrow ^1S_0) = 3 \frac{\lambda^2}{2\pi} = 2.5 \times 10^{-10} \text{cm}^2, \quad (6.13)$$

where Doppler broadening can be neglected because the atoms are trapped and Zeeman broadening is negligible as the probe light is linearly polarized. The calculated absorption cross-section $\sigma_{\text{abs}}(\text{Cd } ^1P_1 \leftarrow ^1S_0)$, is about a factor of 10 lower than e.g., potassium ($\sigma_{\text{abs}}(\text{K } ^2P_{3/2} - ^2S_{1/2}) = 1.9 \times 10^{-9} \text{cm}^2$). This means that in order to measure an absorption on the order of 50%, the density must be $> 10^{11} \text{cm}^{-3}$.

The absorption $A = I/I_0$ of laser intensity I from the incident intensity I_0 on a medium with density distribution n can be expressed with the help of the optical density OD and the absorbance $\ln(I_0/I)$ as

$$I = I_0 \exp(-\sigma n(x, y)) \quad (6.14)$$

$$n(z) = \int \rho(x, y, z) dz \quad (6.15)$$

$$\text{OD}(x, y) = -\ln(1 - A(x, y)) = -\ln(I_0(x, y)/I(x, y)) = \sigma \times n(x, y). \quad (6.16)$$

We find a peak optical density of $n_{\text{peak}} = \frac{\text{OD}_{\text{peak}}}{\sigma_{\text{abs}}} = 7.9 \times 10^9 \text{cm}^{-2}$ and the number of atoms to be $N = \int n(x, y) dx dy = \frac{1}{\sigma_{\text{abs}}} \int \text{OD}(x, y) dx dy = 6.1(1.5) \times 10^6$.

The peak atom density is then $\rho = \frac{N}{(2\pi)^{3/2}\sigma_x\sigma_y\sigma_z} = 2.2(0.5) \times 10^{11} \text{ cm}^{-3}$. The numbers in brackets are due to systematic errors of 10% in the magnification of the imaging system.

In order to further increase the number of atoms in the trap we use an enriched sample of ^{110}Cd in Figure 6.14. The peak absorbance of 0.66 and $\sigma^2 = 0.28 \times 0.24 \text{ mm}^2$ corresponds to $1.1(3) \times 10^7$ atoms. The larger size of the MOT leads to a lower peak density. The increase in atom number is a factor of ≈ 2 , less than the expected factor of 4 from the composition of the enriched target.

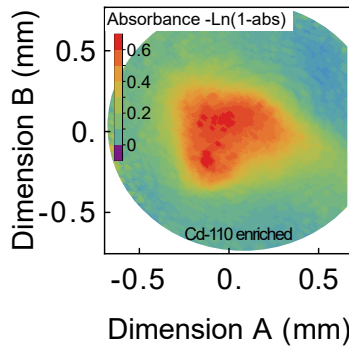


Figure 6.14: Camera images were obtained using absorption imaging of a MOT of ^{110}Cd , loaded from an enriched sample. Using an enriched sample yielded an increase in atom number by a factor of 2.

6.4.5 Loss-rate analysis

Possible loss channels include collisions with background gas, collisions between trapped atoms, and ionization. Electronic losses to the intermediate $^3P_{0,1,2}$ state are minimal due to spin selection rules [225]. Understanding the limiting processes in the lifetime of a MOT is vital for improving the performance of

the system. If the lifetime can be extended to be longer than the time between two pulses, then multiple shots can be accumulated and hence increase the atom number. In this section we will investigate two-photon ionization, which is the dominant loss channel. We present a laser-frequency ramping scheme that allows to increase the lifetime and to accumulate multiple pulses.

Photoionization cross-section

The most significant loss channel for our MOT is 1+1 photoionization. Typically the MOT is operated at a laser detuning of $\Delta = -1.45\Gamma$ from the resonance of a given isotope, e.g., ^{112}Cd . To estimate the loss rate A , we fit an exponential function

$$N(t) = N_0 \exp(-At) + d \quad (6.17)$$

with initial atom number N_0 and constant background signal d to the decay curve of the MOT signal from 45-850 ms after ablation. The extracted loss rates together with their statistical errors from the fit are shown in Figure 6.15 as a function of the total MOT laser intensity. The total loss rate can be described as the sum of background collisions A_0 and ionization A_{ion} as

$$A = A_0 + A_{\text{ion}} \quad \text{with} \quad A_{\text{ion}} = I \frac{\sigma_{\text{ion}} \rho_{ee}}{\hbar \omega} \quad \text{where} \quad \rho_{ee} = \frac{s_{\text{eff}}/2}{(1 + s_{\text{eff}} + (\frac{2\Delta}{\Gamma})^2)}. \quad (6.18)$$

The ionization rate in the MOT is dependent on the photoionization cross-section σ_{ion} , the angular frequency ω , and the saturation parameter $s_{\text{eff}} = 3/2 \frac{I}{I_{\text{sat}}}$. A_{ion} is quadratic for low intensities but above 5 W cm^{-2} starts to

Table 6.5: Literature values for the ionization cross section in cm^2 for cadmium and systems with comparable energy level structure.

Cd [215]	Mg [226, 227]	Sr [228, 229]	Ba [230, 231]
$(0.3 - 3) \times 10^{-17}$ *	$8(2) \times 10^{-17}$	1×10^{-17}	$8(2) \times 10^{-17}$
$2(1) \times 10^{-16}$	9×10^{-17}	$2.2(5) \times 10^{-16}$	$1.8(2) \times 10^{-17}$

* *this work*

become linear.

We see that below $I=2 \text{ W cm}^{-2}$, a departure from equation 6.18 is seen. This may indicate the trap depth is too low to confine the atoms, or that the trap is increasingly sensitive to intensity imbalance between the MOT beams when near the threshold for trapping. The grey data points are thus not considered for the fit. The fit yields an ionization cross-section of $9.1(2) \times 10^{-18} \text{ cm}^2$. Including an error of factor two in the total intensity, we arrive at $1.4(14) \times 10^{-17}$. Due to the large error bar, we estimate the ionization cross section from the excited state in an order-of-magnitude estimate as

$$\sigma_{\text{ion}}(^1P_1) = (0.3 - 3) \times 10^{-17} \text{ cm}^2.$$

This is a factor of 7 below the literature value of $2(1) \times 10^{-16} \text{ cm}^2$, which was also measured in a similar way [215]. However, Table 6.5 shows that literature values for the ionization cross section of atomic systems with comparable energy level structure as Cd can vary by one order of magnitude.

Extending the lifetime and mitigating ionization

We attempt two strategies to reduce photoionization loss. Both methods reduce the scattering rate and thus the ionization probability in the time after loading a pulse. Controlling the laser intensity by varying the RF power of the AOM

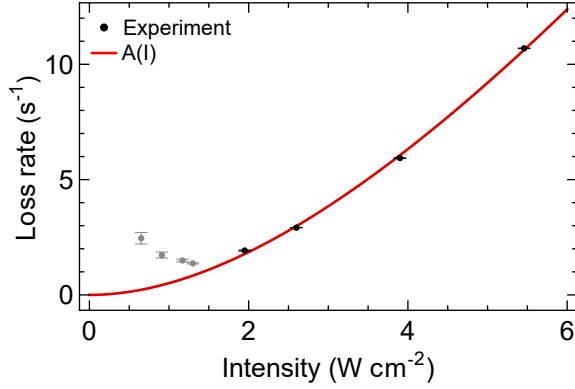


Figure 6.15: The loss rate for a detuning of $\Delta = -1.45\Gamma$ is recorded to extract the ionization loss-rate as a function of laser intensity. Data points in grey are not considered for the fit.

for the MOT beams resulted in misalignment of the laser beams on the order of 1 mrad per 10 MHz frequency shift. This method is thus not suitable, as the MOT is very sensitive to small changes in beam pointing. The second method is frequency detuning the laser by applying a voltage ramp to the resonator cavity of the fundamental TiSa laser. Figure 6.16a) shows the number of atoms and the lifetime of the MOT as the detuning Δ is varied. The initial atom number is optimized at $\Delta_1 = -130$ MHz, whereas the optimum lifetime occurs at $\Delta_2 = -210$ MHz. Therefore we opted to load the MOT at Δ_1 before linearly ramping further from resonance. Figure 6.16b) shows accumulation of 8 successive atomic pulses in the MOT with fixed detuning, and when detuning the laser after loading the trap. For these experiments, we fired the ablation

YAG at a repetition rate of 10 Hz for $0 < t < 0.8$ s. The loss rate for the measurement with constant frequency at Δ_1 is 5 s^{-1} and 2.56 s^{-1} when the laser is detuned to Δ_2 in between shots. At $t = 0.85$ s, after the loading sequence, the trap conditions are identical and the fluorescence signal from the methods can be directly compared. The loading scheme involving detuning the laser between shots leads to an increase of 1.6 times more fluorescence signal, compared to when the laser frequency remains fixed. Compared to loading a single pulse, the fluorescence signal is increased by a factor of 3.5. These results suggest that accumulating multiple pulses can significantly increase the number of atoms in the trap.

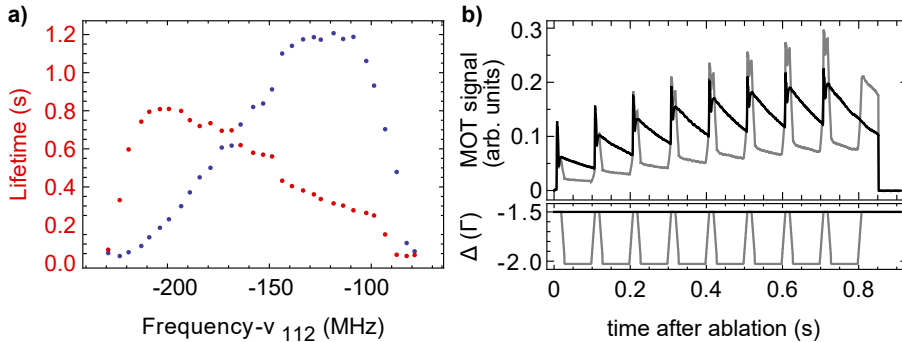


Figure 6.16: a) lifetime in the trap (red datapoints) and peak atom number (blue datapoints, arbitrary scale) as a function of laser detuning. In order to accumulate multiple shots, the MOT is loaded at peak atom number and then tuned to peak lifetime. b) A laser ramping scheme (grey curves) is used to accumulate multiple shots at 10 Hz repetition rate and compared to fixed frequency MOT lasers (black curves). Detuning the laser between shots leads to an increase in signal of a factor of 1.6 at $t = 0.8$ s.

Figure 6.17 shows that the number of atoms in the trap can be further increased by increasing the repetition rate of the experiment to 20 Hz. Again, the laser is detuned in between shots by about 0.5Γ . In this example, 15 pulses

are loaded and the number of atoms in the trap reaches at an equilibrium where the loading rate is equal to the ionization rate. The maximum number of atoms in the trap is increased by a factor of 6 compared to a single pulse.

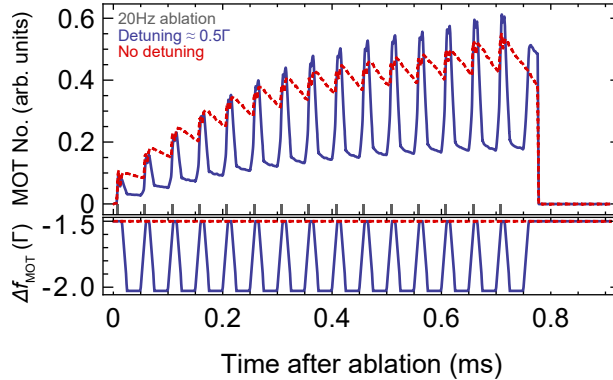


Figure 6.17: Accumulation of ^{112}Cd isotopes from 18 pulses at 20 Hz. This increases the atom number in the trap by a factor of 6. The MOT laser is detuned by 0.5Γ in between shots to reduce the ionization rate.

Background gas collisions

From Figure 6.18, we can see that the loss rate of a typical MOT doubles from 2s^{-1} to about 4s^{-1} , when increasing the gas flow by a factor of 10. In these measurements, we measure the MOT lifetime as a function of the opening duration of the helium shutter and scan this parameter forward and backward, giving the result with error bars as indicated in the plot. If we consider this a linear effect, then at a flow of 0.5sccm the loss rate due to helium “wind” is $\approx 0.2\text{s}^{-1}$. With an influence of 5-10% of the lowest measured value, this effect can be considered negligible in most cases. Note that the shutter is not sealing perfectly and about 1% of cadmium signal can be measured even when the shutter is closed. It is however suitable to block a direct stream of helium

buffer gas.

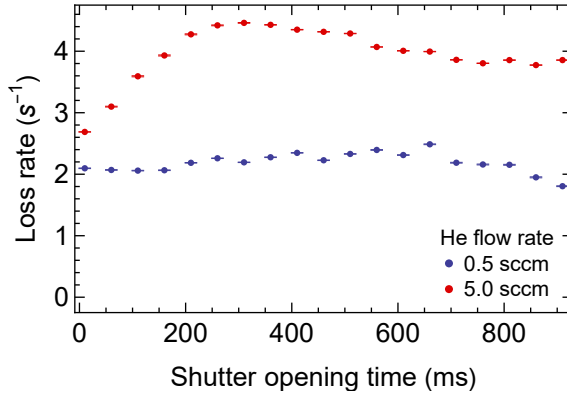


Figure 6.18: Loss rate from a ^{112}Cd MOT at fixed intensity and detuning, for different opening durations of the in-vacuum shutter and two different He flow rates into the buffer gas source. Increasing the flow rate by a factor of 10 doubles the peak loss rate.

6.4.6 Temperature and phase space density

The measured MOT sizes for the trap frequency measurements shown in Fig 6.8 are $\sigma_{\text{high}} = 0.21$ mm for the large magnetic field gradient and $\sigma_{\text{low}} = 0.34$ mm for the low magnetic field gradient. We can relate the equilibrium size of the MOT to the temperature via the equipartition theorem $E_{\text{pot}} = \frac{1}{2}\omega^2 m x^2 = \frac{1}{2}k_B T$ (see section 6.2). For a Gaussian particle distribution with radius ω , $T = \frac{\sigma^2 m \omega^2}{k_B}$ [232]. We calculate the temperatures as $T = 12$ mK for the smaller MOT and $T = 31$ mK for the larger MOT.

Another way of measuring the MOT temperature is to measure the ballistic

expansion after the MOT has been switched off. Since there was no independent probe laser available, we use the setup shown in Figure 6.19a). One AOM is used to detune the frequency by -200 MHz for the MOT beams. A small fraction of that beam is split off and detuned close to resonance for absorption. The switching sequence includes a laser shutter that can switch the MOT light completely off, independent of the absorption laser. The minimum dead time between switching off the MOT and measuring absorption is then defined by the shutting speed of the optical shutter, which is around 1 ms. However, the previous temperature estimate suggests that the MOT will expand on the timescale of 1 ms at which point the gas is no longer dense enough to be imaged in absorption. The shutter is thus carefully positioned to minimize the actual time it takes to shut the laser light in less than 200 μ s. Figure 6.19b) presents the switching diagram, which consists of three phases. Phase I is the loading phase, the length of phase II is determined by the time it takes to close the optical shutter, and phase III varies in time in $0.2 \text{ ms} < \Delta t < 1 \text{ ms}$. Figure 6.19c) shows a selection of absorption images after different expansion durations. We fit a Gaussian model to the absorbance and plot the width against the expansion time in Figure 6.20. We follow Reference [220] and model the expansion as

$$\sigma = \sqrt{\sigma_0^2 + k_B T (\Delta t)^2 / m} \quad (6.19)$$

where σ_0 is the initial cloud size, T is the temperature of the gas and m is the atomic mass. The fit in Figure 6.20 results in a temperature of $T = 17(2)$ mK and $\sigma_0 = 0.51(4)$ mm. The averaged initial cloud size is however 0.33(1) mm, which is inconsistent with the fit result. There seems to be a discontinuity after

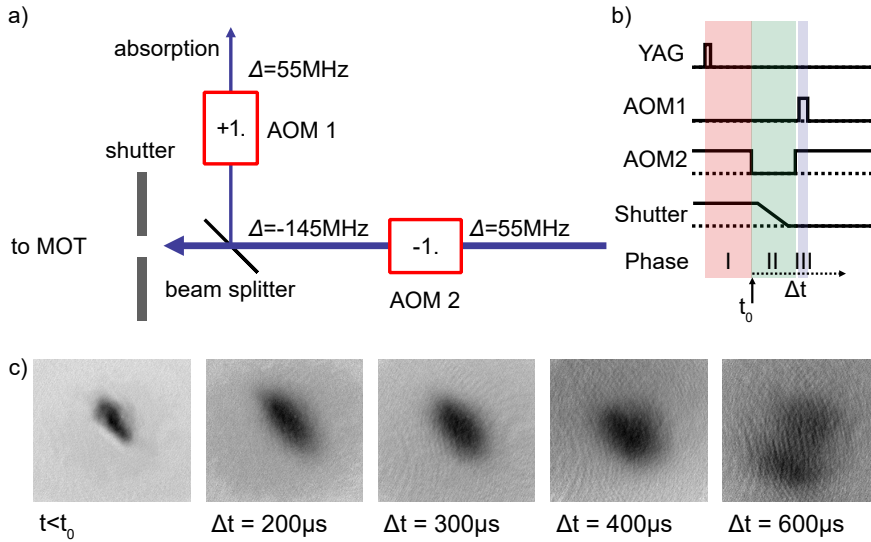


Figure 6.19: a) schematic of the optical setup for measuring the ballistic expansion of the MOT with the same laser that powers the trap lasers. Two AOMs are used to rapidly switch the MOT and absorption beams. Additionally, an optical shutter is needed to block the MOT light while probing with the absorption beam. b) the switching scheme of this measurement consists of three phases: loading the MOT, ballistic expansion, and probing with a varying delay time Δt . c) absorption camera images after different expansion times show that the time dynamic is on the order of one millisecond.

switching the laser off, which could be caused by the finite time the shutter takes to fully close. From the initial size, and a typical trap frequency of $\omega = 4.5 \times 10^3 \text{ s}^{-1}$ we calculate $T = 30 \text{ mK}$. Since the trap frequency is not precisely known for this measurement, we can only take it as an estimate.

For a peak density of $2.2 \times 10^{11} \text{ cm}^{-3}$ (as found in Section 6.4.4) and $T = 12 \text{ mK}$ for the small MOT in the large magnetic field gradient configuration, the phase space density is 1.0×10^{-9} . In comparison, a typical red-detuned rubidium MOT has a phase space density of 10^{-12} [233].

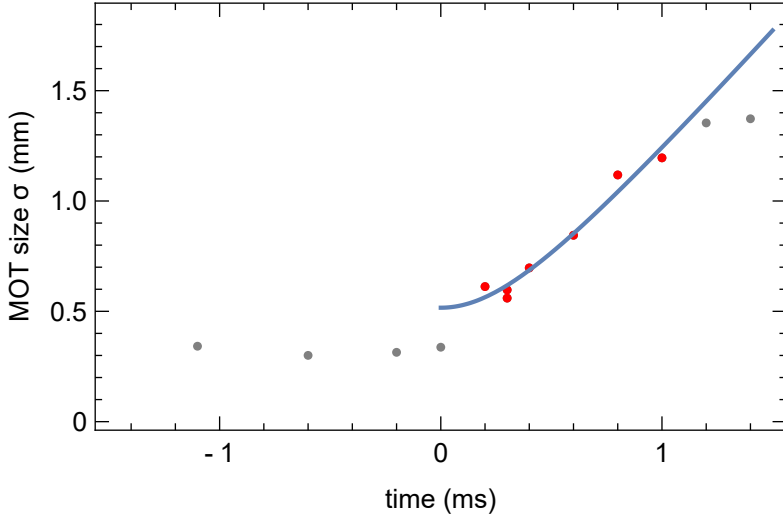


Figure 6.20: The expansion of the MOT when no radiation pressure is present can be a means to measure the trap temperature. We fit a model to the size of the MOT after different release times. Datapoints before the release time ($t = 0$) and after 1 ms are not considered in the fit.

6.5 Summary

In this chapter, we demonstrate the successful magneto-optical trapping of cadmium on its deep ultraviolet (DUV) transition, as a step towards the more challenging AIF trap. This chapter highlights the potential for using MOTs with DUV transitions for future experiments. The size of the laser beams and thus the MOT diameter is limited by the laser power that can be produced in this wavelength regime. One of the biggest challenges is achieving the large magnetic field gradient of several hundred Gauss/cm that is required to achieve the Zeeman splitting of the excited state to excite selected hyperfine transitions.

Despite these challenges, we find that a loading rate of $\gg 4 \times 10^8 \text{ s}^{-1}$ can be achieved, which is described well by approximating the loading process with a Gaussian pulse of atoms with a width of 4 ms. We show that up to

$1.1(3) \times 10^7$ atoms with a phase space density of 4×10^{-9} can be loaded in just a few milliseconds. We measure the trap frequency and find that it is significantly lower than expected, yet more than an order of magnitude larger than for other atomic species with transitions in the visible range. The magnetic field of the trap provides a small region (a few cm) for Zeeman slowing. This is significantly shorter than for Zeeman slowers made of electric coils. The use of permanent magnets makes the vacuum setup more compact. The Zeeman slower increases the capture velocity of the trap and thus the fraction of atoms that is loaded into the MOT by at least a factor of 10. This allows us to measure the trap density in absorption and to measure the temperature through ballistic expansion. To increase the number of atoms in the trap further, we use an isotope-enriched target. However, this does not result in the expected increase in atom number, the reasons for which are currently unknown. We find that the presence of background buffer gas does not significantly affect the trap lifetime. To reduce losses due to ionization, we ramp the laser frequency to be further from resonance in the time between shots. This allows us to establish a continuous reservoir of cold atoms.

Cryogenic buffer gas beam sources can significantly reduce the loading time to milliseconds, compared to several seconds that are typical for experiments with continuous sources. This leads to a significantly increased repetition rate, particularly beneficial for applications in high-precision spectroscopy and atomic clocks. Pulsed sources also enable working with smaller sample masses, which is advantageous for toxic or costly substances, or elements with high heat of vaporisation, where the use of ovens is impractical. As shown in Chapter 5, the measurement accuracy on the 229 nm transition is limited by the broad linewidth, the significant overlap between neighboring isotopes, and

strong quantum interference effects in the observed hyperfine splitting of the fermions. These issues could be resolved by selectively loading one isotope in the trap to measure the transition frequency in absorption or by measuring the blue edge of the MOT. The narrow-line ($^3P_1 \leftarrow ^1S_0$) can potentially cool the gas to $10\ \mu\text{K}$, which corresponds to a Doppler broadening of $3\ \text{kHz}$, small compared to the natural linewidth of $69\ \text{kHz}$ and three orders of magnitude lower than the linewidth in a typical atomic beam spectroscopy setup [152].

6.6 Outlook

This work has provided important technical insights and identified several challenges that need to be addressed in future experiments with AIF. Generating laser light at powers at the edge of what is technically feasible for the experiment and dealing with coating degradation on windows and other optics have been among the major hurdles. Imaging DUV fluorescence and measuring absorption with the limited number of lasers available and their non-Gaussian mode profiles posed significant challenges that had to be overcome. MOT laser alignment proved to be a particularly sensitive issue, compounded by the fact that the laser beam alignment varies from day to day, with temperature and with the laser output power. The necessarily small beam diameters make alignment difficult and require frequent readjustments, making the setup highly alignment-sensitive and requiring constant attention. To entirely solve these challenges, further advances in laser technology are essential, particularly in terms of output power, beam shape, and pointing stability. Finding a solution to the degradation of anti-reflection coatings, or using off-axis rotating flanges for window mounting, will reduce the frequency of replacement and the time

spent baking out the chamber.

In summary, this chapter demonstrated the feasibility of constructing a DUV trap for cadmium atoms that is loaded using a buffer gas beam source. The established techniques and the knowledge gained in overcoming technical hurdles now serve as the first step to transfer the technique to AlF molecules. Attempts to laser cool AlF will require frequency modulation to achieve scattering rates comparable to Cd. This goes with a reduced spectral power density, which means that higher laser powers or additional laser systems are needed to achieve the same scattering rate. Additional laser systems may also be required to address leakage to $v'' = 2$. The additional laser power necessary for repumping will also tend to increase the 1+1 photoionization trap losses. Laser cooling of AlF molecules in a magneto-optical trap is not a low-hanging fruit but is within reach in the coming years.

Summary

Laser-cooled atoms have found widespread applications - ranging from precision spectroscopy and metrology to quantum computing - resulting in advanced instruments such as precise atomic clocks. More recently, progress has been made in laser cooling of molecules. Molecules can rotate and vibrate and thereby have a rich internal energy level structure. Apart from a magnetic dipole moment, molecules can also have an electric dipole moment and together, these properties enable many new applications in fundamental physics and quantum science. However, this complexity also makes it challenging to produce them efficiently and subsequently cool them to low temperatures using laser light. As a result, the number and density of trapped molecular gases is three to four orders of magnitude lower than that of laser-cooled atoms, which severely limits applications for molecules.

This thesis presents significant progress in addressing this challenge by using the deeply-bound polar molecule aluminum monofluoride (AlF), which exhibits a laser cooling transition in the deep ultraviolet (UV). Transitions in the deep UV are particularly useful because the optical force exerted by a laser beam on an atom or molecule typically scales with $1/\lambda^4$. Compared to transitions in the visible, this significantly increases the capture velocity of magneto-optical traps (MOTs) and reduces the stopping distance of an atomic or molecular beam, allowing a larger number of particles to be trapped.

The main goal of this work is to build and characterize a cryogenic helium buffer gas beam source for AlF molecules and to establish an optical cycle that is suitable for laser cooling. It is shown that a buffer gas beam of AlF molecules can be produced that has an order of magnitude higher density compared to other diatomic molecules and that the main cooling transition ($A^1\Pi, v' = 0 \leftarrow X^1\Sigma^+, v'' = 0$) near 228 nm is highly efficient. With a single laser, up to 210 photons can be scattered at a scattering rate of $17(2) \times 10^6 \text{ s}^{-1}$, before the molecules are lost to $v'' = 1$, where they can be recovered with a repump laser. Other potential loss channels from the optical cycle, caused by photoionization or by parity mixing in external electric fields, are measured and means to control them are presented. Furthermore, the electronic decay to the intermediate, metastable $a^3\Pi$ state does not prevent efficient loading of a MOT.

The electronic energy structure and laser wavelengths required for laser cooling of AlF are similar to those of atomic cadmium (Cd). A Cd beam can be produced in the same setup with less effort and is used to qualify the laser setup and optics by performing high-resolution spectroscopy on the $^1P_1 \leftarrow ^1S_0$ and $^3P_1 \leftarrow ^1S_0$ transitions near 229 nm and 326 nm, respectively. The results establish Cd as a promising candidate to search for new physics beyond the Standard Model of Particle Physics through isotope shift measurements. The Cd beam is also used to demonstrate the efficient loading of a prototype deep UV MOT with more than $1.1(3) \times 10^7$ Cd atoms at a peak density of $2.2(5) \times 10^{11} \text{ cm}^{-3}$. An accumulation scheme is implemented that allows the number of atoms to exceed previous Cd MOTs by more than an order of magnitude. This achievement highlights the potential of using a similar setup for laser cooling of AlF molecules in future studies.

Samenvatting

Laserkoeling van atomen heeft tot weidverbreide toepassingen geleid - van precisionspectroscopie en metrologie tot kwantumcomputing - en heeft geresulteerd in geavanceerde instrumentatie, zoals bijvoorbeeld nauwkeurige atoomklokken. Gedurende de laatste jaren is er ook grote vooruitgang geboekt bij het laserkoelen van moleculen. Moleculen kunnen roteren en vibreren en hebben daardoor een rijke structuur van energieniveaus. Ze kunnen naast een magnetisch dipoolmoment ook een elektrisch dipoolmoment hebben en tezamen maken deze eigenschappen vele nieuwe toepassingen in de fundamentele fysica en de kwantumwetenschap mogelijk. De complexe energie-niveau structuur maakt het echter ook uitdagender om grote dichtheden van koude moleculen door middel van laser-koeling te produceren. Als gevolg hiervan is het aantal moleculen in, en de dichtheid van, koude moleculaire gassen drie tot vier orden van grootte lager dan die van lasergekoelde atomen, en dit beperkt de mogelijke toepassingen.

In dit proefschrift wordt beschreven hoe men deze uitdaging aan kan gaan gebruikmakend van het sterk gebonden, polaire molecuul aluminium-monofluoride (AlF), dat een laserkoelingsovergang heeft in het diepe ultraviolet (UV). Overgangen in het diepe UV zijn bijzonder interessant omdat de optische kracht die door een laserstraal op een atoom of molecuul uitgeoefend kan worden schaalst met $1/\lambda^4$. Vergeleken met optische overgangen in het zichtbare

spectrum, verhoogt dit de maximale snelheid van de deeltjes die nog in een magneto-optische val (“magneto-optical trap”; MOT) ingevangen kan worden en verkleint het de afstand waarop een atomaire of moleculaire straal tot stilstand gebracht kan worden, waardoor een groter aantal deeltjes gevangen kan worden.

Het hoofddoel van dit onderzoek is het opzetten en karakteriseren van een cryogene helium buffergasbundelbron voor AlF-moleculen en het demonstreren van een optische cyclus die gebruikt kan worden voor laserkoeling. Aangetoond wordt dat een buffergasbundel van AlF-moleculen kan worden geproduceerd met een orde van grootte hogere dichtheid dan voor andere diatomaire moleculen mogelijk is en dat de belangrijkste laserkoelingsovergang ($A^1\Pi, v' = 0 \leftarrow X^1\Sigma^+, v'' = 0$) rond 228 nm zeer efficiënt is. Met één enkele laser kunnen zo'n 210 fotonen worden verstrooid met een verstrooiingsfrequentie van $17(2) \times 10^6 \text{ s}^{-1}$, voordat de moleculen verloren gaan naar $v'' = 1$, van waar ze kunnen worden teruggewonnen met een terugpompingslaser. Andere potentiële verlieskanalen uit de optische cyclus, veroorzaakt door fotoïonisatie of door pariteitsmenging in externe elektrische velden, zijn gekarakteriseerd en er is aangegeven hoe deze onder controle kunnen worden gehouden. Ook is gemeten dat het elektronische verval naar de tussenliggende, metastabiele $a^3\Pi$ toestand het efficiënt laden van een MOT niet verhindert.

De elektronische energiestructuur en laser golflengten die nodig zijn voor laserkoeling van AlF zijn zeer vergelijkbaar met die van atomaire cadmium (Cd). Een Cd-bundel kan relatief eenvoudig in dezelfde opstelling worden geproduceerd en is gebruikt om de laseropstelling en de optische componenten te testen en te optimaliseren door hoge resolutie spectroscopische experimenten uit te voeren aan de $^1P_1 \leftarrow ^1S_0$ en $^3P_1 \leftarrow ^1S_0$ overgangen bij, respectievelijk, 229 nm en 326 nm. De resultaten laten zien dat Cd een veelbelovende kandidaat is om door middel van het meten van isotoopverschuivingen te zoeken naar nieuwe

fysica, d.w.z. naar fysica die niet beschreven wordt in het Standaard Model van de deeltjesfysica. De Cd-bundel is ook gebruikt om het efficiënt laden van een prototype diepe UV MOT met meer dan $1,1(3) \times 10^7$ Cd-atomen bij een maximale dichtheid van $2,2(5) \times 10^{11} \text{cm}^{-3}$ aan te tonen. Er is een accumulatieschema geïmplementeerd waarmee het mogelijk is het aantal atomen meer dan een orde van grootte te vergroten t.o.v. eerdere magneto-optische vallen voor Cd. Deze bevindingen aan Cd tonen het potentieel aan van het toekomstige gebruik van dezelfde opstelling voor laserkoeling en opslag van AlF-moleculen.

Bibliography

- [1] M. H. Anderson, J. R. Ensher, M. R. Matthews, C. E. Wieman, and E. A. Cornell. “Observation of Bose-Einstein Condensation in a Dilute Atomic Vapor.” In *Science* **269**(5221), (1995), 198–201. doi:10.1126/science.269.5221.198.
- [2] M. Tomza, K. Jachymski, R. Gerritsma, A. Negretti, T. Calarco, Z. Idziaszek, and P. S. Julienne. “Cold hybrid ion-atom systems.” In *Reviews of Modern Physics* **91**(3), (2019), 035001. doi:10.1103/revmodphys.91.035001.
- [3] D. Gotta. “Precision spectroscopy of light exotic atoms.” In *Progress in Particle and Nuclear Physics* **52**(1), (2004), 133–195. doi:10.1016/j.pnpnp.2003.09.003.
- [4] F. Schäfer, T. Fukuhara, S. Sugawa, Y. Takasu, and Y. Takahashi. “Tools for quantum simulation with ultracold atoms in optical lattices.” In *Nature Reviews Physics* **2**(8), (2020), 411–425. doi:10.1038/s42254-020-0195-3.
- [5] N. Behbood, F. M. Ciurana, G. Colangelo, M. Napolitano, M. W. Mitchell, and R. J. Sewell. “Real-time vector field tracking with a cold-atom magnetometer.” In *Applied Physics Letters* **102**(17), (2013), 173504. doi:10.1063/1.4803684.
- [6] T. Bothwell, C. J. Kennedy, A. Aeppli, D. Kedar, J. M. Robinson, E. Oelker, A. Staron, and J. Ye. “Resolving the gravitational redshift across a millimetre-scale atomic sample.” In *Nature* **602**(7897), (2022), 420–424. doi:10.1038/s41586-021-04349-7.
- [7] Y. Cohen, K. Jadeja, S. Sula, M. Venturelli, C. Deans, L. Marmugi, and F. Renzoni. “A cold atom radio-frequency magnetometer.” In *Applied Physics Letters* **114**(7), (2019), 073505. doi:10.1063/1.5084004.

- [8] M. Snadden, J. McGuirk, P. Bouyer, K. Haritos, and M. Kasevich. “Measurement of the Earth’s Gravity Gradient with an Atom Interferometer-Based Gravity Gradiometer.” In *Physical Review Letters* **81**(5), (1998), 971–974. doi:10.1103/physrevlett.81.971.
- [9] J. B. Fixler, G. T. Foster, J. M. McGuirk, and M. A. Kasevich. “Atom Interferometer Measurement of the Newtonian Constant of Gravity.” In *Science* **315**(5808), (2007), 74–77. doi:10.1126/science.1135459.
- [10] J. M. McGuirk, G. T. Foster, J. B. Fixler, M. J. Snadden, and M. A. Kasevich. “Sensitive absolute-gravity gradiometry using atom interferometry.” In *Physical Review A* **65**(3), (2002), 033608. doi:10.1103/physreva.65.033608.
- [11] H. Bethlem, G. Berden, and G. Meijer. “Decelerating Neutral Dipolar Molecules.” In *Physical Review Letters* **83**(8), (1999), 1558–1561. doi:10.1103/PhysRevLett.83.1558.
- [12] N. Vanhaecke, U. Meier, M. Andrist, B. H. Meier, and F. Merkt. “Multistage Zeeman deceleration of hydrogen atoms.” In *Physical Review A* **75**(3), (2007), 031402. doi:10.1103/PhysRevA.75.031402.
- [13] A. Prehn, M. Ibrügger, R. Glöckner, G. Rempe, and M. Zeppenfeld. “Optoelectrical Cooling of Polar Molecules to Submillikelvin Temperatures.” In *Physical Review Letters* **116**(6), (2016), 63005. doi:10.1103/PhysRevLett.116.063005.
- [14] N. Bigagli, D. W. Savin, and S. Will. “Laser Scheme for Doppler Cooling of the Hydroxyl Cation (OH+).” In *The Journal of Physical Chemistry A* **127**(39), (2023), 8194–8199. doi:10.1021/acs.jpca.3c03248. PMID: 37738380.
- [15] M. Nötzold, R. Wild, C. Lochmann, and R. Wester. “Spectroscopy and ion thermometry of C_2^- using laser-cooling transitions.” In *Physical Review A* **106**, (2022), 023111. doi:10.1103/PhysRevA.106.023111.
- [16] “SI base unit: second (s) at the bureau international des poids et mesures BIPM.” <https://www.bipm.org/en/si-base-units/second>. [Accessed 21-10-2023].
- [17] G. Barontini, L. Blackburn, V. Boyer, F. Butuc-Mayer, X. Calmet, J. R. C. López-Urrutia, E. A. Curtis, B. Darquié, J. Dunningham, N. J.

- Fitch, E. M. Forgan, K. Georgiou, P. Gill, R. M. Godun, J. Goldwin, V. Guarrera, A. C. Harwood, I. R. Hill, R. J. Hendricks, M. Jeong, M. Y. H. Johnson, M. Keller, L. P. K. Sajith, F. Kuipers, H. S. Margolis, C. Mayo, P. Newman, A. O. Parsons, L. Prokhorov, B. I. Robertson, J. Rodewald, M. S. Safronova, B. E. Sauer, M. Schioppo, N. Sherrill, Y. V. Stadnik, K. Szymaniec, M. R. Tarbutt, R. C. Thompson, A. Tofful, J. Tunesi, A. Vecchio, Y. Wang, and S. Worm. “Measuring the stability of fundamental constants with a network of clocks.” In *EPJ Quantum Technology* **9**(1), (2022), 12. doi:10.1140/epjqt/s40507-022-00130-5.
- [18] A. M. Kaufman and K.-K. Ni. “Quantum science with optical tweezer arrays of ultracold atoms and molecules.” In *Nature Physics* **17**(12), (2021), 1324–1333. doi:10.1038/s41567-021-01357-2.
- [19] L. Henriot, L. Beguin, A. Signoles, T. Lahaye, A. Browaeys, G.-O. Raymond, and C. Jurczak. “Quantum computing with neutral atoms.” In *Quantum* **4**, (2020), 327. doi:10.22331/q-2020-09-21-327.
- [20] J. A. Blackmore, L. Caldwell, P. D. Gregory, E. M. Bridge, R. Sawant, J. Aldegunde, J. Mur-Petit, D. Jaksch, J. M. Hutson, B. E. Sauer, M. R. Tarbutt, and S. L. Cornish. “Ultracold molecules for quantum simulation: rotational coherences in CaF and RbCs.” In *Quantum Science and Technology* **4**(1), (2018), 014010. doi:10.1088/2058-9565/aaee35.
- [21] The ACME collaboration, J. Baron, W. C. Campbell, D. DeMille, J. M. Doyle, G. Gabrielse, Y. V. Gurevich, P. W. Hess, N. R. Hutzler, E. Kirilov, I. Kozyryev, B. R. O’Leary, C. D. Panda, M. F. Parsons, E. S. Petrik, B. Spaun, A. C. Vutha, and A. D. West. “Order of Magnitude Smaller Limit on the Electric Dipole Moment of the Electron.” In *Science* **343**(6168), (2014), 269–272. doi:10.1126/science.1248213.
- [22] D. M. Kara, I. J. Smallman, J. J. Hudson, B. E. Sauer, M. R. Tarbutt, and E. A. Hinds. “Measurement of the electron’s electric dipole moment using YbF molecules: methods and data analysis.” In *New Journal of Physics* **14**(10), (2012), 103051. doi:10.1088/1367-2630/14/10/103051.
- [23] W. B. Cairncross, D. N. Gresh, M. Grau, K. C. Cossel, T. S. Roussy, Y. Ni, Y. Zhou, J. Ye, and E. A. Cornell. “Precision Measurement of the Electron’s Electric Dipole Moment Using Trapped Molecular Ions.” In *Physical Review Letters* **119**(15), (2017), 153001. doi:10.1103/physrevlett.119.153001.

- [24] T. S. Roussy, L. Caldwell, T. Wright, W. B. Cairncross, Y. Shagam, K. B. Ng, N. Schlossberger, S. Y. Park, A. Wang, J. Ye, and E. A. Cornell. “An improved bound on the electrons electric dipole moment.” In *Science* **381**(6653), (2023), 46–50. doi:10.1126/science.adg4084.
- [25] J. Cernicharo and M. Guélin. “Metals in IRC+ 10216-Detection of NaCl, AlCl, and KCl, and tentative detection of AlF.” In *Astronomy and Astrophysics* **183**, (1987), L10–L12.
- [26] L. Ziurys, A. Apponi, and T. Phillips. “Exotic fluoride molecules in IRC+ 10216: confirmation of AlF and searches for MgF and CaF.” In *The Astrophysical Journal* **433**, (1994), 729–732. doi:10.1086/174682.
- [27] M. Agúndez, J. Fonfría, J. Cernicharo, C. Kahane, F. Daniel, and M. Guélin. “Molecular abundances in the inner layers of IRC+ 10216.” In *Astronomy & Astrophysics* **543**, (2012), A48. doi:10.1051/0004-6361/201218963.
- [28] J. Highberger, C. Savage, J. Biegging, and L. Ziurys. “Heavy-metal chemistry in proto-planetary nebulae: Detection of MgNC, NaCN, and AlF toward CRL 2688.” In *The Astrophysical Journal* **562**(2), (2001), 790. doi:10.1086/323231.
- [29] M. Saberi, T. Khouri, L. Velilla-Prieto, J. P. Fonfría, W. H. T. Vlemmings, and S. Wedemeyer. “First detection of AlF line emission towards M-type AGB stars.” In *Astronomy and Astrophysics* **663**, (2022), A54. doi:10.1051/0004-6361/202141704.
- [30] T. Kamiński, R. Tyllenda, K. M. Menten, A. Karakas, J. M. Winters, A. A. Breier, K. T. Wong, T. F. Giesen, and N. A. Patel. “Astronomical detection of radioactive molecule ^{26}AlF in the remnant of an ancient explosion.” In *Nature Astronomy* **2**(10), (2018), 778–783. doi:10.1038/s41550-018-0541-x.
- [31] I. Estermann, R. Frisch, and O. Stern. “Magnetic Moment of the Proton.” In *Nature* **132**(3326), (1933), 169–170. doi:10.1038/132169a0.
- [32] O. Frisch. *What little I remember*. Cambridge University Press (1979). ISBN 9780521222976.
- [33] R. Frisch. “Experimenteller Nachweis des Einsteinschen Strahlungsrückstoßes.” In *Zeitschrift für Physik* **86**(1), (1933), 42–48. doi:10.1007/BF01340182.

- [34] K. B. Davis, M. O. Mewes, M. R. Andrews, N. J. van Druten, D. S. Durfee, D. M. Kurn, and W. Ketterle. “Bose-Einstein Condensation in a Gas of Sodium Atoms.” In *Physical Review Letters* **75**(22), (1995), 3969–3973. doi:10.1103/physrevlett.75.3969.
- [35] J.-L. Picqué and J.-L. Vialle. “Atomic-beam deflection and broadening by recoils due to photon absorption or emission.” In *Optics Communications* **5**(5), (1972), 402–406. doi:10.1016/0030-4018(72)90043-0.
- [36] J. E. Bjorkholm, R. R. Freeman, A. Ashkin, and D. B. Pearson. “Experimental observation of the influence of the quantum fluctuations of resonance-radiation pressure.” In *Optics Letters* **5**(3), (1980), 111–113. doi:10.1364/OL.5.000111.
- [37] E. S. Shuman, J. F. Barry, D. R. Glenn, and D. Demille. “Radiative force from optical cycling on a diatomic molecule.” In *Physical Review Letters* **103**(22), (2009), 223001. doi:10.1103/PhysRevLett.103.223001.
- [38] T. Chen, W. Bu, and B. Yan. “Radiative deflection of a BaF molecular beam via optical cycling.” In *Physical Review A* **96**(5), (2017), 053401. doi:10.1103/PhysRevA.96.053401.
- [39] R. L. McNally, I. Kozyryev, S. Vazquez-Carson, K. Wenz, T. Wang, and T. Zelevinsky. “Optical cycling, radiative deflection and laser cooling of barium monohydride ($^{138}\text{Ba}^1\text{H}$).” In *New Journal of Physics* **22**(8), (2020), 083047. doi:10.1088/1367-2630/aba3e9.
- [40] A. Ashkin. “Atomic-Beam Deflection by Resonance-Radiation Pressure.” In *Physical Review Letters* **25**(19), (1970), 1321–1324. doi:10.1103/physrevlett.25.1321.
- [41] T. Hänsch and A. Schawlow. “Cooling of gases by laser radiation.” In *Optics Communications* **13**(1), (1975), 68–69. doi:10.1016/0030-4018(75)90159-5.
- [42] D. Wineland and H. Dehmelt. “Proposed $10^{14} \Delta\nu < \nu$ laser fluorescence spectroscopy on Tl^+ mono-ion oscillator III.” In **20**, (1975), 637. <https://tf.nist.gov/general/pdf/2208.pdf>.
- [43] S. Chu, L. Hollberg, J. E. Bjorkholm, A. Cable, and A. Ashkin. “Three-dimensional viscous confinement and cooling of atoms by resonance radiation pressure.” In *Physical Review Letters* **55**(1), (1985), 48–51. doi:10.1103/physrevlett.55.48.

- [44] E. S. Shuman, J. F. Barry, and D. DeMille. “Laser cooling of a diatomic molecule.” In *Nature* **467**(7317), (2010), 820–823. doi:10.1038/nature09443.
- [45] J. F. Barry, D. J. McCarron, E. B. Norrgard, M. H. Steinecker, and D. DeMille. “Magneto-optical trapping of a diatomic molecule.” In *Nature* **512**(7514), (2014), 286–289. doi:10.1038/nature13634.
- [46] V. Zhelyazkova, A. Cournol, T. E. Wall, A. Matsushima, J. J. Hudson, E. A. Hinds, M. R. Tarbutt, and B. E. Sauer. “Laser cooling and slowing of CaF molecules.” In *Physical Review A* **89**(5), (2014), 053416. doi:10.1103/physreva.89.053416.
- [47] S. Truppe, H. J. Williams, M. Hambach, L. Caldwell, N. J. Fitch, E. A. Hinds, B. E. Sauer, and M. R. Tarbutt. “Molecules cooled below the Doppler limit.” In *Nature Physics* **13**(12), (2017), 1173–1176. doi:10.1038/nphys4241.
- [48] A. L. Collopy, S. Ding, Y. Wu, I. A. Finneran, L. Anderegg, B. L. Augenbraun, J. M. Doyle, and J. Ye. “3D Magneto-Optical Trap of Yttrium Monoxide.” In *Physical Review Letters* **121**(21), (2018), 213201. doi:10.1103/physrevlett.121.213201.
- [49] J. Lim, J. Almond, M. Trigatzis, J. Devlin, N. Fitch, B. Sauer, M. Tarbutt, and E. Hinds. “Laser Cooled YbF Molecules for Measuring the Electron’s Electric Dipole Moment.” In *Physical Review Letters* **120**(12), (2018), 123201. doi:10.1103/physrevlett.120.123201.
- [50] S. F. Vázquez-Carson, Q. Sun, J. Dai, D. Mitra, and T. Zelevinsky. “Direct laser cooling of calcium monohydride molecules.” In *New Journal of Physics* **24**(8), (2022), 083006. doi:10.1088/1367-2630/ac806c.
- [51] Y. Zhang, Z. Zeng, Q. Liang, W. Bu, and B. Yan. “Doppler cooling of buffer-gas-cooled barium monofluoride molecules.” In *Physical Review A* **105**(3), (2022), 033307. doi:10.1103/physreva.105.033307.
- [52] E. B. Norrgard, E. R. Edwards, D. J. McCarron, M. H. Steinecker, D. DeMille, S. S. Alam, S. K. Peck, N. S. Wadia, and L. R. Hunter. “Hyperfine structure of the $B^3\Pi_1$ state and predictions of optical cycling behavior in the $X \rightarrow B$ transition of TlF.” In *Physical Review A* **95**, (2017), 062506. doi:10.1103/PhysRevA.95.062506.

- [53] J. R. Daniel, C. Wang, K. Rodriguez, B. Hemmerling, T. N. Lewis, C. Bardeen, A. Teplukhin, and B. K. Kendrick. “Spectroscopy on the $A^1\Pi \leftarrow X^1\Sigma^+$ transition of buffer-gas-cooled AlCl.” In *Physical Review A* **104**, (2021), 012801. doi:10.1103/PhysRevA.104.012801.
- [54] J. C. Shaw, S. Hannig, and D. J. McCarron. “Stable 2 W continuous-wave 261.5 nm laser for cooling and trapping aluminum monochloride.” In *Optics Express* **29**(23), (2021), 37140–37149. doi:10.1364/OE.441741.
- [55] J. Schnaubelt, J. Shaw, and D. McCarron. “Cold CH radicals for laser cooling and trapping.” In *arXiv preprint arXiv:2109.03953* .
- [56] R. Gu, K. Yan, D. Wu, J. Wei, Y. Xia, and J. Yin. “Radiative force from optical cycling on magnesium monofluoride.” In *Physical Review A* **105**, (2022), 042806. doi:10.1103/PhysRevA.105.042806.
- [57] E. B. Norrgard, Y. Chamorro, C. C. Cooksey, S. P. Eckel, N. H. Pilgram, K. J. Rodriguez, H. W. Yoon, L. c. v. F. Pařteka, and A. Borschevsky. “Radiative decay rate and branching fractions of MgF.” In *Physical Review A* **108**, (2023), 032809. doi:10.1103/PhysRevA.108.032809.
- [58] I. Kozyryev and N. R. Hutzler. “Precision Measurement of Time-Reversal Symmetry Violation with Laser-Cooled Polyatomic Molecules.” In *Physical Review Letters* **119**, (2017), 133002. doi:10.1103/PhysRevLett.119.133002.
- [59] B. L. Augenbraun, Z. D. Lasner, A. Frenett, H. Sawaoka, C. Miller, T. C. Steimle, and J. M. Doyle. “Laser-cooled polyatomic molecules for improved electron electric dipole moment searches.” In *New Journal of Physics* **22**(2), (2020), 022003. doi:10.1088/1367-2630/ab687b.
- [60] D. Mitra, N. B. Vilas, C. Hallas, L. Anderegg, B. L. Augenbraun, L. Baum, C. Miller, S. Raval, and J. M. Doyle. “Direct laser cooling of a symmetric top molecule.” In *Science* **369**(6509), (2020), 1366–1369. doi:10.1126/science.abc5357.
- [61] N. B. Vilas, C. Hallas, L. Anderegg, P. Robichaud, A. Winnicki, D. Mitra, and J. M. Doyle. “Magneto-optical trapping and sub-Doppler cooling of a polyatomic molecule.” In *Nature* **606**(7912), (2022), 70–74. doi:10.1038/s41586-022-04620-5.

- [62] L. Anderegg, B. L. Augenbraun, Y. Bao, S. Burchesky, L. W. Cheuk, W. Ketterle, and J. M. Doyle. “Laser cooling of optically trapped molecules.” In *Nature Physics* **14**(9), (2018), 890–893. doi:10.1038/s41567-018-0191-z.
- [63] L. Anderegg, L. W. Cheuk, Y. Bao, S. Burchesky, W. Ketterle, K. Ni, and J. M. Doyle. “An optical tweezer array of ultracold molecules.” In *Science* **365**(6458), (2019), 1156–1158. doi:10.1126/science.aax1265.
- [64] H. J. Williams, L. Caldwell, N. J. Fitch, S. Truppe, J. Rodewald, E. A. Hinds, B. E. Sauer, and M. R. Tarbutt. “Magnetic Trapping and Coherent Control of Laser-Cooled Molecules.” In *Physical Review Letters* **120**(16), (2018), 163201. doi:10.1103/PhysRevLett.120.163201.
- [65] D. J. McCarron, M. H. Steinecker, Y. Zhu, and D. DeMille. “Magnetic Trapping of an Ultracold Gas of Polar Molecules.” In *Physical Review Letters* **121**(1), (2018), 013202. doi:10.1103/PhysRevLett.121.013202.
- [66] L. W. Cheuk, L. Anderegg, Y. Bao, S. Burchesky, S. S. Yu, W. Ketterle, K.-K. Ni, and J. M. Doyle. “Observation of Collisions between Two Ultracold Ground-State CaF Molecules.” In *Physical Review Letters* **125**(4), (2020), 043401. doi:10.1103/PhysRevLett.125.043401.
- [67] L. Caldwell, H. J. Williams, N. J. Fitch, J. Aldegunde, J. M. Hutson, B. E. Sauer, and M. R. Tarbutt. “Long Rotational Coherence Times of Molecules in a Magnetic Trap.” In *Physical Review Letters* **124**(6), (2020), 063001. doi:10.1103/PhysRevLett.124.063001.
- [68] C. M. Holland, Y. Lu, and L. W. Cheuk. “On-Demand Entanglement of Molecules in a Reconfigurable Optical Tweezer Array.” (2022). doi:10.48550/ARXIV.2210.06309.
- [69] J. T. Bahns, W. C. Stwalley, and P. L. Gould. “Laser cooling of molecules: A sequential scheme for rotation, translation, and vibration.” In *The Journal of Chemical Physics* **104**(24), (1996), 9689–9697. doi:10.1063/1.471731.
- [70] S. C. Wright, M. Doppelbauer, S. Hofsäss, H. C. Schewe, B. Sartakov, G. Meijer, and S. Truppe. “Cryogenic buffer gas beams of AlF, CaF, MgF, YbF, Al, Ca, Yb and NO – a comparison.” In *Molecular Physics* (Wim Ubachs Festschrift), (2022), e2146541. doi:10.1080/00268976.2022.2146541.

- [71] X. Liu, S. Truppe, G. Meijer, and J. Pérez-Ríos. “The diatomic molecular spectroscopy database.” In *Journal of Cheminformatics* **12**(1), (2020), 1–8. doi:10.1186/s13321-020-00433-8.
- [72] S. Truppe, S. Marx, S. Kray, M. Doppelbauer, S. Hofsäss, H. C. Schewe, N. Walter, J. Pérez-Ríos, B. G. Sartakov, and G. Meijer. “Spectroscopic characterization of aluminum monofluoride with relevance to laser cooling and trapping.” In *Physical Review A* **100**, (2019), 052513. doi:10.1103/PhysRevA.100.052513.
- [73] D. R. Crosley and W. R. Anderson. “Laser Excitation of Fluorescence in the A-X System of NH.” Tech. Rep., Army Ballistic Research Laboratory Aberdeen Proving Ground, MD (1980).
- [74] B. Ohayon, S. Hofsäss, J. E. Padilla-Castillo, S. C. Wright, G. Meijer, S. Truppe, K. Gibble, and B. K. Sahoo. “Isotope shifts in cadmium as a sensitive probe for physics beyond the standard model.” In *New Journal of Physics* **24**(12), (2022), 123040. doi:10.1088/1367-2630/acacbb.
- [75] V. A. Dzuba and A. Derevianko. “Blackbody radiation shift for the optical clock transition in zinc and cadmium atoms.” In *Journal of Physics B: Atomic, Molecular and Optical Physics* **52**(21), (2019), 215005. doi:10.1088/1361-6455/ab4434.
- [76] W. F. McGrew, X. Zhang, R. J. Fasano, S. A. Schäffer, K. Beloy, D. Nicolodi, R. C. Brown, N. Hinkley, G. Milani, M. Schioppo, T. H. Yoon, and A. D. Ludlow. “Atomic clock performance enabling geodesy below the centimetre level.” In *Nature* **564**(7734), (2018), 87–90. doi:10.1038/s41586-018-0738-2.
- [77] T. Bothwell, D. Kedar, E. Oelker, J. M. Robinson, S. L. Bromley, W. L. Tew, J. Ye, and C. J. Kennedy. “JILA SrI optical lattice clock with uncertainty of 2.0×10^{-18} .” In *Metrologia* **56**(6), (2019), 065004. doi:10.1088/1681-7575/ab4089.
- [78] Y. Hisai, D. Akamatsu, T. Kobayashi, K. Hosaka, H. Inaba, F.-L. Hong, and M. Yasuda. “Improved frequency ratio measurement with ^{87}Sr and ^{171}Yb optical lattice clocks at NMIJ.” In *Metrologia* **58**(1), (2021), 015008. doi:10.1088/1681-7575/abc104.
- [79] S. Hofsäss, M. Doppelbauer, S. Wright, S. Kray, B. Sartakov, J. Pérez-Ríos, G. Meijer, and S. Truppe. “Optical cycling of AlF molecules.”

- In *New Journal of Physics* **23**(7), (2021), 075001. doi:10.1088/1367-2630/ac06e5.
- [80] M. D. Di Rosa. “Laser-cooling molecules.” In *The European Physical Journal D* **31**(2), (2004), 395–402. doi:10.1140/epjd/e2004-00167-2.
- [81] P. W. Atkins and R. S. Friedman. *Molecular quantum mechanics*. Oxford University Press (2011).
- [82] A. E. van Arkel. *Molecules and Crystals in Inorganic Chemistry*. New York: Interscience Publishers (1956).
- [83] L. Pauling. *The nature of the chemical bond and the structure of molecules and crystals: an introduction to modern structural chemistry (3rd ed.)*. Ithaca, N. Y.: Cornell University Press (1986).
- [84] P. Mori-Sánchez, A. M. Pendás, and V. Luaña. “A classification of covalent, ionic, and metallic solids based on the electron density.” In *Journal of the American Chemical Society* **124**(49), (2002), 14721–14723. doi:10.1021/ja027708t.
- [85] T. L. Meek and L. D. Garner. “Electronegativity and the bond triangle.” In *Journal of Chemical Education* **82**(2), (2005), 325. doi:10.1021/ed082p325.
- [86] S. Hou and P. F. Bernath. “Relationship between dipole moments and harmonic vibrational frequencies in diatomic molecules.” In *The Journal of Physical Chemistry A* **119**(8), (2015), 1435–1438. doi:/10.1021/acs.jpca.5b00993.
- [87] J. V. Pototschnig, A. W. Hauser, and W. E. Ernst. “Electric dipole moments and chemical bonding of diatomic alkali–alkaline earth molecules.” In *Physical Chemistry Chemical Physics* **18**(8), (2016), 5964–5973. doi:10.1039/C5CP06598D.
- [88] D. V. Dearden, R. D. Johnson, and J. W. Hudgens. “New Rydberg states of aluminum monofluoride observed by resonance-enhanced multiphoton ionization spectroscopy.” In *The Journal of Physical Chemistry* **95**(11), (1991), 4291–4296. doi:10.1021/j100164a022.
- [89] S. P. So and W. G. Richards. “A theoretical study of the excited electronic states of AlF.” In *Journal of Physics B: Atomic and Molecular Physics* **7**(14), (1974), 1973–1980. doi:10.1088/0022-3700/7/14/021.

- [90] R. F. Barrow, I. Kopp, and C. Malmberg. “The Electronic Spectrum of Gaseous AlF.” In *Physica Scripta* **10**(1-2), (1974), 86–102. doi:10.1088/0031-8949/10/1-2/008.
- [91] M. Yousefi and P. F. Bernath. “Line Lists for AlF and AlCl in the $X^1\Sigma^+$ Ground State.” In *The Astrophysical Journal Supplement Series* **237**(1), (2018), 8. doi:10.3847/1538-4365/aacc6a.
- [92] H.-J. Werner, P. J. Knowles, G. Knizia, F. R. Manby, M. Schütz, P. Celani, W. Györfy, D. Kats, T. Korona, R. Lindh, A. Mitrushenkov, G. Rauhut, K. R. Shamasundar, T. B. Adler, R. D. Amos, S. J. Bennie, A. Bernhardsson, A. Berning, D. L. Cooper, M. J. O. Deegan, A. J. Dobyn, F. Eckert, E. Goll, C. Hampel, A. Hesselmann, G. Hetzer, T. Hrenar, G. Jansen, C. Köppl, S. J. R. Lee, Y. Liu, A. W. Lloyd, Q. Ma, R. A. Mata, A. J. May, S. J. McNicholas, W. Meyer, T. F. Miller III, M. E. Mura, A. Nicklass, D. P. O’Neill, P. Palmieri, D. Peng, K. Pflüger, R. Pitzer, M. Reiher, T. Shiozaki, H. Stoll, A. J. Stone, R. Tarroni, T. Thorsteinsson, M. Wang, and M. Welborn. “MOLPRO, version 2019.2, a package of ab initio programs.” (2019).
- [93] K. L. Schuchardt, B. T. Didier, T. Elsethagen, L. Sun, V. Gurumoorthi, J. Chase, J. Li, and T. L. Windus. “Basis Set Exchange: A Community Database for Computational Sciences.” In *Journal of Chemical Information and Modeling* **47**(3), (2007), 1045–1052. doi:10.1021/ci600510j.
- [94] M. V. Ivanov, F. H. Bangerter, and A. I. Krylov. “Towards a rational design of laser-coolable molecules: insights from equation-of-motion coupled-cluster calculations.” In *Physical Chemistry Chemical Physics* **21**(35), (2019), 19447–19457. doi:10.1039/C9CP03914G.
- [95] G. D. Rochester. “The Absorption Spectrum of Aluminum Fluoride (AlF).” In *Physical Review* **56**(4), (1939), 305–307. doi:10.1103/PhysRev.56.305.
- [96] H. C. Rowlinson and R. F. Barrow. “The Band-Spectrum of Aluminium Monofluoride.” In *Proceedings of the Physical Society. Section A* **66**(5), (1953), 437–446. doi:10.1088/0370-1298/66/5/303.
- [97] S. M. Naudé and T. J. Hugo. “The Emission Spectrum of Aluminum Monofluoride.” In *Physical Review* **90**(2), (1953), 318–318. doi:10.1103/PhysRev.90.318.

- [98] S. M. Naudé and T. J. Hugo. “The Emission Sepctrum of Aluminum Monofluoride I.” In *Canadian Journal of Physics* **31**(7), (1953), 1106–1114. doi:10.1139/p53-095.
- [99] S. M. Naudé and T. J. Hugo. “The Emission Sepctrum of Aluminum Monofluoride II.” In *Canadian Journal of Physics* **32**(3), (1954), 246–258. doi:10.1139/p54-023.
- [100] S. Rosenwaks, R. E. Steele, and H. P. Broida. “Observation of a $^3\Pi - X^1\Sigma$ intercombination emission in AlF.” In *Chemical Physics Letters* **38**(1), (1976), 121–124. doi:10.1016/0009-2614(76)80270-9.
- [101] I. Kopp, B. Lindgren, and C. Malmberg. “Rotational Analysis of the $a^3\Pi - X^1\Sigma^+$ Transition of AlF.” In *Physica Scripta* **14**(4), (1976), 170–174. doi:10.1088/0031-8949/14/4/008.
- [102] D. R. Lide. “Microwave Spectrum of Aluminum Monofluoride.” In *The Journal of Chemical Physics* **38**(8), (1963), 2027. doi:10.1063/1.1733914.
- [103] F. C. Wyse, W. Gordy, and E. F. Pearson. “Millimeter and Submillimeter Wave Spectrum and Molecular Constants of Aluminum Monofluoride.” In *The Journal of Chemical Physics* **52**(8), (1970), 3887–3889. doi:10.1063/1.1673587.
- [104] J. Hoeft, F. J. Lovas, E. Tiemann, and T. Törring. “Microwave Absorption Spectra of AlF, GaF, InF, and TlF.” In *Zeitschrift für Naturforschung A* **25**(7), (1970), 1029–1035. doi:10.1515/zna-1970-0706.
- [105] R. Honerjäger and R. Tischer. “Zeeman-Effekt im Mikrowellenrotationsspektrum der AlF-Molekel / Zeeman Effect in the Microwave Rotational Spectrum of the AlF Molecule.” In *Zeitschrift für Naturforschung A* **29**(2), (1974), 342–345. doi:10.1515/zna-1974-0224.
- [106] H. Lefebvre-Brion and R. Field. *The Spectra and Dynamics of Diatomic Molecules: Revised and Enlarged Edition*. Elsevier Science (2004). ISBN 9780080517506.
- [107] J. M. Hollas. *Modern spectroscopy*. John Wiley & Sons (2004).
- [108] B. K. Stuhl, B. C. Sawyer, D. Wang, and J. Ye. “Magneto-optical Trap for Polar Molecules.” In *Physical Review Letters* **101**(24), (2008), 243002. doi:10.1103/PhysRevLett.101.243002.

- [109] J. Brown, J. Hougen, K.-P. Huber, J. Johns, I. Kopp, H. Lefebvre-Brion, A. Merer, D. Ramsay, J. Rostas, and R. Zare. “The labeling of parity doublet levels in linear molecules.” In *Journal of Molecular Spectroscopy* **55**(1-3), (1975), 500–503. doi:10.1016/0022-2852(75)90291-X.
- [110] J. M. Brown and A. Carrington. *Rotational Spectroscopy of Diatomic Molecules*. Cambridge University Press (2003). doi:10.1017/cbo9780511814808.
- [111] X. Liu, W. Wang, S. C. Wright, M. Doppelbauer, G. Meijer, S. Truppe, and J. Pérez-Ríos. “The chemistry of AlF and CaF production in buffer gas sources.” In *The Journal of Chemical Physics* **157**(7), (2022), 074305. doi:10.1063/5.0098378.
- [112] J. K. Parker, N. L. Garland, and H. H. Nelson. “Kinetics of the Reaction Al + SF₆ in the Temperature Range 499–813 K.” In *The Journal of Physical Chemistry A* **106**(2), (2001), 307–311. doi:10.1021/jp012895n.
- [113] G. Tomassetti and G. Sanna. *Introduction to molecular beams gas dynamics*. World Scientific (2005).
- [114] M. D. Morse. “Supersonic beam sources.” In *Experimental methods in the physical sciences* **29**, (1996), 21–47.
- [115] G. Scoles. *Atomic and Molecular Beam Methods, Vol 1*. Oxford University Press (1988).
- [116] S. Y. T. van de Meerakker, H. L. Bethlem, N. Vanhaecke, and G. Meijer. “Manipulation and Control of Molecular Beams.” In *Chemical Reviews* **112**(9), (2012), 4828–4878. doi:10.1021/cr200349r.
- [117] H. Metcalf and P. van der Straten. “Cooling and trapping of neutral atoms.” In *Physics reports* **244**(4-5), (1994), 203–286. doi:10.1016/0370-1573(94)90035-3.
- [118] J. C. Shaw and D. J. McCarron. “Bright, continuous beams of cold free radicals.” In *Physical Review A* **102**(4), (2020), 041302. doi:10.1103/PhysRevA.102.041302.
- [119] F. G. Major and H. G. Dehmelt. “Exchange-Collision Technique for the rf Spectroscopy of Stored Ions.” In *Physical Review* **170**(1), (1968), 91–107. doi:10.1103/physrev.170.91.

- [120] D. Patterson and J. M. Doyle. “Bright, guided molecular beam with hydrodynamic enhancement.” In *Journal of Chemical Physics* **126**(15), (2007), 154307. doi:10.1063/1.2717178.
- [121] H.-I. Lu, J. Rasmussen, M. J. Wright, D. Patterson, and J. M. Doyle. “A cold and slow molecular beam.” In *Physical Chemistry Chemical Physics* **13**(42), (2011), 18986. doi:10.1039/c1cp21206k.
- [122] S. E. Maxwell, N. Brahm, R. Decarvalho, D. R. Glenn, J. S. Helton, S. V. Nguyen, D. Patterson, J. Petricka, D. Demille, and J. M. Doyle. “High-flux beam source for cold, slow atoms or molecules.” In *Physical Review Letters* **95**(17), (2005), 173201. doi:10.1103/PhysRevLett.95.173201.
- [123] J. F. Barry, E. S. Shuman, and D. DeMille. “A bright, slow cryogenic molecular beam source for free radicals.” In *Physical Chemistry Chemical Physics* **13**(42), (2011), 18936. doi:10.1039/c1cp20335e.
- [124] N. R. Hutzler, H.-I. Lu, and J. M. Doyle. “The Buffer Gas Beam: An Intense, Cold, and Slow Source for Atoms and Molecules.” In *Chemical Reviews* **112**(9), (2012), 4803–4827. doi:10.1021/cr200362u.
- [125] M. Karra, M. T. Cretu, B. Friedrich, S. Truppe, G. Meijer, and J. Pérez-Ríos. “Dynamics of translational and rotational thermalization of AlF molecules via collisions with cryogenic helium.” In *Physical Review A* **105**, (2022), 022808. doi:10.1103/PhysRevA.105.022808.
- [126] D. Budker, D. Kimball, and D. DeMille. *Atomic physics: An exploration through problems and solutions*. Oxford University Press (2008). ISBN 9780199532414.
- [127] G. Z. Iwata. *A Cryogenic Buffer-Gas Cooled Beam of Barium Monohydride for Laser Slowing, Cooling, and Trapping*. Ph.D. thesis, Columbia University (2018).
- [128] M. Doppelbauer, N. Walter, S. Hofsäss, S. Marx, H. C. Schewe, S. Kray, J. Pérez-Ríos, B. G. Sartakov, S. Truppe, and G. Meijer. “Characterisation of the $b^3\Sigma^+, v = 0$ state and its interaction with the $A^1\Pi$ state in aluminium monofluoride.” In *Molecular Physics* **119**, (2020), e1810351. doi:10.1080/00268976.2020.1810351.
- [129] N. Radwell, G. Walker, and S. Franke-Arnold. “Cold-atom densities of more than 10^{12} cm^{-3} in a holographically shaped dark

- spontaneous-force optical trap.” In *Physical Review A* **88**, (2013), 043409. doi:10.1103/PhysRevA.88.043409.
- [130] L. Anderegg, B. L. Augenbraun, E. Chae, B. Hemmerling, N. R. Hutzler, A. Ravi, A. Collopy, J. Ye, W. Ketterle, and J. M. Doyle. “Radio Frequency Magneto-Optical Trapping of CaF with High Density.” In *Physical Review Letters* **119**(10), (2017), 103201. doi:10.1103/PhysRevLett.119.103201.
- [131] M. Petzold, P. Kaebert, P. Gersema, M. Siercke, and S. Ospelkaus. “A Zeeman slower for diatomic molecules.” In *New Journal of Physics* **20**(4), (2018), 042001. doi:10.1088/1367-2630/aab9f5.
- [132] P. Kaebert, M. Stepanova, T. Poll, M. Petzold, S. Xu, M. Siercke, and S. Ospelkaus. “Characterizing the Zeeman slowing force for $40\text{Ca}19\text{F}$ molecules.” In *New Journal of Physics* **23**(9), (2021), 093013. doi:10.1088/1367-2630/ac1ed7.
- [133] Z. Lasner, D. Mitra, M. Hiradfar, B. Augenbraun, L. Cheuk, E. Lee, S. Prabhu, and J. Doyle. “Fast and high-yield loading of a D_2 magneto-optical trap of potassium from a cryogenic buffer-gas beam.” In *Physical Review A* **104**(6), (2021), 063305. doi:10.1103/PhysRevA.104.063305.
- [134] B. Hemmerling, E. Chae, A. Ravi, L. Anderegg, G. K. Drayna, N. R. Hutzler, A. L. Collopy, J. Ye, W. Ketterle, and J. M. Doyle. “Laser slowing of CaF molecules to near the capture velocity of a molecular MOT.” In *Journal of Physics B: Atomic, Molecular and Optical Physics* **49**(17), (2016), 174001. doi:10.1088/0953-4075/49/17/174001.
- [135] S. Xu, P. Kaebert, M. Stepanova, T. Poll, M. Siercke, and S. Ospelkaus. “Maximizing the capture velocity of molecular magneto-optical traps with Bayesian optimization.” In *New Journal of Physics* **23**(6), (2021), 063062. doi:10.1088/1367-2630/ac06e6.
- [136] I. Kovács. *Rotational structure in the spectra of diatomic molecules*. Akadémiai Kiadó Budapest (1969).
- [137] A. Hansson and J. K. Watson. “A comment on Hönl-London factors.” In *Journal of Molecular Spectroscopy* **233**(2), (2005), 169–173. doi:10.1016/j.jms.2005.06.009.

- [138] M. R. Tarbutt, J. J. Hudson, B. E. Sauer, and E. A. Hinds. “Preparation and manipulation of molecules for fundamental physics tests.” In *Cold Molecules*, pp. 587–628. CRC Press (2009). ISBN 9780429149504.
- [139] R. J. Le Roy. “LEVEL: A computer program for solving the radial Schrödinger equation for bound and quasibound levels.” In *Journal of Quantitative Spectroscopy and Radiative Transfer* **186**, (2017), 167–178. doi:10.1016/j.jqsrt.2016.05.028.
- [140] N. Wells and I. C. Lane. “Electronic states and spin-forbidden cooling transitions of AlH and AlF.” In *Physical Chemistry Chemical Physics* **13**(42), (2011), 19018. doi:10.1039/c1cp21313j.
- [141] N. L. Garland and D. R. Crosley. “Relative transition probability measurements in the A-X and B-X systems of CH.” In *Journal of Quantitative Spectroscopy and Radiative Transfer* **33**(6), (1985), 591–595. doi:10.1016/0022-4073(85)90026-3.
- [142] M. J. Doppelbauer. *The AlF Molecule as a Candidate for Laser Cooling and Trapping*. Ph.D. thesis, Radboud University (2022).
- [143] N. Walter, J. Seifert, S. Truppe, H. C. Schewe, B. G. Sartakov, and G. Meijer. “Spectroscopic characterization of singlet–triplet doorway states of aluminum monofluoride.” In *The Journal of Chemical Physics* **156**(18), (2022), 184301. doi:10.1063/5.0088288.
- [144] K. Fehre, D. Trojanowskaja, J. Gatzke, M. Kunitski, F. Trinter, S. Zeller, L. P. H. Schmidt, J. Stohner, R. Berger, A. Czasch, O. Jagutzki, T. Jahnke, R. Dörner, and M. S. Schöffler. “Absolute ion detection efficiencies of microchannel plates and funnel microchannel plates for multi-coincidence detection.” In *Review of Scientific Instruments* **89**(4), (2018), 045112. doi:10.1063/1.5022564.
- [145] V. S. Letokhov and V. G. Minogin. “Laser radiation pressure on free atoms.” In *Physics Reports* **73**(1), (1981), 1–65. doi:10.1016/0370-1573(81)90116-2.
- [146] D. J. Berkeland and M. G. Boshier. “Destabilization of dark states and optical spectroscopy in Zeeman-degenerate atomic systems.” In *Physical Review A* **65**(3), (2002), 033413. doi:10.1103/PhysRevA.65.033413.
- [147] L. Caldwell, J. A. Devlin, H. J. Williams, N. J. Fitch, E. A. Hinds, B. E. Sauer, and M. R. Tarbutt. “Deep Laser Cooling and Efficient Magnetic

- Compression of Molecules.” In *Physical Review Letters* **123**(3), (2019), 33202. doi:10.1103/PhysRevLett.123.033202.
- [148] N. Fitch and M. Tarbutt. *Laser-cooled molecules*, vol. 70 of *Advances In Atomic, Molecular, and Optical Physics*. Academic Press (2021). doi:10.1016/bs.aamop.2021.04.003.
- [149] P. J. Ungar, D. S. Weiss, E. Riis, and S. Chu. “Optical molasses and multilevel atoms: theory.” In *Journal of the Optical Society of America B* **6**(11), (1989), 2058. doi:10.1364/JOSAB.6.002058.
- [150] J. A. Devlin and M. R. Tarbutt. “Laser cooling and magneto-optical trapping of molecules analyzed using optical Bloch equations and the Fokker-Planck-Kramers equation.” In *Physical Review A* **98**(6), (2018), 063415. doi:10.1103/PhysRevA.98.063415.
- [151] O. Grasdijk, O. Tingren, J. Kastelic, T. Wright, S. Lamoreaux, D. DeMille, K. Wenz, M. Aitken, T. Zelevinsky, T. Winick, and D. Kowall. “CeNTREX: a new search for time-reversal symmetry violation in the ^{205}Tl nucleus.” In *Quantum Science and Technology* **6**(4), (2021), 044007. doi:10.1088/2058-9565/abdca3.
- [152] S. Hofsäss, J. E. Padilla-Castillo, S. C. Wright, S. Kray, R. Thomas, B. G. Sartakov, B. Ohayon, G. Meijer, and S. Truppe. “High-resolution isotope-shift spectroscopy of Cd I.” In *Physical Review Research* **5**, (2023), 013043. doi:10.1103/PhysRevResearch.5.013043.
- [153] W. H. King. “Comments on the Article “Peculiarities of the Isotope Shift in the Samarium Spectrum”.” In *Journal of the Optical Society of America* **53**(5), (1963), 638–639. doi:10.1364/JOSA.53.000638.
- [154] C. Solaro, S. Meyer, K. Fisher, J. C. Berengut, E. Fuchs, and M. Drewsen. “Improved Isotope-Shift-Based Bounds on Bosons beyond the Standard Model through Measurements of the $^2\text{D}_{3/2} - ^2\text{D}_{5/2}$ Interval in Ca^+ .” In *Physical Review Letters* **125**, (2020), 123003. doi:10.1103/PhysRevLett.125.123003.
- [155] I. Counts, J. Hur, D. P. L. Aude Craik, H. Jeon, C. Leung, J. C. Berengut, A. Geddes, A. Kawasaki, W. Jhe, and V. Vuletić. “Evidence for Nonlinear Isotope Shift in Yb^+ Search for New Boson.” In *Physical Review Letters* **125**, (2020), 123002. doi:10.1103/PhysRevLett.125.123002.

- [156] N. L. Figueroa, J. C. Berengut, V. A. Dzuba, V. V. Flambaum, D. Budker, and D. Antypas. “Precision Determination of Isotope Shifts in Ytterbium and Implications for New Physics.” In *Physical Review Letters* **128**, (2022), 073001. doi:10.1103/PhysRevLett.128.073001.
- [157] J. Hur, D. P. L. Aude Craik, I. Counts, E. Knyazev, L. Caldwell, C. Leung, S. Pandey, J. C. Berengut, A. Geddes, W. Nazarewicz, P.-G. Reinhard, A. Kawasaki, H. Jeon, W. Jhe, and V. Vuletic. “Evidence of Two-Source King Plot Nonlinearity in Spectroscopic Search for New Boson.” In *Physical Review Letters* **128**, (2022), 163201. doi:10.1103/PhysRevLett.128.163201.
- [158] K. Ono, Y. Saito, T. Ishiyama, T. Higomoto, T. Takano, Y. Takasu, Y. Yamamoto, M. Tanaka, and Y. Takahashi. “Observation of Nonlinearity of Generalized King Plot in the Search for New Boson.” In *Physical Review X* **12**, (2022), 021033. doi:10.1103/PhysRevX.12.021033.
- [159] D. Schussheim and K. Gibble. “Laser system to laser-cool and trap cadmium: towards a cadmium optical lattice clock.” In *Frontiers in Optics / Laser Science*, p. LTh1F.2. OSA (2018). doi:10.1364/ls.2018.lth1f.2.
- [160] A. Yamaguchi, M. S. Safronova, K. Gibble, and H. Katori. “Narrow-line cooling and determination of the magic wavelength of Cd.” In *Physical Review Letters* **123**(11), (2019), 113201. doi:10.1103/PhysRevLett.123.113201.
- [161] Y. Kaneda, J. M. Yarborough, Y. Merzlyak, A. Yamaguchi, K. Hayashida, N. Ohmae, and H. Katori. “Continuous-wave, single-frequency 229 nm laser source for laser cooling of cadmium atoms.” In *Optics Letters* **41**(4), (2016), 705. doi:10.1364/OL.41.000705.
- [162] M. Hammen, W. Nörtershäuser, D. L. Balabanski, M. L. Bissell, K. Blaum, I. Budinčević, B. Cheal, K. T. Flanagan, N. Frömmgen, G. Georgiev, C. Geppert, M. Kowalska, K. Kreim, A. Krieger, W. Nazarewicz, R. Neugart, G. Neyens, J. Papuga, P.-G. Reinhard, M. M. Rajabali, S. Schmidt, and D. T. Yordanov. “From Calcium to Cadmium: Testing the Pairing Functional through Charge Radii Measurements of $^{100-130}\text{Cd}$.” In *Physical Review Letters* **121**, (2018), 102501. doi:10.1103/PhysRevLett.121.102501.
- [163] Á. Koszorús, X. F. Yang, W. G. Jiang, S. J. Novario, S. W. Bai, J. Billowes, C. L. Binnersley, M. L. Bissell, T. E. Cocolios, B. S. Cooper,

- R. P. de Groote, A. Ekström, K. T. Flanagan, C. Forssén, S. Franchoo, R. F. G. Ruiz, F. P. Gustafsson, G. Hagen, G. R. Jansen, A. Kanelakopoulos, M. Kortelainen, W. Nazarewicz, G. Neyens, T. Papenbrock, P.-G. Reinhard, C. M. Ricketts, B. K. Sahoo, A. R. Vernon, and S. G. Wilkins. “Charge radii of exotic potassium isotopes challenge nuclear theory and the magic character of $N=32$.” In *Nature Physics* **17**(4), (2021), 439–443. doi:10.1038/s41567-020-01136-5.
- [164] J. S. Schelfhout and J. J. McFerran. “Multiconfiguration Dirac-Hartree-Fock calculations for Hg and Cd with estimates for unknown clock-transition frequencies.” In *Physical Review A* **105**(2), (2022), 022805. doi:10.1103/PhysRevA.105.022805.
- [165] R. F. G. Ruiz, M. L. Bissell, K. Blaum, A. Ekström, N. Frömmgen, G. Hagen, M. Hammen, K. Hebeler, J. D. Holt, G. R. Jansen, M. Kowalska, K. Kreim, W. Nazarewicz, R. Neugart, G. Neyens, W. Nörtershäuser, T. Papenbrock, J. Papuga, A. Schwenk, J. Simonis, K. A. Wendt, and D. T. Yordanov. “Unexpectedly large charge radii of neutron-rich calcium isotopes.” In *Nature Physics* **12**(6), (2016), 594–598. doi:10.1038/nphys3645.
- [166] A. A. Michelson. “On the application of interference methods to spectroscopic measurements.” In *The London, Edinburgh, and Dublin Philosophical Magazine and Journal of Science* **34**(208), (1892), 280–299. doi:10.1080/14786449208620318.
- [167] A. Russell and R. Rossi. “An investigation of the spectrum of ionium.” In *Proceedings of the Royal Society of London. Series A, Containing Papers of a Mathematical and Physical Character* **87**(598), (1912), 478–484. doi:10.1098/rspa.1912.0100.
- [168] P. Ehrenfest. “The difference between series spectra of isotopes.” In *Nature* **109**(2745), (1922), 745. doi:10.1038/109745c0.
- [169] N. Bohr. “The difference between series spectra of isotopes.” In *Nature* **109**(2745), (1922), 746. doi:10.1038/109746a0.
- [170] J. E. Rosenthal and G. Breit. “The isotope shift in hyperfine structure.” In *Physical Review* **41**(4), (1932), 459. doi:10.1103/PhysRev.41.459.
- [171] G. Racah. “Isotopic displacement and hyperfine structure.” In *Nature* **129**(3263), (1932), 723–724. doi:10.1038/129723a0.

- [172] C. Cohen-Tannoudji, B. Diu, and F. Laloe. *Quantum Mechanics*, vol. 2. John Wiley & Sons Inc (1977). ISBN 0471164356.
- [173] J. C. Berengut, D. Budker, C. Delaunay, V. V. Flambaum, C. Frugieule, E. Fuchs, C. Grojean, R. Harnik, R. Ozeri, G. Perez, and Y. Soreq. “Probing New Long-Range Interactions by Isotope Shift Spectroscopy.” In *Physical Review Letters* **120**, (2018), 091801. doi:10.1103/PhysRevLett.120.091801.
- [174] R. C. Brown, S. Wu, J. V. Porto, C. J. Sansonetti, C. E. Simien, S. M. Brewer, J. N. Tan, and J. D. Gillaspay. “Quantum interference and light polarization effects in unresolvable atomic lines: Application to a precise measurement of the $^{6,7}\text{Li}$ D_2 lines.” In *Physical Review A* **87**, (2013), 032504. doi:10.1103/PhysRevA.87.032504.
- [175] W. Kuhn. “Intensität von Absorptionslinien in Cadmiumdampf.” In *Naturwissenschaften* **14**(3), (1926), 48–49. doi:10.1007/BF01506834.
- [176] M. W. Zemansky. “Absorption der Cadmium-Resonanzstrahlung $\lambda=2288\text{\AA}$ und Lebensdauer des Cd 2^1P_1 -Zustandes.” In *Zeitschrift für Physik* **72**(9-10), (1931), 587–599. doi:10.1007/bf01338497.
- [177] P. Soleillet and J. Ploquin. “A very short period of life of the cadmium atom at excited state by the line 2288\AA .” In *Comptes Rendus Hebdomadaires Des Seances De L’Académie Des Sciences* **217**, (1943), 368–370.
- [178] H. W. Webb and H. A. Messenger. “Lifetimes of Resonance Lines of Cadmium.” In *Physical Review* **66**(3-4), (1944), 77–86. doi:10.1103/PhysRev.66.77.
- [179] H. L. Welsh, J. Kastner, and A. C. Lauriston. “selective reflection from mercury and cadmium vapors.” In *Canadian Journal of Research Section a-Physical Sciences* **28**(2), (1950), 93. doi:10.1139/cjr50a-008.
- [180] A. Lurio and R. Novick. “Lifetime and hfs of the $(5s5p)^1\text{P}_1$ State of Cadmium.” In *Physical Review* **134**, (1964), A608–A614. doi:10.1103/PhysRev.134.A608.
- [181] M. Spitzer. “Duree de vie de letat excite dans le cadmium par la raie de resonance 2288\AA .” In *Comptes Rendus Hebdomadaires Des Seances De L’Académie Des Sciences* **260**(14), (1965), 3907.

- [182] H. Saussereau and M. Barrat. “Effective sections of cadmium atom depolarization at level- 5^1P^1 during collisions with rare gases.” In *Comptes Rendus Hebdomadaires Des Seances De L’Académie Des Sciences Serie B* **268**(6), (1969), 475.
- [183] S. R. Baumann and W. H. Smith. “Atomic Transition Probabilities: Ultraviolet Multiplets of Zn I,II AND Cd I,II.” In *Journal of the Optical Society of America* **60**(3), (1970), 345. doi:10.1364/josa.60.000345.
- [184] R. Pepperl. “Relaxation des 5^1P_1 -Zustandes von Cadmium bei Stößen mit Edelgasatomen und Wasserstoffmolekülen.” In *Zeitschrift für Naturforschung A* **25**(6), (1970), 927–936. doi:10.1515/zna-1970-0622.
- [185] T. Andersen and G. Sørensen. “Systematic trends in atomic transition probabilities in neutral and singly-ionized zinc, cadmium and mercury.” In *Journal of Quantitative Spectroscopy and Radiative Transfer* **13**(4), (1973), 369–376. doi:10.1016/0022-4073(73)90066-6.
- [186] H. L. Xu, A. Persson, S. Svanberg, K. Blagoev, G. Malcheva, V. Pentchev, E. Biemont, J. Campos, M. Ortiz, and R. Mayo. “Radiative lifetime and transition probabilities in Cd I and Cd II.” In *Physical Review A* **70**, (2004), 042508. doi:10.1103/PhysRevA.70.042508.
- [187] P. Thaddeus and R. Novick. “Optical detection of level crossing in the ($5s5p$) 3P_1 state of Cd¹¹¹ and Cd¹¹³.” In *Physical Review* **126**(5), (1962), 1774. doi:10.1103/PhysRev.126.1774.
- [188] F. W. Byron Jr, M. N. McDermott, and R. Novick. “Self-broadening of optical double resonance lines in cadmium.” In *Physical Review* **134**(3A), (1964), A615. doi:10.1103/PhysRev.134.A615.
- [189] W. E. Van der Veer, D. P. Van der Blonk, and A. Donszelmann. “Determination of the Radiative Properties of the $5s5p^3P_1$ and the $5s6s^3S_1$ Levels in Cadmium.” In *Astronomy and Astrophysics* **231**, (1990), 277.
- [190] A. R. Schaefer. “Measured lifetimes of excited states in Cd.” In *Journal of Quantitative Spectroscopy and Radiative Transfer* **11**(2), (1971), 197–201. doi:10.1016/0022-4073(71)90078-1.
- [191] H. D. Koenig and A. Ellett. “Direct Measurement of Mean Lives of Atomic States.” In *Physical Review* **39**(4), (1932), 576. doi:10.1103/PhysRev.39.576.

- [192] M. Czajkowski, R. Bobkowski, and L. Krause. “ $O_u^+(^3\Pi_u)\leftarrow XO_g^+(\Sigma_g^+)$ transitions in Cd_2 excited in crossed molecular and laser beams.” In *Physical Review A* **40**(8), (1989), 4338. doi:10.1103/PhysRevA.40.4338.
- [193] E.-C. Geneux. “Etude, par le résonance magnétique dans des jets atomiques, d’états excités de l’atome de cadmium.” In *Helvetica Physica Acta* **33**(II), (1960), 185. doi:10.5169/seals-113073.
- [194] C. G. Matland. “Natural lifetime of the cadmium 5^3P_1 state.” In *Physical Review*, vol. 91/2, pp. 436–436. American Physical Society (1953).
- [195] J. N. Tinsley, S. Bandarupally, J.-P. Penttinen, S. Manzoor, S. Ranta, L. Salvi, M. Guina, and N. Poli. “Watt-level blue light for precision spectroscopy, laser cooling and trapping of strontium and cadmium atoms.” In *Optics Express* **29**(16), (2021), 25462–25476. doi:10.1364/OE.429898.
- [196] F. M. Kelly and E. Tomchuk. “Isotope Shift in the CdI Intercombination Resonance Line λ 3261 Å.” In *Proceedings of the Physical Society* **74**(6), (1959), 689–692. doi:10.1088/0370-1328/74/6/304.
- [197] R. Kloch, P. E. G. Baird, M. G. Boshier, M. J. Macpherson, C. W. P. Palmer, D. N. Stacey, and V. Stacey. “Isotope shifts in λ 326.1 nm of CdI.” In *Zeitschrift für Physik D -Atoms Molecules and Clusters* **6**(4), (1987), 315–317. doi:10.1007/BF01437057.
- [198] G. R. Hanes. *Hyperfine Structure and Nucleon Configuration Assignments of Cadmium*. Ph.D. thesis, University of Toronto (1955).
- [199] P. Masłowski, K. Bielska, A. Cygan, J. Domysławska, D. Lisak, R. Ciuryło, A. Bielski, and R. S. Trawiński. “The hyperfine and isotope structure of the Cd intercombination line – revisited.” In *The European Physical Journal D* **51**(3), (2009), 295–302. doi:10.1140/epjd/e2008-00242-8.
- [200] J. Z. Han, C. Pan, K. Y. Zhang, X. F. Yang, S. Q. Zhang, J. C. Berengut, S. Goriely, H. Wang, Y. M. Yu, and J. Meng. “Multidimensional Kingplot analysis for accurate extraction of Cd nuclear charge radii: a challenge for nuclear structure theory.” In *arXiv preprint arXiv:2111.04464* doi:10.48550/arXiv.2111.04464.
- [201] G. Fricke and K. Heilig. “48-Cd Cadmium.” In *Nuclear Charge Radii*, pp. 1–9. Springer-Verlag (2004). doi:10.1007/10856314_50.

- [202] J. Z. Han, C. Pan, K. Y. Zhang, X. F. Yang, S. Q. Zhang, J. C. Berengut, S. Goriely, H. Wang, Y. M. Yu, J. Meng, J. W. Zhang, and L. J. Wang. “Isotope shift factors for the $\text{Cd}^+ 5s^2S_{1/2} \rightarrow 5p^2P_{3/2}$ transition and determination of Cd nuclear charge radii.” In *Physical Review Research* **4**, (2022), 033049. doi:10.1103/PhysRevResearch.4.033049.
- [203] R. F. Lacey. *Investigation of the $(5S5P)^3P_1$ Level of Cadmium*. Ph.D. thesis, Massachusetts Institute of Technology (1952).
- [204] R. J. Hull, H. H. Stroke, R. F. Lacey, and H. R. Hirsch. “Nuclear Magnetic Resonance and Hyperfine Structure.” Tech. Rep., Research Laboratory of Electronics (RLE) at the Massachusetts Institute of Technology (MIT) (1959).
- [205] B. Lu and H. Chang. “Theoretical calculations on Landé g-factors and quadratic Zeeman shift coefficients of nsnp 3P_0 clock states in Mg and Cd optical lattice clocks.” In *Chinese Physics B* **32**(1), (2023), 013101. doi:10.1088/1674-1056/ac90b0.
- [206] K. Burns and K. B. Adams. “Energy Levels and Wavelengths of Natural Cadmium and of Cadmium-114.” In *Journal of the Optical Society of America* **46**(2), (1956), 94–99. doi:10.1364/JOSA.46.000094.
- [207] P. W. Spence and M. N. McDermott. “Optical orientation of $6.7\text{h}^{107}\text{Cd}$.” In *Physics Letters A* **42**(4), (1972), 273–274. doi:10.1016/0375-9601(72)90418-5.
- [208] Y. Ting and H. Lew. “Hyperfine Structure of Cu^{63} and Cu^{65} .” In *Physical Review* **105**, (1957), 581–588. doi:10.1103/PhysRev.105.581.
- [209] G. Bardizza. “Setup of a narrow bandwidth UV/VIS laser system for high-resolution spectroscopy of cold large molecules.” M.Sc. Thesis, University Milano, Italy (2005).
- [210] M. Doppelbauer, S. Wright, S. Hofsäss, B. Sartakov, G. Meijer, and S. Truppe. “Hyperfine-resolved optical spectroscopy of the $A^2\Pi \leftarrow X^2\Sigma^+$ transition in MgF .” In *The Journal of Chemical Physics* **156**(13), (2022), 134301. doi:10.1063/5.0081902.
- [211] W. Fairbank Jr, S. Lee, W. Czajkowski, and J. Kluck. “A Laser-cooled Single-atom-on-demand Source For Si Quantum Computing.” In *AIP Conference Proceedings*, vol. 1363, pp. 173–176. American Institute of Physics (2011).

- [212] S. R. Ronald. *Investigation of Laser Cooling and Trapping of Atomic Silicon: Towards the Development of a Deterministic Single Ion Source*. Ph.D. thesis, Colorado State University (2023).
- [213] Y. Colombe, D. H. Slichter, A. C. Wilson, D. Leibfried, and D. J. Wineland. “Single-mode optical fiber for high-power, low-loss UV transmission.” In *Optics Express* **22**(16), (2014), 19783. doi:10.1364/oe.22.019783.
- [214] F. Gebert, M. H. Frosz, T. Weiss, Y. Wan, A. Ermolov, N. Y. Joly, P. O. Schmidt, and P. S. J. Russell. “Damage-free single-mode transmission of deep-UV light in hollow-core PCF.” In *Optics Express* **22**(13), (2014), 15388. doi:10.1364/oe.22.015388.
- [215] K. A. Brickman, M. S. Chang, M. Acton, A. Chew, D. Matsukevich, P. C. Haljan, V. S. Bagnato, and C. Monroe. “Magneto-optical trapping of cadmium.” In *Physical Review A* **76**(4), (2007), 043411. doi:10.1103/PhysRevA.76.043411.
- [216] Q. Lavigne, T. Groh, and S. Stellmer. “Magneto-optical trapping of mercury at high phase-space density.” In *Physical Review A* **105**, (2022), 033106. doi:10.1103/PhysRevA.105.033106.
- [217] C. Foot. *Atomic Physics*. Oxford Master Series in Physics. Oxford University Press (2005). ISBN 9780198506959.
- [218] H. J. Metcalf and P. Van der Straten. *Laser cooling and trapping*. Springer Science & Business Media (1999).
- [219] E. L. Raab, M. Prentiss, A. Cable, S. Chu, and D. E. Pritchard. “Trapping of Neutral Sodium Atoms with Radiation Pressure.” In *Physical Review Letters* **59**(23), (1987), 2631–2634. doi:10.1103/physrevlett.59.2631.
- [220] H. J. Williams, S. Truppe, M. Hambach, L. Caldwell, N. J. Fitch, E. A. Hinds, B. E. Sauer, and M. R. Tarbutt. “Characteristics of a magneto-optical trap of molecules.” In *New Journal of Physics* **19**(11), (2017), 113035. doi:10.1088/1367-2630/aa8e52.
- [221] K. Kim, K.-H. Lee, M. Heo, H.-R. Noh, and W. Jhe. “Measurement of the trap properties of a magneto-optical trap by a transient oscillation method.” In *Physical Review A* **71**, (2005), 053406. doi:10.1103/PhysRevA.71.053406.

- [222] G. Moon, M.-S. Heo, Y. Kim, H.-R. Noh, and W. Jhe. “Measurement of the trap parameters of a magneto-optical trap by external periodic perturbation.” In *Physical Review A* **81**, (2010), 033425. doi:10.1103/PhysRevA.81.033425.
- [223] P. D. Lett, R. N. Watts, C. I. Westbrook, W. D. Phillips, P. L. Gould, and H. J. Metcalf. “Observation of Atoms Laser Cooled below the Doppler Limit.” In *Physical Review Letters* **61**(2), (1988), 169–172. doi:10.1103/physrevlett.61.169.
- [224] B. Hemmerling, G. K. Drayna, E. Chae, A. Ravi, and J. M. Doyle. “Buffer gas loaded magneto-optical traps for Yb, Tm, Er and Ho.” In *New Journal of Physics* **16**(6), (2014), 063070. doi:10.1088/1367-2630/16/6/063070.
- [225] K. Honda, Y. Takahashi, T. Kuwamoto, M. Fujimoto, K. Toyoda, K. Ishikawa, and T. Yabuzaki. “Magneto-optical trapping of Yb atoms and a limit on the branching ratio of the 1P_1 state.” In *Physical Review A* **59**, (1999), R934–R937. doi:10.1103/PhysRevA.59.R934.
- [226] D. N. Madsen and J. W. Thomsen. “Measurement of absolute photoionization cross sections using magnesium magneto-optical traps.” In *Journal of Physics B: Atomic, Molecular and Optical Physics* **35**(9), (2002), 2173–2181. doi:10.1088/0953-4075/35/9/314.
- [227] M. Rafiq, S. Hussain, M. Saleem, M. A. Kalyar, and M. A. Baig. “Measurement of photoionization cross section from the $3s3p^1P_1$ excited state of magnesium.” In *Journal of Physics B: Atomic, Molecular and Optical Physics* **40**(12), (2007), 2291–2305. doi:10.1088/0953-4075/40/12/006.
- [228] S.-U. Haq, S. Mahmood, M. Kalyar, M. Rafiq, R. Ali, and M. Baig. “Photoionization cross section and oscillator strength distribution in the near-threshold region of strontium.” In *The European Physical Journal D* **44**(3), (2007), 439–447. doi:10.1140/epjd/e2007-00219-1.
- [229] M. Witkowski, S. Bilicki, M. Bober, D. Kovačić, V. Singh, A. Tonoyan, and M. Zawada. “Photoionization cross sections of ultracold ^{88}Sr in 1P_1 and 3S_1 states at 390 nm and the resulting blue-detuned magic wavelength optical lattice clock constraints.” In *Optics Express* **30**(12), (2022), 21423–21438. doi:10.1364/OE.460554.

- [230] B. Willke and M. Kock. “Photoionization cross sections from the Ba I (6s6p)¹P₁^o state.” In *Physical Review A* **43**, (1991), 6433–6436. doi:10.1103/PhysRevA.43.6433.
- [231] C. Burkhardt, J. Libbert, J. Xu, J. Leventhal, and J. Kelley. “Absolute measurement of photoionization cross sections of excited atoms: Application to determination of atomic beam densities.” In *Physical Review A* **38**(11), (1988), 5949. doi:10.1103/PhysRevA.38.5949.
- [232] C. D. Wallace, T. P. Dinneen, K. Y. N. Tan, A. Kumarakrishnan, P. L. Gould, and J. Javanainen. “Measurements of temperature and spring constant in a magneto-optical trap.” In *Journal of the Optical Society of America B* **11**(5), (1994), 703. doi:10.1364/josab.11.000703.
- [233] K. N. Jarvis, J. Devlin, T. Wall, B. Sauer, and M. Tarbutt. “Blue-detuned magneto-optical trap.” In *Physical Review Letters* **120**(8), (2018), 083201. doi:10.1103/PhysRevLett.120.083201.

Curriculum Vitae

Simon Lennart Tonio Hofsäss,
born February 08, 1991, in Freiburg im Breisgau, Germany.

2018 – 2022	Ph.D. candidate Molecular Physics Department Fritz-Haber-Institut der Max-Planck-Gesellschaft, Berlin
2015 – 2018	M.Sc Physics University of Freiburg Thesis: “A source of magnetic-quantum-state-selected metastable helium for Penning reaction studies” (Prof. F. Stienkemeier and Dr. K. Dulitz-Erath)
2011 – 2015	B.Sc Physics University of Freiburg and Fraunhofer Institute for Applied Solid State Physics (IAF) Thesis: “Fernfeld Charakterisierung an Hochleistungs-Quantenkaskadenlasern” (Far-field characterization on high-performance quantum cascade lasers) (Prof. J. Wagner and Dr. R. Ostendorf)
2001 – 2010	A-levels (Abitur) Staudinger-Gesamtschule, Freiburg

List of Publications

1. S. Hofsäss, S. C. Wright, J. E. Padilla-Castillo, L. Palanki, R. Thomas, S. Kray, B. G. Sartakov, G. Meijer and S. Truppe. **A large magneto-optical trap of cadmium atoms loaded from a cryogenic buffer gas beam.** *in preparation.*
2. S. Hofsäss, J. E. Padilla-Castillo, S. C. Wright, S. Kray, R. Thomas, B. G. Sartakov, B. Ohayon, G. Meijer and S. Truppe. **High-resolution isotope-shift spectroscopy of Cd I.** *Physical Review Research* **5**, (2023), 013043.
3. B. Ohayon, S. Hofsäss, J. E. Padilla-Castillo, S. C. Wright, G. Meijer, S. Truppe, K. Gibble and B. K. Sahoo. **Isotope shifts in cadmium as a sensitive probe for physics beyond the standard model.** *New Journal of Physics* **24**, (2022), 123040.
4. S. C. Wright, M. Doppelbauer, S. Hofsäss, H. C. Schewe, B. G. Sartakov, G. Meijer and S. Truppe. **Cryogenic Buffer Gas beams of AlF, CaF, MgF, YbF, Al, Ca, Yb and NO – a comparison.** *Molecular Physics*, (2022), e2146541.
5. M. Doppelbauer, S. C. Wright, S. Hofsäss, B. G. Sartakov, G. Meijer and S. Truppe. **Hyperfine-resolved optical spectroscopy of the $A^2\Pi \leftarrow X^2\Sigma^+$ transition in MgF.** *The Journal of Chemical Physics* **156**(13), (2022), 134301.
6. P. Straňák, L. Ploenes, S. Hofsäss, K. Dulitz, F. Stienkemeier and S. Willitsch. **Development and characterization of high-repetition-rate sources for supersonic beams of fluorine radicals.** *Review of Scientific Instruments* **92**, (2021), 103203.

7. S. Hofsäss, M. Doppelbauer, S. C. Wright, S. Kray, B. G. Sartakov, J. Pérez-Ríos, G. Meijer and S. Truppe. **Optical cycling of AlF molecules.** *New Journal of Physics* **23**(7), (2021), 075001.
8. T. Sixt, J. Guan, A. Tsoukala, S. Hofsäss, T. Muthu-Arachchige, F. Stienkemeier and K. Dulitz. **Preparation of individual magnetic sub-levels of $^4\text{He}(2^3\text{S}_1)$ in a supersonic beam using laser optical pumping and magnetic hexapole focusing.** *Review of Scientific Instruments* **92**, (2021), 073203.
9. M. Doppelbauer, N. Walter, S. Hofsäss, S. Marx, H. C. Schewe, S. Kray, J. Pérez-Ríos, B. G. Sartakov, S. Truppe and G. Meijer. **Characterisation of the $b^3\Sigma^+, v = 0$ state and its interaction with the $A^1\Pi$ state in aluminium monofluoride.** *Molecular Physics* **119**(1-2), (2021), e1810351.
10. J. Guan, V. Behrendt, P. Shen, S. Hofsäss, T. Muthu-Arachchige, J. Grzesiak, F. Stienkemeier and K. Dulitz. **Optical Quenching of Metastable Helium Atoms using Excitation to the 4P State.** *Physical Review Applied* **1**, (2019), 054073.
11. S. Truppe, S. Marx, S. Kray, M. Doppelbauer, S. Hofsäss, H. C. Schewe, N. Walter, J. Pérez-Ríos, B. G. Sartakov and G. Meijer. **Spectroscopic characterization of aluminum monofluoride with relevance to laser cooling and trapping.** *Physical Review A* **100**(5), (2019), 052513.

Acknowledgements

I would like to thank the people who have supported, guided or inspired me during my time as a Ph.D. student. I am very grateful to Gerard Meijer, who enabled the AIF project at the Fritz. Gerard's dedicated support, especially on the spectroscopy of AIF, and his frequent inquiries about the status of measurements ("What have you learned?") accelerated my learning progress a lot. I am very thankful to Stefan Truppe for leading the group with great dedication and energetic hands-on support whenever needed. I am especially grateful for the many countless hours we spent together aligning lasers, crawling under the laser table, improving the signal to noise ratio, working on manuscripts, and finally celebrating our results.

During my first weeks as a new Ph.D. student, Silvio and Max took the time to show me how to make a supersonic beam of AIF and how to do some basic spectroscopy. During that time, Sebastian finished assembling a new buffer gas beam machine, which then became my own experiment where I did most of my measurements. Sebastian provided invaluable engineering work and was the driving force in manufacturing of new parts of the experiment and many other projects. With Eduardo I later shared the lab, the office, many laughs and also a passion for grilled deserts. Thanks to Russell "Tommaso" Thomas we worked with perfectly aligned lasers and our lab was always supplied with delicacies for every occasion. When Stefan left to bring AIF to London, Sid made sure the group remained on track and provided invaluable support in writing my thesis and deciphering complex data. The regular tournaments with Henrik, Sandy, Katja and Sebastian made the days of thesis writing more enjoyable. I appreciate Giacomo's input and the collaborative atmosphere between our groups inside and outside the lab. I need to thank Colin Dale, who excavated for me one of the only two remaining copies of a dissertation from 1955 at the University of Toronto. Klaus-Peter Vogelgesang deserves special recognition for his selfless way of finding last-minute solutions to mechanical challenges

and for sharing his invaluable expertise in metalworking and aviation.

Experimenting is one thing, understanding is another, and therefore I am very grateful to our theoreticians Boris, Jesús and Xiangyue for their reliable support and steady interest. Without the technical support of Andreas, Henrik, Marco, Sandy, Stefan S., Thomas and Uwe this work would not have been possible. The same goes for the excellent infrastructure at the Fritz, the mechanical and electronic workshops, PPB, Haustechnik, GNZ, “the Verwaltung”, Martin Schmidt and Carmen Meijer. I would also like to mention the support of my dear colleagues America, Bruno, Dr. H.C. Schewe, Jan, Jenny, Johannes (2), Ju-Hyeon, Katja, Malerz, Marian, Nicole, Sandra and Sascha. I am very happy that Max and I continue to be colleagues in the same field. A special place must be reserved for those who kept the department running and organized. Last but not least, a big thank you to Karin, Manuela, Evelyn and Inga.

I am deeply grateful to my family, with special mention of Marlena’s boundless support and encouragement, which played a pivotal role in the successful completion of my studies and this thesis. My parents have always supported me without hesitation, and despite the geographical distance, Leonie’s moral support and encouragement have been a constant source of inspiration. It was a stroke of luck that my sister, Linda, was pursuing her Ph.D. in Dahlem at the same time, which allowed us to share ideas and support each other during this transformative chapter of our lives.

